To the Graduate Council:
I am submitting herewith a thesis written by Harini Radhakrishnan entitled "Alice in 1D-Land: Fluctuations and particle entanglement in one dimensional systems of identical particles." I have examined the final paper copy of this thesis for form and content and recommend that it be accepted in partial fulfillment of the requirements for the degree of Doctor of Philosophy, with a major in Physics.

Adrian Del Maestro,
Major Professor

We have read this thesis
and recommend its acceptance:

Steve Johnston

Elbio Dagotto

Vasileios Maroulas

Accepted for the Council:

Dixie L. Thompson
Vice Provost and Dean of the Graduate School

To the Graduate Council:
I am submitting herewith a thesis written by Harini Radhakrishnan entitled "Alice in 1D-Land: Fluctuations and particle entanglement in one dimensional systems of identical particles." I have examined the final electronic copy of this thesis for form and content and recommend that it be accepted in partial fulfillment of the requirements for the degree of Doctor of Philosophy, with a major in Physics.

Adrian Del Maestro, Major Professor

We have read this thesis
and recommend its acceptance:

Steve Johnston

Elbio Dagotto

Vasileios Maroulas

Accepted for the Council:

Dixie L. Thompson

Vice Provost and Dean of the Graduate School

(Original signatures are on file with official student records.)

Alice in 1D-Land: Fluctuations and particle entanglement in one dimensional systems of identical particles

A Dissertation Presented for the

Doctor of Philosophy

Degree

The University of Tennessee, Knoxville

Harini Radhakrishnan

August 2025

To my sister, Kiki

One of the secrets of life is that all that is really worth doing is what we do for others.

Lewis Carroll

I can't go back to yesterday because I was a different person then.

— Alice, *Alice's Adventures in Wonderland*

ACKNOWLEDGMENTS

The process of completing a PhD — while often rewarding — is also full of unexpected challenges, shifting perspectives, and sudden turns. The rules don't always make sense, and the answers often lead to new questions. I am extraordinarily lucky to have many people, both old and new, to help me along the way.

First and foremost, I am deeply grateful to my advisor, Adrian Del Maestro. Thank you for skillfully guiding me not only through the peculiarities of one-dimensional quantum systems, but also through the larger landscape of research and graduate life — with all its frustrations and surprises. I've appreciated your detailed and thoughtful answers to even the smallest of questions, your ability to balance departmental leadership with science, and the broader set of skills you helped me develop: from presentation and science communication to outreach. And of course, the push to always be selling. Above all, I am grateful for the intellectual freedom you gave me — the trust to pursue questions I found meaningful, and the encouragement to follow my curiosity down certain rabbit holes. To Professor Steven Johnston, thank you for your steady support over the years. Your Advanced Solid State course remains the best class I've ever taken, thanks to your clarity, care, and willingness to go above and beyond for your students. I deeply appreciate your sense of humor, your generosity with your time, and your empathy — not only with your own students but with all of us.

I also want to thank two professors outside my research area whose mentorship left a lasting mark: Dr. Larry Lee, for teaching me how to teach — how to make classes accessible, engaging, and empathetic; and Dr. Tova Holmes, for many thoughtful, amusing, and encouraging conversations over the years.

Other teachers who have helped me along the way include Professors Max Lavrentovich, Amie Wilkinson, David Schuster, Wendy Zhang, and Mark Oreglia. And finally, I owe a special thanks to my high school physics teacher, Eric Conn, who patiently walked me through my first derivation of special relativity and sent me in this direction a long time ago. I would also like to thank Professors Elbio Dagotto and Vasileios Maroulas for serving on my committee and for their thoughtful feedback and time.

My research group formed the daily ecosystem of work — a space to test ideas and celebrate breakthroughs together. Matthias Thamm has been an especially important presence throughout my PhD. I am deeply grateful for the many hours of conversations, derivations, and patient explanations to all my stupid questions — and for his surprising, hidden whimsy that made research less frustrating and certain papers less exasperating. I hope we have the chance to collaborate again in the future. Dr. Hatem Barghathi offered many helpful suggestions and clever tricks that improved both my calculations and my approach to problems. I admire his sharp intuition. Jon D'Emidio brought infectious passion and clarity to our discussions. His explanations and optimistic outlook always helped reframe difficult moments. Rahul Soni's constant enthusiasm, love of physics, and encouragement were a source of real support. I benefited greatly from his guidance throughout my time here. And to my fellow graduate students — Tweedledee and Tweedledum — Sutirtha – thank you for your wonderful friendship, long conversations, shared interests, and commiseration. Will – I'll miss our morning car rides before group meeting, our talks, and hearing about your progress. I'm excited to watch you both grow, and I look forward to everything that's ahead for you. Please do not ever touch liquid nitrogen again though.

People often underestimate the importance of the professional staff who ensure that academic life runs smoothly. I would like to thank Chrisanne Romeo, Yvonne Real, Tamria Cameron, and Paula Keaton for their behind-the-scenes work and steadfast support throughout my time here. In particular, I thank Catherine

Longmire for her endless kindness, wisdom, and wit — and for always being ready with a word of encouragement (and a Werther's). Her presence makes the department a warmer and more human place.

Special thanks to Amin, Will, Sutirtha, Ryan, Love, Andy, Casey, Jinu, and Matthias for taking the time to read and provide thoughtful feedback and LaTeX assistance on parts of this thesis.

I have been unusually fortunate to enjoy many rich and supportive friendships throughout the years — some still present, others now part of earlier chapters. First, I would like to thank Benjamin Killeen for his spontaneous but always welcome phone calls, and Nina for their warmth, mentorship through undergrad and graduate school, and for being present during my defense. Next, in no particular order, I am grateful to Love, who has taught me so much about myself and what I value in friendships. I am lucky to call her a close friend. Andy, thank you for listening patiently, for many delightful office conversations, and for putting up with my quirks; Daniel, for your sass and for reminding me to stand up for myself. Both of you made sure our foodie adventures were always something to look forward to. I thank Cary for the car rides, wild memes, and endless generosity. My roommates Amber and Marcy, and of course Daisy, made home a comforting and pleasant place. Ryan, thank you for keeping me steady — for your truly awful puns, advice, and genuine care. I'm grateful to old friends who shared their own graduate school trials and kept me grounded — David, Albert, Medha, Chris, Ben^2, Aygul, and Amin. Johnny always reminded me there were things beyond physics and provided lots of sarcasm to boot. Jinu, thank you for understanding me so well and always being easy to tease. Evan, thanks for indulging my media preferences, spirals, and my frequent mental acrobatics. I'm especially thankful to the rest of the Johnston group — Debshikha, Sohan, James, Shreekant, Shruti, and Ben — for making the office fun, surprising, and fulfilling. Shikha offered me tremendous support, help, and mentorship throughout graduate school, for which I am truly grateful. I also want to thank some other graduate students in the

department. Conversations with them consistently brightened my day: so thank you to Colter, Casey, Kaylee, Brandi, Caroline, Adam, Isaac, and Jordan. My group chats — Letterloop and McD — helped me stay connected to long-term friends across distances. Last but not least, thank you to my best friends, Margaret and Angelique, who have been there through every high and low for the past seventeen years. You're the real ones.

Finally, to my family, who gave me the foundation of values and support needed to complete a PhD. I thank my mother, who instilled in me hard work, compassion, and a commitment to education, and my father, who taught me discipline, encouraged a love of science, and modeled perseverance. My parents endeavored to provide mew with the best education possible. To my sister — to whom this thesis is dedicated — thank you for your sunshine, love, and optimism.

I am deeply grateful to everyone listed here. I would not be who I am today without each and every one of you. And a special shoutout to Potchke Deli for giving me babka whenever I needed a pick-me-up.

ABSTRACT

One-dimensional quantum matter, like the Wonderland that astonished Alice, breaks the paradigms of higher-dimensional physics: quasiparticles fragment, spin and charge decouple, and correlations exhibit universal power-law decay. The emergent low-energy theory of these systems is the Tomonaga–Luttinger liquid (TLL). In this thesis, we study the *n-particle entanglement entropy*—the entropy obtained by tracing out $N - n$ particles in a system of N identical fermions. This entropy is sensitive to particle statistics, interactions, and proximity to phase transitions, yet independent of external length scales or basis choice. Because it can be computed from experimentally accessible n-point correlation functions, it offers a powerful probe of many-body correlations and entanglement.

Combining bosonization with large-scale density matrix renormalization group (DMRG) simulations, we extend prior studies on particle entanglement. In Section 2.6.2, we propose and verify a scaling form for the Rényi n-particle entropy in an interacting model, identifying universal contributions and subleading corrections. In Section 3.5, we obtain a closed-form expression for the equal-time four-point function in a fermionic TLL, clarifying the microscopic origins of the entropy scaling. Diagonal elements recover known density correlations, while off-diagonal terms encode particle entanglement for $n > 1$.

We then examine nonequilibrium dynamics in Section 4.6, deriving the time-dependent one-particle entropy following an interaction quench. We show that strong coupling alters the entanglement spectrum and modifies late-time decay exponents. In Section 5.7, we turn to bosonic systems and analyze particle number fluctuations in the Bose–Hubbard model. By fitting DMRG and Quantum Monte Carlo data to bosonization predictions, we extract the Luttinger parameter K and resolve the long-standing location of the Berezinskii–Kosterlitz–Thouless transition. Our finite-size RG scaling reveals the critical point $(U/J)_C$ with high precision.

Together, these results deepen our understanding of entanglement scaling and dynamics in one dimension, and bridge the gap between low-energy field theory and microscopic models. Extensions include finite-temperature effects, spinful systems, and particle entanglement in bosons — promising further adventures down the one-dimensional rabbit hole.

CITATIONS TO PUBLISHED WORK

In Section 2.6.2, we analyze the finite-size scaling of particle entanglement entropy in one-dimensional spinless fermions and introduce a universal scaling function that collapses numerical data across interaction strengths and system sizes. This material is adapted from our paper selected as an Editor's Highlight in Journal of Statistical Mechanics: Theory and Experiment.

> A Scaling Function for the Particle Entanglement Entropy of Fermions
>
> **H. Radhakrishnan**, M. Thamm, H. Barghathi, B. Rosenow, and A. Del Maestro. Journal of Statistical Mechanics (2023) 083101. DOI:10.1088/1742-5468/ace430

Section 4.6 focuses on the dynamics of one-particle entanglement following an interaction quantum quench in one-dimensional spinless fermions, providing both analytic predictions and time-dependent numerics. The results were published in Physical Review B.

> One-Particle Entanglement for One-Dimensional Spinless Fermions After an Interaction Quantum Quench
>
> M. Thamm, **H. Radhakrishnan**, H. Barghathi, B. Rosenow, and A. Del Maestro. Physical Review B **106**, 165116 (2022). DOI:10.1103/PhysRevB.106.165116

Section 5.7 investigates the Berezinskii–Kosterlitz–Thouless renormalization group flow at a quantum phase transition, highlighting universal scaling trajectories obtained from large-scale simulations. This work is currently under review at Physical Review Letters.

> Berezinskii–Kosterlitz–Thouless Renormalization Group Flow at a Quantum Phase Transition

M. Thamm, **H. Radhakrishnan**, H. Barghathi, C. M. Herdman, A. Biswas, B. Rosenow, and A. Del Maestro. arXiv:2502.18622 (Feb 2025).
https://arxiv.org/abs/2502.18622

An additional study employing principal component analysis to map the phase diagram of the interacting Bernevig–Hughes–Zhang model was completed during this research but is *not* included in the dissertation.

Topological and Magnetic Properties of the Interacting Bernevig–Hughes–Zhang Model

R. Soni, **H. Radhakrishnan**, B. Rosenow, G. Alvarez, and A. Del Maestro. Physical Review B **109**, 245115 (2024).
DOI:10.1103/PhysRevB.109.245115

TABLE OF CONTENTS

LIST OF TABLES

LIST OF FIGURES

Curiouser and curiouser!

— Alice, *Alice's Adventures in Wonderland*

INTRODUCTION 1

Much like Alice's descent into a world that defied familiar logic, one-dimensional quantum systems challenge our classical and higher-dimensional intuitions. Physicists often understand interacting quantum matter in higher dimensions through the paradigms of symmetry breaking, Fermi liquid theory, and perturbative corrections around a mean-field background. But in one dimension, this intuition collapses: the Fermi surface reduces to two points, low-energy excitations are collective rather than particle-like, and even weak interactions can destroy quasiparticles entirely [1–3]. Under renormalization group (RG) magnification, the theory itself *changes size* – some couplings balloon while others deflate [4, 5]* . Thus, one-dimensional systems are useful for exploring different universality classes and non-perturbative structures.

At low energies, the universal description of a gapless one-dimensional metal is the *Tomonaga–Luttinger liquid* (TLL): a quantum fluid in which spin and charge propagate independently and correlation functions decay with interaction-dependent power-law exponents. Whereas in three dimensions Fermi liquid theory provides a robust framework of long-lived quasiparticles, the same interactions that merely renormalize masses in 3D completely rewrite the spectrum in 1D: spin and charge decouple into separate gapless modes with distinct velocities. Correlation functions exhibit universal power-law singularities. To quote a certain looking glass wanderer, "Curiouser and curiouser!"

Experiments on momentum-resolved tunnelling between parallel quantum wires [6, 7], Bragg spectroscopy of ultracold atoms [8], and transport through

*Relevant ("Eat Me") operators grow, whereas irrelevant ("Drink Me") operators fade under RG coarse-graining.

nanofabricated Josephson-junction chains [9] have confirmed three universal hallmarks of a TLL. First, the elementary excitations split into two separate dispersing branches, corresponding to independent spin and charge modes. Second, key observables, such as the density of states exhibit power-law decay, with exponents that depend on the interaction strength. Finally, both the velocities of excitations and the Luttinger parameters deviate significantly from their non-interacting counterparts. These results establish TLLs as the universal low-energy fixed point for gapless one-dimensional metals, although strong interactions or commensurability can still drive the system into gapped or otherwise exotic phases. Further realizations include carbon nanotubes [10–13], semiconducting nanowires [14, 15], trapped ions [16], strongly interacting bosons in optical lattices [17], and confined helium in nanopores and nanometer-scale channels [18–23].

In one spatial dimension, certain quantum many-body systems become more analytically tractable because reduced dimensionality imposes constraints. As a result, correlation functions that encode experimentally measurable quantities, for example, density–density or spectral function responses, often admit closed-form expressions via bosonization, integrability, or conformal field theory (CFT). Their scaling exponents reveal universal power laws that distinguish critical phases and transitions [3].

Non-equilibrium probes, such as quantum quenches, provide additional tools to uncover dynamical scaling and emergent light-cone structures [24, 25]. The availability of field-theoretic and numerically efficient methods such as the density matrix renormalization group (DMRG) makes 1D systems an ideal testbed for comparing microscopic models with continuum theories and exploring concepts – such as entanglement scaling, quantum criticality, and topological order – that are also relevant to higher dimensions.

A key theme of this thesis is the quantitative role of entanglement in categorizing quantum matter. The bipartite entanglement entropy (EE), in particular, has emerged as a robust and experimentally accessible probe of the

phase structure of a many-body system [26–28]. In 1D critical systems, CFT predicts that the EE of an interval grows logarithmically with its length, with a prefactor proportional to the central charge, thereby counting the number of emergent gapless degrees of freedom [29]. In gapped phases, the EE saturates to a finite constant that can encode, for example, long-range entanglement characteristic of symmetry-protected or topological order. Yet, by construction, CFT discards the short-distance, model-dependent details necessary for comparison with real materials. In this thesis, we reveal how non-universal details modify the CFT predictions via bosonization, which retains microscopic interaction parameters along with finite-size and lattice corrections.

Previous studies have focused predominantly on *spatial* EE [29–31], in which a contiguous region with an observer "Alice" is entangled with its complement held by "Bob". We instead concentrate on the *n-particle* EE [32–35]. Defined by tracing out all but n particles, the n-particle EE is acutely sensitive to particle statistics, interaction strength, and proximity to quantum phase transitions. Because it is independent of *both* the choice of mode and any externally imposed length scale, it offers complementary insight into many-body correlations and is promising for characterizing resources in quantum information protocols. Furthermore, one can compute the n-particle EE exactly from the n-point correlation functions of the system which are experimentally accessible [36, 37]. A detailed analysis of n-particle EE in an interacting model of spinless fermions forms a central pillar of this work.

1.1 Roadmap of this thesis

This dissertation explores four intertwined projects, each probing quantum entanglement and correlations in one dimension. The document is organized as follows.

1. **Section 1.1:** Lays out the analytical toolkit, bosonization, CFT, and the renormalization group flow, alongside the numerical methods (DMRG and exact diagonalization) employed throughout the thesis, as well as a detailed discussion of the bipartite entanglement entropy.

2. **Section 2.6.2:** Derives and proposes the analytic scaling form of the n-particle Rényi entanglement entropy in the J-V model and benchmarks the result against large-scale DMRG simulations.

3. **Section 3.5:** Obtains a closed-form expression for the equal-time four-point function of a fermionic TLL, clarifying the interplay between universal CFT scaling and non-universal short-distance structure.

4. **Section 4.6:** Analyzes the time evolution of the one-particle EE following an interaction quench, revealing how strong coupling modifies both correlation function decay and the entanglement spectrum.

5. **Section 5.7:** Combines bosonization with Quantum Monte Carlo and DMRG data to extract the Luttinger parameter and locate the Berezinskii–Kosterlitz–Thouless transition, reproducing the correct renormalization group flow.

Together, these works refine our understanding of how correlations and entanglement in one dimension emerge in microscopic systems, accounting for finite-size effects, interactions, and particle statistics. Finally, Section 6.5 synthesizes these insights and discusses extensions for future work, such as particle entanglement in bosonic systems and prospects for experimental verification.

The time has come, the Walrus said,
To talk of many things:
Of shoes—and ships—and sealing-wax—
Of cabbages—and kings.

Lewis Carroll

Through the Looking Glass

BACKGROUND 2

This chapter builds the theoretical and technical foundation for the results to follow. We begin with Luttinger liquid theory and bosonization, which are used in every chapter. Two complementary field theory viewpoints then deepen that picture. Conformal field theory provides exact scaling results for correlation functions at criticality, while renormalization group analysis clarifies how microscopic parameters flow toward, or away from, the Luttinger fixed point. Next, we introduce our main observable of interest, entanglement entropy, with special emphasis on the particle bipartition that is uniquely sensitive to statistics and interactions. We anchor these field-theoretic tools by applying them to two microscopic lattice Hamiltonians: the spinless fermion J-V chain and the one-dimensional Bose–Hubbard model. Finally, we introduce the numerical methods – exact diagonalization and the density matrix renormalization group (DMRG) – used to benchmark continuum theories against microscopic models.

2.1 Luttinger liquid theory

The study of strongly correlated one-dimensional quantum systems has a long and distinguished history. In 1931, Hans Bethe introduced one of the first exact solutions [38]: the Bethe ansatz for the spin-$\frac{1}{2}$ Heisenberg chain. Bethe's method revealed a surprising insight: in one dimension, low-energy excitations do not

behave like individual particles but instead manifest as collective modes. Although this was a major step forward, it would take several more decades of theoretical progress for a complete picture of quantum liquids in one dimension to crystallize.

In 1950, Tomonaga [39] significantly advanced the field by developing a model of interacting fermions that linearized the dispersion near the Fermi surface. This approach treats low-energy excitations as sound waves. However, the formalism was semiclassical in nature and did not fully implement the quantum operator structure required for a consistent microscopic theory. Luttinger addressed this limitation in 1963 [40], by constructing a fermionic field theory with linear dispersion and forward scattering (density-density interactions). However, it incorrectly relied on the assumption of a noninteracting ground state and did not properly normalize fermionic correlation functions.

Mattis and Lieb conclusively resolved these inconsistencies in 1965, by constructing a complete solution of the Luttinger model. Their work explicitly demonstrated the absence of well-defined quasiparticles, in sharp contrast with Landau's Fermi-liquid theory applicable in higher dimensions [41]. They showed that excitations in one-dimensional systems were collective bosonic modes, with Green functions decaying according to non-universal power laws, lacking distinct quasiparticle poles.

In 1981, Haldane synthesized these earlier findings into a single unifying framework: the Tomonaga-Luttinger liquid (TLL) [1]. He argued that a remarkably wide class of gapless, interacting one-dimensional systems - including bosons, fermions, and spin chains — shared a universal low-energy description governed by just two parameters: the renormalized velocity of excitations and the dimensionless Luttinger parameter K. Crucially, this formulation does not depend on specific microscopic details, positioning Luttinger liquid theory as a robust low-energy fixed point in the renormalization group sense. Haldane demonstrated that the breakdown of Fermi liquid theory was a fundamental feature of low-energy

physics in systems constrained to one dimension. This emergent Luttinger liquid description constitutes the theoretical backbone of this thesis.

With this historical context established, we are now ready to explore the physical principles that underpin this profound departure from Fermi liquid behavior. We first detail the breakdown of quasiparticles in one-dimensional systems. Building on this foundation, we systematically construct the TLL Hamiltonian and introduce bosonization [42]. Finally, we extend our discussion to bosonic systems, highlighting how seemingly different microscopic ingredients converge to the same universal low-energy description.

Breakdown of Fermi Liquid Theory

In two and three dimensions, Landau's Fermi liquid (FL) theory [43] accurately describes the low-energy behavior of most systems of interacting fermions. Its primary assumption is that low-energy excitations of an interacting electron gas adiabatically evolve from non-interacting quasiparticles that possess renormalized properties. These quasiparticles have a finite lifetime that diverges when approaching the Fermi surface. We define the single particle dispersion $\chi(k)$, so that the momentum distribution $n(k)$ exhibits a finite discontinuity of height $Z > 0$ (quasiparticle residue) at the Fermi momentum k_F, defined by $\chi(k_F) = E_F$. In one spatial dimension, this premise fails: the restricted space forces particles to scatter primarily by *forward* or $\pm 2k_F$ processes, and the latter generate logarithmically divergent perturbative corrections at every order [2, 3]. Here, the energy is measured from the Fermi level, so we write $E = \hbar\omega$, where ω is the corresponding frequency. The single particle self-energy acquires a non-analytic form,

$$\Sigma(\omega) \;\propto\; |\omega|^{\beta}\,\mathrm{sgn}(\omega), \qquad \beta = \tfrac{1}{2}\big(K + K^{-1}\big) - 1,$$

so the quasiparticle residue $Z = \big[1 - \partial_\omega \Sigma\big]^{-1}$ vanishes algebraically with system size. The dimensionless Luttinger parameter K quantifies interaction strength;

more detail is provided in the next section. The Green function therefore decays as a power law rather than exhibiting a pole,

$$G(x) \;=\; \langle \Psi^{\dagger}(x)\Psi(0)\rangle \sim \frac{e^{ik_F x}}{|x|^{(K+K^{-1})/2}}, \tag{2.1}$$

signaling the absence of long-lived quasiparticles.

Several striking phenomena follow. First, the charge and spin degrees of freedom separate into two independent collective modes that propagate at different velocities ($v_c \neq v_s$); in the uncharged case this is mass-spin separation. Second, the tunneling density of states $N(\omega) \propto |\omega|^{\theta}$ ($\theta = \frac{1}{2}(K + K^{-1}) - 1$), replacing the constant FL DOS. Momentum-resolved tunneling between parallel quantum wires [7, 44] confirms this exponent. Third, the $2k_F$ component of the static charge susceptibility diverges, signaling long-range correlations that amplify both charge density wave (CDW) and superconducting tendencies. Finally, coupling the one-dimensional electron gas to lattice phonons produces a Peierls instability: density modulations at momentum $2k_F$ become relevant perturbations, causing the chain to dimerize and a charge density wave gap to open. Although similar nesting driven instabilities can arise in higher-dimensional Fermi liquids when portions of the Fermi surface are well-nested, the effect is inevitable, highlighting the distinctive richness of 1D behavior.

Luttinger Liquid Hamiltonian

At low energies and long wavelengths, weakly interacting fermions and bosons flow to the same universal phase, described by the TLL Hamiltonian Eq. (2.2). Under renormalization, every gapless, interacting one-dimensional fluid – whether bosonic or fermionic – approaches a *quadratic* fixed point theory whose elementary excitations are linearly dispersing *sound waves* [3, 39, 45]. In hydrodynamic language, these modes correspond to fluctuations of the local density and its conjugate phase; in bosonic field theory, they respectively are captured by the

canonically paired fields $\phi(x)$ and $\theta(x)$, satisfying the commutation relation $[\phi(x), \partial_y \theta(y)] = i\pi\delta(x-y)$. The universal Hamiltonian takes the form

$$H_{\mathrm{TLL}} = \frac{v}{2\pi}\int_{-\infty}^{\infty} dx \left[K\left(\partial_x\theta\right)^2 + \frac{1}{K}\left(\partial_x\phi\right)^2\right], \tag{2.2}$$

where v is the velocity of propagating density waves, and the dimensionless Luttinger parameter K encodes both the interaction strength and the quantum statistics. For free fermions, $v \equiv v_F$. Repulsive, spinless fermions have $K < 1$, attractive fermions have $K > 1$, while repulsive bosons also satisfy $K > 1$, and the non-interacting Bose gas formally corresponds to $K \to \infty$. The parameter K quantifies the relative stiffness of phase and density fluctuations: expressed in terms of the microscopic compressibility κ and the superfluid stiffness, or Drude weight, D, one finds

$$K = \pi\sqrt{\kappa D}, \qquad v = \sqrt{D/\kappa},$$

underscoring the dual role of K in determining both phase and density dynamics. Increasing interactions suppresses density fluctuations ($K\downarrow$) and increases phase rigidity, while attractive interactions have the opposite effect. Microscopic couplings enter only through the two parameters K and v at low energies.

Because H_{TLL} is quadratic, we diagonalize it via a Bogoliubov squeezing transformation, and can compute correlation functions exactly through Gaussian integrals. TLL theory thus furnishes a nonperturbative, field-theoretic toolkit that renders otherwise inaccessible many-body correlation functions analytically tractable. In the sections below, we systematically sketch how this framework applies to both fermionic and bosonic systems.

2.1.1 *Fermions*

Throughout this section, we follow the exposition of [46]. First, we linearize the Fermi dispersion so that every low energy excitation appears as small density

fluctuations around an average density background and can be expressed by bosonic operators. Then, we discuss the incorporation of electron-electron interactions. Finally, we outline *refermionization*, the inverse map that reconstructs fermionic field operators from bosonic modes and thereby enables exact calculations of correlation functions.

Linearization of the Fermi dispersion

A faithful TLL description requires that the observables of interest be dominated by low-energy excitations. We therefore confine the allowed momenta to narrow windows around the two Fermi points (where $\chi(k) = 0$),

$$k \in [\,\pm k_F - \Lambda,\, \pm k_F + \Lambda\,],$$

whose half-width Λ is set by the range over which the single-particle dispersion $\chi(k)$ is approximately linear; see Fig. 2.1.

Excitations near $+k_F$ propagate to the right, while those near $-k_F$ propagate to the left. Throughout, we label right ($\alpha = +, R$) and left ($\alpha = -, L$) movers by the index α (and, where useful, β). For now, we assume a generic non-interacting Hamiltonian for spinless fermions

$$H = \sum_k \chi(k) c_k^\dagger c_k \approx \sum_{k=-k_F-\Lambda}^{-k_F+\Lambda} \chi(k) c_k^\dagger c_k + \sum_{k=k_F+-\Lambda}^{k_F+\Lambda} \chi(k) c_k^\dagger c_k. \tag{2.3}$$

Formally expanding the dispersion around the Fermi points to linear order is done by

$$\chi(k) = \chi(\pm k_F) + (k \mp k_F) \left.\frac{\partial \chi(k)}{\partial k}\right|_{\pm k_F} + \mathcal{O}\big((k - k_F)^2\big) \tag{2.4}$$

The slope of the dispersion is just the Fermi velocity,

$$\pm v_F = \left.\frac{\partial \chi(k)}{\partial k}\right|_{\pm k_F} \tag{2.5}$$

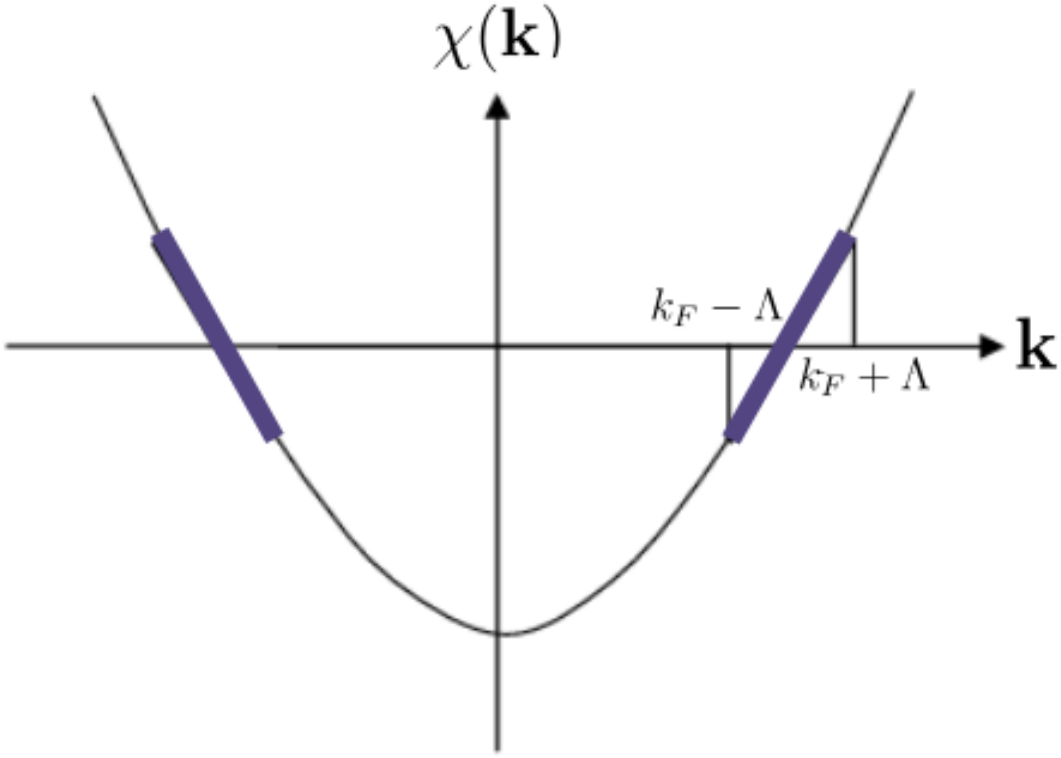

Figure 2.1: Momentum intervals in which the dispersion $\chi(k)$ is linearized. Right movers occupy $k_F - \Lambda < k < k_F + \Lambda$; left movers occupy $-k_F - \Lambda < k < -k_F + \Lambda$.

The fermion operators for left and right operators are defined as $\tilde{c}_{\alpha,q} \equiv c_{\alpha,k_F+q}$ where q is the momentum relative to the Fermi points. The Hamiltonian, Eq. (2.3) in terms of these operators is

$$H \approx \sum_{q=-\Lambda}^{\Lambda} v_F q(\tilde{c}^\dagger_{+,q}\tilde{c}_{+,q} - \tilde{c}^\dagger_{-,q}\tilde{c}_{-,q}) \tag{2.6}$$

We can decompose the second-quantized field operator that annihilates a fermion at position x into its chiral components:

$$\begin{aligned}\Psi(x) &= \frac{1}{\sqrt{L}}\sum_k e^{ikx}c_k \\ &\approx \frac{1}{\sqrt{L}}\sum_q \left(e^{ik_Fx}e^{iqx}\tilde{c}_{+,q} + e^{-ik_Fx}e^{iqx}\tilde{c}_{-,q}\right) \\ &\equiv e^{ik_Fx}\Psi_+(x) + e^{-ik_Fx}\Psi_-(x)\end{aligned} \tag{2.7}$$

$\Psi_\pm(x)$ are slowly varying envelope fields that encode the right- and left-moving degrees of freedom. The sum over q ranges from $-\infty$ to ∞ which is allowed as we have restricted high-energy excitations to not include states $|q| > \Lambda$. This ensures that the chiral operators

$$\Psi_\alpha(x) = \frac{1}{\sqrt{L}}\sum_q e^{iqx}\tilde{c}_{\alpha,q} \tag{2.8}$$

obey the fermionic anticommutator relations, $\{\Psi^\dagger_\alpha(x), \Psi_{\alpha'}(y)\} = \delta_{\alpha\alpha'}\delta(x-y)$ and $\{\Psi_\alpha(x), \Psi_{\alpha'}(y)\} = 0$.

Bosonization

The crux of bosonization is describing low-energy excited states in terms of bosonic operators. Taking a ground state where all states with $|k| < k_F$ are occupied and the higher states are empty, we can construct an excited state by adding excess electrons and shifting the occupied states upward. These shifting operators are

given by

$$\rho_\alpha(q) = \sum_k \tilde{c}^\dagger_{\alpha,k+q}\,\tilde{c}_{\alpha,k}, \tag{2.9}$$

$$\rho^\dagger_\alpha(q) = \rho_\alpha(-q). \tag{2.10}$$

Here, k is a dummy momentum index. Thus, $\rho_\alpha(q)$ is just the q-th Fourier component of the chiral density $n_\alpha(x) = \tilde{c}^\dagger_\alpha(x)\tilde{c}_\alpha(x)$. It removes a fermion with momentum k and recreates it at $k+q$, creating a particle–hole excitation that carries total momentum q.

The commutator between these operators are given by

$$\begin{aligned}[\rho_{\alpha,q_1}, \rho_{\alpha',q_2}] &= \delta_{\alpha,\alpha'} \sum_{q'}\sum_{q''} \left(\delta_{q',q_2+q''}\tilde{c}^\dagger_{\alpha,q_1+q'}\tilde{c}_{\alpha,q''} - \delta_{q'',q_1+q'}\tilde{c}^\dagger_{\alpha,q_2+q''}\tilde{c}_{\alpha,q'}\right) \\ &= \delta_{\alpha,\alpha'} \sum_{q'} \left(\tilde{c}^\dagger_{\alpha,q'+q_1}\tilde{c}_{\alpha,q'-q_2} - \tilde{c}^\dagger_{\alpha,q'+q_2+q_1}\tilde{c}_{\alpha,q'}\right). \end{aligned} \tag{2.11}$$

Evaluating this commutator is subtle, as the dummy indices q' and q'' run over infinite values. This infinite range reflects the filled "Dirac sea" of negative-energy states after linearizing the dispersion; there are infinite occupied states with negative energy. To resolve this divergence, we impose the hard cutoff Λ so all states with $q < -\Lambda$ are occupied. If $q_1 \neq -q_2$, we reindex the sums to cancel so the commutator vanishes. When $q = -q_2$, the divergence collapses to a difference of number operators $n_{\alpha,q} = \tilde{c}^\dagger_{\alpha,q}\tilde{c}_{\alpha,q}$ when $q < -\Lambda$. Using $q = 2\pi m/L, m \in \mathbb{Z}$, the

commutator is therefore

$$\begin{aligned}
[\rho_{\alpha,q_1}, \rho_{\alpha',q_2}] &= \delta_{\alpha,\alpha'}\delta_{q_1,-q_2} \sum_{q' \geq -\Lambda} (n_{\alpha,q'-q_2} - n_{\alpha,q'}) \\
&= \delta_{\alpha,\alpha'}\delta_{q_1,-q_2} \left(\sum_{q' \geq -\Lambda - q_2} n_{\alpha,q'} - \sum_{q' \geq -\Lambda} n_{\alpha,q'} \right) \\
&= \delta_{\alpha,\alpha'}\delta_{q_1,-q_2} \sum_{-\Lambda - q_2 \leq q' \leq -\Lambda} 1 \\
&= \delta_{\alpha,\alpha'}\delta_{q_1,-q_2} \frac{qL}{2\pi}
\end{aligned} \tag{2.12}$$

Since the commutator between two density modes is proportional to a c-number ($\frac{qL}{2\pi}$), it is precisely the algebra of harmonic oscillator creation and annihilation operators. Thus, each density fluctuation $\rho_{\alpha,\pm q}$ behaves like a bosonic mode. It is therefore natural to introduce bosonic ladder operators $b_{\alpha,q}$ and $b^\dagger_{\alpha,q}$ that satisfy the commutation relations $[b_{\alpha,q}, b_{\alpha',q'}] = 0$, $[b_{\alpha,q}, b^\dagger_{\alpha',q'}] = \delta_{\alpha\alpha'}\delta_{qq'}$. These are given by

$$b^\dagger_{\alpha,q} = \alpha i \sqrt{\frac{2\pi}{qL}} \rho_{\alpha,\alpha q} \tag{2.13}$$

$$b_{\alpha,q} = -\alpha\, i \sqrt{\frac{2\pi}{qL}}\, \rho_{\alpha,-\alpha q}, \tag{2.14}$$

Evaluating the commutator $[H, b_{\alpha,q}]$ for free fermions one finds

$$[H, b_{\alpha,q}] = v_F \sum_{\alpha'} \sum_{q'} \alpha'\, q' \sqrt{\frac{2\pi}{q'L}} \left[\tilde{c}^\dagger_{\alpha',q'+q} \tilde{c}_{\alpha',q'} - \tilde{c}^\dagger_{\alpha',q'} \tilde{c}_{\alpha',q'-q} \right] = v_F q\, b_{\alpha,q}, \tag{2.15}$$

which, together with the ladder algebra, identifies $b^\dagger_{\alpha,q}$ and $b_{\alpha,q}$ as harmonic oscillator modes of energy $v_F q$. Hence the non-interacting Hamiltonian becomes

$$H = \sum_{q=-\Lambda}^{\Lambda} v_F q \left(\tilde{c}^\dagger_{+,q} \tilde{c}_{+,q} - \tilde{c}^\dagger_{-,q} \tilde{c}_{-,q} \right) = v_F \sum_{q>0} q \left(b^\dagger_{+,q} b_{+,q} + b^\dagger_{-,q} b_{-,q} \right) + \frac{\pi v_F}{L} \left(N_+^2 + N_-^2 \right), \tag{2.16}$$

where we have rewritten each fermionic number operator $\tilde{c}^{\dagger}_{\alpha,q}\tilde{c}_{\alpha,q}$ in terms of the density modes $\rho_{\alpha,\pm q}$ and then substituted the bosonic representation $\rho_{\alpha,\pm q} = \sqrt{\frac{qL}{2\pi}}\,(b^{\dagger}_{\alpha,\pm q} + b_{\alpha,\pm q})$. The quantity

$$N_{\alpha} = \sum_{q>0} \tilde{c}^{\dagger}_{\alpha,q}\tilde{c}_{\alpha,q} - \sum_{q\leq 0} \tilde{c}_{\alpha,q}\tilde{c}^{\dagger}_{\alpha,q}$$

counts the excess number of right-moving ($\alpha = +$) and left-moving ($\alpha = -$) fermions; the zero-mode term $\frac{\pi v_F}{L}(N_+^2 + N_-^2)$ accounts for the finite energy cost of adding or removing whole particles and originates from the $q = 0$ component that is not included in the sum of the oscillator.

Interactions

The true power of bosonization lies in handling interacting systems: quartic fermion operators translate into quadratic boson operators, rendering many-body interaction terms analytically tractable.

For spinless fermions, the density–density interaction reads

$$H_{\text{int}} = \int dx \int d\Delta x\, \Psi^{\dagger}(x)\Psi(x)\, U(\Delta x)\, \Psi^{\dagger}(x+\Delta x)\Psi(x+\Delta x) \tag{2.17}$$

$$= \frac{1}{2L}\sum_{k,k',q} c^{\dagger}_{k}c_{k-q}\, U(q)\, c^{\dagger}_{k'}c_{k'+q}, \tag{2.18}$$

Fig. 2.2 depicts the generic two-body scattering process mediated by $U(q)$. Now, we repeat the bosonization procedure to include interactions. The Fourier transform of the density–density interaction is

$$U_q = \int d\Delta x\, e^{iq\Delta x} U(\Delta x).$$

Restricting to low-energy excitations and small momentum transfer (so that the interaction never converts a right mover into a left mover) gives

$$\sum_k c_k^\dagger c_{k\pm q} \;\approx\; \rho_{+,q}\rho_{+,-q} + \rho_{-,q}\rho_{-,-q}. \tag{2.19}$$

In oscillating-density notation our bosonized Hamiltonian becomes

$$H_{\text{int}} \approx \frac{1}{2L}\sum_q \Big[g_4\big(\rho_{+,q}\rho_{+,-q} + \rho_{-,q}\rho_{-,-q}\big) + g_2\big(\rho_{+,q}\rho_{-,-q} + \rho_{-,q}\rho_{+,-q}\big)\Big]. \tag{2.20}$$

The various couplings g_2, g_3, and g_4 are traditionally organized in the so-called *g-ology* classification, summarized in Table 2.1 [3]:

1. For small momentum transfer $\Delta k < \Lambda$, forward scattering ($R \to R$, $L \to L$) and forward-dispersion scattering ($R \leftrightarrow L$).
2. For large momentum transfer $\Delta k \approx \pm 2k_F$, backward scattering ($R \leftrightarrow L$).
3. Umklapp scattering (neglected here) at $\Delta k = \pm 4k_F$, where $2L \leftrightarrow 2R$.

Using Eq. (2.14),

$$\begin{aligned} H_{\text{int}} \approx \frac{1}{2\pi}\sum_{q>0}\Big[g_2\big(b_{+,q}b_{+,q}^\dagger + b_{-,q}b_{-,q}^\dagger\big) + g_4\big(b_{+,q}^\dagger b_{+,q} + b_{-,q}^\dagger b_{-,q}\big)\Big] \\ + \frac{g_4}{L}\big(N_+^2 + N_-^2\big) + \frac{2g_2}{L}N_+N_- + \text{const.} \end{aligned} \tag{2.21}$$

In certain chapters to match the literature conventions, we will write

$$H = \sum_{q\neq 0}\big[\omega_0(q) + m(q)\big]\, b_q^\dagger b_q + \frac{1}{2}\sum_{q\neq 0} g_2(q)\big(b_q b_{-q} + b_q^\dagger b_{-q}^\dagger\big), \tag{2.22}$$

where $\omega_0(q) = v_F|q|$ and $m(q) = g_4(q)|q|$, with $q_n = 2\pi n/L$, $n \in \mathbb{Z}\setminus\{0\}$.

Table 2.1: Scattering channels for one-dimensional interacting fermions.

Channel	Δk	Process (chirality)	Coupling
Forward (same-branch)	$\ll k_F$	$R \to R,\ L \to L$	$g_4(q)$
Forward dispersion (opposite-branch)	$\ll k_F$	$R \leftrightarrow L$	$g_2(q)$
Backward (opposite-branch)	$\approx \pm 2k_F$	$R \leftrightarrow L$	$g_2(q)$
Umklapp (neglected)	$\pm 4k_F$	$2R \leftrightarrow 2L$	$g_3(q)$

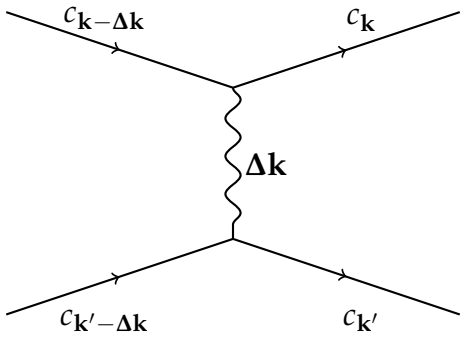

Figure 2.2: Scattering process corresponding to the interaction term in Eq. (2.18). Incoming branches correspond to either a right- or left- moving fermion.

We have thus mapped the full fermionic Hamiltonian $H = H_{\text{nonint}} + H_{\text{int}}$, originally quartic in the c-operators, onto a *quadratic* bosonic Hamiltonian. Because it is harmonic, the model is exactly solvable: we can express every observable in terms of bosonic operators. This analytical technique is a decisive advantage of bosonization, and we will exploit it in Section 3.5 and Section 4.6 to study a continuum description of spinless fermions.

Refermionization

To evaluate correlation functions—and, ultimately, the reduced density matrices used throughout this thesis—we need an explicit representation of the fermionic field operators in terms of the bosonic modes introduced above. We begin by defining the bosonic phase fields [47]

$$\phi_\alpha(x) = -\sum_{q>0} \sqrt{\frac{2\pi}{qL}}\, e^{-q\eta/2} \left[e^{i\alpha qx} b_{\alpha q} + e^{-i\alpha qx} b^\dagger_{\alpha q}\right], \tag{2.23}$$

where η is an ultraviolet regulator measured in units of the lattice spacing that will be sent to 0 in our calculations. We can recover the two field operators in Eq. (2.2) by

$$\begin{aligned} \phi(x) &= \frac{\phi_R(x) + \phi_L(x)}{2} \\ \theta(x) &= \frac{\phi_R(x) - \phi_L(x)}{2}. \end{aligned} \tag{2.24}$$

Consider the inverse Fourier transform of the *normal-ordered* density operator for α-movers:

$$\int dx\, e^{ikx} \;:\psi^\dagger_\alpha(x)\psi_\alpha(x):= \frac{1}{L}\sum_{k'} :\tilde{c}^\dagger_{\alpha,k'+k}\tilde{c}_{\alpha,k'}:, \tag{2.25}$$

with the normal ordering $:f:=f-\langle f\rangle$ removing ground-state divergences. Splitting the sum into $k' \gtrless 0$ one finds

$$:\tilde{c}^{\dagger}_{\alpha,k'+k}\tilde{c}_{\alpha,k'}:=\begin{cases} -i\alpha\sqrt{\dfrac{|k|L}{2\pi}}\,b^{\dagger}_{\alpha,|k|} & \alpha k>0,\\ N_\alpha & \alpha k=0,\\ i\alpha\sqrt{\dfrac{|k|L}{2\pi}}\,b_{\alpha,|k|} & \alpha k<0,\end{cases} \tag{2.26}$$

where N_α counts excess right- or left-moving particles. Re-inserting Eq. (2.26) into Eq. (2.25) and Fourier-inverting yields the normal-ordered product

$$:\psi^{\dagger}_{\alpha}(x)\psi_\alpha(x):=\frac{1}{L}\sum_{q>0}\sqrt{\frac{qL}{2\pi}}\left(\alpha i b_{\alpha,q}e^{i\alpha qx}-\alpha i b^{\dagger}_{\alpha,q}e^{-i\alpha qx}\right)+\frac{N_\alpha}{L}. \tag{2.27}$$

Hence

$$-\frac{\partial_x\phi_\alpha(x)}{2\pi}+\frac{N_\alpha}{L}=:\psi^{\dagger}_{\alpha}(x)\psi_\alpha(x):, \tag{2.28}$$

and the free Hamiltonian takes the compact form

$$H=\frac{v_F}{2}\int dx\sum_\alpha \pi\Big(-\frac{\partial_x\phi_\alpha(x)}{2\pi}+\frac{N_\alpha}{L}\Big)^2 \tag{2.29}$$

$$=v_F\sum_{q>0}q\left(b^{\dagger}_{+,q}b_{+,q}+b^{\dagger}_{-,q}b_{-,q}\right)+\frac{\pi v_F}{L}\left(N_+^2+N_-^2\right). \tag{2.30}$$

Using Eq. (2.23), we *refermionize* the fermionic field operator as an exponential of the bosonic field [47]:

$$\psi_\alpha(x)=\frac{\chi_\alpha}{\sqrt{2\pi\eta}}\,e^{i\left(\phi_{\alpha,0}+\alpha\frac{2\pi}{L}x\,N_\alpha\right)}e^{-i\alpha\phi_\alpha(x)}, \tag{2.31}$$

where χ_α is a Klein factor ensuring $\{\psi_\alpha,\psi_{\alpha'}\}=0$ and $\chi^{\dagger}_\alpha\chi_\alpha=1$. With Eq. (2.31) and Eq. (2.28) one verifies

$$[\rho_\alpha(x),\psi^{\dagger}_{\alpha'}(x')]=\delta_{\alpha\alpha'}\delta(x-x')\psi^{\dagger}_{\alpha}(x),$$

so the definition is self-consistent and reproduces the correct equal-time anticommutation relations [47]:

$$[\psi_\alpha(x), \psi^\dagger_{\alpha'}(x')] = \delta_{\alpha\alpha'}\,\delta(x - x'). \tag{2.32}$$

Equipped with Eq. (2.29)–Eq. (2.31), we can bosonize any density–density interacting Hamiltonian, diagonalize it, and then refermionize to compute correlation functions.

2.1.2 *Bosons*

The bosonic formalism follows the same spirit as its fermionic counterpart, but its motivation is different. In 1D, Bose particles cannot sustain true long-range order: phase fluctuations destroy the condensate even at zero temperature (the Mermin-Wagner theorem in $d = 1$ [48]). The natural low-energy excitations are therefore *collective density waves*, not individual particles. Bosonization makes this viewpoint explicit by expanding the Bose field around a uniform background density and retaining only long-wavelength fluctuations; a strongly non-linear microscopic Hamiltonian is converted into a *quadratic* theory, providing an analytic description of the system's infrared behavior [1, 49].

Density phase representation

We decompose the continuum field operator into slowly varying density and phase components,

$$\Psi(x) = \sqrt{\rho_0 + \Pi(x)}\, e^{i\theta(x)}, \qquad \rho(x) = \Psi^\dagger(x)\Psi(x) = \rho_0 + \frac{1}{\pi}\,\partial_x\phi(x), \tag{2.33}$$

where $\rho_0 = N/L$ is the mean density, $\Pi(x) = \partial_x\phi/\pi$ encodes long-wavelength density fluctuations, and $\theta(x)$ is the conjugate phase. The hydrodynamic fields

obey

$$[\,\phi(x), \partial_y \theta(y)\,] = i\pi\,\delta(x-y). \tag{2.34}$$

Lieb–Liniger expansion

To see how bosonization emerges from a concrete model, we apply this decomposition to the Lieb–Liniger Hamiltonian for contact interacting bosons. Inserting Eq. (2.33) into the Lieb–Liniger Hamiltonian [3],

$$H_{\mathrm{LL}} = \int dx \left[\frac{\hbar^2}{2m} \left|\partial_x \Psi\right|^2 + \frac{g}{2}\,\rho^2(x) \right], \tag{2.35}$$

and expanding to quadratic order in Π/ρ_0 and $\partial_x\theta$ gives, up to an additive constant,

$$H_{\mathrm{TLL}} = \frac{v}{2\pi} \int dx \Big[K\,(\partial_x\theta)^2 + \frac{1}{K}\,(\partial_x\phi)^2 \Big], \tag{2.36}$$

the Tomonaga–Luttinger liquid Hamiltonian familiar from fermionic systems. Its two parameters,

$$K = \pi\sqrt{\frac{\rho_0}{mg}}, \qquad v = \sqrt{\frac{\rho_0 g}{m}}, \tag{2.37}$$

encode all microscopic details: $K > 1$ for repulsive bosons, with $K \to \infty$ in the weak-interaction limit.

This field-theoretic framework underpins the analysis of the one-dimensional Bose–Hubbard chain in Section 5.7, allowing analytic observables to be compared directly with microscopic DMRG calculations.

2.2 Conformal field theory

In one spatial dimension, quantum critical points possess conformal symmetry; the theory is invariant under local scale transformations that preserve angles. Because the Luttinger liquid Hamiltonian described previously is at a scale-invariant fixed point, we can describe its long-distance behavior in conformal language.

Conformal Field Theory (CFT) therefore provides a continuum description that is mathematically equivalent to bosonization, yet conceptually distinct [2]. Bosonization rewrites low-energy physics in terms of hydrodynamic density and phase fields, retaining non-universal amplitudes needed for comparison with microscopic models. CFT, on the other hand, isolates universal exponents (i.e. the scaling dimensions that determine the power-law decay of correlation functions). It organizes the physics into holomorphic ($z = v\tau + ix$) and antiholomorphic ($\bar{z} = v\tau - ix$) sectors that parameterize light cone directions. Here, v is the sound velocity introduced in Eq. (2.2), τ is imaginary time, and x is the spatial coordinate. Right-moving (chiral) excitations in a TLL depend only on the holomorphic coordinate, left-moving ones depend on the antiholomorphic coordinate.

An infinitesimal conformal map $z \to z + \epsilon(z)$ is generated by

$$l_n = -z^{n+1}\partial_z, \qquad n \in \mathbb{Z},$$

and similarly $\bar{l}_n$ for the antiholomorphic sector. The three generators l_{-1}, l_0, l_{+1} produce global conformal moves (i.e. translations, dilations, and rotations). The $l_n, |n| > 1$ generate local deformations that obey the classical *Witt algebra*: $[l_n, l_m] = (n-m)l_{n+m}$. When the theory is quantized, there is a central extension known as the *Virasoro algebra* [50],

$$[L_m, L_n] = (m-n)L_{m+n} + c\,\frac{m(m^2-1)}{12}\,\delta_{m+n,0}, \qquad m, n \in \mathbb{Z}, \tag{2.38}$$

(and an identical copy for $\bar{L}_n$ with $[L_n, \bar{L}_m] = 0$). The commutator guarantees that conformal deformations combine associatively; applying L_m and L_n is equivalent to applying L_{m+n}. Additionally, it ensures energy-momentum conservation. The constant c in Eq. (2.38) is the *central charge*: it measures the number of effective gapless degrees of freedom. In a one-dimensional Luttinger liquid, the fixed point

theory is a *free compact boson*. For a single-component Luttinger liquid, $c = 1$. Additional channels such as a spin sector would increase c.

To connect the central charge to observable scaling, we introduce primary fields which build all the operators in a CFT. A local field $\mathcal{O}(z, \bar{z})$ is called *primary* if, under an analytic change of coordinates $z \to w(z)$, $\bar{z} \to \bar{w}(\bar{z})$ [*], it transforms as

$$\mathcal{O}'(w, \bar{w}) = \left(\frac{dw}{dz}\right)^{-\Delta} \left(\frac{d\bar{w}}{d\bar{z}}\right)^{-\bar{\Delta}} \mathcal{O}(z, \bar{z}), \tag{2.39}$$

where $(\Delta, \bar{\Delta})$ are its holomorphic and antiholomorphic scaling dimensions. In radial quantization the modes act on a primary $\mathcal{O}$ via the contour-shift identity $[L_n, \mathcal{O}(z, \bar{z})] = z^{n+1}\partial_z \mathcal{O} + (n+1)\Delta\, z^n \mathcal{O}$. Thus, $L_{-1}\,\mathcal{O} = \partial_z \mathcal{O} \to L_{-1}$ generates infinitesimal translations along the light-cone coordinate z, while $L_0\,\mathcal{O} = \Delta\,\mathcal{O}$ simply reads off the scaling dimension. Repeated action of $L_{-n} (n > 0)$ produces the *descendant* fields $L_{-n_1} \dots L_{-n_k}\,\mathcal{O} \propto \partial_z^{n_1} \dots \partial_z^{n_k} \mathcal{O}$, which correspond to higher harmonic density waves in the hydrodynamic language of Section 2.1. In the TLL, the natural primary fields are the chiral *vertex operators* [49]

$$V_{\alpha,\beta}(z, \bar{z}) = e^{i\left[\alpha\,\phi_R(z) + \beta\,\phi_L(\bar{z})\right]},$$

where $\phi_{R/L}$ are the right- and left-moving bosonic fields introduced earlier, and $(\alpha, \beta) \in \mathbb{R}$ label charge and current quantum numbers.

The Euclidean action for the free *compact* boson is

$$\mathcal{L}_{\text{CFT}} = \frac{1}{8\pi K}\Big[(\partial_\tau \Phi)^2 + v^2 (\partial_x \Phi)^2\Big], \tag{2.40}$$

where we set $\hbar = 1$ and keep v explicit.[†]

[*] Holomorphic and antiholomorphic sectors are independent, without the assumption of complex conjugation.

[†] Rescaling $\tau \to v\tau$ returns the isotropic form $\mathcal{L} = (8\pi K)^{-1}(\partial_\mu \Phi)^2$, which reproduces the propagator $\langle \Phi(z)\Phi(0)\rangle = -K \ln |z|^2$.

By compactness, we mean the field Φ is single valued on a circle rather than the real line:

$$\Phi \equiv \Phi + 2\pi R \quad \Longrightarrow \quad \Delta\Phi = 2\pi R. \tag{2.41}$$

$\Delta\Phi$ measures the winding as x traverses the system. The constant R is the *compactification radius*. For one-dimensional Luttinger liquids the radius is not a free parameter but fixed by the Luttinger parameter [2]:

$$R^2 = K. \tag{2.42}$$

For a vertex operator $V_\alpha(z) = \exp\big[i\alpha\Phi(z)\big]$, Wick's theorem gives the two-point function $\langle V_\alpha(z) V_{-\alpha}(0)\rangle \propto z^{-\alpha^2 R^2/(2\pi)}$. The exponent is twice the *holomorphic conformal weight* Δ_α; hence

$$\Delta_\alpha = \frac{\alpha^2 R^2}{4\pi} = \frac{\alpha^2 K}{4\pi}\,.$$

For a purely right-moving operator the antiholomorphic weight is $\bar{\Delta}_\alpha = 0$; left-movers exchange the two [‡].

All physical quantities accessible within CFT ultimately depend on c and the conformal weights $(\Delta, \bar{\Delta})$ of the primary operators.

Finally, we outline how to compute correlation functions in this formalism. The central computational tool in CFT is the *operator product expansion* (OPE) [51]. When two local operators approach each other, their product can be replaced by a convergent series of local operators that can be used inside any correlation function. For two local operators $\mathcal{O}_i(z)\,\mathcal{O}_j(0)$ one writes

$$\mathcal{O}_i(z)\,\mathcal{O}_j(0) \;=\; \sum_k C_{ij}^k\, z^{\Delta_k - \Delta_i - \Delta_j}\, \bar{z}^{\bar{\Delta}_k - \bar{\Delta}_i - \bar{\Delta}_j}\, \mathcal{O}_k(0) \;+\; \ldots. \tag{2.43}$$

Here, the sum runs over all primaries and their descendants allowed by symmetry. The C_{ij}^k are structure constants and the ellipsis denotes regular terms, or terms

[‡]The weights here are the same as the scaling dimensions defined earlier. However, the scaling dimension frequently cited in condensed matter is the sum of the two weights $x = \Delta + \bar{\Delta}$

that do not affect long-distance singularities. Multipoint correlators follow directly by repeated OPE insertion.

Both CFT and bosonization stem from the same chiral algebra, and the free boson CFT of Eq. (2.40) is the *fixed point* theory of the bosonized Hamiltonian, Eq. (4.1). Bosonization, however, remains an *effective* framework valid up to the cutoff $v_F\Lambda$, retaining non-universal parameters (K, v) and thereby encoding lattice information. CFT, by contrast, captures only the universal long-distance behavior; its predictions receive controlled corrections once one reinstates the cutoff and irrelevant operators (in the RG sense). Quantitative comparison with finite-lattice simulations requires the additional, interaction specific information retained by bosonization. We show this distinction in Section 3.5 when computing the four-point correlation function for spinless fermions.

2.3 Renormalization Group

Although bosonization and CFT describe the universal fixed-point behavior of the TLL, it is important to understand how and when microscopic perturbations, e.g. lattice scale effects, modify that fixed point. The renormalization group (RG) formalism provides a framework for understanding how a theory evolves under changes in scale. Conceptually, RG describes the process of *zooming out*. By integrating out short-wavelength, or high-energy, fluctuations, one obtains an effective description valid at longer distances. In doing so, the strength of interactions embedded in coupling constants becomes scale dependent; perturbations grow or shrink depending on their scaling dimensions. The theory tracks this flow in three steps:

1. **Coarse–graining**—integrate out high energy modes in a momentum shell $\Lambda/b < |k| < \Lambda$;

2. **Rescaling**—restore the original cutoff by $x \to b\,x$, $\tau \to b\,\tau$ (so the length scale ℓ grows as $\ell \to e^{l}\ell$ with RG "time" $l = \log b$);

3. **Renormalizing**—absorb the change into couplings. [4].

This technique is especially powerful in one dimension; Luther, Peschel, and Haldane applied these ideas to fermionic chains and demonstrated many lattice models flow towards the TLL fixed line [1, 52]. Specifically, couplings in the TLL Hamiltonian are really functions of l ($K \equiv K(l), v \equiv v(l)$), which we will exploit later to examine a system where finite-size scaling is needed.

The Euclidean TLL action in dual bosonic fields ϕ and Θ,

$$\mathcal{S}_0 = \frac{1}{2\pi}\int d\tau\, dx \left[vK(\partial_x\Theta)^2 + v^{-1}K^{-1}(\partial_\tau\phi)^2\right] \tag{2.44}$$

defines the Gaussian fixed point of the theory. The fields are compact, $\phi \equiv \phi + 2\pi$ and $\Theta \equiv \Theta + 2\pi$ and canonically conjugate $[\phi(x), \partial_{x'}\Theta(x')] = i\pi\delta(x - x')$ [§].

Adding symmetry allowed ($U(1)$ and lattice translation invariant) perturbations, $\mathcal{O}_{m,n} = \cos\big(m\phi + n\theta\big)$ with couplings, $g_{m,n}$, models lattice effects. The cosine term acts like a periodic "pinning" potential for the field combination $m\phi + n\theta$. When its amplitude becomes large enough, the system lowers its energy by locking that combination into one of the potential minima. If the locked field is ϕ, the long-wavelength density $\rho(x) \propto \partial_x\phi(x)$ freezes into a spatially periodic pattern, yielding a charge density wave with wave-vector $2\pi m/a$ fixed by the lattice. Decomposing ϕ and Θ into chiral parts $\phi_{R/L}(z, \bar{z}) = (\phi \pm \Theta)/2$ shows that $O_{m,n}$ factorizes into vertex operators $e^{\pm i(\alpha\phi_R + \beta\phi_L)}$ whose holomorphic/antiholomorphic weights are

$$(\Delta^R_{m,n},\ \Delta^L_{m,n}) \ = \ \Big(\tfrac{1}{4}\big(m\sqrt{K} + n/\sqrt{K}\big)^2,\ \tfrac{1}{4}\big(m\sqrt{K} - n/\sqrt{K}\big)^2\Big).$$

[§]Capital Θ is the same canonical phase field θ introduced in the original TLL Hamiltonian; we use Θ here to stress its compactness

Adding the two gives the *conformal dimension*

$$\Delta_{m,n} \;=\; \Delta^{R}_{m,n} + \Delta^{L}_{m,n} \;=\; \tfrac{1}{2}\big(m^2 K + n^2/K\big). \tag{2.45}$$

The Hamiltonian here becomes

$$H = H_0 + \sum_{m,n} g_{m,n}\mathcal{O}_{m,n}, \tag{2.46}$$

where H_0 is the TLL Hamiltonian and *dimensionless* couplings $g_{m,n} \equiv \lambda_{m,n}\, a^{2-\Delta_{m,n}}$ ($\lambda_{m,n}$ is the bare lattice amplitude and a the short-distance cutoff), which model lattice effects. Linearizing the RG gives [4]

$$\frac{dg_{m,n}}{dl} \;=\; (2-\Delta_{m,n})\, g_{m,n} + \mathcal{O}(g^2). \tag{2.47}$$

Operators with $\Delta_{m,n} < 2$ are *relevant*; their coupling grows under coarse-graining, modifying the infrared (long-distance) physics. They can therefore drive the system away from criticality. If $\Delta_{m,n} > 2$, the operator is *irrelevant*; if $\Delta_{m,n} = 0$ it is *marginal*. Relevance quantifies whether a perturbation dominates the low-energy behavior. Because H_0 is Gaussian, one can compute $\Delta_{m,n}$ exactly from LL theory [3, 53]. The parameters (K, v) are strictly marginal so that $dK/dl = dv/dl = 0$ to all orders. Relevant examples including $\cos(\beta\phi)$ or $\cos(\beta\Theta)$ (*e.g.* dimerization or commensurate Umklapp scattering) grow under RG and open a spectral gap.

The Berezinskii–Kosterlitz–Thouless (BKT) Transition

The TLL describes the low-energy fixed point of a one-dimensional quantum fluid only when all symmetry-allowed couplings are irrelevant. We now look at the canonical case where a vertex operator becomes relevant, driving the system away from criticality and opening a gap in the spectrum: the Berezinskii-Kosterlitz-Thouless (BKT) transition [54, 55]. Its simplest realization is the classical XY

model

$$H_{XY} = -J \sum_{\langle ij \rangle} \cos\left(\theta_i - \theta_j\right), \tag{2.48}$$

where $\theta_i \in [0, 2\pi]$ is the angular degree of freedom at each site. In the continuum, the Hamiltonian becomes a Gaussian free field part with a vertex perturbation of the form introduced above known as the Sine-Gordon Hamiltonian [3],

$$H_{\mathrm{SG}}^{(\mathrm{XY})} = \frac{K}{2\pi} \int d^2x \, (\nabla\theta)^2 + y_0 \int d^2x \, \cos(2\Theta), \tag{2.49}$$

where Θ is a dual variable $\epsilon_{\mu\nu}\, \partial_\mu \theta \;=\; \partial_\nu \Theta$. The perturbation has $m = 0, n = 2$. The dimensionless coupling $K_{\mathrm{cl}} = J/T$ is just the classical spin stiffness, with T the temperature, and plays an analogous role to the Luttinger parameter K in the quantum theory. The phase field θ is compact, implying the existence of topological excitations. Windings of 2π correspond to vortices in the classical model; the energy cost of creating a vortex is encoded in a fugacity term, y_0, or a dimensionless coupling $g_{0,2}$.

Under coarse-graining, the Hamiltonian leads to the coupled flow [56]

$$\begin{aligned} \frac{dK}{dl} &= -y^2 K^2, \\ \frac{dy}{dl} &= (2 - K)\, y, \end{aligned} \tag{2.50}$$

where y is the running fugacity ($y_0 = y(l = 0)$) [57]. The perturbation $\cos(2\Theta)$ has a scaling dimension $\Delta = K$, so the linear term in Eq. (2.47) is $(2 - K)y$.

The RG trajectories form two disconnected regions separated by the marginal line $K(\infty) = 2$: for $K > 2$ the vortex term is irrelevant, whereas for $K < 2$ it is relevant and flows to strong coupling, driving the system away from the TLL fixed line. This global separation of flow lines is what makes the BKT flow *topological*.

The fugacity grows, and vortices unbind. This results in a finite correlation length,

$$\xi^{-1} = c\,\Lambda_0\,\exp\Big[-\frac{\pi}{2\sqrt{2-K_0}}\Big], \tag{2.51}$$

where $K_0 = K(l=0)$ and $c \sim 1$. Physically, ξ^{-1} sets the energy gap $\Delta \sim v/\xi$. The unbound vortices act as defects, disordering the phase field and moving the spectrum away from zero energy.

At unit filling, the 1D Bose–Hubbard model, which describes interacting bosons on a lattice, bosonizes to the Sine-Gordon Hamiltonian

$$H_{\mathrm{SG}}^{(\mathrm{BH})} = \frac{v}{2\pi}\int dx\,\left[K(\partial_x\theta)^2 + \frac{1}{K}(\partial_x\phi)^2\right] + V\int dx\,\cos(2\Theta(x)), \tag{2.52}$$

where $K = K(J/U)$ and $V \propto (U/J)^{1/2}$ [3]. J denotes the boson hopping amplitude and U the on site repulsion. More details on the microscopic Hamiltonian will be provided in the next section. The dual field satisfies

$$\partial_x\Theta(x) \;=\; \pi\,\Pi_\theta(x),$$

where Π_θ is the *canonical momentum* conjugate to the phase field $\theta(x)$, i.e. $[\theta(x), \Pi_\theta(x')] = i\,\delta(x-x')$. The cosine term inserts 2π phase slips (vortices) in imaginary time, mirroring the vortex term in the classical XY model. It further acts as a pinning potential for the field Θ. When V grows under renormalization, the minima of $\cos(2\theta)$ pins Θ into one of its preferred values, opening a gap in the excitation spectrum and driving the system into a Mott-insulating state.

The BKT line $K = 2$ marks the superfluid ($V \to 0$) to Mott insulator ($V \to \infty$) transition. In the RG flow diagram shown in Fig. 2.3, the red line at $K = 2$ marks the BKT transition. For $K > 2$, the theory remains a gapless Luttinger liquid (superfluid), whereas for $K < 2$, V grows and eventually pins Θ, producing the gapped Mott insulator phase.

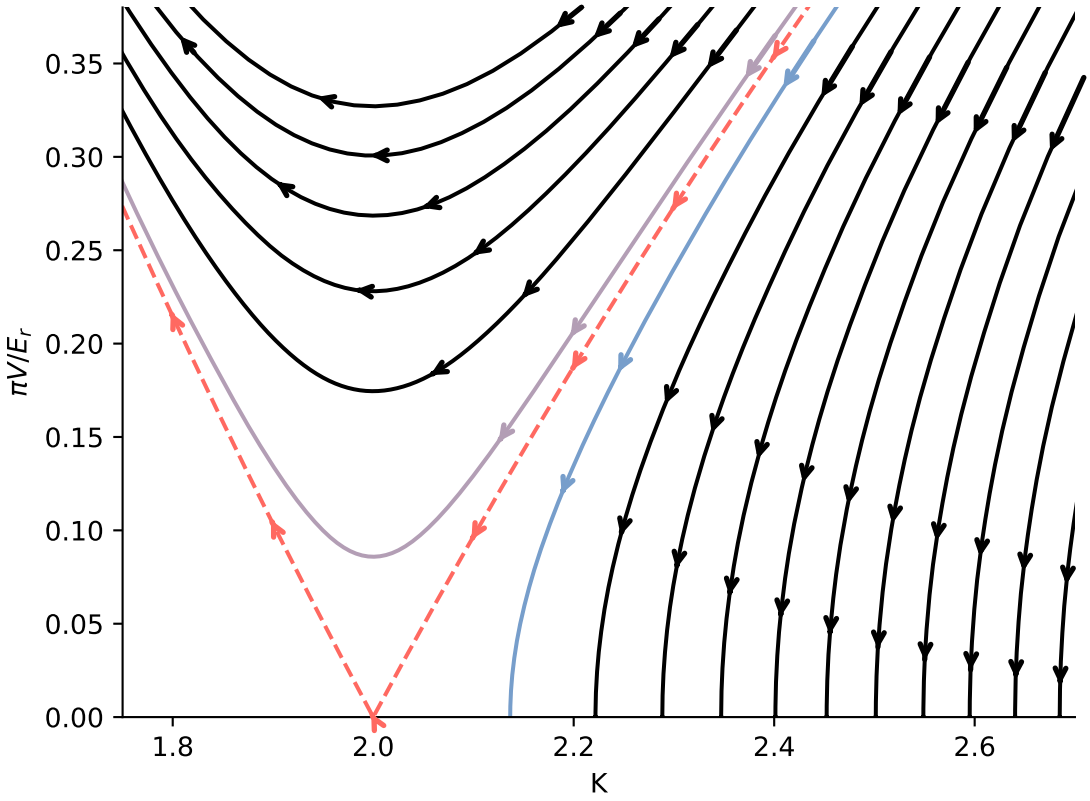

Figure 2.3: RG flow for the one-dimensional Bose–Hubbard model expressed in Sine-Gordon variables (K, V). The red line $K = 2$ marks the BKT transition separating the gapless superfluid phase ($V \to 0$) from the gapped Mott-insulator phase ($V \to \infty$).

The link between the 2D XY action and the 1D quantum chain can be understood through the standard quantum–classical mapping: the zero-temperature partition function of a d-dimensional quantum system is isomorphic to a classical statistical model in $(d+1)$ dimensions, where the extra dimension is imaginary time τ [58].

In Section 5.7, we test this flow numerically for finite systems by extracting K from observables derived with bosonization for numerical results at different interaction strengths. We then locate the critical $(U/J)_C$ with high precision. Throughout this thesis, we invoke the RG picture – explicitly in Section 5.7, implicitly in the bosonization and CFT calculations – to connect microscopic lattice couplings with universal low-energy behavior.

2.4 Models

2.4.1 *J-V Model*

We model the microscopic physics in Chapters 3–5 with a chain of spin-polarized (spinless) fermions that hop between nearest-neighbor sites and interact via a density–density coupling. The literature usually refers to this as the one-dimensional t–J (or t–V) model; here we keep the notation J for the hopping parameter and V for the nearest-neighbor interaction. For N fermions on L lattice sites, the Hamiltonian reads

$$H = -J\sum_i (c_i^\dagger c_{i+1} + \text{h.c.}) \; + \; V\sum_i n_i n_{i+1}, \tag{2.53}$$

with anticommutation relations $\{c_i, c_j^\dagger\} = \delta_{ij}$ and number operator $n_i = c_i^\dagger c_i$. To avoid ground-state degeneracies, we impose antiperiodic boundary conditions for even N and periodic conditions for odd N. Throughout this thesis, we focus on

half-filling, $L = 2N$, and write basis states as

$$|n_1, n_2, \ldots, n_L\rangle = \prod_{i\,:\,n_i=1} c_i^\dagger\,|0\rangle.$$

A Jordan–Wigner transformation maps Eq. (2.53) to the spin-$\frac{1}{2}$ XXZ chain [59, 60]. The Bethe ansatz solution of that model produces the zero-temperature phase diagram in Fig. 2.4. Beginning with the spin–$\frac{1}{2}$ one–dimensional XXZ chain on a lattice of L sites,

$$H_{\mathrm{XXZ}} = \sum_i J_{xy}\left(S^x_{i+1}S^x_i + S^y_{i+1}S^y_i\right) + J_z\sum_i S^z_{i+1}S^z_i, \tag{2.54}$$

where $S^k = \sigma_k/2$ are spin operators that obey the SU(2) commutation relations

$$\left[S^k, S^{k'}\right] = i\varepsilon_{kk'k''}S^{k''}. \tag{2.55}$$

Eq. (2.54) is exactly solvable by the Bethe Ansatz [59, 60]. The ground state changes character at $J_z/J_{xy} = \pm 1$: for $J_z/J_{xy} < -1$ the spins align ferromagnetically; for $J_z/J_{xy} > 1$ the system is antiferromagnetic; and in between it is a gapless Luttinger liquid. Introducing the ladder operators $S^\pm_j = S^x_j \pm iS^y_j$ and performing the Jordan-Wigner mapping [3]

$$S^+_j \longrightarrow (-1)^j\, c^\dagger_j\, e^{i\pi\sum_{k=1}^{j-1} n_k}, \tag{2.56}$$

$$S^-_j \longrightarrow (-1)^j\, e^{-i\pi\sum_{k=1}^{j-1} n_k}\, c_j, \tag{2.57}$$

$$S^z_j \longrightarrow n_j - \tfrac{1}{2}, \tag{2.58}$$

one recovers the canonical anticommutation relations for the fermion operators $c_j^{(\dagger)}$. Using identities such as $S^x_{i+1}S^x_i + S^y_{i+1}S^y_i = \frac{1}{2}(S^+_{i+1}S^-_i + S^-_{i+1}S^+_i)$ and

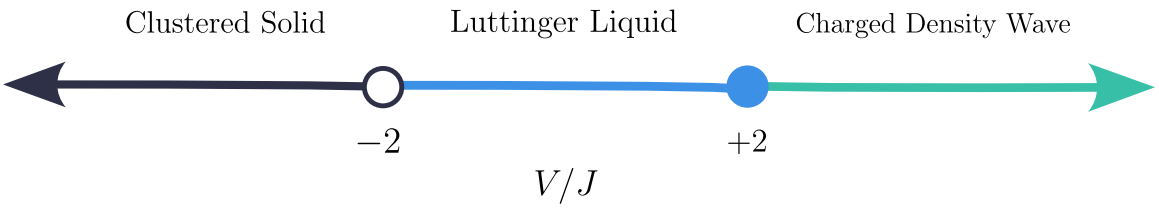

Figure 2.4: Zero temperature phase diagram of the J–V (t–J) chain at half-filling. The intermediate $-2 < V/J < 2$ region is a Tomonaga–Luttinger liquid; it terminates at a first-order transition into a clustered phase ($V/J = -2$) and at a continuous transition into a charge density wave phase ($V/J = 2$).

Eq. (2.56)–Eq. (2.58), the Hamiltonian (Eq. (2.54)) becomes

$$H_{\mathrm{XXZ}} = -\frac{J_{xy}}{2}\sum_i \left(c_{i+1}^\dagger c_i + c_i^\dagger c_{i+1}\right) + J_z \sum_i n_{i+1} n_i + J_z\left(L/4 - N/2\right), \tag{2.59}$$

where $N = \sum_i n_i$ is the total fermion number. Fixing N is equivalent to fixing the total S^z magnetization of the XXZ chain.

Mapping to the J–V model

Identifying

$$\frac{J_{xy}}{2} \longrightarrow J, \qquad J_z \longrightarrow V, \tag{2.60}$$

the transformed Hamiltonian Eq. (2.59) coincides with the spinless fermion J–V chain introduced in Eq. (2.53). Half filling ($L = 2N$) maps onto zero magnetization of the XXZ chain.

For $V/J > 0$ (no external field in the XXZ language), one has $\langle S^z \rangle = 0$ and therefore zero net magnetization. The case $V/J < 0$ is more subtle: the unrestricted XXZ model would favor a ferromagnetic ground state, but Ref.[61] shows that imposing zero magnetization leaves the phase boundaries unchanged—the clustered solid phase still appears. Hence, the J–V chain inherits its quantum phase transitions directly from the XXZ model:

$$\frac{J_z}{J_{xy}} = \pm 1 \implies \frac{V}{J} = \pm 2.$$

Therefore, we have the following phases.

1. **Clustered solid ($V/J < -2$):** Strong attraction binds all fermions into a single block. The ground state approaches $|\Psi\rangle_{V/J\to-\infty} = L^{-1/2}\sum_{n=1}^{L} T^n |11\cdots10\cdots0\rangle$, where T translates the block by one site.

2. **Tomonaga–Luttinger liquid ($-2 < V/J < 2$):** Moderate interactions keep the chain gapless; a low-energy TLL description applies. The ground state is a weighted superposition of all occupation configurations [62].

3. **Charge-density wave ($V/J > 2$):** Strong repulsion maximizes separation, yielding $|\Psi\rangle_{V/J\to+\infty} = 2^{-1/2}(|1010\ldots\rangle + |0101\ldots\rangle)$.

The transition at $V/J = -2$ is first-order, whereas the continuous transition at $V/J = 2$ falls into the two-dimensional Ising universality class. At half-filling the Bethe ansatz links the microscopic ratio V/J to the Luttinger parameters [3]:

$$K = \frac{\pi}{2\arccos(-V/2J)}, \qquad v = \frac{\pi J\sqrt{1-(V/2J)^2}}{2\arccos(-V/2J)}. \tag{2.61}$$

A larger (smaller) K signals weaker (stronger) density-wave stiffness: $K < 1$ enhances $2k_F$ correlations and pushes the chain toward the CDW phase, whereas $K > 1$ softens density fluctuations and favors pairing tendencies.

We employ Eq. (2.53) in our exact diagonalization and density matrix renormalization group calculations, and we compare those microscopic results to the field-theory predictions that follow from the Tomonaga–Luttinger liquid with parameters in Eq. (2.61).

2.4.2 *Bose-Hubbard Model*

For bosons, we employ a different microscopic description: the one-dimensional Bose–Hubbard model at unit filling ($N = L$), which describes itinerant, interacting bosons on a lattice [63]. Its Hamiltonian reads

$$H = -J\sum_i (b_i^\dagger b_{i+1} + b_{i+1}^\dagger b_i) + \frac{U}{2}\sum_i n_i\,(n_i - 1) - \sum_i \mu_i n_i, \tag{2.62}$$

where J is the nearest-neighbor hopping amplitude, $U > 0$ the on-site repulsion, and μ_i the chemical potential that fixes the particle density. The operators $b_i^\dagger$ and b_i create and annihilate a boson at site i, while $n_i = b_i^\dagger b_i$ counts the local occupation.

Fig. 2.5 illustrates the phase diagram at unit filling. At zero temperature, strong repulsion ($U/J \gg 1$) localizes the bosons, producing a gapped Mott insulator with integer site occupancy. When U/J is small the particles delocalize, long-range phase coherence develops, and the low-energy physics maps onto TLL theory [3]. The superfluid–insulator transition belongs to the Berezinskii–Kosterlitz–Thouless universality class; numerical studies locate the critical coupling in the range $3.13 < U/J < 4.76$ [64–77]. Section 5.7 revisits this transition in detail, deriving the renormalization group flow of the Luttinger parameter and benchmarking it against large-scale DMRG data.

2.5 Quantum Entanglement

Entanglement entropy (EE) is a powerful tool for quantifying quantum correlations, offering deep insights into quantum phase transitions, topological order, and critical phenomena. In low-dimensional systems, EE reveals nonlocal correlations that are often invisible to traditional order parameters. Before formalizing the particle entanglement, which is the focus of this thesis, we outline the classical analogue of the quantum entanglement entropy and the measures used to quantify both.

Entropy first appeared in Clausius's formulation of the second law, but Boltzmann gave it statistical meaning by counting microstates [78]. Gibbs generalized the concept to arbitrary ensembles, defining the quantity that Shannon later recast as information entropy [79, 80],

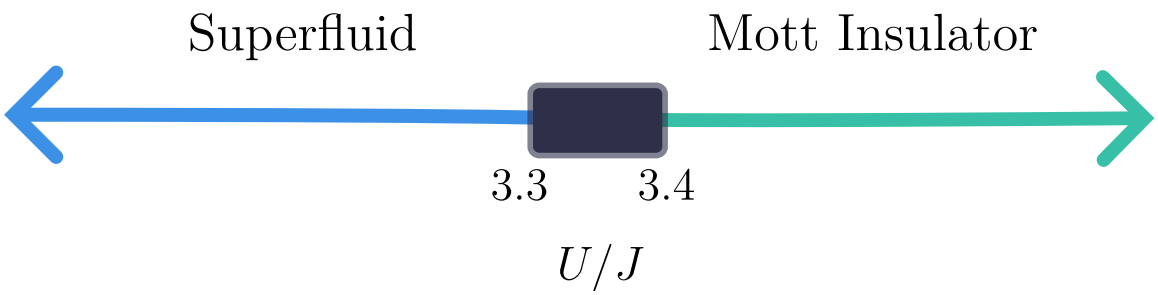

Figure 2.5: Zero temperature phase diagram of the Bose–Hubbard chain without disorder. For $U/J \gg 1$ the system forms a Mott insulator with integer filling and a charge gap. For weaker interactions it enters a gapless superfluid phase that TLL theory describes. Quantum Monte Carlo and DMRG studies place the Berezinskii–Kosterlitz–Thouless transition in the window $3.13 \lesssim U/J \lesssim 4.76$.

$$S_{\mathrm{cl}}[p] \;=\; -\sum_i p_i \ln p_i, \tag{2.63}$$

which measures our uncertainty about the microstate when only coarse-grained probabilities $\{p_i\}$ are known.

Quantum mechanics required a new language: probabilities reside off-diagonal in a density matrix ρ, and classical ensembles no longer suffice. Von Neumann supplied the analogue by replacing p_i with the eigenvalues of the density matrix ρ [81],

$$S_1(\rho) \;=\; -\mathrm{Tr}\,\rho \ln \rho, \tag{2.64}$$

creating an information-theoretic bridge between classical and quantum settings.

2.5.1 *Entanglement Measures*

A pure many-body state $|\Psi\rangle \in \mathcal{H}$ is *bipartite entangled* when it cannot be written as a tensor product

$$|\Psi\rangle \neq |\Psi_A\rangle \otimes |\Psi_B\rangle\,, \qquad \mathcal{H} = \mathcal{H}_A \otimes \mathcal{H}_B.$$

Physically, ρ_A captures everything an observer (Alice) restricted to subsystem A could know about the total quantum state. Tracing over subsystem B produces the reduced density matrix $\rho_A = \mathrm{Tr}_B\big[|\Psi\rangle\langle\Psi|\big]$, whose spectrum $\{\lambda_i\}$ captures the correlations between A and B.

The Rényi entropies form a one-parameter family that sample those eigenvalues in different ways

$$S_\alpha(\rho_A) = \frac{1}{1-\alpha}\,\ln\big[\mathrm{Tr}(\mathrm{æ}_{\mathrm{A}}^{\mathrm{ff}})\big]. \qquad \mathrm{ff} > 0. \tag{2.65}$$

Taking the limit $\alpha \to 1$ with l'Hôpital's rule reproduces the von Neumann entropy,

$$\begin{aligned}\lim_{\alpha\to 1} S_\alpha(\rho_A) &= -\lim_{\alpha\to 1} \partial_\alpha \ln \mathrm{Tr}[\log\left(æ_A^{ff}\right)] \\ &= -\lim_{\alpha\to 1} \mathrm{Tr}\frac{\partial_{ff} æ_A^{ff}}{\mathrm{Tr} æ_A^{ff}} \\ &= -\lim_{\alpha\to 1} \mathrm{Tr}\frac{æ_A^{ff}\log æ_A}{\mathrm{Tr} æ_A^{ff}} \\ &= -\mathrm{Tr}\frac{æ_A \log æ_A}{\mathrm{Tr} æ_A}, \end{aligned} \tag{2.66}$$

recovering the standard measure of quantum uncertainty by using $\mathrm{Tr} æ_A = 1$. Because $\mathrm{Tr} æ_A^{ff} = \sum_i \check{}_i^{ff}$, $\exp\big[(1-\alpha)S_\alpha\big]$ is the *power mean* of order α:

1. $\alpha = 0$ counts the non-zero eigenvalues;
2. $\alpha = 2$ emphasizes the largest eigenvalues and is experimentally accessible in cold atom interference;
3. $\alpha \to \infty$ isolates the leading eigenvalue;
4. $\alpha \to 1$ recovers the geometric mean, yielding the von Neumann entropy.

Rényi entropies inherit the basic properties of classical entropy, positivity and for $\alpha \geq 1$ strong sub-additivity, and pragmatically are often *easier* to compute: raising a matrix to a power is numerically straightforward, while evaluating $\rho \log \rho$ requires diagonalizing ρ to obtain the spectrum.

2.5.2 *Entanglement Bipartitions*

The majority of this subsection is adapted from [82].

Most studies partition the Hilbert space into two non-overlapping *spatial* regions [30**?**]; the resulting Rényi entropies, S_α, reveal the universal logarithmic scaling characteristic of 1D critical points. Here we adopt a different cut: we trace over

$N - n$ *indistinguishable particles*. To leading order, this particle bipartition is more sensitive to statistics, interactions, and phase transitions, and often serves as a sharper probe of correlation structure [33]. Fig. 2.6 shows a periodic chain with $N = 6$ particles under (a) a particle bipartition ($n = 3$ versus $N - n = 3$) and (b) a spatial bipartition of length ℓ.

This particle perspective is most transparent in first–quantized language. We compute the *particle* entanglement entropy from the n-body reduced density matrix (n-RDM) $\rho_{A\equiv n} \equiv \rho_n$, defined with the information-theoretic normalization $\operatorname{Tr}\rho_n = 1$ [83–86]. Fig. 2.7 shows the construction for $N = 4$ particles.

For an N-particle state on a one-dimensional lattice we fix n coordinates $\{i_1, \ldots, i_n\}$ in the symmetrized (or antisymmetrized) as appropriate wave-function $\Psi(i_1, \ldots, i_N) = \langle i_1, \ldots, i_N | \Psi \rangle$ and trace over the remaining $N - n$ coordinates [87]:

$$\rho_n^{i_1,\ldots,i_n;j_1,\ldots,j_n} = \sum_{i_{n+1},\ldots,i_N} \langle \Psi | i_1, \ldots, i_n, i_{n+1}, \ldots, i_N \rangle \langle j_1, \ldots, j_n, i_{n+1}, \ldots, i_N | \Psi \rangle , \quad (2.67)$$

where the $2n$ indices label the matrix elements of ρ_n. In higher dimensions, or in the continuum, we generalize Eq. (2.67) with the appropriate coordinate labels.

The von Neumann entropy $S_1(\rho_n)$ satisfies three universal inequalities:

1. *Monotonicity:* $S_1(\rho_n) \leq S_1(\rho_{n+1})$ for $1 \leq n \leq \lfloor N/2 \rfloor - 1$;
2. *Reflection:* $S_1(\rho_n) = S_1(\rho_{N-n})$ (illustrated in Fig. 2.7);
3. *Concavity:* $S_1(\rho_n) \geq \left[S_1(\rho_{n-1}) + S_1(\rho_{n+1})\right]/2$ for $1 \leq n \leq N - 1$.

Consequently $S_1(\rho_{\lfloor N/2 \rfloor})$ maximizes particle entanglement. The reflection property extends to any Rényi index α. For brevity, we write $S_\alpha(n)$, leaving the dependence on ρ_n implicit.

For non-interacting bosons, the ground state is a tensor product, so ρ_n is pure and the particle entanglement vanishes. By contrast, a non-interacting fermionic ground state is a single Slater determinant; ρ_n therefore possesses $\binom{N}{n}$ identical

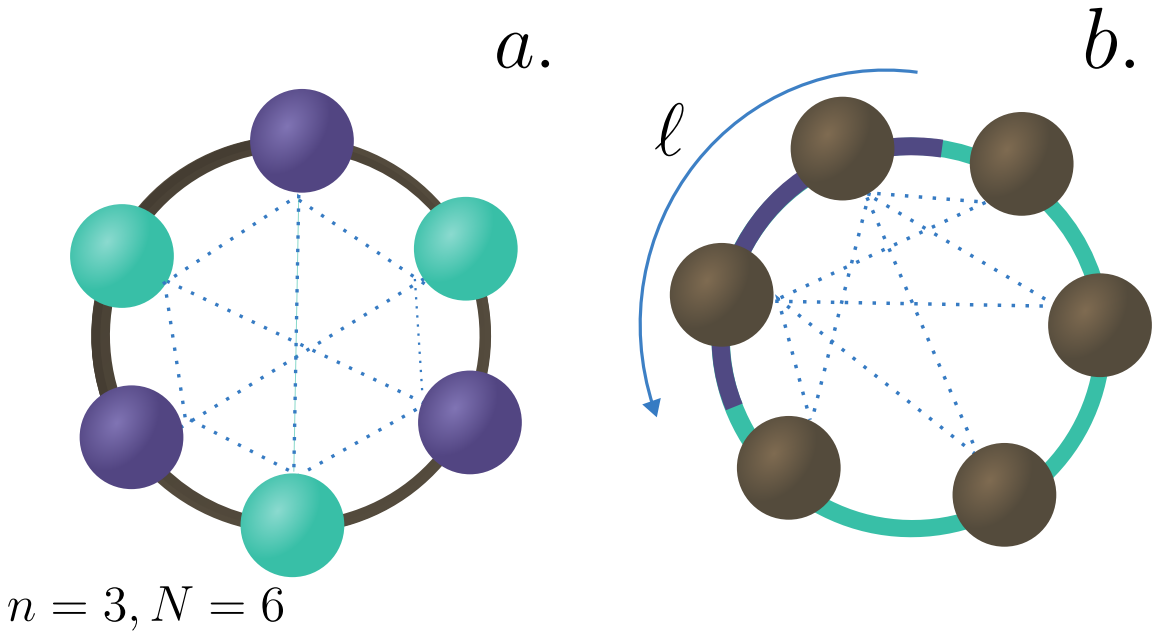

Figure 2.6: Indistinguishable particles ($N = 6$) under a (a) particle bipartition with $n = 3$ and $N - n = 3$ particles and (b) spatial bipartition with subregion ℓ.

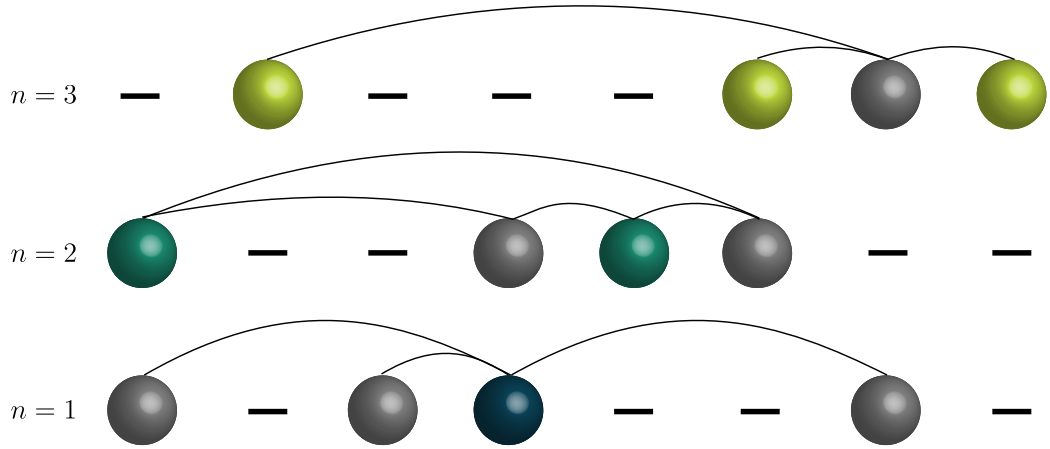

Figure 2.7: Partitioning N indistinguishable particles into two subsets of n and $N - n$. Grey sites are traced out; coloured sites are retained. For $n = 1$ and $n = 3$ ($N = 4$) the entanglement entropies coincide, illustrating the reflection symmetry $S_\alpha(n) = S_\alpha(N - n)$.

eigenvalues [86] and

$$S_\alpha(n) = \ln \binom{N}{n}, \qquad \text{independent of } \alpha. \tag{2.68}$$

Interacting fermions

Carlen and Lieb proved the lower bound $S_1(n) \geq \ln N$ [88, 89]. Extensive evidence [32, 34, 35, 90] supports the scaling ansatz

$$S_\alpha(n)\big|_{\text{fermions}} = \ln \binom{N}{n} + a_\alpha(n) + \mathcal{O}\big(N^{-\gamma_\alpha(n)}\big), \tag{2.69}$$

with $a_\alpha(n)$ and the exponent $\gamma_\alpha(n) \geq 1$ set by interactions and the size of n. Free fermions have $a_\alpha(n) = 0$ and no finite-N corrections. Known constants include $a_\alpha(n) = \ln 2$ for a one-dimensional charge-density wave [91] and $a_1(n) = -n \ln \nu$ for fermionic Laughlin states of filling ν [33]. For a Luttinger liquid $\gamma_2(1) = K + K^{-1} - 1$ [91, 92], tying the subleading decay directly to the Luttinger parameter.

Interacting bosons

Bosonic results are more rare. At fixed $n = 1$, the leading term is non-universal [93], while the ground state of free bosons remains a product and yields zero particle entanglement. Numerical results for two bosons on two sites (Fig. 2.8) show that turning on interactions immediately generates particle entanglement, even though the spatial entanglement is non-zero at all U/J. For a detailed derivation of the

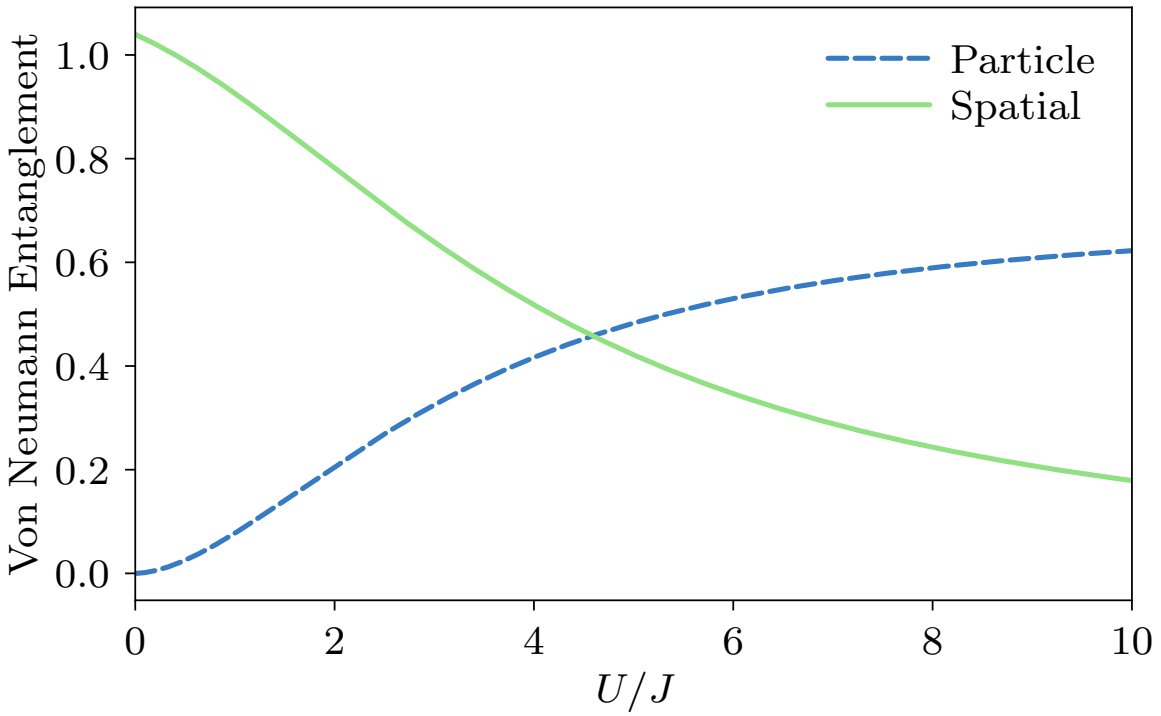

Figure 2.8: Von Neumann entanglement entropy for two spinless bosons on two sites. Spatial entanglement is present for all U/J, whereas particle entanglement turns on with finite interactions.

entanglement under each bipartition, see Appendix A. In the Lieb–Liniger gas, Ref. [93] found, for $\alpha = 2$ and $n \leq 2$,

$$S_2(n)\big|_{\text{bosons}} = \frac{n}{K} \ln N + b_2(n) + \mathcal{O}\big(N^{1-1/K}\big), \tag{2.70}$$

so the leading coefficient tracks the interaction-dependent K.

Outlook

Comparing Eq. (2.69) and Eq. (2.70) underscores the leading-order sensitivity of particle entanglement to both statistics and interactions, yet highlights how few general results exist beyond special 1D cases. Recent protocols can, however, transfer particle entanglement to mode entanglement [94], renewing interest in its role and enabling its access in quantum computing. A key open problem is to determine the constants $a_\alpha(n)$ and exponents $\gamma_\alpha(n)$ for generic interactions, and how they scale with n, N, and α. This thesis concentrates on the fermionic case, where the universal $\ln \binom{N}{n}$ term provides a clean starting point for uncovering the sub-leading structure. We revisit the form of Eq. (2.69) in Section 2.6.2.

2.6 Numerical Methods

The majority of this subsection is adapted from [82].

2.6.1 *Exact Diagonalization*

Throughout this thesis, in particular Chapters 2-5, we rely on exact diagonalization (ED) to benchmark analytic predictions for the J-V chain. Below, we summarize the technique, emphasizing the symmetry reductions that make ED feasible for lattices of $\mathcal{O}(30\text{–}40)$ sites

Lanczos ground state

We enumerate the $\binom{L}{N}$ Fock states for N fermions on a periodic L-site lattice and encode each configuration as an *integer-fermion basis*: the occupation pattern serves as the bits of an integer ($|1010\rangle_{\text{bin}} \to 10$, $|1100\rangle_{\text{bin}} \to 12$). The Hamiltonian, Eq. (2.53), is then a sparse matrix on this ordered integer list, and its ground state follows from the standard Lanczos algorithm [95].

To shrink the Hilbert space, we exploit lattice symmetries. Translation T commutes with H, so basis states fall into cycles $\{|\varphi_\nu\rangle, T|\varphi_\nu\rangle, \ldots, T^{M_\nu-1}|\varphi_\nu\rangle\}$. Projecting onto momentum q within each cycle,

$$|\psi_{\nu,q}\rangle = \frac{1}{\sqrt{M_\nu}} \sum_{m=0}^{M_\nu-1} e^{i\frac{2\pi q}{M_\nu} m} T^m |\varphi_\nu\rangle , \tag{2.71}$$

block-diagonalizes H. The ground state resides in the $q = 0$ sector [96], which we can further reduce by a factor of $1/4$ by inversion and particle-hole symmetries [92]. The resulting block is small enough to reach $L = 40$ with modest memory.

Particle entanglement from the structure matrix

To compute the n-particle Rényi entanglement entropy we require the Schmidt coefficients between the n-particle sector A and its complement B. Writing the Lanczos ground state as $|\Psi_0\rangle = \sum_{ab} C_{ab} |\theta_a\rangle_A \otimes |\chi_b\rangle_B$, we assemble the coefficient matrix C directly from the integer basis.

The key is a *structure matrix* $\mathcal{A}_{\mu\nu i} \in \mathbb{Z} \times \{\pm 1\}$ that maps each product state $|\theta_{\mu,i}\rangle_A \otimes |\chi_{\nu,1}\rangle_B$ to (i) its integer label in the full basis (magnitude of $\mathcal{A}_{\mu\nu i}$) and (ii) the fermionic sign incurred when merging creation operators (phase of $\mathcal{A}_{\mu\nu i}$). Fast bit operations generate the integer label, while the sign follows from (a) boundary crossings inside a translation cycle and (b) fermionic reordering between partitions, e.g. $c_1^\dagger c_4^\dagger |0\rangle = -\, c_4^\dagger c_1^\dagger |0\rangle$.

Once $\mathcal{A}$ is determined, the entries of C are computed and symmetry related rows are summed via a discrete Fourier transform, diagonalizing C in momentum space. The singular values $\{\lambda_i\}$ obtained from this reduced matrix yield the Rényi entropy of order α,

$$S_\alpha(n) = \frac{1}{1-\alpha} \ln\Big[\sum_i |\lambda_i|^{2\alpha}\Big], \tag{2.72}$$

as originally done in Ref. [87].

2.6.2 *Density Matrix Renormalization Group*

To reach the much larger system sizes necessary for scaling analyses, we switch to the density matrix renormalization group (DMRG) [97, 98]. Ground states are obtained with the `ITensors.jl` implementation [**?**], which variationally optimizes a matrix product state (MPS). We initialize the MPS according to the interaction ratio V/J and explicitly enforce orthogonality to higher translation sectors, following Ref. [92]. This strategy reliably converges to the true ground state of the J–V Hamiltonian for chains up to $L = 128$.

Particle entanglement from the n-RDM

The n-particle Rényi entropy requires the n-particle reduced density matrix (RDM)

$$\rho_n^{(i_1,\dots,i_n),(j_1,\dots,j_n)} = \frac{\langle \Psi_0 | c_{i_1}^\dagger \dots c_{i_n}^\dagger \, c_{j_1} \dots c_{j_n} | \Psi_0 \rangle}{\binom{N}{n}}, \tag{2.73}$$

whose naive evaluation scales as $\binom{L}{n}^2$. This becomes feasible through three optimization steps:

1. **Integer–fermion encoding** Each ordered string $c_{i_1}^\dagger \dots c_{i_n}^\dagger$ maps to the binary integer $\sum_{k=1}^{n} 2^{i_k - 1}$. The resulting sparse, ordered list allows $\mathcal{O}(\log \binom{L}{n})$ access and rapid translation back to physical site indices for operator construction in `ITensors.jl`.

2. **Fermionic symmetry** Anticommutation implies that permutations of the creation (or annihilation) operators change only the *sign* of Eq. (2.73). It therefore suffices to compute the upper triangular block with $i_1 < \cdots < i_n$ and $j_1 < \cdots < j_n$ and impose Hermiticity by symmetry, normalizing the final singular spectrum via $\sum_i |\lambda_i|^2 = 1$.

3. **Translational symmetry** Translation of $|\Psi_0\rangle$ by one site gives

$$\rho_n^{(i_1,\ldots,i_n),(j_1,\ldots,j_n)} = (-1)^{\delta_{i_n,L}+\delta_{j_n,L}}\, \rho_n^{(i_1+1,\ldots,i_n+1),(j_1+1,\ldots,j_n+1)},$$

which reduces the number of independent matrix elements by another factor L; in the integer basis, both the translation and the table lookup cost only $\mathcal{O}(\log\binom{L}{n})$.

These MPS results extend our particle entanglement analysis of the J–V chain closer to the thermodynamic limit.

Would you tell me, please, which
way I ought to go from here?
That depends a good deal on where
you want to get to, said the Cat.

Lewis Carroll

Alice's Adventures in Wonderland

A SCALING FUNCTION FOR THE PARTICLE ENTANGLEMENT OF FERMIONS

3

This chapter contains text from published first author work by the author [82] with minor modifications where appropriate for this format. The author's contribution was doing all derivations with input from Hatem Barghathi, running the simulations to collect the data, performing the fitting, and producing the figures. The code used to run the simulations was developed by Hatem Barghathi and Matthias Thamm. The author wrote most of the manuscript with input from the coauthors. Adrian Del Maestro primarily wrote the introduction and discussion with editing from the author. Adrian Del Maestro supervised the project.

3.1 Introduction

Any n-body observable of a quantum N-particle system can be calculated from its n-particle reduced density matrix (n-RDM) without the need to construct the complete wavefunction. The spectrum of the n-RDM contains explicit information on non-classical correlations, and its von Neumann or Rényi entropy can be used to quantify the quantum entanglement between partitions of n and $N-n$ indistinguishable particles [33, 35, 99–101]. In one spatial dimension (1D) this *particle* entanglement entropy $S(n)$ can be sensitive to interactions, phase transitions

[102, 103], and particle statistics at leading order. It has been used to probe quantum Hall states [32, 34, 104–107] as well as systems of non-interacting [108], and interacting bosons [90, 93, 109–111], fermions [91, 112–114], and anyons [115].

Thus, the particle entanglement can provide complementary information to the well studied and more conventional *mode* entanglement entropy most commonly computed from a reduced density matrix of spatial modes. For example, in 1D, spatial mode entanglement entropy is known to be universal at leading order in the subsystem size ℓ for gapless systems describable by a conformal field theory with central charge c [116], *i.e.* $S(\ell) \sim (c/3) \ln \ell + \ldots$ for the von Neumann entropy. In contrast, it was empirically proposed by Haque et al. [32] that the particle entanglement entropy behaves as $S(n) \sim n \ln N$ for $n \ll N$ and $N \gg 1$ for fermions. This was subsequently confirmed for the 2nd Rényi entropy within the Luttinger liquid framework for $n = 1$ by a subset of the authors of this work [91]. For bosons in 1D described by Luttinger liquid theory, it was found that for $n = 1$, the leading term may become non-universal [93]. Existing results are all consistent with Coleman's theorem [85] stating that the 1-particle von Neumann entropy is minimal for a Slater determinant: $S(n = 1) \geq \ln N$. For $n > 1$ exact results are scarce, and it was conjectured in 2016 [88] that for $n = 2$, $S(n = 2) \geq \ln \binom{N}{2}$ which was adapted in Ref. [89] to general n: $S(n) \geq \ln N$, demonstrating that all possible particle bipartitions of a N fermion system are entangled, a rather striking result! In spite of this recent progress, a more complete understanding of the particle entanglement entropy as a function of n, N, or Rényi index remains elusive.

Here, we address this question by considering a system of interacting spinless lattice fermions in 1D through a combination of bosonization techniques for $n = 1$ and large scale exact diagonalization (ED) and density matrix renormalization group (DMRG) for general n. By exploiting all symmetries of the n-RDM, we explore large values of both n and N, as well as various Rényi indices α and dimensionless interaction strengths g. We identify the numerical form of a general shape function Φ describing the scaling of the particle entanglement entropy for

fermions

$$S_\alpha = \ln \binom{N}{n} + N\Phi\left(\sin\frac{n\pi}{N}, N; g, \alpha\right). \tag{3.1}$$

We find:

1. $\Phi \sim \mathrm{O}(N^0)$ at fixed n/N for $N \gg 1$;
2. $\Phi \sim n/N$ for fixed n at large N, such that $S_\alpha \sim n\left[\ln N + \mathrm{O}(N^0)\right]$;
3. $\Phi \to 0$ for $g \to 0$ such that $S_\alpha = \ln \binom{N}{n}$ for non-interacting fermions.

Property (iii) can be understood as a direct result of the constant eigenvalues below the Fermi surface of the n-RDM for a single Slater determinant wavefunction describing non-interacting fermions [117].

The scaling of this shape function is confirmed by comparing with a bosonization calculation employing the known fermionic 1-RDM (obtained from exponentials of bosonic correlation functions [3]) for $\alpha = 2$, and a self-consistent non-linear least squares fitting analysis of numerical results up to $N = 40$ fermions and $n \leq 7$.

The main contributions of this work are: (1) an asymptotic expansion of the 1-particle entanglement entropy in powers of $1/N$, which includes both integer and g-dependent exponents and high-precision estimates for multiplicative prefactors for a 1D model of interacting fermions in the Luttinger liquid regime; (2) confirmation of the subleading extensive scaling (analogous to a volume law) in Eq. (3.1) in the presence of interactions between fermions for general n and N; (3) numerical determination of the scaling shape function Φ, as a function of the ratio n/N; and (4) a procedure to obtain particle entanglement for large system sizes using limited data for small n and N.

The remainder of this chapter is organized as follows. We begin with a detailed introduction to particle entanglement entropy and highlight previous results before defining the microscopic lattice model that is the focus of this work and describing its low energy sector. Beginning with the analytically tractable case of $n = 1$ and

$\alpha = 2$ we derive an asymptotic expansion of S_2, and discuss some implications for the case of general n. We then proceed to a careful analysis of a numerical data set for S_2 computed with exact diagonalization and the density matrix renormalization group. This allows for the confirmation of our bosonization procedure, a high precision non-linear fitting procedure to a general expansion form and ultimately a proposal for the shape function introduced in Eq. (3.1). The remainder of our results are presented in the context of understanding the form of Φ and we end with some remarks on implications for an improved understanding of particle entanglement and some future directions.

3.2 Tomonaga-Luttinger liquid theory and bosonization

In the Luttinger liquid regime, which is characterized by relatively weak interactions and long wavelength fluctuations, the dynamics of the system are primarily governed by low-energy excitations in the form of density variations about a mean density [3]. In this region, the microscopic Hamiltonian in Eq. (2.53), can be recast in terms of these bosonic density variations, enabling us to write an effective Hamiltonian in bosonization language to account for the low-energy physics. Following the linearization of the energy dispersion near the Fermi points [1, 47]

$$H = \sum_{q\neq 0} [\omega_0(q) + m(q)] b_q^\dagger b_q + \frac{1}{2} \sum_{q\neq 0} g_2(q) [b_q b_{-q} + b_q^\dagger b_{-q}^\dagger] \,,$$

where $b_q (b_q^\dagger)$ are bosonic annihilation (creation) operators, $\omega_0(q) = v_F|q|$, and q are discrete momenta: $q = 2\pi n/L, n \in \mathbb{Z} \setminus \{0\}$. For small q, $g_2(q) = g_2|q|$ and $m(q) = g_4|q|$ where g_2 and g_4 are parameters obtained from the mapping from the J-V Hamiltonian. To account for the short-range interactions in the J-V model, an interaction cutoff ϵ is implemented such that $m(q)$ and $g_2(q)$ vanish for $q\epsilon \gg 1$. This Hamiltonian is quadratic with respect to the boson operators, in contrast to the fermionic Hamiltonian which is of fourth order. Utilizing bosonization, we

recast operators for the fermionic field in terms of exponentiated bosonic fields and thus calculate the one-point correlation function for both right- and left-movers, yielding the one-body density matrix.

$$C_{\pm}(x) = \langle \Psi_{\pm}^{\dagger}(x)\Psi_{\pm}(0)\rangle$$
$$\rho_1(x) = \frac{1}{N}[e^{-ik_F x}C_{+}(x) + e^{ik_F x}C_{-}(x)] \ ,$$

where Ψ_α are the fermionic field operators, $\pm$ corresponds to right/left movers, and $k_F = N\pi/L$ is the Fermi momentum. For full details on the analytic computation of the one body reduced density matrix in this model within the bosonization framework, see Ref. [92].

3.3 1-Particle entanglement in fermionic Tomonaga-Luttinger liquids

We begin by analytically deriving the asymptoptic finite size scaling for the Rényi entanglement entropy with $\alpha = 2$ for a bipartition of $n = 1$ and $N - 1$ particles which is given by

$$S_2(n = 1) = -\ln \mathrm{Tr}\rho_1^2 \ , \tag{3.2}$$

where ρ_1 is the one body reduced density matrix at zero temperature. Taking into account periodic boundary conditions, the distance, or chord length, between two points is $\frac{L}{\pi}\sin\frac{\pi}{L}|x_1 - x_2|$.

3.3.1 Non-interacting spinless fermions

Starting with the non-interacting case ($V = 0$, indicated by a superscript 0), the one body density matrix (n=1) is given by

$$\rho_1^0 = \frac{1}{N}\frac{\sin\left(k_F|x_1 - x_2|\right)}{L\sin\left(\pi|x_1 - x_2|/L\right)} \ , \tag{3.3}$$

where $k_F = \frac{N\pi}{L}$. To compute the entanglement entropy we need the trace of this quantity squared,

$$\begin{aligned} \mathrm{Tr}\left[(\rho_1^0)^2\right] &= \int_{-L/2}^{L/2} dx_2 \int_{-L/2}^{L/2} dx_1 \frac{1}{N^2} \frac{\sin^2(\pi\rho_0|x_1 - x_2|)}{L^2 \sin^2(\pi|x_1 - x_2|/L)} \\ &= \frac{2}{N^3} \int_0^{N/2} dy \frac{\sin^2(\pi y)}{\sin^2(\pi y/N)} , \end{aligned} \tag{3.4}$$

where we have used the translational invariance of the system and defined $y = \rho_0|x_1 - x_2|$. While this is analytically solvable in the case of free fermions (and gives $1/N$), for interacting fermions we will later require the use of some approximations (ignoring the effects of periodic boundary conditions and replacing the chord length with separations $\frac{L}{\pi}\sin\frac{\pi}{L}|x_1 - x_2| \to |x_1 - x_2|$) whose accuracy can be demonstrated here. Replacing the chord length in the denominator of Eq. (3.3) yields a modified density matrix (indicated by a tilde) that is correct only for separations $|x_1 - x_2| \ll L$:

$$\tilde{\rho}_1^0 = \frac{\sin(\pi\rho_0|x_1 - x_2|)}{\pi\rho_0 L|x_1 - x_2|} . \tag{3.5}$$

The trace of the square of the modified density matrix is then given by

$$\begin{aligned} \mathrm{Tr}\left[(\tilde{\rho}_1^0)^2\right] &= \int_{-L/2}^{L/2} dx_2 \int_{-L/2}^{L/2} dx_1 \frac{\sin^2(\pi\rho_0|x_1 - x_2|)}{\pi^2\rho_0^2 L^2|x_1 - x_2|^2} \\ &= \frac{2}{N} \int_0^{N/2} dy \frac{\sin^2(\pi y)}{\pi^2 y^2} . \end{aligned} \tag{3.6}$$

We can rewrite Eq. (3.4) by adding and subtracting Eq. (3.6) as

$$\begin{aligned} \mathrm{Tr}\left[(\rho_1^0)^2\right] &= \frac{2}{N^3} \int_0^{N/2} dy \frac{\sin^2(\pi y)}{\sin^2(\pi y/N)} - \frac{2}{N} \int_0^{N/2} dy \frac{\sin^2(\pi y)}{\pi^2 y^2} + \frac{2}{N} \int_0^{N/2} dy \frac{\sin^2(\pi y)}{\pi^2 y^2} \\ &= f(y, N) + g(y, N) \end{aligned} \tag{3.7}$$

where:

$$f(y,N) = \frac{2}{N^3}\int_0^{N/2} dy \frac{\sin^2(\pi y)}{\sin^2(\pi y/N)} - \frac{2}{N}\int_0^{N/2} dy \frac{\sin^2(\pi y)}{\pi^2 y^2} \tag{3.8}$$

$$g(y,N) = \frac{2}{N}\int_0^{N/2} dy \frac{\sin^2(\pi y)}{\pi^2 y^2}\,. \tag{3.9}$$

To compute $f(y,N)$, we use that the integral of $\sin^2(x)$ is $1/2$ over its period 2π, and thus we approximate the highly oscillating function $\sin^2(\pi y) \to \frac{1}{2}$. In the large N limit this gives

$$\begin{aligned} f(y,N) &= \frac{1}{N}\left[\frac{1}{N^2}\int_0^{N/2} dy \frac{1}{\sin^2(\pi y/N)} - \int_0^{N/2} dy \frac{1}{\pi^2 y^2}\right] \\ &= \frac{2}{N^2\pi^2}\,. \end{aligned} \tag{3.10}$$

While we can compute $g(y,N)$ directly, we will demonstrate another approximation that is necessary for the interacting case. We rewrite

$$\begin{aligned} g(y,N) &= \frac{2}{N}\int_0^{N/2} dy \frac{\sin^2(\pi y)}{\pi^2 y^2} \\ &= \frac{1}{N}\left[\int_0^{\infty} dy \frac{2\sin^2(\pi y)}{\pi^2 y^2} - \int_{N/2}^{\infty} dy \frac{2\sin^2(\pi y)}{\pi^2 y^2}\right]\,. \end{aligned} \tag{3.11}$$

The first term can be directly integrated and in the second term, we again approximate $\sin^2(\pi y) \to 1/2$. This gives

$$\begin{aligned} g(y,N) &= \frac{1}{N}\left[\int_0^{\infty} dy \frac{2\sin^2(\pi y)}{\pi^2 y^2} - \int_{N/2}^{\infty} dy \frac{1}{\pi^2 y^2}\right] \\ &= \frac{1}{N}\left[1 - \frac{2}{N\pi^2}\right]\,. \end{aligned} \tag{3.12}$$

Combining, Eq. (3.10) and Eq. (3.12) yields

$$\begin{aligned} \mathrm{Tr}\left[(\rho_1^0)^2\right] &= \frac{2}{N^2\pi^2} + \frac{1}{N}\left[1 - \frac{2}{N\pi^2}\right] \\ &= \frac{1}{N} \\ \rightarrow S_2(1) &= -\ln \mathrm{Tr}\left[(\rho_1^0)^2\right] = \ln N \end{aligned} \tag{3.13}$$

which is the expected result for free fermions (for a full derivation of the exact result, see Appendix B), supporting the use of the replacement of $\sin^2 \pi y$ for N large.

3.3.2 *1-Particle entanglement in Luttinger Liquid*

We now consider interacting fermions. At zero temperature in the thermodynamic limit, the reduced density matrix for $n = 1$ is given by [92, 118]

$$\begin{aligned} \rho_1(x_1, x_2) &= \frac{1}{N} \frac{\sin\left(k_F|x_1 - x_2|\right)}{L \sin\left(\pi|x_1 - x_2|/L\right)} \left| \frac{\sin\left(\pi i\epsilon/L\right)}{\sin\left(\frac{\pi}{L}(|x_1 - x_2| + i\epsilon)\right)} \right|^{2g} \\ &= \frac{1}{N} \frac{\sin\left(k_F|x_1 - x_2|\right)}{L \sin\left(\pi|x_1 - x_2|/L\right)} \left| \frac{1}{1 + \sin^2\left(\pi|x_1 - x_2|/L\right)/\sinh^2\left(\pi\epsilon/L\right)} \right|^{g}, \end{aligned} \tag{3.14}$$

where ϵ is an interaction dependent short distance cutoff, and $g = (K + K^{-1} - 2)/4$. The values of g for different interactions are shown in Fig. 3.1. Squaring and computing the trace:

$$\begin{aligned} \mathrm{Tr}\left[\rho_1^2\right] &= \int_{-L/2}^{L/2} dx_2 \int_{-L/2}^{L/2} dx_1 \frac{\sin^2\left(k_F|x_1 - x_2|\right)}{N^2 L^2 \sin^2\left(\pi|x_1 - x_2|/L\right)} \frac{1}{\left[1 + \frac{N^2}{\pi^2\epsilon^2\rho_0^2}\sin^2\left(\pi|x_1 - x_2|/L\right)\right]^{2g}} \\ &= \frac{2}{N^3}\int_0^{N/2} dy \frac{\sin^2 \pi y}{\sin^2\left(\pi y/N\right)} \frac{1}{\left[\frac{N^2}{\pi^2\rho_0^2\epsilon^2}\sin^2\left(\pi y/N\right) + 1\right]^{2g}}, \end{aligned} \tag{3.15}$$

where we have made the same change of variables as before, $y = \rho_0|x - x'|$. We have further approximated $\sinh \frac{\pi\epsilon}{L} \approx \frac{\pi\epsilon}{L}$. Though this quantity cannot be

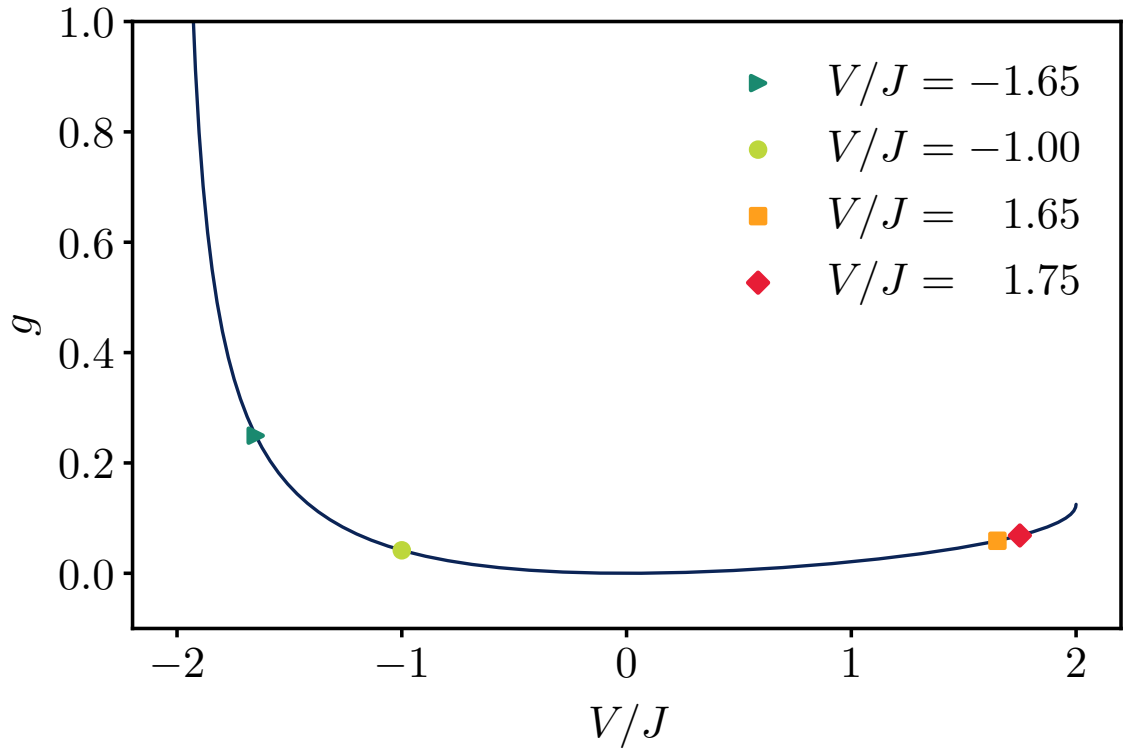

Figure 3.1: Values of the exponent g in the one body density matrix as a function of interaction strength V/J in the Tomonaga-Luttinger Liquid phase. Markers correspond to the g values of the interaction strengths we primarily consider.

integrated directly, we can utilize the same technique that we employed for free fermions,

$$\mathrm{Tr}\left[\rho_1^2\right] = \frac{1}{N}\left[\frac{1}{N^2}\int_0^{N/2} dy \frac{2\sin^2\pi y}{\sin^2 \pi y/N} \frac{1}{\left[\frac{N^2}{\pi^2\rho_0^2\epsilon^2}\sin^2(\pi y/N)+1\right]^{2g}} - \int_0^{N/2} dy \frac{2\sin^2(\pi y)}{\pi^2 y^2[1+y^2/\rho_0^2\epsilon^2]^{2g}}\right] + \frac{1}{N}\int_0^{N/2} dy \frac{2\sin^2(\pi y)}{\pi^2 y^2[1+y^2/\rho_0^2\epsilon^2]^{2g}} \,. \tag{3.16}$$

Evaluating the first two terms by replacing $\sin^2(\pi y) \to \frac{1}{2}$ and in the large N limit yields,

$$\Delta = \frac{1}{N}\left[\frac{2}{N\pi^2}\,{}_1F_2\left(-\frac{1}{2}; 2g, \frac{1}{2}; -\frac{N^2}{4\epsilon^2\rho_0^2}\right) - \frac{gN\,{}_1F_2\left(\frac{1}{2}; 1+2g, 2; -\frac{N^2}{\pi^2\epsilon^2\rho_0^2}\right)}{\pi^2\epsilon^2\rho_0^2}\right] , \tag{3.17}$$

where ${}_1F_2(a_1; b_1, b_2, z)$ is the generalized hypergeometric function. The term added in Eq. (3.16) is given by

$$\frac{1}{N}\int_0^{N/2} dy \frac{2\sin^2(\pi y)}{\pi^2 y^2(1+y^2/\epsilon^2\rho_0^2)^{2g}} = \frac{1}{N}\int_0^{\infty} dy \frac{2\sin^2(\pi y)}{\pi^2 y^2(1+y^2/\rho_0^2\epsilon^2)^{2g}} - \frac{1}{N}\int_{N/2}^{\infty} dy \frac{2\sin^2(\pi y)}{\pi^2 y^2(1+y^2/\rho_0^2\epsilon^2)^{2g}} \,. \tag{3.18}$$

The first integral can be computed exactly:

$$\frac{1}{N}\int_0^{\infty} dy \frac{2\sin^2(\pi y)}{\pi^2 y^2(1+y^2/\rho_0^2\epsilon^2)^{2g}} = \frac{\rho_0^{4g}\epsilon^{4g}\pi^{\frac{1}{2}+4g}\,{}_1F_2\left(2g; 1+2g, \frac{3}{2}+2g; \pi^2\rho_0^2\epsilon^2\right)\sec(2g\pi)}{2N\Gamma(1+2g)\Gamma(\frac{3}{2}+2g)} + \frac{\Gamma(\frac{1}{2}+2g)}{N\epsilon\rho_0\pi^{\frac{3}{2}}\Gamma(2g)}\left[{}_1F_2\left(-\frac{1}{2}; \frac{1}{2}, \frac{1}{2}-2g, \pi^2\epsilon^2\rho_0^2\right) - 1\right] , \tag{3.19}$$

where $\Gamma(z)$ is the Euler gamma function. For the second integral, we again send $\sin^2(\pi y) \to 1/2$, so the denominator can be integrated in the large N limit.

$$\frac{1}{N}\int_{N/2}^{\infty} dy \frac{1}{\pi^2 y^2 (1+y^2/\rho_0^2\epsilon^2)^{2g}} = -\frac{i(-1)^{-2g}\beta\left(-\frac{4\epsilon^2\rho_0^2}{N^2}, \frac{1}{2}+2g, 1-2g\right)}{2\epsilon\rho_0\pi^2}, \tag{3.20}$$

where $\beta(p,q)$ is the beta integral. To obtain the final expression for the finite-size corrected quantity Eq. (3.16), we plug in the terms derived in Eq. (3.17), Eq. (3.19), and Eq. (3.20)

$$\begin{aligned}\mathrm{Tr}\left[\rho_1^2\right] = \frac{1}{N}\Bigg[&\frac{2}{N\pi}\,{}_1F_2\left(-\frac{1}{2}; 2g, \frac{1}{2}; -\frac{N^2}{4\epsilon^2\rho_0^2}\right) - \frac{gN\,{}_1F_2\left(\frac{1}{2}; 1+2g, 2; -\frac{N^2}{\pi^2\epsilon^2\rho_0^2}\right)}{\pi^2\epsilon^2\rho_0^2}\Bigg] \\ &+ \frac{\rho_0^{4g}\epsilon^{4g}\pi^{\frac{1}{2}+4g}\,{}_1F_2\left(2g; 1+2g, \frac{3}{2}+2g; \pi^2\rho_0^2\epsilon^2\right)\sec(2g\pi)}{2N\Gamma(1+2g)\Gamma(\frac{3}{2}+2g)} \\ &+ \frac{\Gamma(\frac{1}{2}+2g)}{N\epsilon\rho_0\pi^{\frac{3}{2}}\Gamma(2g)}\left[{}_1F_2\left(-\frac{1}{2}; \frac{1}{2}, \frac{1}{2}-2g, \pi^2\epsilon^2\rho_0^2\right) - 1\right] \\ &+ \frac{i(-1)^{-2g}\beta\left(-\frac{4\epsilon^2\rho_0^2}{N^2}, \frac{1}{2}+2g, 1-2g\right)}{2\epsilon\rho_0\pi^2}.\end{aligned} \tag{3.21}$$

Eq. (3.21) represents a new result that can be checked by taking the limit $g \to 0$ ($K = 1$). In this case, $\mathrm{Tr}\,\rho_1^2 = 1/N$, and thus the second Rényi entropy at $n = 1$ is given by $\ln N$, the exact result for free fermions on a lattice [35, 91]. Using Eq. (3.21), the asymptotic scaling form for the second Rényi entropy at $n = 1$ can

be obtained by dividing out $1/N$ and expanding:

$$
\begin{aligned}
e^{-\Delta S_2(n=1)} = N \operatorname{Tr}\left[\rho_1^2\right] = & \frac{\Gamma(\frac{1}{2}+2g)\left[{}_1F_2\left(-\frac{1}{2};\frac{1}{2},\frac{1}{2}-2g;\pi^2\epsilon^2\rho_0^2\right)-1\right]}{\pi^{3/2}\epsilon\rho_0\Gamma(2g)} \\
& + \frac{(2\pi)^{4g}(\epsilon\rho_0)^{4g}{}_1F_2\left(2g;1+2g,\frac{3}{2}+2g;\pi^2\epsilon^2\rho_0^2\right)\sec(2g\pi)}{\Gamma(2+4g)} \\
& + \frac{\sqrt{\pi}\epsilon\rho_0\Gamma(-\frac{1}{2}+2g)}{4\Gamma(2g)N^2} + \frac{3\pi^{5/2}(\epsilon\rho_0)^3\Gamma(-\frac{3}{2}+2g)}{32\Gamma(2g)N^4} \\
& - \frac{2g\pi^{-\frac{1}{2}+4g}(\epsilon\rho_0)^{4g}\Gamma(-\frac{1}{2}-2g)}{2\Gamma(1-2g)}\frac{1}{N^{1+4g}} \\
& - \frac{2g\pi^{\frac{3}{2}+4g}(\epsilon\rho_0)^{2+4g}\Gamma(-\frac{3}{2}-2g)}{2\Gamma(-1-2g)}\frac{1}{N^{3+4g}} \\
& + \mathcal{O}\left(\frac{1}{N}\right)^{\min\{6,5+4g\}},
\end{aligned}
\tag{3.22}
$$

where we have introduced the notation:

$$
\Delta S_\alpha(n) \equiv S_\alpha(n) - \ln\binom{N}{n}. \tag{3.23}
$$

Defining $C_0(\alpha=2,n=1)$ as the N-independent term in Eq. (3.22), we can write

$$
\Delta S_2(n=1) = -\ln C_0(\alpha=2,n=1) + \mathcal{O}\left(\frac{1}{N^{\min\{2,1+4g\}}}\right) \tag{3.24}
$$

which is consistent with conjectured scaling of fermionic particle entanglement entropy Eq. (2.69).

3.3.3 *n-Particle entanglement*

Without information about the form of the higher n density matrices, it is difficult to determine an exact form for the Rényi entropy. However, the general properties of the entanglement discussed in Section 2.5 can be used to direct a systematic analysis of numerical data to construct a shape function for the general n-particle

entanglement entropy. First, the result for free fermions is given by $\ln \binom{N}{n}$ and thus the remaining terms must vanish in the absence of interactions suggesting that the coefficients of each subleading term are dependent on interaction strength g. Furthermore, this leading order scaling is independent of the Rényi index, so the α dependence can only appear in the subleading terms, either in the coefficients or as exponents of finite size corrections. Finally, we know that the n-particle entanglement is equivalent to the $N-n$-particle entanglement, suggesting the entanglement as a function of n/N reaches a maximum at $n = \lfloor N/2 \rfloor$ and is symmetric about this point.

3.4 Results

To empirically construct the shape function describing the n-particle entanglement entropy for the ground state of the J-V Hamiltonian given by Eq. (2.53), we carry out large scale numerical computations using both exact diagonalization (ED) and approximate density matrix renormalization group (DMRG) techniques. While ED gives approximation-free results, the exponential dependence of the size of the Hilbert space on the length of the system L limits the possible values of (n, N, L) that we can consider. To mitigate this, we encode the basis states with an integer fermion basis and exploit the translational, inversion, and particle-hole symmetries of the system, increasing the efficiency of operations performed on the states and reducing the size of the space we need to consider by up to a factor of $1/(4L)$. This allows us to perform exact diagonalization for even the 7-particle entanglement at $L = 28$ sites. We further supplement the ED data with DMRG results to study much larger systems at the cost of truncation errors, using ED to benchmark the data at small system sizes. Utilizing the `ITensors.jl` [119] package, the ground state is obtained as a matrix product state which is then used to compute the n-RDM and, by extension, the n-particle entanglement entropy. To reduce the necessary computation, several tricks are deployed such as mapping the fermion

operators onto an integer basis, and leveraging the anticommutation relations of the fermion operators. This allows us to compute the two-particle entanglement entropy for systems up to $L = 80$ lattice sites, the three-particle entanglement entropy for up to $L = 48$, and even the four-particle entanglement entropy for up to $L = 32$ sites. *

All code to reproduce the numerical simulations, fits, and figures is open source and has been made available online [120].

3.4.1 1-Particle entanglement

In this section, we exclusively study the 1-particle entanglement ($n = 1$). Using ED and DMRG, we numerically test our analytic scaling at $\alpha = 2$ and $n = 1$ to (i) verify finite size corrections in powers of $1/N$ and (ii) determine the coefficients of the scaling along with their error and relative importance. This procedure will serve as a benchmark for determining how the scaling of the shape function depends on α. Finally, we will motivate generalizing to $n > 1$ where no analytic form for the particle entanglement entropy is known to exist. To simplify our analysis, we focus on the exponentiated subleading terms in the particle entanglement which admit the expansion (using as yet unknown coefficients C_j)

$$e^{-\Delta S_2(n=1)} = C_0 + \frac{C_{1+4g}}{N^{1+4g}} + \frac{C_2}{N^2} + \frac{C_{3+4g}}{N^{3+4g}} + \frac{C_4}{N^4}\,, \tag{3.25}$$

where we only include terms up to fourth order in $1/N$ as was done previously in Eq. (3.22). To test this scaling, we calculate $S_2(n = 1)$ deep within the TLL phase, away from the phase transitions, using the ground state of the J-V model. At each interaction strength, exponents are computed using $g = (K + K^{-1} - 2)/4$ with K determined by Eq. (2.61). The coefficients of Eq. (3.25) are extracted from a

*While it is possible to compute higher order reduced density matrices with DMRG we find that systematic errors related to the number of states we keep begin to affect the ability to perform high precision non-linear fits to proposed scaling functions.

polynomial fit to $e^{-\Delta S_2(n=1)}$. The results are illustrated in Fig. 3.2 where we include only system sizes with $N > 10$ along with a fit to the form given by Eq. (3.25).

The markers show $e^{-(S_2(n=1)-\ln N)}$ results from ED and DMRG, while the solid lines correspond to the polynomial fit, and the data exhibits excellent agreement with the predicted scaling form. The numerical values of the coefficients of the N dependent terms and the constant term C_0 in Eq. (3.25) are presented in Table 3.1 and Table 3.2 respectively. We utilize parenthetical notation for the error to denote modification of the last digit; for example, C_4 at $V/J = -1.65$ is expressed as $-13.5(7) \equiv -13.5 \pm 0.7$. We additionally report the constant terms predicted by our bosonization formula Eq. (3.22)

$$C_0(g) = \frac{\Gamma(\frac{1}{2}+2g)[{}_1F_2\left(-\frac{1}{2};\frac{1}{2},\frac{1}{2}-2g;\pi^2\epsilon^2\rho_0^2\right)-1]}{\pi^{3/2}\epsilon\rho_0\Gamma(2g)} + \frac{(2\pi)^{4g}(\epsilon\rho_0)^{4g}{}_1F_2\left(2g;1+2g,\frac{3}{2}+2g;\pi^2\epsilon^2\rho_0^2\right)\sec(2g\pi)}{\Gamma(2+4g)}. \tag{3.26}$$

To facilitate comparison, the non-universal cutoff ϵ has been extracted using the same approach presented in Ref. [92]. We find close agreement between the predicted values for C_0 and the extracted values from the fit. We can extract the leading order terms, (constants in the scaling form), with high precision, determining uncertainties on the order of 10^{-5} for $V/J = -1.65$ and 10^{-7} otherwise. The increase in error for $V/J = -1.65$ is expected due to proximity to the first order phase transition at $V/J = -2$ where the TLL picture should begin to break down. We now attempt to identify the dependence of the asymptotic scaling of the shape function on the order of the Rényi entanglement entropy α. For $\alpha = 1$ (the von Neumann case), we extract the coefficients in Eq. (3.25) through a polynomial fit. The results are shown in Fig. 3.3 for the same values of V/J used to test $\alpha = 2$. The numerical values of the coefficients extracted from the hypothesized scaling relation and the leading order terms are shown in Table 3.3 and Table 3.4 respectively. We find that the errors in the coefficients are on the

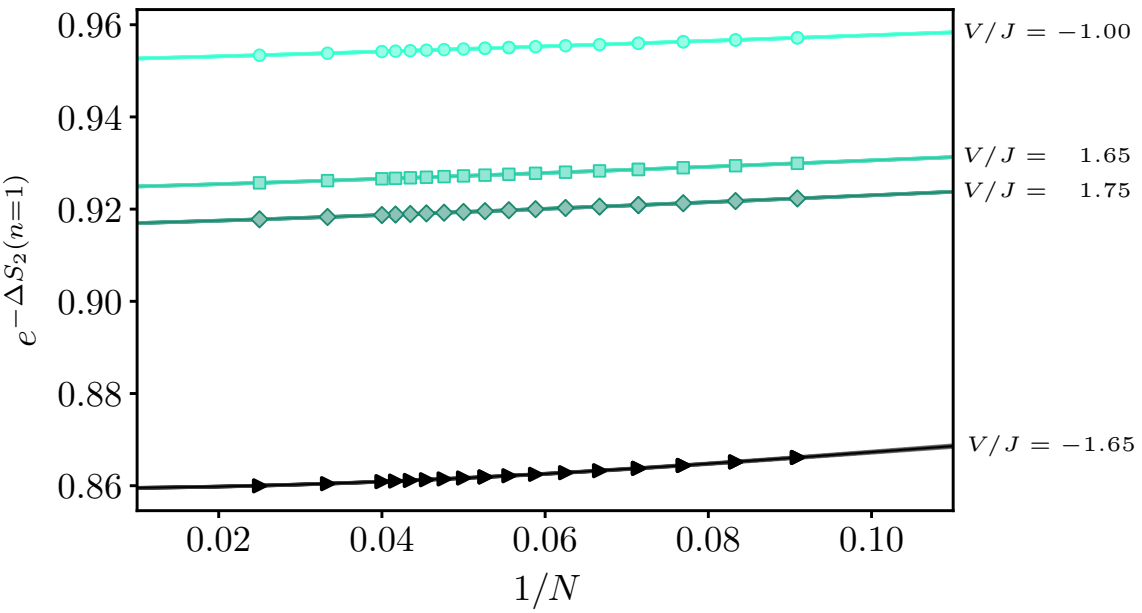

Figure 3.2: $e^{-\Delta S_2(n=1)}$ for different V/J at $\alpha = 2$. Solid lines correspond to fitting the data according to Eq. (3.25). Symbols correspond to data for $N > 10$ collected from DMRG and ED at four different values of the interaction strength V/J indicated by the different markers and colors.

Table 3.1: Interaction dependence for $\alpha = 2$. Coefficients for Eq. (3.25) at different values of V/J. For the special interaction strength $V/J = -1.65 \simeq -2\cos[\pi/(3+\sqrt{5})]$, $g \simeq 1/4$ and thus we fit to a reduced form containing only even inverse powers of $1/N$ corresponding to C_2 and C_4.

$n = 1,\ \alpha = 2$

V/J	C_{1+4g}	C_2	C_{3+4g}	C_4
-1.65	–	$0.918(6)$	–	$-13.5(7)$
-1.00	$8.1197(1) \times 10^{-2}$	$-1.070(1) \times 10^{-2}$	$1.3(2) \times 10^{-3}$	$-1.58(9) \times 10^{-2}$
1.65	$0.11576(1)$	$-7.52(1) \times 10^{-2}$	$0.176(3)$	$-0.31(1)$
1.75	$0.13827(2)$	$-1.078(3) \times 10^{-2}$	$0.368(8)$	$-0.69(2)$

Table 3.2: Interaction dependence for $\alpha = 2$. Leading order coefficient/constant term in Eq. (3.25) at different values of V/J.

$n = 1,\ \alpha = 2$

V/J	$C_0\|_{\text{predicted}}$	$C_0\|_{\text{fit}}$
-1.65	0.85555	$0.85945(1)$
-1.00	0.95170138	$0.95229438(1)$
1.65	0.92378681	$0.92452681(8)$
1.75	0.915705201	$0.91659419(9)$

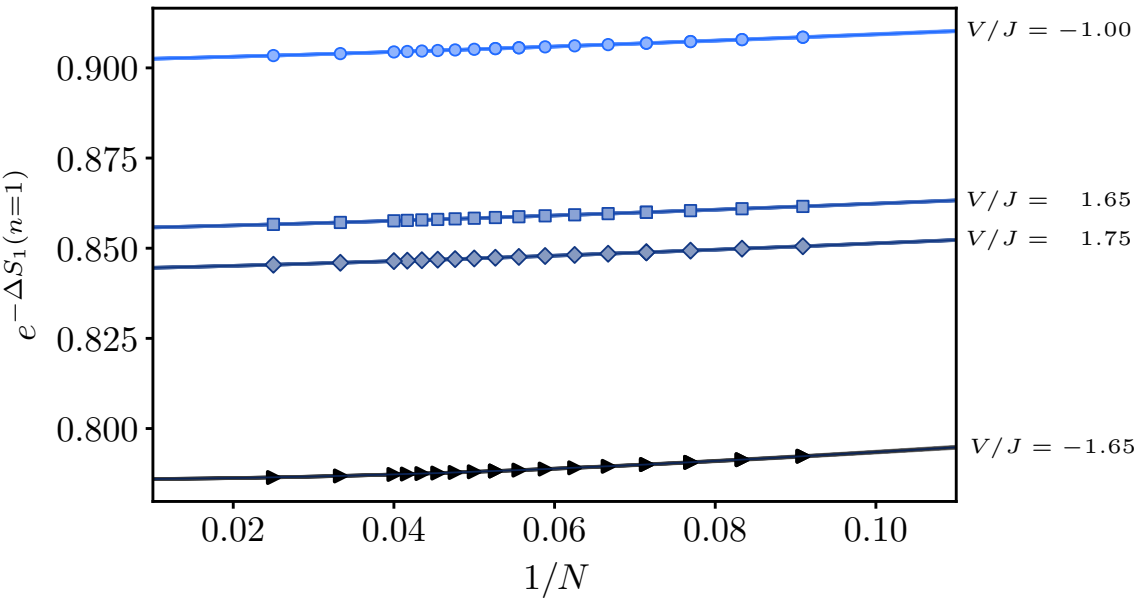

Figure 3.3: $e^{-\Delta S_1(n=1)}$ for different interaction strengths V/J and fixed $\alpha = 1$. Solid lines correspond to fitting to Eq. (3.25), while points correspond to data collected from DMRG and ED. Different markers are used to indicate four values of V/J.

Table 3.3: Interaction dependence for $\alpha = 1$. Coefficients for Eq. (3.25) at different values of V/J.

$n = 1,\ \alpha = 1$				
V/J	C_{1+4g}	C_2	C_{3+4g}	C_4
-1.65	–	$8.55(6) \times 10^{-1}$	–	$-10.1(6)$
-1.00	$9.011(1) \times 10^{-2}$	$1.45(2) \times 10^{-1}$	$9.3(4) \times 10^{-1}$	$2.4(1)$
1.65	$1.144(7) \times 10^{-2}$	$5.93(9) \times 10^{-2}$	$-6.9(2) \times 10^{-1}$	$1.63(6)$
1.75	$1.317(6) \times 10^{-2}$	$3.0(7)$	$-5.5(1) \times 10^{-1}$	$1.28(5) \times 10^{-2}$

Table 3.4: Interaction dependence for $\alpha = 1$. Leading order coefficient/constant term in Eq. (3.25) at different values of V/J.

$n = 1,\ \alpha = 1$	
V/J	C_0
-1.65	$0.78592(1)$
-1.00	$0.9021179(9)$
1.65	$0.8553804(2)$
1.75	$0.8442061(2)$

same order of magnitude, with equal precision in the constant terms as for the case $\alpha = 2$ where the exact scaling relation is known.

This suggests that the exponents in the scaling form of $1/N$ are solely dependent on the interaction strength and independent of the order of the Rényi entropy. Focusing on two fixed interactions $V/J = -1.65, 1.75$, the fit to the scaling form in Eq. (3.25) is shown for different values of α in Fig. 3.5. The coefficients extracted for each α have the same order of magnitude in their error. The extracted coefficients are available as data files online [120]. This gives numerical confirmation that the functional form of the scaling of the Rényi entanglement entropy is independent of the Rényi index α. To further understand how the leading order coefficient behaves as a function of interaction strength, we fix α and vary V/J. We find that the constant term C_0 in Eq. (3.29) shows similar scaling with the interaction dependent parameter g at each α. Similarly, at fixed interaction, we determine the constant term as a function of the order α and see that it exhibits similar scaling for each value of V/J. This suggests that unlike the exponents of the N scaling, coefficients depend on both the interaction and the order of the Rényi entropy. The results for both cases are illustrated in Fig. 3.4. In the left panel we plot $C_0(g)$ extracted from our non-linear fitting to Eq. (3.25) along with a guide to the eye (dashed line) except in the case $\alpha = 2$ where we use a solid line to indicate our definitive prediction from bosonization given in Eq. (3.22), again using ϵ values as extracted in Ref. [92]. We observe excellent agreement for weak interactions with some deviations appearing for large g as we approach the first order phase transition (we only include $V/J < 0$ here). This provides further confirmation of Eq. (3.26). Taken together, the above numerical investigation strongly suggests that the overall scaling of $\Delta S_\alpha(n = 1)$ is consistent with Eq. (2.69) even for $\alpha \neq 2$ where bosonization results are not available, i.e.

$$\Delta S_\alpha(n = 1) = -\ln C_0(\alpha, n = 1) + \mathcal{O}\left(\frac{1}{N^{\min\{2,1+4g\}}}\right). \tag{3.27}$$

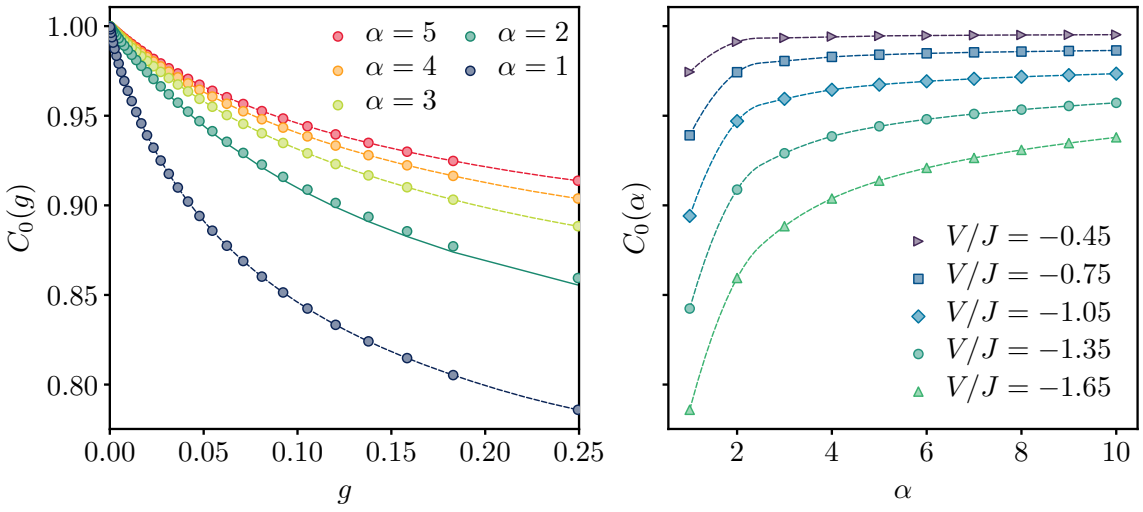

Figure 3.4: Constant term in fit of $e^{-\Delta S_\alpha(n=1)}$ as a function of the interaction g for different α. Dotted lines are a guide to the eye, while the solid line for $\alpha = 2$ in the left panel is a prediction from bosonization.

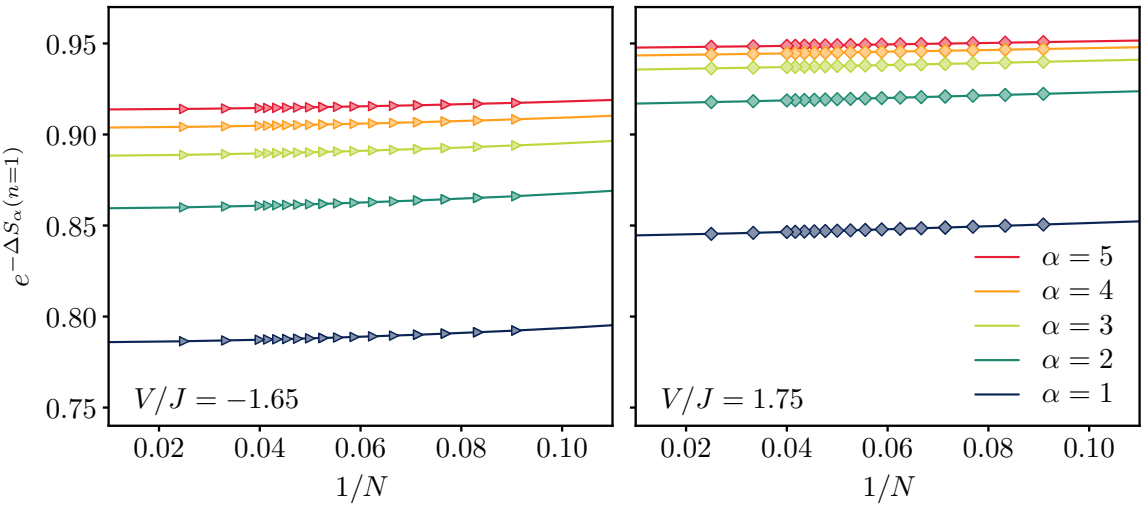

Figure 3.5: $e^{-\Delta S_\alpha(n=1)}$ for $V/J = -1.65$ (left) and 1.75 (right). Solid lines correspond to fitting the data according to Eq. (3.25). The points correspond to data collected from DMRG and ED with different colors used to indicate each α.

Taken together, the above numerical investigation strongly suggests that the overall scaling of $\Delta S_\alpha(n=1)$ is consistent with Eq. (2.69) even for $\alpha \neq 2$ where bosonization results are not available, i.e.

$$\Delta S_\alpha(n=1) = -\ln C_0(\alpha, n=1) + \mathcal{O}\left(\frac{1}{N^{\min\{2,1+4g\}}}\right), \tag{3.28}$$

where we also observe from the data that the exponent of the leading finite size correction $\gamma_\alpha(n=1) = \min\{2, 1+4g\}$ is independent of α.

3.4.2 *n-Particle entanglement*

Having analyzed numerical results for particle entanglement scaling at a fixed bipartition of $n=1$ and $N-1$ particles, we now generalize to the behavior of $e^{-\Delta S_\alpha(n)}$ for $n > 1$. As there are no analytical results to motivate the form of the scaling for $n > 1$, we assume a general finite-size expansion holds and focus primarily on the constant term C_0:

$$e^{-\Delta S_\alpha(n)} = C_0 + \frac{C_1}{N} + \frac{C_2}{N^2} + \frac{C_3}{N^3} + \frac{C_4}{N^4} + \dots . \tag{3.29}$$

Comparisons between this scaling for $n = 1, 2, 3$ are shown in Fig. 3.6 for the first and second Rényi entropy at $V/J = 1.75$ using Eq. (3.25) for $n = 1$ and Eq. (3.29) for $n = 2, 3$. The resulting coefficients for $\alpha = 2, 1$ are given in Table 3.5 and Table 3.6 respectively. We observe that the coefficients can be obtained with the same precision as for $n = 1$, which suggests that the scaling form provided by Eq. (3.29) does not significantly differ from the true form. Particularly, when forcing the exponent $\gamma_\alpha(n > 1)$ of the leading correction term to be equal to unity, we find a high quality of fit over a wide range of interactions, which suggests that the exponent $\gamma_\alpha(n > 1) \approx 1$ and has (if any) very weak dependence on the interaction strength. Additionally, we observe that the negative logarithm of the

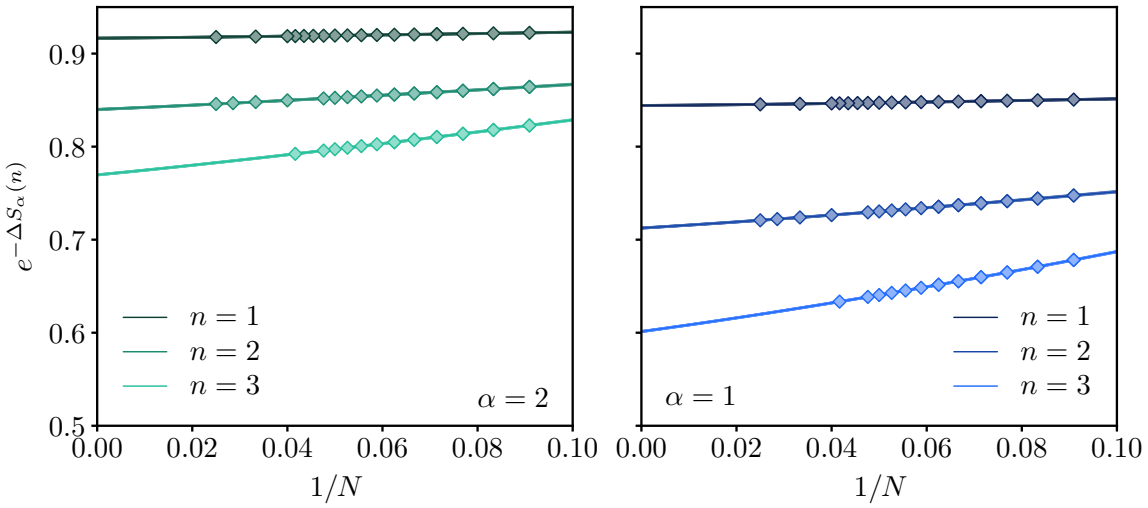

Figure 3.6: $e^{-\Delta S_\alpha(n)}$ for different bipartitions n and $N-n$. Solid lines represent the fit to Eq. (3.25) for $n = 1$ and to Eq. (3.29) for $\alpha = 1, 2$ and $V/J = 1.75$. Markers represent data collected from ED and DMRG.

Table 3.5: n dependence for $\alpha = 2$. Coefficients for Eq. (3.29) for $n = 2, 3$ at $V/J = 1.75$.

$\alpha = 2, V/J = 1.75$					
n	C_0	C_1	C_2	C_3	C_4
2	0.839916(5)	0.2163(4)	0.906(1)	−5.2(1)	14.3(6)
3	0.769652(6)	0.4906(4)	1.504(9)	−6.55(9)	15.5(3)

Table 3.6: n dependence for $\alpha = 1$. Coefficients of Eq. (3.29) for $n = 2, 3$ at $V/J = 1.75$.

$\alpha = 1, V/J = 1.75$					
n	C_0	C_1	C_2	C_3	C_4
2	0.712477(5)	0.3071(4)	1.25(1)	−5.8(1)	16.1(6)
3	0.601253(6)	0.6949(3)	2.059(8)	−5.79(2)	16.2(3)

of the constant term C_0 shows a linear dependence on n irrespective of both the interaction strength and order of the Rényi entropy as shown in Fig. 3.7. Thus, we predict

$$\ln C_0(\alpha, n) \approx n \ln C_0(\alpha, n = 1). \tag{3.30}$$

confirming and characterizing the previously postulated n dependence of the subleading constant, where this result can summarized by the scaling form

$$\Delta S_\alpha(n) = -n \ln C_0(\alpha, 1) + \mathcal{O}\left(\frac{1}{N^{\gamma(n)}}\right),$$

with

$$\begin{aligned} \gamma(n = 1) &= \min\{2, 1 + 4g\} \\ \gamma(n > 1) &\approx 1 \quad . \end{aligned} \tag{3.31}$$

3.4.3 *Construction of a general shape function*

Having numerically analyzed the entanglement for $n \leq 3$, we now turn towards motivating a function for the general n-particle scaling that reproduces the observed asymptotic scaling with $1/N$. We expect the general form to depend on both N and n, or more conveniently, one can use N and the ratio n/N. Here, we additionally expect $S_\alpha(n)$ to vanish for $n/N = 0$ or 1, and to be symmetric around $n/N = 1/2$, which can be embedded in the expression of the shape function by assuming it to be a function of $\sin(n\pi/N)$ instead of n/N. Therefore, without loss of generality, we introduce the shape function Φ defined via

$$\Delta S_\alpha = S_\alpha(n) - \ln \binom{N}{n} = N\Phi\left(\sin\frac{n\pi}{N}, N; g, \alpha\right).$$

We begin our analysis for the case where $\nu = n/N$ is fixed and $0 < \nu < 1$. At half-filling the upper bound on ΔS_α is $\ln \binom{2N}{n} - \ln \binom{N}{n} \sim \ln \left[\frac{4(1-\nu)^{1-\nu}}{(2-\nu)^{2-\nu}}\right] N$, *e.g.*, if we consider $n/N = 1/2$ then the bound scales as $N \ln\left(\frac{8}{9}\sqrt{3}\right) \approx 0.4315N$. Therefore,

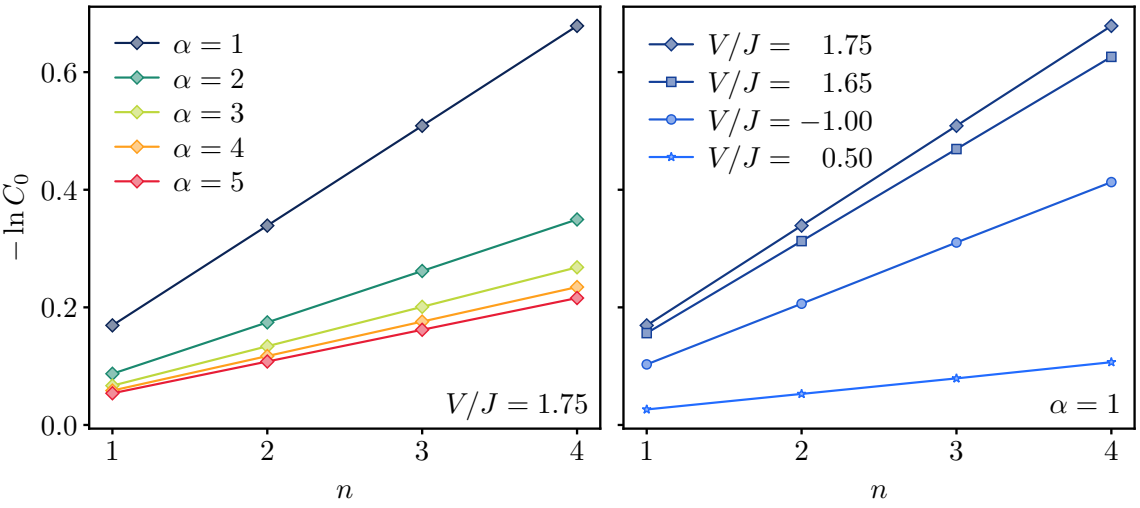

Figure 3.7: At fixed interaction $V/J = 1.75$ and at fixed $\alpha = 1$, the subleading constant term of the Rényi entropy scales linearly with n for bipartitions of $n = 1 \ldots 4$ and $N - n$ particles.

the leading term in ΔS_α is expected at best to scale linearly with N. Thus we can approximate

$$\Delta S_\alpha \sim N\Phi_0\left(\sin\frac{n\pi}{N}; g, \alpha\right) , \tag{3.32}$$

where we have introduced a new simplified shape function with the explicit N dependence removed. To numerically investigate the scaling of this function, we separate the data into fixed ratios $n/N = 1/2 \ldots 1/8$ and plot ΔS_α as a function of N in Fig. 3.8.

We find that for each ratio, the data collapses onto a straight line suggesting that this function produces a constant at a given n/N, an *a posteriori* justification for our assumption of the form of Φ_0. The plot for each ratio is shown in the left panel of Fig. 3.8 where each line is fitted to

$$\Delta S_\alpha = \Phi_0 N + \Phi_1, \tag{3.33}$$

where we have introduced a correction term Φ_1, quantifying the deviation of Φ from Φ_0. The resulting coefficients and their corresponding errors are given in Table 3.7. With the extensive scaling of ΔS_α confirmed, we next examine the simplified shape function Φ_0. To gain insight into the dependence of Φ_0 on the ratio n/N, we expand as

$$\Phi_0\left(\sin\frac{n\pi}{N}; g, \alpha\right) = \sum_{m=1}^{m_{\max}} A_m \sin^m\left(\frac{\pi n}{N}\right) , \tag{3.34}$$

where we ignore the constant term since $\Phi_0\left(\sin\frac{n\pi}{N}; g, \alpha\right)$ vanishes for $n/N = 0$ and 1. By performing a standard non-linear fitting procedure using Eq. (3.34), we find that a high-precision fit can be obtained using only the first four terms *i.e.*, $m_{\max} = 4$

$$\Phi_0(\alpha, n, N, g) \approx A_1 \sin\left(\frac{\pi n}{N}\right) + A_2 \sin^2\left(\frac{\pi n}{N}\right) + A_3 \sin^3\left(\frac{\pi n}{N}\right) + A_4 \sin^4\left(\frac{\pi n}{N}\right) , \tag{3.35}$$

Table 3.7: n/N dependence for $\alpha = 1$. Coefficients in Eq. (3.33) for fixed ratios of n/N at $V/J = 1.75$.

$\alpha = 1, V/J = 1.75$		
n/N	Φ_0	Φ_1
$1/2$	$0.0430(2)$	$0.01706(3)$
$1/3$	$0.03821(2)$	$0.01517(2)$
$1/4$	$0.03209(4)$	$0.0141(1)$
$1/5$	$0.02734(3)$	$0.01094(2)$
$1/6$	$0.02372(1)$	$0.0109(2)$
$1/7$	$0.020897(8)$	$0.0098(2)$
$1/8$	$0.018654(4)$	$0.00893(7)$

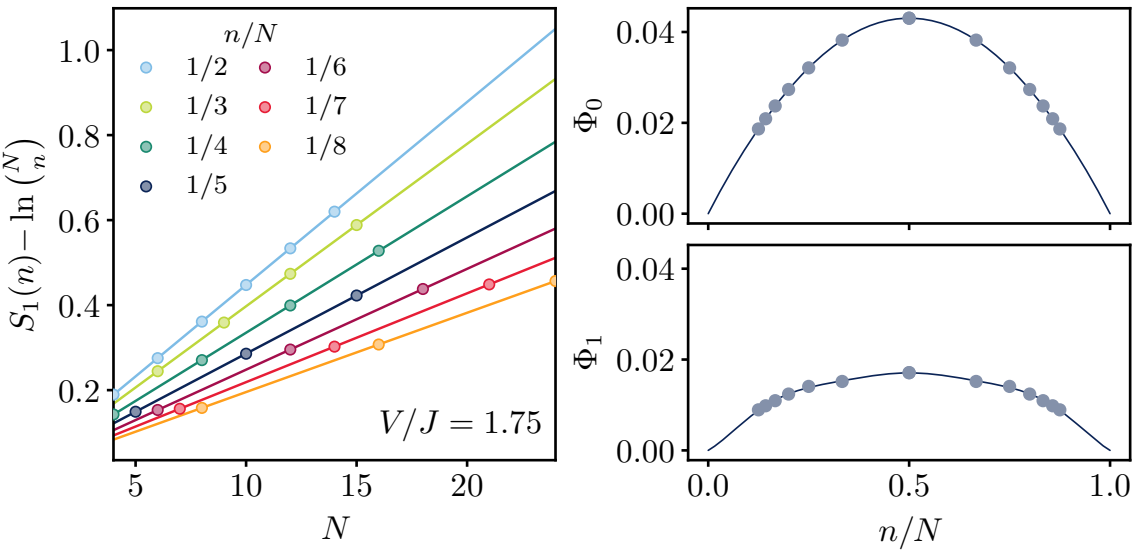

Figure 3.8: The lefthand panel shows scaling of $S_1 - \ln\binom{N}{n}$ with N at fixed ratios of n/N at $V/J = 1.75$ for $\alpha = 1$. Solid lines correspond to a fit of the data to Eq. (3.33) confirming the linear N scaling. Markers correspond to data collected from ED and DMRG with equivalent ratios n/N. The righthand panel shows the values of Φ_0 and Φ_1 for each ratio fitted to the truncated shape function given by Eq. (3.34).

as demonstrated by the solid lines in the right-upper panel of Fig. 3.8. However, to account for the finite size effects we apply the same analysis to the correction term Φ_1 as demonstrated in the right-lower panel of Fig. 3.8 and the corresponding fitting coefficients for both of Φ_0 and Φ_1 are listed in Table 3.8.

We calculate the shape function for a large set of ratios n/N and for N in the range $11 \leq N \leq 40$. The results are illustrated in Fig. 3.9, which includes data corresponding to different interaction strengths and Rényi indices α. For each interaction strength and Rényi index in Fig. 3.9, we use the same subset of ratios n/N as in Table 3.7 to calculate fitting coefficients for the asymptotic shape function Φ_0 and the corresponding finite-size correction Φ_1. The solid curves represent $\Phi = \Phi_0 + \Phi_1/N$ for each ratio in Fig. 3.9. We find excellent agreement between the fitted curve and the data points, validating the asymptotic shape function Φ_0 for ratios n/N beyond the set in Table 3.7. We further compute $\Phi_0(n/N, V/J)$ for each data point at interactions $V/J = -1.65, -2, -0.5, 0.5, 1.75$ and $\alpha = 1$ and interpolate to generate a surface plot of Φ_0. We find that the surface exhibits a saddle shape, with a pommel and cantle that grow with interaction strength. The surface along with the data is shown in Fig. 3.10. To this point, the numerical analysis of the shape function we have carried out suggests that for $N \gg 1$, the interaction-induced entanglement of particles follows the general scaling form:

$$\Delta S_\alpha \sim N \sum_{m=1} A_m \sin^m\left(\frac{\pi n}{N}\right) . \tag{3.36}$$

Building on this, we can consider the asymptotic scaling of ΔS_α for $n \ll N$ by Taylor expanding the sine functions in Eq. (3.36), which yields

$$\Delta S_\alpha \sim A_1 \pi n + \mathcal{O}(n^2/N) . \tag{3.37}$$

This deduced scaling form is consistent with the result of the previous subsection, *i.e.*, Eq. (3.4.2), where both relations suggest that as $N \to \infty$, ΔS_α approaches a

Table 3.8: Values of coefficients in Eq. (3.35) for both functions Φ_0 and Φ_1 at $V/J = 1.75$ and $\alpha = 1$.

$\alpha = 1, V/J = 1.75$				
	A_1	A_2	A_3	A_4
Φ_0	$0.0551(2)$	$-0.021(1)$	$0.014(2)$	$-0.0052(8)$
Φ_1	$0.016(4)$	$0.04(2)$	$-0.08(3)$	$0.04(1)$

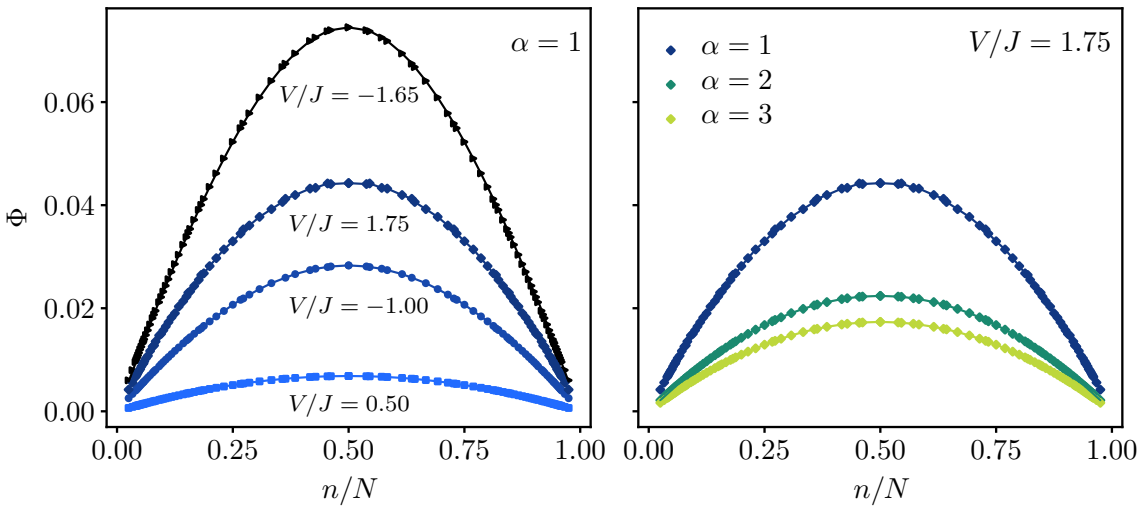

Figure 3.9: The left panel shows the dependence of $[S_1 - \ln \binom{N}{n}]/N$ on n/N at different values of V/J for fixed $\alpha = 1$. The right side shows the same quantity at $V/J = 1.75$ for different values of α. Markers represent data collected from DMRG and ED while solid lines represent a fit to Eq. (3.34). The dark blue diamonds for $V/J = 1.75$ and $\alpha = 1$ are included in both panels for comparison.

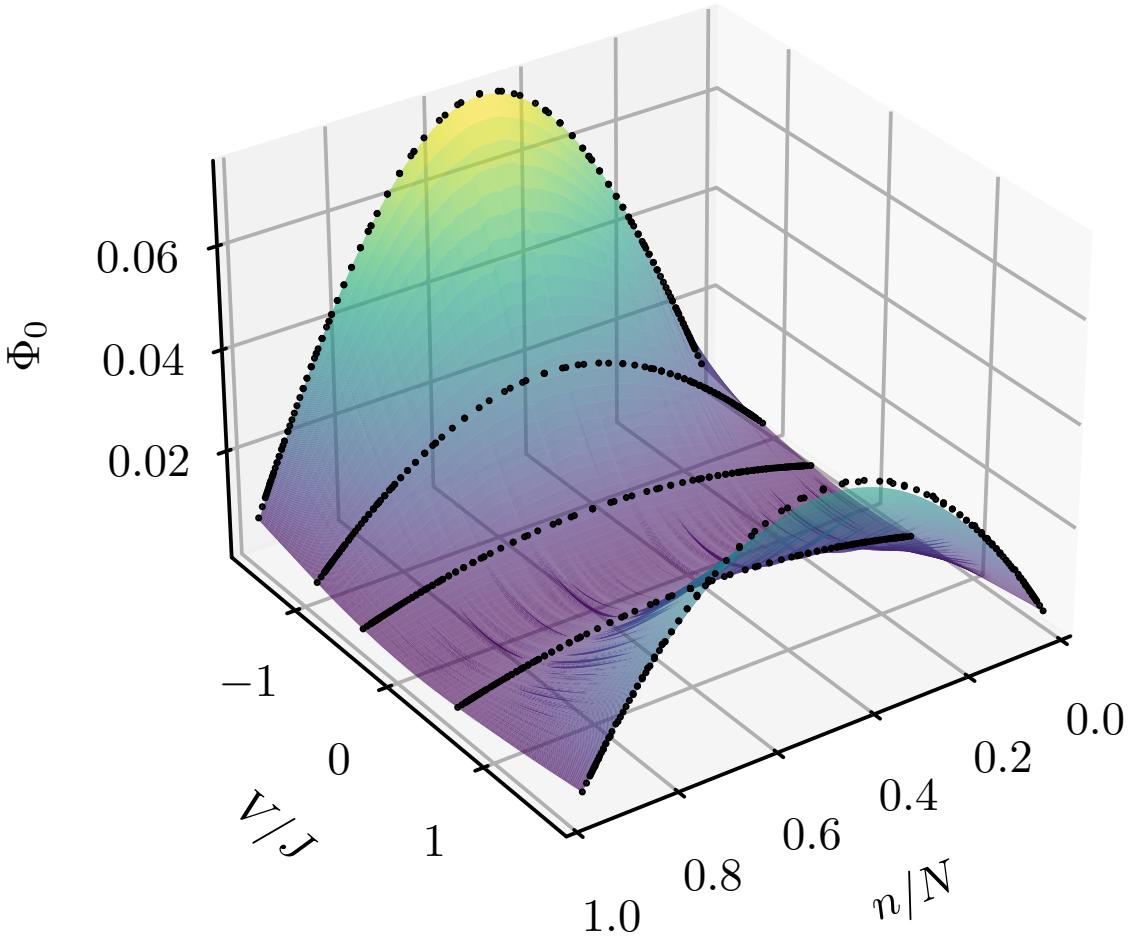

Figure 3.10: Interpolation of the surface given by $\Phi_0(n/N, V/J)$ along with the data (black circles) for S_1 at $V/J = -1.65, -1.00, -0.5, 0.5, 1.75$. The surface follows the shape of a saddle that reflects the asymmetry of the importance of interactions near the first order and continuous quantum phase transitions.

constant value that scales linearly with n. Comparing the slope of both linear relations suggests that $\ln C_0(n)/n \approx \ln C_0(1)$, which is obtained by fixing n at large N, should be equal to $-\pi A_1$, where A_1 is obtained from the fitting of the shape function to Eq. (3.35). In order to test this prediction, we extract the value of the coefficient $A_1 = -\ln C_0(n)/(n\pi)$ and then compare it with the value of A_1 obtained from a direct non-linear fit of the shape function. Table 3.9 shows this comparison for the case of $V/J = 1.75$ and $\alpha = 1$, where the value of A_1 shows deviations that are on the order of 2%.

3.5 Conclusions

In this chapter, we combined bosonization techniques with exact diagonalization and density matrix renormalization group calculations to study the entanglement entropy between subsets of n and $N - n$ particles in the ground state of the J-V model of one-dimensional interacting spinless lattice fermions within a delocalized quantum liquid phase. Understanding the scaling of the entanglement $S_\alpha(n)$ as a function of total system size N, subsystem size n, Rényi index α and interaction strength V/J required pushing numerics to unprecedented system sizes, possible only by exploiting all symmetries of the ground state and n-body reduced density matrix. The resulting systematic analysis confirms the empirical scaling previously proposed in the literature, and, extends it in two different directions: (i) we identify an interaction induced extensive correction in N at fixed n/N and (ii) determine that in the limit of large N, interactions increase entanglement from the non-interacting case by a term that is proportional to the subsystem size n. This increase in particle entanglement in an interacting system above its free fermion value (arising for the antisymmetrization of the N-particle wavefunction) is encapsulated in a symmetric shape function Φ which we numerically determine as a function of the ratio n/N and interaction strength V/J. It has a non-trivial saddle-like shape as a result of the fact that both repulsive and attractive interactions

Table 3.9: Extraction of the A_1 coefficient for $\alpha = 1, V/J = 1.75$ through fitting $e^{-\Delta S_1(n)}$ for different values of n. Percent differences are determined by comparing the computed coefficients (using C_0) to $A_1 = 0.0551(2)$ extracted from Eq. (3.35).

$\alpha = 1, V/J = 1.75$

n	$C_0(n)$	$-\ln C_0(n)$	$A_1 = -\ln C_0(n)/(\pi n)$	% Difference
1	0.8442062(2)	0.1693585(2)	0.05390848(8)	2.2(4)
2	0.712477(6)	0.339008(8)	0.053955(1)	2.1(4)
3	0.601253(6)	0.508739(9)	0.053979(1)	2.0(4)

between fermions generate non-trivial entanglement combined with the purity of the ground state of the J-V model under consideration.

It is natural to speculate how our results, computed for a 1D critical system, would generalize in the presence of integrability breaking terms in the Hamiltonian, to higher dimensions, or under a change of particle symmetry (e.g. bosons or anyons). For the first, our bosonization calculation would support similar scaling in all critical fermionic systems, and this could be straightforwardly confirmed by adding a next nearest neighbor interaction to the Hamiltonian (see e.g. Ref. [87] where the particle entanglement dynamics of a J-V-V' model was considered). Eq. (3.1) should also be applicable to itinerant quantum phases of fermions in two and higher dimensions, motivated by the extensive sub-leading behavior of the particle entanglement, unlike the dimension-dependent area law that exists for entanglement between spatial sub-regions. For bosons, the prefactor of the leading order $\ln \binom{N}{n}$ term in the particle entanglement is no longer universal and we leave a systematic study of this case to future work, where it may be possible to study extremely large bosonic lattice models via ground state quantum Monte Carlo [121].

The n-particle entanglement provides a useful way to quantify quantum correlations generated by interactions encoded in the n-particle reduced density matrix, a non-local correlation function that forms a mainstay of many-body methods in both chemistry and physics. Having detailed knowledge of its finite size scaling behavior and interaction dependence may have practical implications for the measurement and exploitation of this unique form of entanglement as a resource.

I daresay you haven't had much practice, said the Queen,
When I was your age, I always did it for half-an-hour a day.
Why, sometimes I've believed as many as six
impossible things before breakfast.
Lewis Carroll
Through the Looking Glass

THE TWO BODY REDUCED DENSITY MATRIX OF A LUTTINGER LIQUID

4

This chapter contains text from first author work by the author in an in-progress manuscript, with minor modifications where appropriate for this format. The author performed all the derivations, fitted results to the numeric data, produced the figures, and wrote the majority of text with contributions from the other coauthors. Hatem Barghathi wrote sections on the analysis of the 2-RDM and parts of the discussion with editing by the author. Matthias Thamm performed the numerical simulations and assisted in the fitting to the microscopic model and the production of the structure factor figure. Matthias contributed to the writing of the application sections. Hatem Barghathi contributed significantly to the analysis of the structure of the 2-RDM. Bernd Rosenow and Adrian Del Maestro supervised this work.

4.1 Introduction

Understanding the many-body correlations that emerge in interacting quantum systems is a fundamental problem in condensed matter physics, nuclear many-body theory, quantum chemistry, and quantum information. In this context, the n-body reduced density matrix, ρ_n, is a powerful tool as it provides a complete snapshot of all n-particle correlations, and can be used to compute any n-body

observable. A key part of the density matrix is the diagonal components, or density-density correlations, which have been experimentally measurable in a variety of systems [122, 123]. From these elements, one can compute key quantities such as the static structure factor, which plays a central role in characterizing the response of a system to external probes and can be directly accessed in scattering experiments [37, 124]. Beyond density correlations, the one-particle reduced density matrix (1-RDM) plays a key role in characterizing many-fermion wavefunctions. It defines canonical orbitals that capture single-particle coherence and short-range correlations, particularly relevant in nuclear physics [125]. It has additional applications in quantum chemistry, where the N-representability problem places constraints on the allowable forms of reduced density matrices [126].

While density-density correlations capture important aspects of quantum fluctuations, the off-diagonal elements of reduced density matrices, or coherences, encode additional information about quantum phases and the nature of correlations. In ultracold atomic systems, coherences have helped understand quantum phase transitions, dynamical instabilities, and the characterization of quantum entanglement [127–129]. Computing entanglement entropies from the density matrix allows us to identify of phase transitions [130], as well as gain access to rich observables such as the particle entanglement and many-body localization phenomena [113, 131]. Beyond entanglement measures, coherences provide direct information on the stability of a given phase, including pairing symmetries and competing orders in correlated electron systems [132]. In particular, analyzing the short-distance structure of the 2-RDM reveals p-wave symmetry in spinless fermions, indicating the presence of a superconducting instability [133–135]. Similarly, in systems exhibiting charge density wave (CDW) order, coherences serve as a probe of the order parameter by capturing the full correlation function rather than just the density-density limit [136]. In the presence of true long-range

order, factorization would occur, whereas the full 2-RDM reveals the extent of fluctuations in the finite system.

Despite their fundamental importance, higher-order reduced density matrices remain notoriously difficult to compute analytically. The primary challenge is that the number of independent elements in the n-RDM scales exponentially with system size. In addition, one has to account for finite-size effects, interactions, and boundary conditions. To overcome these difficulties, we focus on the one-dimensional Tomonaga-Luttinger liquid (TLL) phase, where bosonization techniques allow for the computation of correlation functions in terms of exponentials of bosonic fields. This approach provides an analytic framework for exactly deriving reduced density matrices in strongly correlated systems. In particular, we focus on the 2-RDM $\rho_2(x_2', x_1', x_2, x_1) = \langle \Psi^\dagger(x_2')\Psi^\dagger(x_1')\Psi(x_2)\Psi(x_1)\rangle$ which describes the probability two holes are created on sites x_1, x_2, and two holes are removed on sites x_1', x_2'. This configuration is shown in Fig. 4.1.

In our analysis, we identify six primary contributions to the 2-RDM that differentiate correlations between right- and left-moving fermions. In doing so, we uncover an exponent, λ, corresponding to scattering between fermions of opposite chirality not present in the one-body density matrix. Intriguingly, λ can take negative values, in contrast with the exponent γ in the 1-RDM, underscoring the additional complexity present in higher order density matrices. Fig. 4.2 plots the two exponents as a function of the Luttinger parameter K, which show very distinct behavior in the attractive regime. The interactions along the top axis correspond to the microscopic model of spinless fermions we simulate numerically to benchmark the analytics. To gain further intuition, we show the 2-RDM can be viewed geometrically as four pairwise-intersecting hyperplanes in $\mathbb{R}^4$. We then introduce a set of relative coordinates that provides a framework for understanding both density-density correlations and off-diagonal coherences. We plot the 2-RDM in these coordinates in Fig. 4.3 on a sphere as a function of the relative coordinates and center-of-mass coordinate of the system ΔR for $K = 8/5$, in the attractive

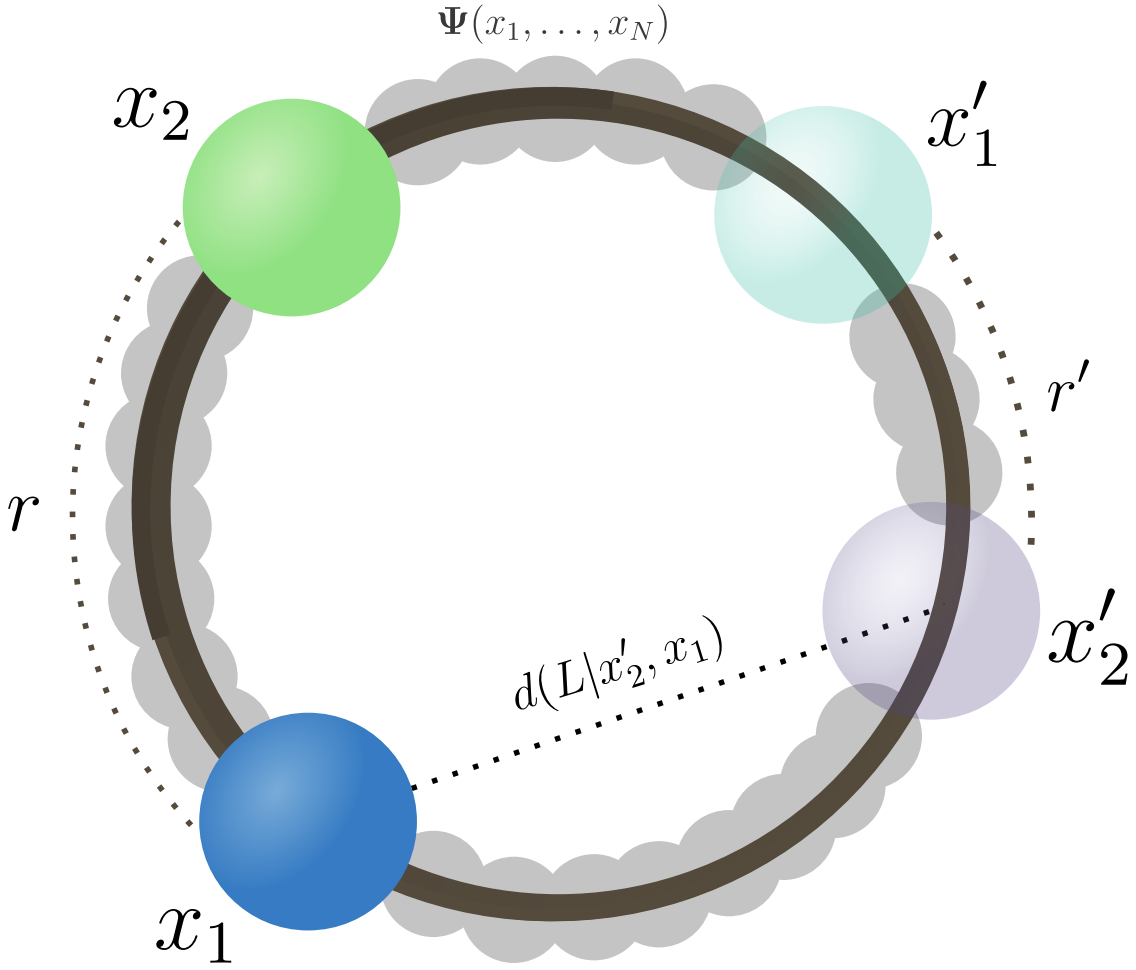

Figure 4.1: Graphical depiction of the two-body density matrix on a lattice, represented in a many body system. The quantity $\rho_2(x_2', x_1', x_2, x_1)$ denotes the matrix element obtained when two fermions are annihilated at sites x_1 and x_2 while two are created at coordinates x_1' and x_2'.

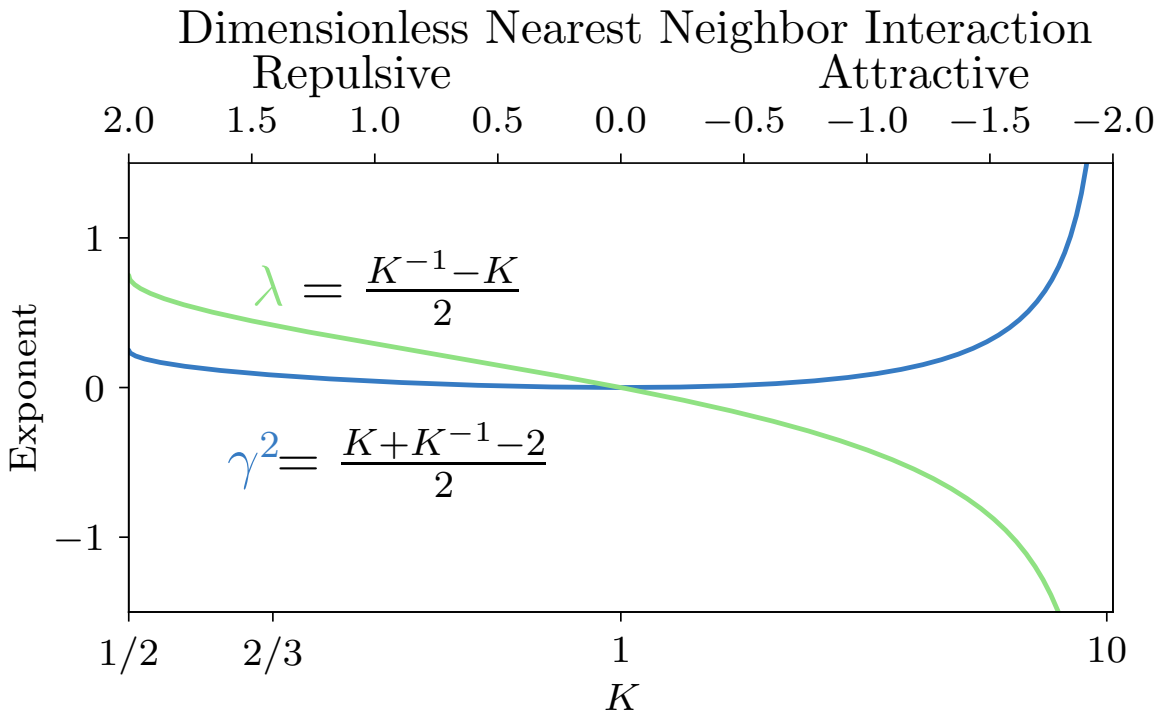

Figure 4.2: Dependence of the two interaction dependent exponents in the correlation function, γ^2 and λ, on the Luttinger parameter K. γ^2 is strictly positive, while λ, the new exponent in this work can attain negative values.

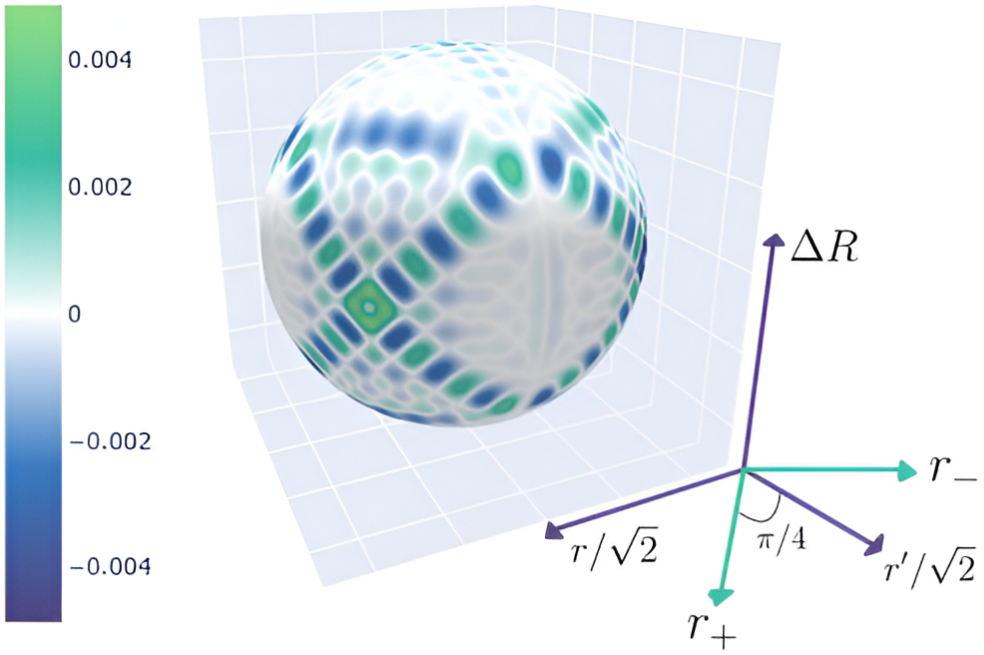

Figure 4.3: The four point correlator $\rho(x_2', x_1', x_2, x_1)$ plotted in a spherical geometry as a function of relative coordinates $r = x_2 - x_1$ and $r' = x_2' - x_1'$, and the center of mass coordinate ΔR. Alternating blue-green regions signal the sign change from fermion antisymmetry, while the vanishing of the function along $r = 0, r' = 0$ is due to the Pauli exclusion principle.

regime. Using the diagonal elements, we obtain an explicit expression for the density-density correlation function and show the presence of a chord length is necessary to captural oscillations in finite size systems.

We demonstrate how our analytical result can be applied to a microscopic lattice model of spinless fermions. Specifically, we numerically compute the ground state density matrix of the J-V chain of interacting spinless fermions using high-precision density matrix renormalization group (DMRG) calculations. At half-filling, the Bethe ansatz provides an exact mapping between the model parameters and the Luttinger parameter K. We find excellent agreement in the TLL phase between the numerical data and our analytic results. The interaction cutoff ϵ is determined self-consistently by fitting the expression for the one body density matrix to DMRG data, linking the continuum and lattice pictures [92]. We also derive a closed-form expression for the static structure factor, a quantity that could potentially be measured experimentally (e.g. via Bragg spectroscopy) [37, 124]. Additionally, we demonstrate the usefulness of the 2-RDM in computing observables, in particular, the ground-state energy for the spinless fermion model. Beyond the diagonal elements, the off-diagonal elements of the 2-RDM provide additional insights into order in the J-V model, revealing the expected p-wave pairing symmetry in the strongly attractive regime and signatures of charge density wave (CDW) order in the repulsive regime [132].

The rest of the chapter is organized as follows. Section II provides a step-by-step derivation of the exact expression for the 2-RDM, while Section III discusses the structure of the 2-RDM and various limits alongside our numerical data. In Section IV, we examine the real space structure of the 2-RDM, focusing on the effects of interactions. Finally, in Section V, we show how our results can be used to compute observables, including the ground state energy and static structure factor, and reveal signatures of CDW and p-wave pairing instabilities in the coherence terms.

4.2 Luttinger Liquid Theory and Bosonization

Following the formalism outlined in Section 2.1, the effective bosonized Hamiltonian is given by

$$H = \sum_{q\neq 0}[\omega_0(q) + m(q)]b_q^\dagger b_q + \frac{1}{2}\sum_{q\neq 0} g_2(q)(b_q b_{-q} + b_q^\dagger b_{-q}^\dagger), \tag{4.1}$$

where $\omega_0(q) = v_F|q|$, $m(q) = g_4(q)|q|$, and the sum is taken over momenta $q_n = \frac{2\pi n}{L}, n \in \mathbb{Z}/\{0\}$. The g_4 term denotes the interaction from forward scattering while g_2 corresponds to the interactions from forward dispersion and backward scattering.

We can write the bosonic field operators

$$\phi_\alpha(x) = -\sum_{q>0}\sqrt{\frac{2\pi}{qL}}e^{-q\eta/2}[e^{i\alpha qx}b_{\alpha,q} + e^{-i\alpha qx}b_{\alpha,q}^\dagger], \tag{4.2}$$

where η is a short distance cutoff measured in units of the lattice spacing a_0. The fermionic field operators can be rewritten in terms of these chiral operators as

$$\Psi_\alpha(x) = \frac{\chi_\alpha}{\sqrt{2\pi\eta}}e^{i(\varphi_{0,\alpha}+\alpha\frac{2\pi x}{L}N_\alpha)}e^{-i\phi_\alpha(x)}, \tag{4.3}$$

where $\chi_\alpha = e^{i\alpha\frac{\pi}{2}N_{-\alpha}}, \chi_\alpha^\dagger\chi_\alpha = 1$ is a Klein factor that ensures fermionic commutation relations ($\{\psi(x), \psi^\dagger(x')\} = \delta(x-x'), \{\psi(x), \psi(x')\} = \{\psi^\dagger(x), \psi^\dagger(x')\} = 0$), N_α is the particle number operator, and $\varphi_{0,\alpha}$ is the zero mode operator ($[N_\alpha, \varphi_{0,\alpha}] = i$) [3, 46]. Crucially, when we compute the expectation values in ρ_2 and insert the expressions for the bosonic field operators, in order to obtain terms of the form $\langle\phi_\alpha(x_2)\phi_\alpha(x_1)\rangle, \langle\phi_\alpha(x_2)\phi_\beta(x_1)\rangle$ (β denotes the opposite fermion species), we will need to work in the diagonal basis of the Hamiltonian in a way that preserves the bosonic commutation relations [118]. We apply a Bogoliubov transformation and

obtain new operators that can diagonalize the Hamiltonian, Eq. (4.1)

$$\begin{aligned} a_q &= \cosh(\theta_q) b_q + \sinh(\theta_q) b_{-q}^\dagger, \\ a_{-q}^\dagger &= \sinh(\theta_q) b_q + \cosh(\theta_q) b_{-q}^\dagger. \end{aligned} \tag{4.4}$$

The ground state expectation values obey $\langle a_q^\dagger, a_{q'} \rangle = \delta_{q,q'} f_b(q)$ where $f_b(q)$ is the Bose-Einstein distribution function, which vanishes at zero temperature for $q > 0$. The Luttinger parameter K is related to the interaction strength of the system and can be obtained from the twist parameter with $K = \lim_{q \to 0} e^{2\theta_q}$.

4.3 Derivation of the 2-Body Density Matrix

We now show the derivation of the exact two body density matrix in the Luttinger regime. Explicitly, we are trying to compute $\rho_2(x_2', x_1', x_2, x_1) = \langle \Psi^\dagger(x_2') \Psi^\dagger(x_1') \Psi(x_1) \Psi(x_2) \rangle$ which which is the *ensemble average* (quantum expectation value) of creating fermions at x_1', x_2' and annihilating them at x_1, x_2. We expand the fermionic field operators in terms of their right- and left- moving components.

$$\begin{aligned} &\langle \Psi^\dagger(x_2') \Psi^\dagger(x_1') \Psi(x_1) \Psi(x_2) \rangle \\ &= \frac{1}{N^2} \langle (e^{ik_F x_2'} \Psi_L^\dagger(x_2') + e^{-ik_F x_2'} \Psi_R^\dagger(x_2')) \\ &\qquad \times (e^{ik_F x_1'} \Psi_L^\dagger(x_1') + e^{-ik_F x_1')} \Psi_R^\dagger(x_1')) \\ &\qquad \times (e^{-ik_F x_2} \Psi_L(x_2) + e^{ik_F x_2} \Psi_R(x_2)) \\ &\qquad \times (e^{-ik_F x_1} \Psi_L(x_1) + e^{ik_F x_1} \Psi_R(x_1)) \rangle \end{aligned} \tag{4.5}$$

Carrying out the multiplication, we obtain sixteen total terms; however, the majority will vanish. In order to satisfy the condition $\langle 0 | \Psi^\dagger(x_2') \Psi^\dagger(x_1') \Psi(x_2) \Psi(x_1) | 0 \rangle \neq 0$, if a right or left moving fermion is created, one must also be destroyed. The surviving terms are of the form $\langle \Psi_\alpha^\dagger(x_2') \Psi_\alpha^\dagger(x_1') \Psi_\alpha(x_1) \Psi_\alpha(x_2) \rangle$, $\langle \Psi_\alpha^\dagger(x_2') \Psi_\beta^\dagger(x_1') \Psi_\beta(x_1) \Psi_\alpha(x_2) \rangle$,

or $\langle \Psi^\dagger_\alpha(x_2')\Psi^\dagger_\beta(x_1')\Psi_\alpha(x_1)\Psi_\beta(x_2)\rangle$. Then, for example, $\langle \Psi^\dagger_\alpha(x_2')\Psi^\dagger_\beta(x_1')\Psi_\beta(x_1)\Psi_\alpha(x_2)\rangle$ corresponds to the terms $\langle \Psi^\dagger_R(x_2')\Psi^\dagger_L(x_1')\Psi_L(x_1)\Psi_R(x_2)\rangle$ and $\langle \Psi^\dagger_L(x_2')\Psi^\dagger_R(x_1')\Psi_R(x_1)\Psi_L(x_2)\rangle$. We now insert the expressions for $\Psi_\alpha(x)$ given by Eq. (4.3) and make repeated use of the Baker-Campbell-Hausdoff formula, $e^A e^B = e^{A+B}e^{[A,B]/2}$, to obtain expressions for the surviving terms in Eq. (4.5).

Next, we need a more convenient way to express the expectation value of the exponentials of the bosonic operators. We utilize the boson cumulant formula $\langle e^{i(\phi_\alpha(x)-\phi_\alpha(x'))}\rangle = e^{-\frac{1}{2}\langle(\phi_\alpha(x)-\phi_\alpha(x'))^2\rangle}$, which at equilibrium holds for any linear combination of bosonic operators $\sum_n A_n b_n + B_n b_n^\dagger$ [46].

$$
\begin{aligned}
\left\langle \Psi^\dagger_\alpha(x_2')\Psi^\dagger_\alpha(x_1')\Psi_\alpha(x_1)\Psi_\alpha(x_2)\right\rangle &= \frac{1}{4\pi^2\eta^2} e^{\frac{i\pi}{L}\alpha(x_2'+3x_1'-3x_2-x_1)} \\
&\times e^{-\frac{1}{2}[\phi_\alpha(x_2'),\phi_\alpha(x_1')]} e^{\frac{1}{2}[\phi_\alpha(x_2'),\phi_\alpha(x_2)]} e^{\frac{1}{2}[\phi_\alpha(x_2'),\phi_\alpha(x_1)]} e^{\frac{1}{2}[\phi_\alpha(x_1'),\phi_\alpha(x_2)]} \\
&\times e^{\frac{1}{2}[\phi_\alpha(x_1'),\phi_\alpha(x_1)]} e^{-\frac{1}{2}[\phi_\alpha(x_2),\phi_\alpha(x_1)]} e^{-\frac{1}{2}\langle(\phi_\alpha(x_2')+\phi_\alpha(x_1')-\phi_\alpha(x_2)-\phi_\alpha(x_1))^2\rangle} \\
\left\langle \Psi^\dagger_\alpha(x_2')\Psi^\dagger_\beta(x_1')\Psi_\beta(x_1)\Psi_\alpha(x_2)\right\rangle &= \frac{1}{4\pi^2\eta^2} e^{\frac{i\pi}{L}(\alpha x_2'+\beta x_1'-\beta x_2-\alpha x_1)} \\
&\times e^{-\frac{1}{2}[\phi_\alpha(x_2'),\phi_\beta(x_1')]} e^{\frac{1}{2}[\phi_\alpha(x_2'),\phi_\beta(x_2)]} e^{\frac{1}{2}[\phi_\alpha(x_2'),\phi_\alpha(x_1)]} e^{\frac{1}{2}[\phi_\beta(x_1'),\phi_\beta(x_2)]} \\
&\times e^{\frac{1}{2}[\phi_\beta(x_1'),\phi_\alpha(x_1)]} e^{-\frac{1}{2}[\phi_\beta(x_2),\phi_\alpha(x_1)]} e^{-\frac{1}{2}\langle(\phi_\alpha(x_2')+\phi_\beta(x_1')-\phi_\beta(x_2)-\phi_\alpha(x_1))^2\rangle} \\
\left\langle \Psi^\dagger_\alpha(x_2')\Psi^\dagger_\beta(x_1')\Psi_\beta(x_1)\Psi_\alpha(x_2)\right\rangle &= -\left\langle \Psi^\dagger_\alpha(x_2')\Psi^\dagger_\beta(x_1')\Psi_\alpha(x_2)\Psi_\beta(x_1)\right\rangle
\end{aligned}
\tag{4.6}
$$

where we used $[N_\alpha, \varphi_{0,\alpha}] = i$.

First, we must evaluate the expectation values of pairs of bosonic operators that appear in the exponentials of Eq. (4.6). As previously stated, we need to work in the diagonal basis of the Hamiltonian, so we can apply Eq. (4.4) and get a new

definition for the bosonic field operator,

$$\begin{aligned}\phi_\alpha(x) = &-\sum_{q>0}\sqrt{\frac{2\pi}{qL}}e^{-q\eta/2} \\ &\times\left[e^{i\alpha qx}(\cosh(\theta_q)a_q - \sinh(\theta_q)a^\dagger_{-q})\right. \\ &\left.+\, e^{-\alpha qx}(\cosh(\theta_q)a^\dagger_q - \sinh(\theta_q)a_{-q})\right] \end{aligned} \tag{4.7}$$

We start with the expectation values of pairs of bosonic operators of the same species $\langle\phi_\alpha(x)\phi_\alpha(x')\rangle$. To write the expression in a more simple way, we compute the sum

$$\begin{aligned}\langle\phi_\alpha(x)\phi_\alpha(x')\rangle + \langle\phi_\alpha(x')\phi_\alpha(x)\rangle = \\ \sum_{q>0}\frac{2\pi}{|q|L}e^{-\eta q}[e^{i\alpha q(x-x')}\cosh^2(\theta_q) + e^{i\alpha q(x'-x)}\sinh^2(\theta_q) \\ + e^{i\alpha q(x'-x)}\cosh^2(\theta_q) + e^{i\alpha q(x-x')}\sinh^2(\theta_q)]. \end{aligned} \tag{4.8}$$

We factor out the trignometric functions and obtain

$$\begin{aligned}\langle\phi_\alpha(x)\phi_\alpha(x')\rangle + \langle\phi_\alpha(x')\phi_\alpha(x)\rangle = \\ \sum_{q>0}\frac{2\pi}{|q|L}e^{-\eta q}[\sinh^2(\theta_q) + \cosh^2(\theta_q) - 1 + 1] \\ \times\,[e^{i\alpha q(x-x')} + e^{i\alpha q(x'-x)}], \end{aligned} \tag{4.9}$$

where we have included $(-1+1)$ to separate the free and interaction terms in the correlation function [92]. Using the definition of the Luttinger parameter $K = \lim_{q\to 0} e^{2\theta_q}$, we introduce a UV cutoff ϵ [118], with

$$\begin{aligned}\cosh^2(\theta_q) + \sinh^2(\theta_q) - 1 &\approx \frac{K + K^{-1} - 2}{2}e^{-\epsilon|q|} \\ &\equiv \gamma^2 e^{-\epsilon|q|}, \end{aligned} \tag{4.10}$$

that regulates interactions and allows us to perform the q-summation while sending the short distance cutoff $\eta \to 0$. The cutoff ϵ now determines the smallest physically meaningful length scale. Although there are multiple methods to regularize the sum, this soft cutoff will ultimately allow us to make connections between the continuum expression and specific microscopic models. Because ϵ is non-universal, we can tune it to match lattice data—something a pure CFT treatment (which implicitly sets $\epsilon = 0$) cannot capture, as we will show in Appendix C. We further define an interaction dependent exponent γ^2 that is always positive and is plotted as a function of the Luttinger parameter in Fig. 4.2. We can now use this sum to compute the exponential terms

$$e^{-\frac{1}{2}\langle(\phi_\alpha(x)-\phi_\alpha(x'))^2\rangle} = \frac{-i\sin\left(\frac{i\pi}{L}\eta\right)}{\left|\sin\left(\frac{\pi}{L}(\alpha(x-x')+i\eta)\right)\right|} \times \left[\frac{i\sin\left(\frac{\pi}{L}i(\eta+\epsilon)\right)}{\left|\sin\left(\frac{\pi}{L}(\alpha(x-x')+i(\eta+\epsilon))\right)\right|}\right]^{\gamma^2}. \tag{4.11}$$

We perform the same analysis for $\langle\phi_\alpha(x)\phi_\beta(x')$, which is the known anomalous correlator in Luttinger liquid theory. Their sum is given by

$$\begin{aligned}\langle\phi_\alpha(x)\phi_\beta(x')\rangle + \langle\phi_\alpha(x')\phi_\beta(x)\rangle = \\ 2\sum_{q>0}\frac{2\pi}{|q|L}e^{-\eta q}[-\sinh(\theta_q)\cosh(\theta_q)] \\ \times[e^{i\alpha q(x-x')} + e^{i\alpha q(x'-x)}]\end{aligned} \tag{4.12}$$

We find in this work a different interaction dependent exponent λ that arises from the correlations between right- and left- moving fermions,

$$\begin{aligned}-2\sinh(\theta_q)\cosh(\theta_q) &\approx \frac{K^{-1}-K}{2}e^{-\epsilon|q|} \\ &\equiv \lambda e^{-\epsilon|q|}\end{aligned} \tag{4.13}$$

where the interaction cutoff is defined as before. Its behavior as a function of K is shown in Fig. 4.2; unlike γ^2, it can take negative values.

$$e^{-\frac{1}{2}\langle(\phi_\alpha(x)\phi_\beta(x'))^2\rangle}e^{-\frac{1}{2}\langle(\phi_\alpha(x')\phi_\beta(x))^2\rangle} = \\ |e^{-\frac{\pi}{L}(\eta+\epsilon)}\sin\frac{\pi}{L}(\alpha(x-x')+i(\eta+\epsilon)|, \tag{4.14}$$

where we again send $\beta \to -\alpha$. Notably, there is no free fermionic contribution here.

Now, we need to compute the exponentials of the commutators of the bosonic field operators. Inserting the definition of $\phi_\alpha(x)$ given by Eq. (4.2), sending $\beta \to -\alpha$ we get

$$\begin{aligned}[\phi_\alpha(x),\phi_\beta(x')] &= \sum_{q>0}\sum_{q'>0}\frac{2\pi}{L}\frac{1}{\sqrt{qq'}}e^{-\frac{\eta}{2}(q+q')}\Big(\\ &\quad e^{i\alpha(qx-q'x')}[b_{\alpha q},b_{-\alpha q'}] + e^{-i\alpha(qx+q'x')}[b^\dagger_{\alpha q'},b_{-\alpha q'}] \\ &\quad + e^{i\alpha(qx+q'x')}[b_{\alpha q},b^\dagger_{-\alpha q'}] + e^{i\alpha(-qx+q'x')}[b^\dagger_{\alpha q},b^\dagger_{-\alpha q'}]\Big) \\ &= 0 = [\phi_\beta(x),\phi_\alpha(x')] \\ [\phi_\alpha(x),\phi_\alpha(x')] &= \sum_{q>0}\sum_{q'>0}\frac{2\pi}{L}\frac{1}{\sqrt{qq'}}e^{-\frac{\eta}{2}(q+q')}\Big(\\ &\quad e^{i\alpha(qx+q'x')}[b_{\alpha q},b_{\alpha q'}] + e^{-i\alpha(qx+q'x')}[b_{\alpha q},b^\dagger_{\alpha q'}] \\ &\quad + e^{i\alpha(qx-q'x')}[b^\dagger_{\alpha q},b^\dagger_{\alpha q'}] + e^{i\alpha(-qx+q'x')}[b^\dagger_{\alpha q},b_{\alpha q'}]\Big) \\ &= \sum_{q>0}\frac{2\pi}{Lq}e^{-\eta q}\left(e^{i\alpha q(x-x')} - e^{-i\alpha q(x-x')}\right)\end{aligned} \tag{4.15}$$

where we have used $[b_q, b^\dagger_{q'}] = \delta_{q,q'}$. Straightforwardly, for $\alpha \neq \beta$, $e^{[\phi_\alpha(x'),\phi_\beta(x)]} = 1$. In the case of the non-vanishing commutator, we obtain [92],

$$e^{\frac{1}{2}[\phi_\alpha(x),\phi_\alpha(x')]} = i\mathrm{sgn}(\alpha(x-x'))e^{-i\alpha\frac{\pi}{L}(x-x')}. \tag{4.16}$$

after taking the limit $\eta \to 0$

We now have all the pieces to compute the terms in Eq. (4.6). As stated, by keeping ϵq finite, we can take the limit $\eta \to 0$. Using Eq. (4.11) and Eq. (4.14), with limit $\eta/x \to 0, \eta q \to 0, \eta/L \to 0$ and the substitutions $\sin\frac{i\pi\eta}{L}/\eta \to i\pi/L$, $i\sin(ix) = -|\sin(ix)|$, we obtain

$$\begin{aligned}\langle \Psi^\dagger_\alpha(x_2')\Psi^\dagger_\alpha(x_1')\Psi_\alpha(x_2)\Psi_\alpha(x_1)\rangle = &-\frac{1}{4L^2}\frac{1}{\sin\left(\frac{\pi}{L}(x_2'-x_2)\right)\sin\left(\frac{\pi}{L}(x_1'-x_1)\right)}\\ &\times\frac{\sin\left(\frac{\pi}{L}(x_2'-x_1')\right)\sin\left(\frac{\pi}{L}(x_2-x_1)\right)}{\sin\left(\frac{\pi}{L}(x_2'-x_1)\right)\sin\left(\frac{\pi}{L}(x_1'-x_2)\right)}\\ &\times\frac{\left|\sin\left(\frac{i\pi}{L}\epsilon\right)\right|^{2\gamma^2}}{\left|\sin\left(\frac{\pi}{L}(x_2'-x_2+i\epsilon)\right)\right|^{\gamma^2}\left|\sin\left(\frac{\pi}{L}(x_1'-x_1+i\epsilon)\right)\right|^{\gamma^2}}\\ &\times\frac{\left|\sin\left(\frac{\pi}{L}(x_2'-x_1'+i\epsilon)\right)\right|^{\gamma^2}\left|\sin\left(\frac{\pi}{L}(x_2-x_1+i\epsilon)\right)\right|^{\gamma^2}}{\left|\sin\left(\frac{\pi}{L}(x_2'-x_1+i\epsilon)\right)\right|^{\gamma^2}\left|\sin\left(\frac{\pi}{L}(x_1'-x_2+i\epsilon)\right)\right|^{\gamma^2}}\end{aligned} \tag{4.17}$$

$$\begin{aligned}\langle \Psi^\dagger_\alpha(x_2')\Psi^\dagger_\beta(x_1')\Psi_\beta(x_2)\Psi_\alpha(x_1)\rangle = &\frac{1}{4L^2}\frac{1}{\sin\left(\frac{\pi}{L}(x_2'-x_1)\right)\sin\left(\frac{\pi}{L}(x_1'-x_2)\right)}\\ &\times\frac{|\sin\left(\frac{\pi}{L}((x_2'-x_1')+i\epsilon)\right)|^{\lambda}|\sin\left(\frac{\pi}{L}((x_2-x_1)+i\epsilon)\right)|^{\lambda}}{|\sin\left(\frac{\pi}{L}((x_2'-x_2)+i\epsilon)\right)|^{\lambda}|\sin\left(\frac{\pi}{L}((x_1'-x_1)+i\epsilon)\right)|^{\lambda}}\\ &\times\frac{|\sin\left(\frac{i\pi}{L}\epsilon\right)|^{2\gamma^2}}{|\sin\left(\frac{\pi}{L}((x_2'-x_1)+i\epsilon)\right)|^{\gamma^2}|\sin\left(\frac{\pi}{L}((x_1'-x_2)+i\epsilon)\right)|^{\gamma^2}}\end{aligned} \tag{4.18}$$

$$\langle \Psi^\dagger_\alpha(x_2')\Psi^\dagger_\beta(x_1')\Psi_\alpha(x_2)\Psi_\beta(x_1)\rangle = -\langle \Psi^\dagger_\alpha(x_2')\Psi^\dagger_\beta(x_1')\Psi_\beta(x_1)\Psi_\alpha(x_2)\rangle \tag{4.19}$$

where we used $\alpha, \beta = +1$ for right-movers and -1 for left-movers. Combining all non-zero terms, e.g. $\langle \Psi^\dagger_R(x_2')\Psi^\dagger_R(x_1')\Psi_R(x_2)\Psi_R(x_1)\rangle$ and $\langle \Psi^\dagger_L(x_2')\Psi^\dagger_L(x_1')\Psi_L(x_2)\Psi_L(x_1)\rangle$) we obtain a final expression for the 2-RDM:

$$
\begin{aligned}
&\langle \Psi^\dagger(x_2')\Psi^\dagger(x_1')\Psi(x_1)\Psi(x_2)\rangle = \\
&\quad \frac{1}{2\pi^2}\cos\left(k_F(x_2'+x_1'-x_2-x_1)\right) \\
&\qquad \times \left[\frac{h_0(x_2'-x_1', x_2-x_1)}{h_0(x_2'-x_2, x_1'-x_1)h_0(x_2'-x_1, x_1'-x_2)}\right]\left|\frac{h_\epsilon(0,0)h_\epsilon(x_2'-x_1', x_2-x_1)}{h_\epsilon(x_2'-x_2, x_1'-x_1)h_\epsilon(x_2'-x_1, x_1'-x_2)}\right|^{\gamma^2} \\
&\quad + \frac{1}{2\pi^2}\cos\left(k_F(x_2'-x_1'-x_2+x_1)\right) \\
&\qquad \times \left[\frac{1}{h_0(x_2'-x_2, x_1'-x_1)}\right]\left|\frac{h_\epsilon(0,0)}{h_\epsilon(x_2'-x_2, x_1'-x_1)}\right|^{\gamma^2}\left|\frac{h_\epsilon(x_2'-x_1', x_2-x_1)}{h_\epsilon(x_2'-x_1, x_1'-x_2)}\right|^{\lambda} \\
&\quad - \frac{1}{2\pi^2}\cos\left(k_F(x_2'-x_1'+x_2-x_1)\right) \\
&\qquad \times \left[\frac{1}{h_0(x_2'-x_1, x_1'-x_2)}\right]\left|\frac{h_\epsilon(0,0)}{h_\epsilon(x_2'-x_1, x_1'-x_2)}\right|^{\gamma^2}\left|\frac{h_\epsilon(x_2'-x_1', x_2-x_1)}{h_\epsilon(x_2'-x_2, x_1'-x_1)}\right|^{\lambda}
\end{aligned}
\tag{4.20}
$$

where we have defined new shorthand notation,

$$h_\epsilon(x,y) = d_\epsilon(x)d_\epsilon(y), \tag{4.21}$$

$$d_\epsilon(x) = \frac{L}{\pi}\sin\left[\frac{\pi}{L}(x+i\epsilon)\right]. \tag{4.22}$$

Here, $|d_0(x_2-x_1)|$ represents the chord length between the two coordinates x_1 and x_2 across the ring (due to the presence of periodic boundary conditions in 1D, see e.g. Fig. 4.1), and $|d_\epsilon(x_2-x_1)|$ is its generalization including the interaction cutoff ϵ.

We see that the exponent γ^2 appears in all three terms of Eq. (4.20), whereas the exponent λ only appears in the latter two due to the effect of anomalous correlators.

4.4 Analysis of the 2-RDM

The complete expression for the two-particle density matrix given in Eq. (4.20) is at first glance rather unwieldy. Without taking into account any symmetries, it is naively a function of four separate coordinates. In this section, we present an extensive analysis of its structure, focusing on its diagonal elements, and various limiting cases to build intuition before a final discussion of its power in elucidating the effects of interactions and exchange statistics in the Luttinger model.

In the limit $x_1' = x_1$, and using the definition of the density operator $\hat{\rho}(x_1) = \Psi^\dagger(x_1)\Psi(x_1)$, we can write the 2-RDM as $\langle \Psi^\dagger(x_2')\hat{\rho}(x_1)\Psi(x_2)\rangle$. This correlates the hopping of a one particle between positions x_2 and x_2' with the presence of another particle at x_1. Thus, it measures fermions correlated-hopping. The limits $x_2' = x_2$, $x_2' = x_1$ and $x_1' = x_2$ can relate to $x_1' = x_1$ by exchanging the particle coordinates labels ($x_1 \leftrightarrow x_2$ or/and $x_1' \leftrightarrow x_2'$) and thus the resulting 2-RDM can be related to $\langle \Psi^\dagger(x_2')\hat{\rho}(x_1)\Psi(x_2)\rangle$ by anti-commuting the field operators. The intersection between hyperplanes $x_1' = x_1$ and $x_2' = x_2$ gives rise to the diagonal elements of the 2-RDM while the intersection between hyperplanes $x_2' = x_1$ and $x_1' = x_2$ generates a negative copy of the diagonal elements due to anti-symmetrization ($x_1' \leftrightarrow x_2'$). However, for all of the other four intersections between the hyperplanes, the 2-RDM vanishes as it requires having ($x_1 = x_2$) or ($x_1' = x_2'$), which is forbidden by the fermionic symmetrization.

Furthermore, glancing at the arguments of the $\cos(\cdot)$ functions in the three terms forming the 2-RDM, one notices that the arguments define a set of three orthogonal hyperplanes $\{x_2' + x_1' - x_2 - x_1, x_2' - x_1' - x_2 + x_1, x_2' - x_1' + x_2 - x_1\}$, which accordingly defines the fourth hyperplane that is orthogonal to the set to be the sum of all coordinates, i.e., $x_1 + x_2 + x_1' + x_2'$. To understand the origin of such a set of hyperplanes and before adopting it in the description of the 2-RDM, let's start with a more natural choice for describing the coordinates of a two-body object, i.e., the relative coordinate $r = x_2 - x_1$ and the center of mass coordinate

$R = (x_2 + x_1)/2$. Equivalently, $r' = x_2' - x_1'$ and $R' = (x_2' + x_1')/2$. Recalling that ρ_2 describes the correlations in a translationally invariant system suggests that the 2-RDM is invariant concerning a constant shifting of all cartesian coordinates. In this case, r' and r are independent of such a shift, while for R' and R, we can define the difference $\Delta R = R' - R = (x_2' + x_1' - x_2 - x_1)/2$ as the third independent argument from such a change, and the sum $\Sigma R = R' + R = (x_2' + x_1' + x_2 + x_1)/2$ is what is expected to drop out from the expression of the 2-RDM, due to translation symmetry.

For the following analysis, we consider a system of N fermions on a ring of length L and set the unit for all lengths such that the density $\rho_0 = N/L = 1/2$ and we fix $\epsilon = 1$. To set the stage for the promised analyses, we observe that in the expression Eq. 4.20, $h_\epsilon(x, y)$ appears with only three sets of arguments. Using this observation, we define the following.

$$\begin{aligned} h_{\epsilon,-} &= h_\epsilon(x_2' - x_2, x_1' - x_1) \\ h_{\epsilon,0} &= h_\epsilon(x_2' - x_1', x_2 - x_1) \\ h_{\epsilon,+} &= h_\epsilon(x_2' - x_1, x_1' - x_2), \end{aligned} \tag{4.23}$$

and the constant $h_\epsilon(0,0) = h_\epsilon = (\frac{L}{\pi})^2 \sin^2(\frac{\pi}{L} i\epsilon)$. Therefore, we can write

$$\begin{aligned} \langle \Psi^\dagger(x_2')\Psi^\dagger(x_1')\Psi(x_1)\Psi(x_2)\rangle = &\frac{\cos\left(k_F(x_2' + x_1' - x_2 - x_1)\right)}{2\pi^2} \left[\frac{h_{0,0}}{h_{0,-}h_{0,+}}\right] \left|\frac{h_\epsilon h_{\epsilon,0}}{h_{\epsilon,-}h_{\epsilon,+}}\right|^{\gamma^2} \\ &+ \frac{\cos\left(k_F(x_2' - x_1' - x_2 + x_1)\right)}{2\pi^2} \left[\frac{1}{h_{0,-}}\right] \left|\frac{h_\epsilon}{h_{\epsilon,-}}\right|^{\gamma^2} \left|\frac{h_{\epsilon,0}}{h_{\epsilon,+}}\right|^{\lambda} \\ &- \frac{\cos\left(k_F(x_2' - x_1' + x_2 - x_1)\right)}{2\pi^2} \left[\frac{1}{h_{0,+}}\right] \left|\frac{h_\epsilon}{h_{\epsilon,+}}\right|^{\gamma^2} \left|\frac{h_{\epsilon,0}}{h_{\epsilon,-}}\right|^{\lambda} \end{aligned}$$

The intricate functional form of 2-RDM lives in the four-dimensional hyperspace defined by the cartesian coordinates x_1, x_2, x_1', and x_2'.

Finally, to connect with the set of orthogonal hyperplanes we mentioned earlier in this section, we define $r_\pm = (r' \pm r)/2 = (x_2' - x_1' \pm x_2 \mp x_1)/2$. Now, we write

the 2-RDM using the new set of coordinates as

$$\begin{aligned}\tilde{\rho}_2(\Delta R, r_+, r_-) = &\frac{\cos(2k_F\Delta R)}{2\pi^2}\left[\frac{h_{0,0}}{h_{0,-}h_{0,+}}\right]\left|\frac{h_\epsilon h_{\epsilon,0}}{h_{\epsilon,-}h_{\epsilon,+}}\right|^{\gamma^2}\\ &+\frac{\cos(2k_F r_-)}{2\pi^2}\left[\frac{1}{h_{0,-}}\right]\left|\frac{h_\epsilon}{h_{\epsilon,-}}\right|^{\gamma^2}\left|\frac{h_{\epsilon,0}}{h_{\epsilon,+}}\right|^{\lambda}\\ &-\frac{\cos(2k_F r_+)}{2\pi^2}\left[\frac{1}{h_{0,+}}\right]\left|\frac{h_\epsilon}{h_{\epsilon,+}}\right|^{\gamma^2}\left|\frac{h_{\epsilon,0}}{h_{\epsilon,-}}\right|^{\lambda}\end{aligned} \tag{4.25}$$

where now,

$$\begin{aligned}h_{\epsilon,-} &= h_\epsilon(\Delta R + r_-, \Delta R - r_-)\\ h_{\epsilon,0} &= h_\epsilon(r_+ + r_-, r_+ - r_-)\\ h_{\epsilon,+} &= h_\epsilon(\Delta R + r_+, \Delta R - r_+).\end{aligned} \tag{4.26}$$

Here, the subscripts $+$ and $-$ in $h_{\epsilon,\pm}$ signal the explicit dependence on the coordinates r_+ or r_-, respectively, while the 0 in $h_{\epsilon,0}$ is to indicate the dependence of the function on both r_+ and r_-. Clearly, the hyperplane $x_2' = x_2$, $x_1' = x_1$, $x_2' = x_1$ and $x_1' = x_2$ can be identified by $\Delta R = -r_-$, $\Delta R = r_-$, $\Delta R = -r_+$ and $\Delta R = r_+$, respectively. This gives

$$\begin{aligned}\tilde{\rho}_{2,\mathrm{FF}}(\Delta R, r_+, r_-) = &\, rac\cos(2k_F\Delta R)2\pi^2\left[\frac{h_{0,0}}{h_{0,-}h_{0,+}}\right]\\ &+\frac{\cos(2k_F r_-)}{2\pi^2}\left[\frac{1}{h_{0,-}}\right]\\ &-\frac{\cos(2k_F r_+)}{2\pi^2}\left[\frac{1}{h_{0,+}}\right],\end{aligned} \tag{4.27}$$

This shows that $\tilde{\rho}_{2,\mathrm{FF}}$ is a combination of three terms, each led by an oscillation in the directions of ΔR, r_- and r_+. The amplitude of oscillations depends on the functions $h_{0,0}$, $h_{0,-}$, and $h_{0,+}$. The same holds for $\tilde{\rho}_2$ but with the additional modification of the amplitude of the oscillating terms by an interaction-dependent

positive factors, and thus we can write

$$\begin{aligned}\Delta\tilde{\rho}_2(\Delta R, r_+, r_-) =& \frac{\cos(2k_F\Delta R)h_{0,0}}{2\pi^2 h_{0,-}h_{0,+}}\left[\left|\frac{h_\epsilon h_{\epsilon,0}}{h_{\epsilon,-}h_{\epsilon,+}}\right|^{\gamma^2}-1\right]\\ &+\frac{\cos(2k_F r_-)}{2\pi^2 h_{0,-}}\left[\left|\frac{h_\epsilon}{h_{\epsilon,-}}\right|^{\gamma^2}\left|\frac{h_{\epsilon,0}}{h_{\epsilon,+}}\right|^{\lambda}-1\right]\\ &-\frac{\cos(2k_F r_+)}{2\pi^2 h_{0,+}}\left[\left|\frac{h_\epsilon}{h_{\epsilon,+}}\right|^{\gamma^2}\left|\frac{h_{\epsilon,0}}{h_{\epsilon,-}}\right|^{\lambda}-1\right].\end{aligned} \tag{4.28}$$

4.4.1 *Density-Density Correlation Function*

We now scrutinize the resulting 2-RDM, starting with its diagonal elements defined by taking the limits $x_1' \to x_1$ and $x_1' \to x_1$ of Eq. (4.20), which due to the translational invariance, can be captured by the single variable $r = x_2 - x_1$, hence

$$\begin{aligned}\langle\Psi^\dagger(r)\hat{\rho}(0)\Psi(r)\rangle =& \rho_0^2 - \frac{1}{2L^2\sin^2\left(\frac{\pi}{L}r\right)}\\ &+\frac{(K-1)\cos\left(\frac{2\pi}{L}r\right)}{2L^2\left|\sin\left(\frac{\pi}{L}(r+i\epsilon)\right)\right|^2}-\frac{(K-1)\sin^2\left(\frac{2\pi}{L}r\right)}{4L^2\left|\sin\left(\frac{\pi}{L}(r+i\epsilon)\right)\right|^4}\\ &+\frac{\left|\sin\left(\frac{i\pi}{L}\epsilon\right)\right|^{2(K-1)}}{2L^2\left|\sin\left(\frac{\pi}{L}(r+i\epsilon)\right)\right|^{2(K-1)}}\frac{\cos(2k_F r)}{\sin^2\left(\frac{\pi}{L}r\right)},.\end{aligned} \tag{4.29}$$

where, as expected, the above expression vanishes in the limit $r \to 0$. Details of the limits calculations are in Appendix D. This gives us direct access to the pair correlation function as defined by

$$g_2(x_1, x_2) = \langle\Psi^\dagger(x_2)\hat{\rho}(x_1)\Psi(x_2)\rangle / (\langle\hat{\rho}(x_2)\rangle)\langle\hat{\rho}(x_1)\rangle), \tag{4.30}$$

with the uniform fermionic density $\langle\hat{\rho}(x)\rangle = \rho_0$, where

$$g_2(0,r) = \langle\Psi^\dagger(r)\hat{\rho}(0)\Psi(r)\rangle/\rho_0^2. \tag{4.31}$$

Also, by reconciling the definition of density-density correlation matrix

$$\int dx_1 dx_2 \langle\hat{\rho}(x_2)\hat{\rho}(x_1)\rangle|x_2\rangle\langle x_1|$$

and using the anticommutation of the fermionic fields, we can write the elements of the density-density correlation matrix as

$$\langle\hat{\rho}(r)\hat{\rho}(0)\rangle = \rho_0^2 g_2(0,r) - \rho_0\delta(r), \tag{4.32}$$

Thus $g_2(0,r)$ captures $\langle\hat{\rho}(r)\hat{\rho}(0)\rangle$ away from $r = 0$.
In the non-interacting limit ($K \to 1$), Eq. (4.29) yields the known exact result for free fermions, where

$$\langle\hat{\rho}(r)\hat{\rho}(0)\rangle_{\text{FF}} = \rho_0^2 - \frac{\sin^2(k_F r)}{L^2\sin^2\left(\frac{\pi}{L}r\right)} + \rho_0\delta(r), \tag{4.33}$$

Furthermore, in limit $L \gg r \gg \epsilon$, we have Haldane's result [1, 137]*

$$\langle\hat{\rho}(r)\hat{\rho}(0)\rangle \approx \rho_0^2\left[1 - \eta(2\pi\rho_0 r)^{-2} + \sum_{m=1}^{\infty} A_m(\rho_0 r)^{-m^2\eta}\cos(2\pi m\rho_0 r)\right]. \tag{4.34}$$

where the exponent $\eta = 2K$ and the coefficients A_m are model-dependent. In this limit, our expression Eq. (4.29) yields

$$\langle\hat{\rho}(r)\hat{\rho}(0)\rangle \approx \rho_0^2\left[1 - \frac{K}{2\pi^2(\rho_0 r)^2} + \frac{(\rho_0\epsilon)^{2K-2}\cos(2\pi\rho_0 r)}{2\pi^2|\rho_0 r|^{2K}}\right], \tag{4.35}$$

*In [1], the second term in Eq. (4.32) has the wrong sign [137]

which fixes the coefficient A_1 to $(\rho_0\epsilon)^{2K-2}/(2\pi^2)$. It is worth mentioning that in the noninteracting limit $K \to 1$, all higher-order coefficients $A_{m>1}$ vanish while A_1 approaches $1/(2\pi^2)$. This can be seen from the comparison of Eq. (4.34) and Eq. (4.33).

Apparently, for attractive interactions ($K > 1$), determining the dependence of the coefficient A_1 on ϵ and ρ_0 influences only the sub-subleading term of the density-density correlations. However, the presence of attractive interactions ($K < 1$) promotes the strength of oscillating terms to the subleading order. This can be seen in Fig. 4.4, where the oscillations in the pair correlation function $g_2(0, r)$ persist at larger distances for small K values. In fact, the oscillating term is the leading term concerning the connected density-density correlations Eq. (D.22) which is the main ingredient in finding the corresponding structure factor

$$S(q) = 1 + \rho_0 \int_0^L dr\, [g_2(0, r) - 1]\, e^{irq}. \tag{4.36}$$

We now analyze the behavior of our two body density matrix expression in a distinct limit, focusing on the density-density correlation function $g(x_2 - x_1) = \langle \rho(x_2)\rho(x_1)\rangle = \langle \Psi^\dagger(x_2)\Psi(x_2)\Psi^\dagger(x_1)\Psi(x_1)\rangle$, which, in the continuum limit where spatial separations are significantly smaller than the system size $x_2 - x_1 << L$, is known to be [1]

$$\begin{aligned}\langle \rho(x_2)\rho(x_1) \sim \rho_0^2 \big[1 + \eta(2\pi\rho_0(x_2 - x_1)^{-2} \\ + \sum_{m=1}^{\infty} A_m(\rho_0(x_2 - x_1))^{-m^2\eta} \cos 2\pi m\rho_0(x_2 - x_1)\big].\end{aligned} \tag{4.37}$$

Here, $\rho_0 = \frac{N}{L}$ and for fermions, the exponent $\eta = 2K$. We can reproduce this result by carefully taking the limits $x_1' \to x_1$ and $x_2' \to x_2$ in our two-body density matrix expression and subsequently rearranging according to the anticommutation

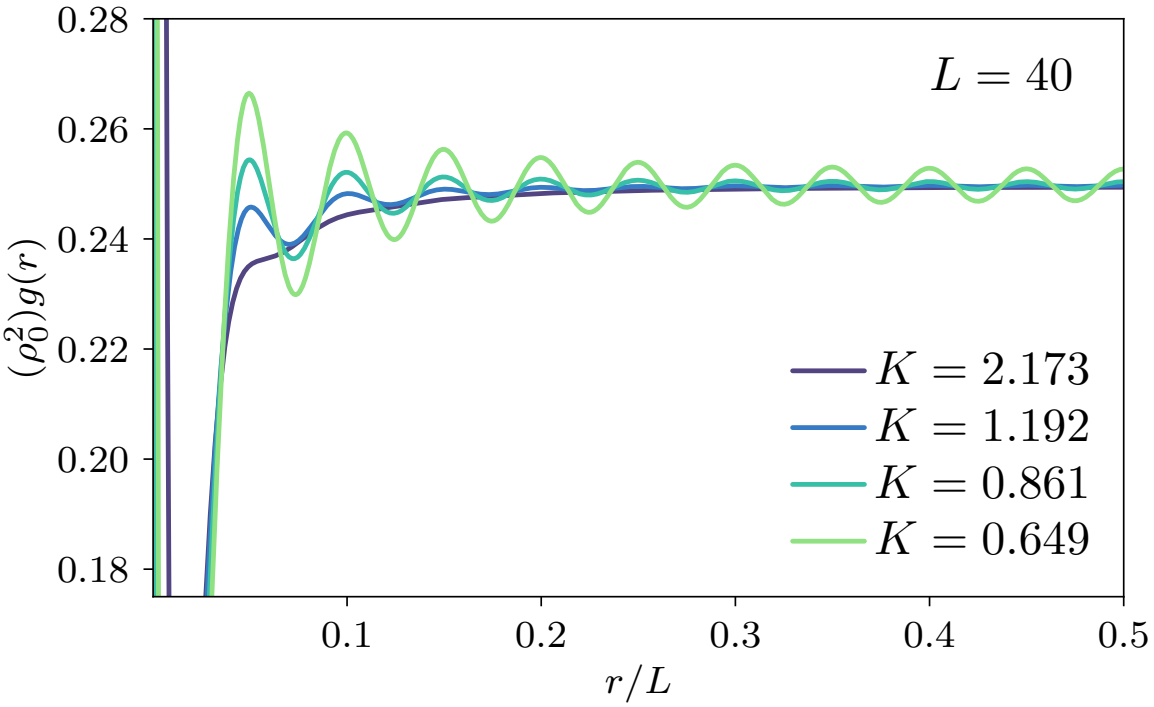

Figure 4.4: The density-density correlation function $g(r) \equiv -\rho_2(x_2, x_1, x_2, x_1)$ at fixed interaction $K = 0.861$ for different system sizes L and for different values of the Luttinger parameter K at fixed $L = 40$.

relations of the fermionic field operators. Consequently, we obtain the density-density correlation function in terms of the two body density matrix as $\langle \Psi^\dagger(x_2)\Psi(x_2)\Psi^\dagger(x_1)\Psi(x_1)\rangle = \langle \Psi^\dagger(x_2)\delta(x_2-x_1)\Psi(x_1) + \langle \Psi^\dagger(x_2)\Psi^\dagger(x_1)\Psi(x_1)\Psi(x_2)\rangle$. In the limit $\epsilon \ll x_2 - x_1 \ll L$, we successfully reproduce the result given by [1], bearing in mind for our derivation we truncated our definition of the field operators to include only the leading order $m = 1$ term in Eq. (4.37). This can be observed in Fig. 4.6, where we observe that our expression matches results obtained from numerical data.

Fig. 4.4 shows the density-density correlation function plotted as a function of the relative coordinate $r = x_2 - x_1$ divided by the total system size for different values of L with $K = 0.861$ and different values of K at $L = 50$. We observe a slower decay for smaller system sizes and increased oscillations for lower values of K, indicative of repulsive interactions.

4.4.2 *Interaction-induced two-body correlations*

Now we turn our attention to the effect of interactions on the structure of the correlation function. To do this, we isolate the interaction-induced contribution by subtracting the free fermions contribution $\rho_{2,\mathrm{FF}}$ and thus define $\Delta\rho_2 = \rho_2 - \rho_{2,\mathrm{FF}}$, where $\rho_{2,\mathrm{FF}}$ corresponds to ρ_2 in the limit $K \to 1$ ($\gamma^2 \to 0$ and $\lambda \to 0$).

To gain some insight into the structure of $\Delta\tilde{\rho}_2$, we fix $\Delta R = const. > 0$ and plot a heat map of $\Delta\tilde{\rho}_2$ in terms of the relative coordinates r and r' as shown in Fig. 4.5. In the left panels, we neutralize the first term in Eq. (4.28) by choosing $\Delta R = \Delta R_0$ such that $\cos(2k_F\Delta R_0) = 0$ while for the left panels, we chose $\Delta R = \Delta R_1$ such that $|\cos(2k_F\Delta R_1)| = 1$. The upper and lower panels correspond to attractive ($K = 8/5 > 1$) and repulsive ($K = 5/8 < 1$) interactions, respectively. Here, we chose the values of the Luttinger parameter K such that the attractive and repulsive cases have the same $\gamma^2 = (K + K^{-1} - 2)/2$ exponent while the $\lambda = (K^{-1} - K)/2$ exponents have the same magnitude but opposite signs (see Fig. 4.2). This choice

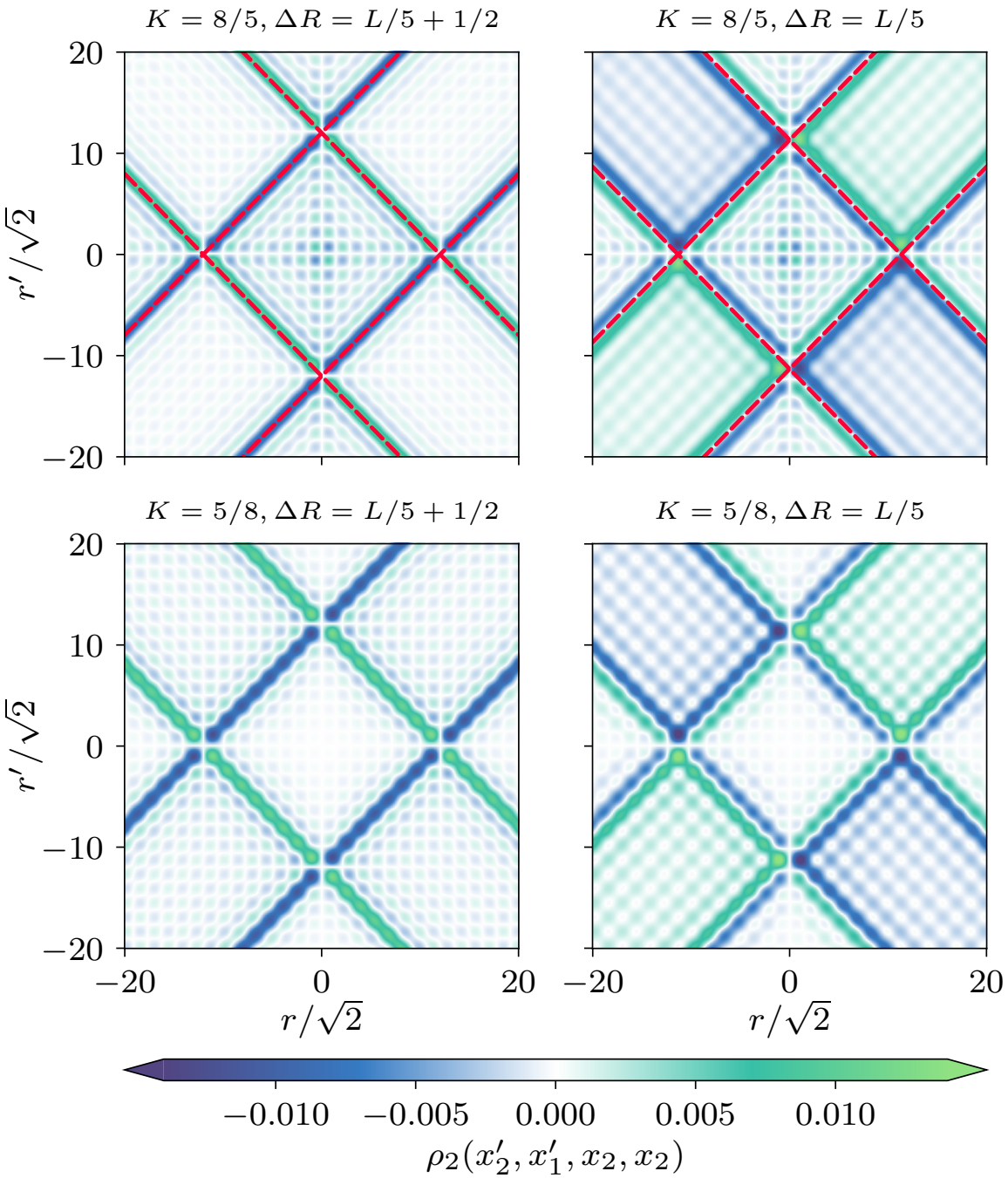

Figure 4.5: Heat maps of the interaction–induced 2-RDM $\Delta\tilde{\rho}_2(r, r'; \Delta R)$ at fixed center of mass separation ΔR. Left: $\Delta R = \Delta R_0$ with $\cos(2k_F \Delta R_0) = 0$; right: $\Delta R = \Delta R_1$ with $|\cos(2k_F \Delta R_1)| = 1$. Top row: attractive interaction ($K = 8/5$); bottom row: repulsive ($K = 5/8$). Both cases share $\gamma^2 = (K + K^{-1} - 2)/2$; the anomalous exponent $\lambda = (K^{-1} - K)/2$ has equal magnitude and opposite sign.

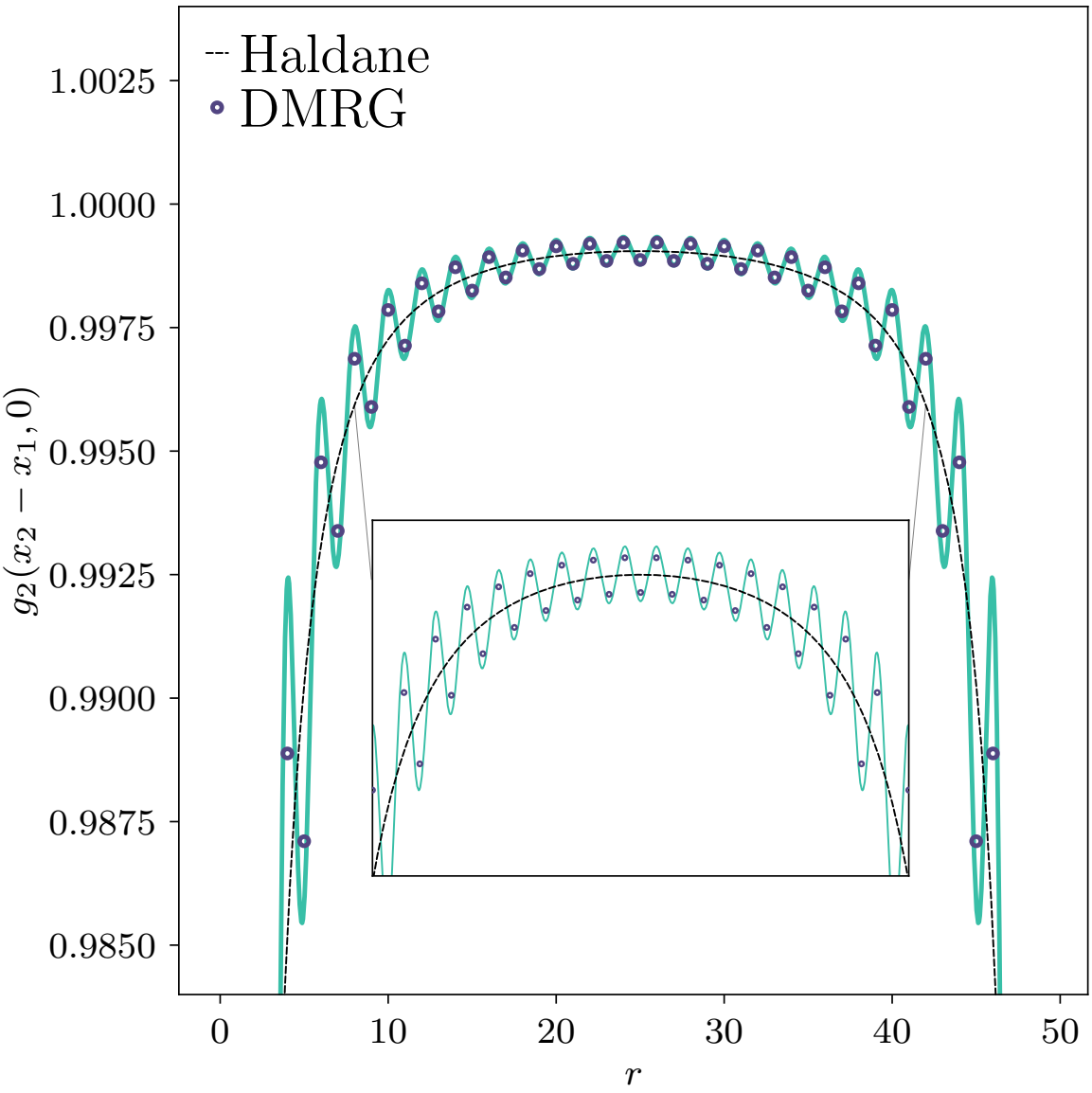

Figure 4.6: The density-density correlation function $g_2(r)$ at fixed $x_2 = 0$ plotted as a function of $r = x_2 - x_1$. The green line shows the analytic result obtained from the two-body density matrix while the blue circles are DMRG results at $L = 50$, $V/J = -0.5$. The solid black line represents the result derived in Ref. [1] that holds for $\epsilon \ll r \ll L$.

of parameters is motivated by the fact that the dependence of the 1-RDM on K is only through the exponent γ^2. Thus, the corresponding 1-RDMs for both cases are expected to be the same.

$$\langle \Psi^\dagger(x')\Psi(x)\rangle = \frac{1}{N}\frac{\sin\left(k_F\Delta x\right)}{L\sin\left(\frac{\pi}{L}\Delta x\right)}\left|\frac{\sin\left(i\pi\epsilon/L\right)}{\sin\left(\frac{\pi}{L}(\Delta x+i\epsilon)\right)}\right|^{\gamma^2}, \tag{4.38}$$

However, the presence of the additional exponent λ in the 2-RDM guarantees the difference between the two cases, as evidenced in the difference between the top and bottom panels of Fig. 4.5.

Furthermore, in the left panels of the figure, we see a strong signal along the two pairs of parallel lines defined by $r_- = \pm\Delta R_0$ and $r_+ = \pm\Delta R_0$. However, in the right panels, the strong presence of the term in Eq. (4.28)($|\cos(2k_F\Delta R_1)| = 1$), alters the structure along the lines $r_- = \pm\Delta R_1$ and $r_+ = \pm\Delta R_1$, where along each line we see a pair of opposite-sign signals, enveloping a zero, which indicates oscillations in the planes $r_+ = \pm\Delta R$, and $r_- = \pm\Delta R$ concerning changing ΔR. In all cases, the signal seems to persist at large $|r_-|$ and $|r_+|$.

Another mark of the difference between attractive and repulsive cases can be seen in the middle of the diamond shapes enclosing the origin in Fig. 4.5. In the attractive case, a grid-like formation with an oscillating signal appears around the origin. The signal appears to oscillate and decay with increasing r and r'. At the same time, the same area is mostly whitened out in the repulsive case. The above analyses suggest that the four limits (hyperplanes) $x_1' \to x_1$, $x_2' \to x_2$, $x_2' \to x_1$, and $x_1' \to x_2$ form the skeleton of the 2-RDM, where the magnitude of $\Delta\tilde{\rho}_2$ for points on these hyperplanes and in their vicinity persists at large distances. In addition, attractive interaction shows a strong signal near small r and r' values if compared with the repulsive interaction case signaling the tendency for fermions to cluster in response to attractive interactions. Fig. 4.7 summarizes this picture, where we exclude the hyperplane $x_1' - x_1 = 0$ ($\Delta R = r_-$) by evaluating $\Delta\tilde{\rho}_2$ on the

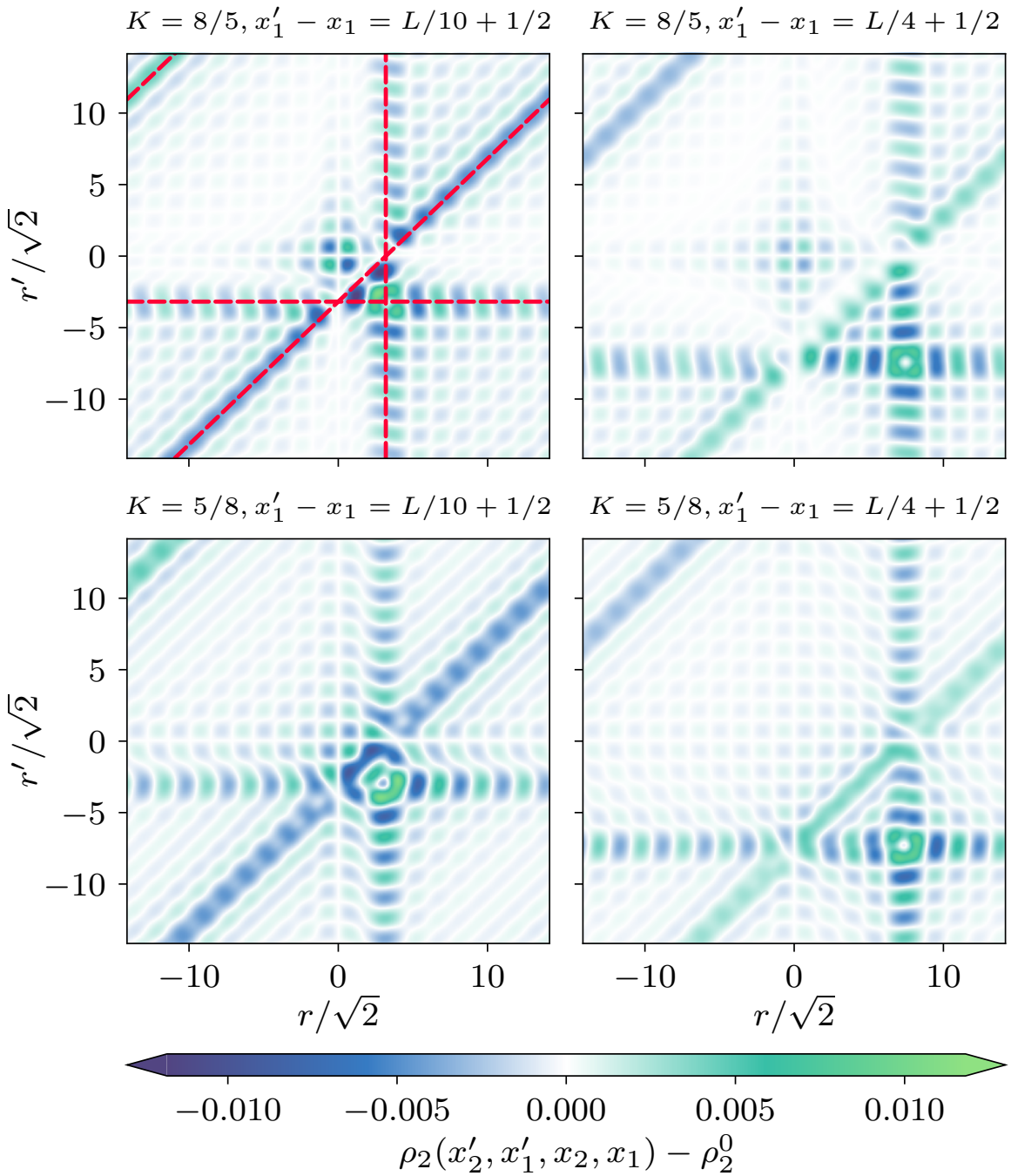

Figure 4.7: The 2-RDM $\rho_2(x_2', x_1', x_2, x_1)$ minus the non-interacting contribution as derived from Wick's theorem p_2^0. We plot in terms of the relative coordinates r vs r' after fixing the difference $x_1' - x_1$ to $L/4$ and $L/10$, to obtain two degrees of freedom for two different interactions, $V/J = -1.5, K = 2.173$ and $V/J = 1.5, K = 0.649$.

parallel hyperplane $x_1' - x_1 = Const. \neq 0$. The figure shows a strong signal at the intersection of the hyperplanes $x_2' - x_1 = 0$ ($\Delta R = -r_+$) and $x_1' - x_2 = 0$ ($\Delta R = r_+$) as this corresponds to a negative copy of the diagonal elements $(-\Delta\tilde{\rho}_2(0, r, r))$. Also, both mentioned hyperplanes intersect destructively with $x_2' - x_2 = 0$ at $r = 0$ and $r' = 0$ as one expects from the antisymmetry of the corresponding fermionic wave function.

4.5 Application: Spinless Fermions on a Lattice

The 2-RDM provides a complete description of all two-body observables, allowing for the computation of key quantities such as interaction energies, pair correlations, and response functions in lattice models describable by TLL theory. In principle, given an appropriate mapping between the continuum and lattice descriptions, the 2-RDM formalism can be applied to any microscopic model, making it a versatile tool for studying strongly correlated systems. We demonstrate this explicitly in the J-V model of spinless fermions, where we show that the ultraviolet cutoff ϵ introduced in the analytic formulation can be directly linked to the microscopic parameters of the lattice model, ensuring consistency between the low-energy field theory and numerical simulations.

We compare the TLL 2-RDM with numerical results obtained from Density Matrix Renormalization Group (DMRG) techniques for the J-V model of spinless fermions on a 1D lattice with L sites at half-filling $L = 2N$, previously discussed in Section 2.4.1.

4.5.1 *Exact Simulation*

To test the interaction component of the analytic TLL 2-RDM result, we compare to numerical density matrix renormalization group (DMRG) simulations of the J-V model, Eq. (2.53), in the Luttinger phase $|V/J| < 2$. To perform DMRG computations, we use the `ITensors.jl` library [119]. By carefully choosing initial

states and projecting an orthogonal subspace to the desired ground state [92], we can reach system sizes of $N > 50$ fermions on $L = 2N$ lattice sites even for (anti-)periodic boundary conditions.

Using `ITensors.jl`, we then compute the 2-RDM

$$\rho_2^{(i,j),(n,m)} = \langle \Psi_0 | \, c_i^\dagger c_j^\dagger c_n c_m \, | \Psi_0 \rangle \tag{4.39}$$

from the ground state $|\Psi_0\rangle$ obtained with DMRG. The key step to make the calculation of the 2-RDM numerically feasible for large systems is to use all symmetries of the J-V Hamiltonian and general properties of the 2-RDM, which allows us to drastically reduce the number of computed expectation values [82]. In particular, we use (i) the translational symmetry $(i, j, n, m) \to (i+1, j+1, n+1, m+1)$, (ii) the reflection symmetry $(i, j, n, m) \to (L-i, L-j, L-n, L-m)$, and (iii) the particle-hole symmetry $(i, j, n, m) \to (m, n, j, i)$. Here, a phase factor of -1 may occur in the case of antiperiodic boundary conditions. In addition, we can further reduce the number of computed entries in 2-RDM by using fermionic commutation relations that result in $\rho_2^{(i,j),(n,m)} = -\rho_2^{(j,i),(n,m)} = -\rho_2^{(i,j),(m,n)} = \rho_2^{(j,i),(m,n)}$.

At the discrete positions of the lattice sites, we can then compare the analytic TLL expression Eq. (4.20) to the DMRG results (see Fig. 4.8). To make this comparison, we need to fix the interaction cutoff ϵ in the analytic expression. We obtain ϵ from a fit of the TLL 1-RDM result $\rho_1(x', x)$ to DMRG simulations for $\rho_1^{(i,j)} = \langle \Psi_0 | \, c_i^\dagger c_j \, | \Psi_0 \rangle$ [panel (a)], showing excellent agreement for $\epsilon(V/J = 0.5, L = 50) = 0.81$. Using this value of the interaction cutoff ϵ, we also find excellent agreement for the 2-RDM [panel (b)]. For visual clarity, we here focus on a cut through $\rho_2(x_2', x_1', x_2, x_1)$ for fixed x_2', x_2, x_1. For fixed x_2', x_2, we show a cut through the 2-RDM as a function of x_1, x_1' in Fig. 4.9(a). To demonstrate the agreement between the analytic result and numerical simulations, we show various cuts in panels (b)-(d), along the dashed black lines in panel (a).

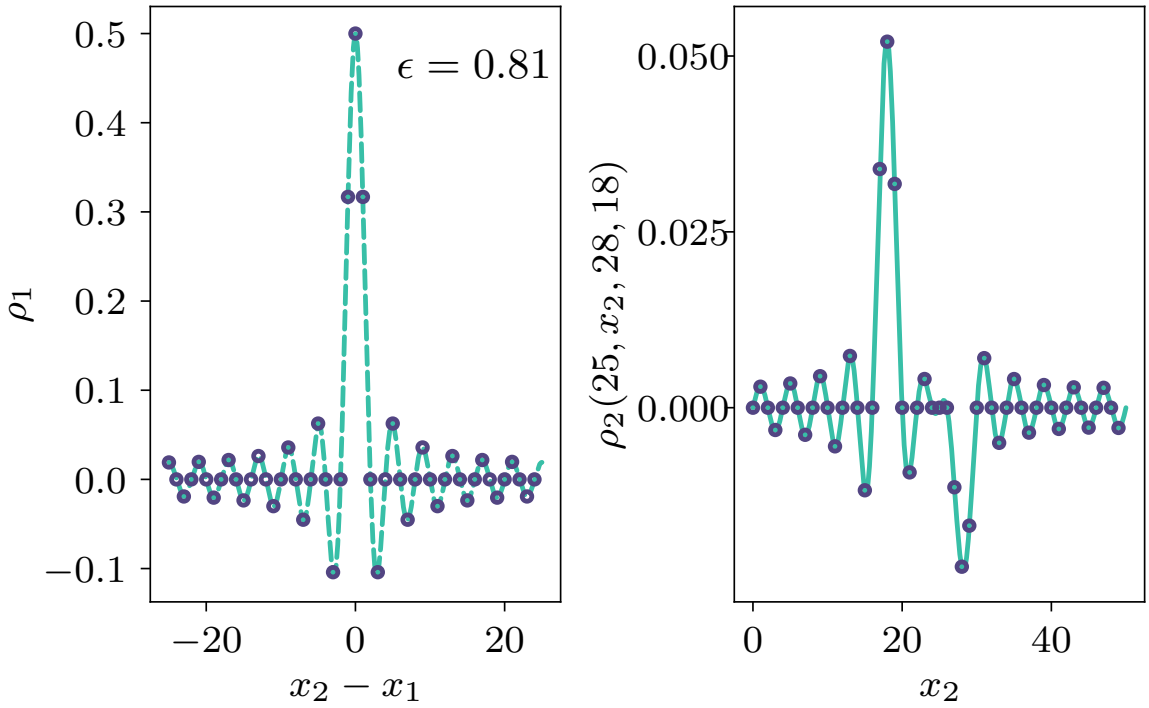

Figure 4.8: We plot the one body reduced density matrix ρ_1 as a function of the relative coordinate $x_2 - x_1$ at fixed interaction $V/J = -0.5$ and system size $L = 50$. From fitting DMRG results to our expression for the OBDM, we obtain a value for the interaction cutoff $\epsilon = 0.81$. Blue dots represent the DMRG data points. On the right panel, we use the same value of ϵ for our computation of the 2-RDM as a function of the coordinate x_2 and find similarly strong agreement with the numerical results.

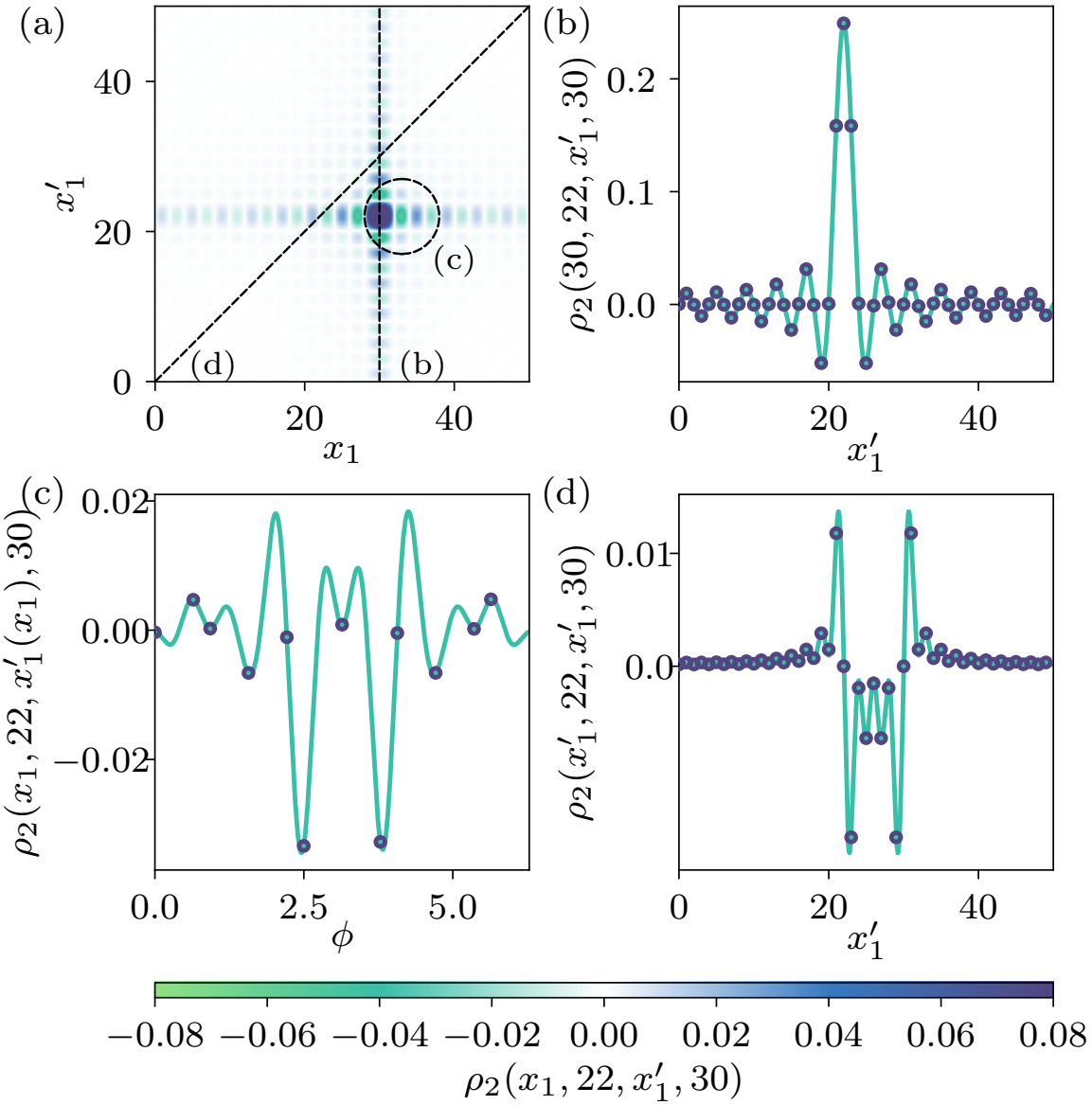

Figure 4.9: Panel (a) shows a heat map of the full correlation function $\rho_2(L//2-4, x_1', L/20, x_1)$ with two fixed coordinates for the interaction strength $V/J = -0.5$ and system size $L = 50$. Dashed lines indicate what is plotted in the remaining panels. Panel (b) shows agreement between the DMRG data and analytic result where only the coordinate x_1' is free. Panel (c) shows the analytic and numerical results for a circular cut of the 2-RDM as a function of the angle ϕ where x_1' depends on x_1 and the other two coordinates are fixed. Panel (d) shows the agreement between DMRG and the analytic result when $x_1' = x_1$.

4.5.2 *Two Body Observables*

Static Structure Factor

In this section, we consider the static structure factor, which is an experimentally accessible quantity defined via the density-density correlations g_2 as [138]

$$g_2(i-j) = \frac{\langle n_i n_j \rangle}{\rho_0^2} - \frac{\delta_{ij}}{\rho_0} \tag{4.40}$$

$$s(q) = 1 + \rho_0 \sum_{j=0}^{L-1} \left[g_2(j) - 1 \right] e^{-iqj} \, . \tag{4.41}$$

Here, the momentum takes values $q = 2\pi n/L$ with $n \in \mathbb{N}$. An important property of $s(q)$ for experiments which can be described by the Luttinger theory, is its small momentum behavior. In the canonical case of a fixed particle number N, it is directly proportional to the Luttinger parameter, $s(q \to 0) \sim K \frac{|q|}{2k_F}$ [3], allowing for the extraction of K and connection to the continuum theory.

We compute the structure factor for filling fractions $1/2$ and $1/5$ from the analytical expression by discretizing it on L lattice sites using that $g_2(x_j) = -\rho_2(x_j, 0, x_j, 0)$. As before, we extract the interaction cutoff ϵ from a fit to the DRMG data for the 1-RDM. Here, we numerically computed the Luttinger parameter at $1/5$ filling for $V/J = -1.0$ as described in Appendix F of Ref. [3] and find $K_{1/5}(V/J = -1) = 1.34135(1)$.

In the absence of a fixed particle number, the zero momentum structure factor is determined by the variance of the particle number $S(q = 0) = \Delta N^2/N$. Related to this, the trace of the discretized expression, $\sum_j g_2(x_j)$, shows small deviations from the value $(N-1)/\rho_0$, obtained from g_2 for the canonical lattice model. Therefore, to apply the analytical Luttinger liquid result to the canonical numerical lattice simulation, we correct for the trace offset by shifting the value of $g_2(x_j)$ at sites $j = 1$ and $j = L-1$ in a symmetric manner, i.e. $g_2(x_j) \to g_2(x_j) -$

$\frac{1}{2}(\delta_{j,1} + \delta_{j,L-1})\left(\sum_j g_2(x_j) - \frac{N-1}{\rho_0}\right)$. By correcting the trace, we ensure that $\Delta N^2 = \langle \hat{N}^2 \rangle - N^2 = 0$.

In addition, we obtain the density-density correlations, and from it the structure factor, using numerical DMRG simulations of the lattice model for both filling fractions. We again find excellent agreement of the numerical and analytical results for $s(q)$ (Fig. 4.10) for g_2 in both cases (inset). As expected, the structure factor for small momenta q follows the linear relation with slope $K/2k_F$ (dotted line).

Ground State Lattice Energy

As a proof of concept, we compute the two body lattice energy given by

$$E_0 = \langle -J \sum_i (c_i^\dagger c_{i+1} + c_{i+1}^\dagger c_i) + V \sum_i n_i n_{i+1} \rangle \tag{4.42}$$

where $c_i^\dagger c_{i+1}$ is just the one body density matrix $\rho_1(x_i, x_{i+1})$ and the number operators are defined as $n_i = c_i^\dagger c_i$. We can then write

$$\begin{aligned} E_0 &= -J \sum_i (\rho_1(x_i, x_{i+1}) + \rho_1(x_{i+1}, x_i)) - V \sum_i g_2(x_i, x_{i+1}) \\ g_2(x_i, x_{i+1}) &= \langle c_i^\dagger c_i c_{i+1}^\dagger c_{i+1} \rangle \end{aligned} \tag{4.43}$$

as we are on a lattice. Using translational invariance to rewrite in terms of relative coordinates, this becomes $E_0 = -JL(\rho_1(1) + \rho_1(-1)) - VLg_2(1)$.

We can verify our expression for the ground state energy through comparison with numerics. Fig. 4.11 shows the ground state energy divided by the hopping parameter J at different system sizes. Blue circles indicate DMRG results while the solid lines are the analytic result. The righthand panel shows the energy density per particle, which, as expected, is the same regardless of N demonstrating the absence of finite size effects. We see good agreement with the numerics, with a breakdown at larger values of K. This is most likely due to the breakdown of the

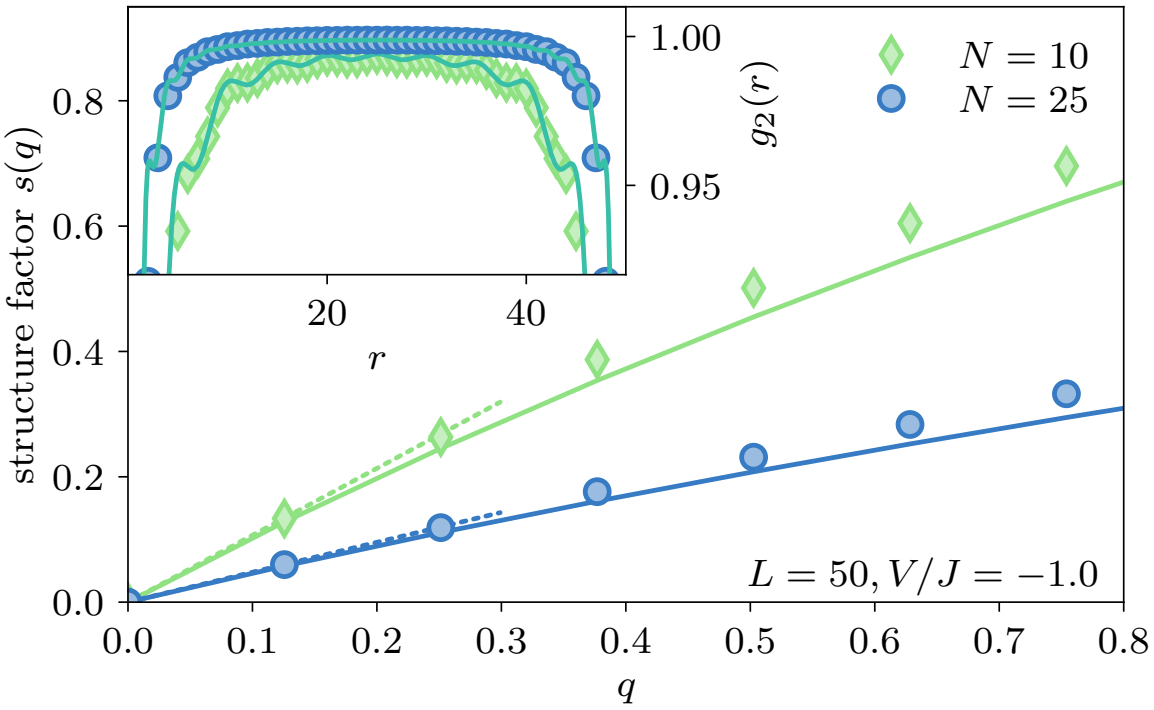

Figure 4.10: Structure factor $s(q)$ and density-density correlations $g_2(r)$ (inset) for filling fractions $1/5$ (green diamonds) and $1/2$ (blue circles) obtained from DMRG simulations of the lattice model with size $L = 50$ and $V/J = -1.0$. The dashed lines show the analytically obtained $q \to 0$ limiting behavior, $s(q \to 0)$, a linear function with slope $K/(2k_F)$. The solid lines depict the analytical result in very good agreement with the numerical data.

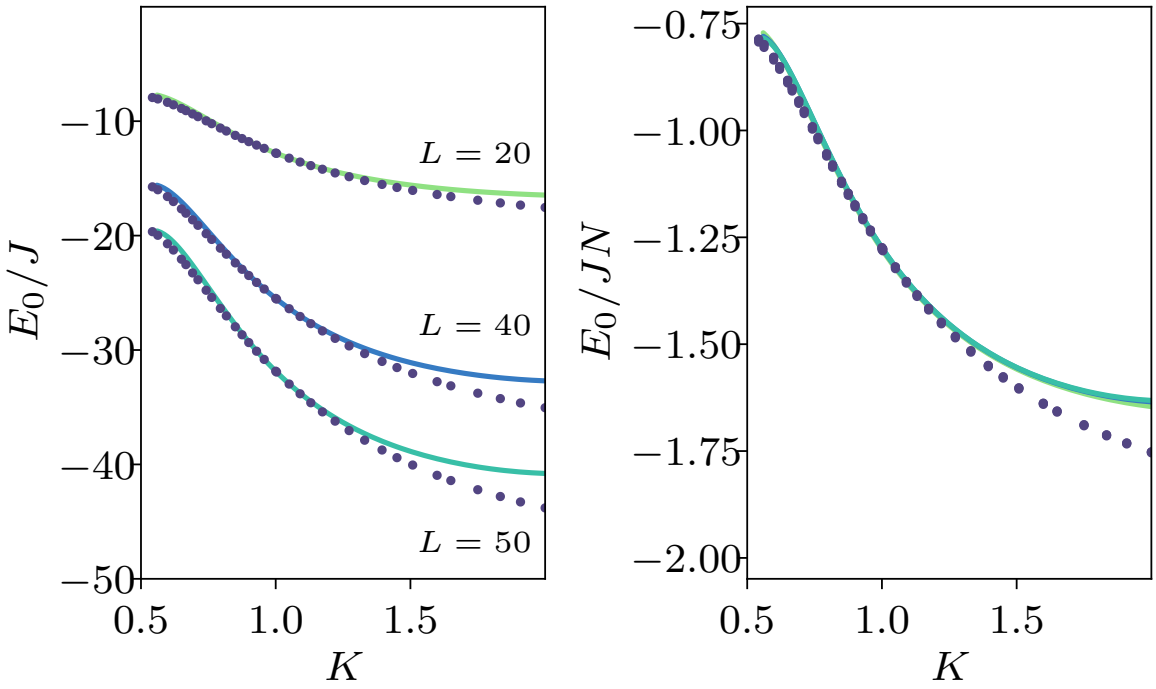

Figure 4.11: The two body ground state energy E_0 divided by the hopping parameter J as a function of the Luttinger parameter K for different system sizes. Solid lines show the analytic result while dark blue circles are the numerical results from DMRG. The righthand panel shows the energy density per particle. Strong agreement is shown for values of K below 1.5.

theory while approaching the first order phase transition to the clustered solid phase in the J-V model, but could also be partially due to ignoring the higher summation m terms in the expression for the density-density correlation function Eq. (4.37). Further manipulation of the expression would be necessary for the computation of different two-body observables.

4.5.3 *Coherences*

We now look at a case where the off-diagonal elements, or *coherences*, of the 2-RDM are useful and provide insight into the phase structure of our spinless fermion system. First, in the repulsive interaction range $1/2 \leq K \leq 1$, we study the off diagonal two-body coherence

$$\rho(\chi) = \left\langle \Psi^\dagger(0)\Psi^\dagger\left(\tfrac{L}{2}+\chi\right)\Psi(0)\Psi\left(\tfrac{L}{2}\right)\right\rangle. \tag{4.44}$$

Fig. 4.12 plots this quantity as a function of the displacement χ for $L = 40$. We observe that the peak at $\chi = 0$ is largest for the strongest repulsive interaction ($K = \frac{1}{2}$), at the phase transition to the charge density wave (CDW) phase. At small values of χ, the damping is less pronounced for free fermions ($K = 1$). We also see that the matrix element changes sign for even values of the displacement χ.

We can understand this behavior as follows – in the repulsive regime, ($K < 1$), the coherence $\rho(\chi)$ is expected to decay according to [2, 3, 136]

$$\rho(\chi) = \frac{\cos\left(2k_F\chi\right)}{|\chi|^{-2K}}. \tag{4.45}$$

Smaller values of K, corresponding to stronger repulsion, exhibit slower decay, less damping, and a sharper peak at $\chi = 0$. For free fermions ($K = 1$), other short-range terms compete with CDW contributions, resulting in stronger oscillations. To understand the sign change, we note that permuting the operators results in a minus sign due to fermion antisymmetrization, and the lattice spacing contributes

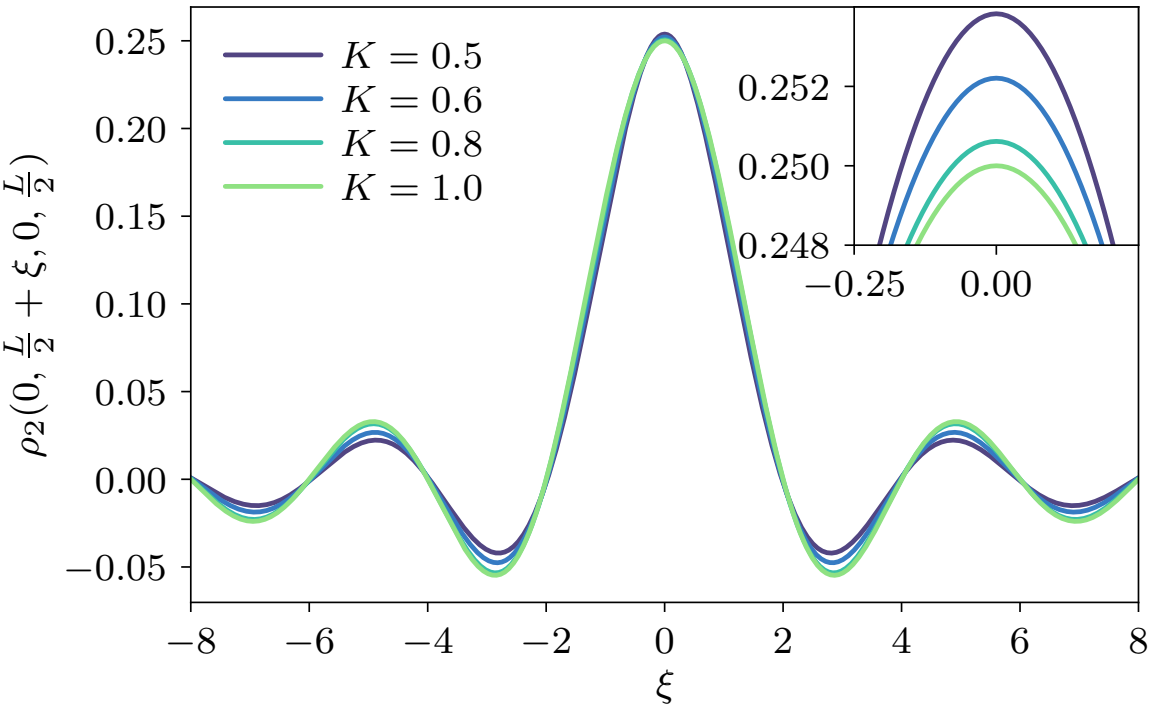

Figure 4.12: Short-distance behavior of the off-diagonal two-particle density matrix $\rho_2(0, L/2 + \xi, 0, L/2$ as a function of separation χ, for several values of the Luttinger parameter K. For smaller K (stronger repulsion), the oscillations decay more slowly, indicating stronger CDW correlations. As K decreases, the oscillations become more damped.

a factor $(-1)^{\chi}$. This results in an overall phase $(-1)^{\chi+1}$. Together, these features signal CDW order as the interaction strength becomes more repulsive.

We now examine the attractive regime, $K > 1$, where the system should exhibit a superconducting instability with p-wave pairing [3]. Although true long-range order is suppressed in one dimension due to strong phase fluctuations, bosonization predicts an algebraic decay of the pair correlator, $\rho_2 \propto |x|^{-1/K}$, consistent with quasi-long range order [132]. We verify this by considering the off-diagonal element $\rho_2(L/2+\nu, L/2, \mu, 0)$, plotted in Fig. 4.13 as a function of the relative displacements μ and ν for $K = 8$. A key feature of p-wave symmetry is its odd parity, meaning the pair wavefunction changes sign under spatial inversion. We find that the correlator vanishes at $\mu = 0, \nu = 0$ due to Pauli exclusion and forms distinct lobes that alternate in sign across these lines, consistent with antisymmetric pairing.

4.6 Conclusions

In this chapter, we derived an exact expression for the two-body density matrix (2-RDM) of interacting, spinless fermions in the Tomonaga-Luttinger liquid framework. A notable outcome is the appearance of the interaction-dependent exponent $\lambda = (K^{-1} - K)/2$, which enters only when correlations between right- and left-moving sectors are relevant ($n > 1$ density matrices). In the $n = 2$ case, we also obtained a lattice-corrected density–density correlation function that reduces to the familiar continuum form when the separations are small compared with the system size L.

We benchmarked the analytic predictions benchmarked against exact diagonalization and DMRG data for the J-V chain at half-filling. Using an ultraviolet cutoff, obtained through a self-consistent fitting procedure of the 1-RDM, the analytic expressions agree closely with the lattice results in both attractive ($K > 1$) and repulsive ($K < 1$) regimes. This demonstrated that lattice effects, encoded by

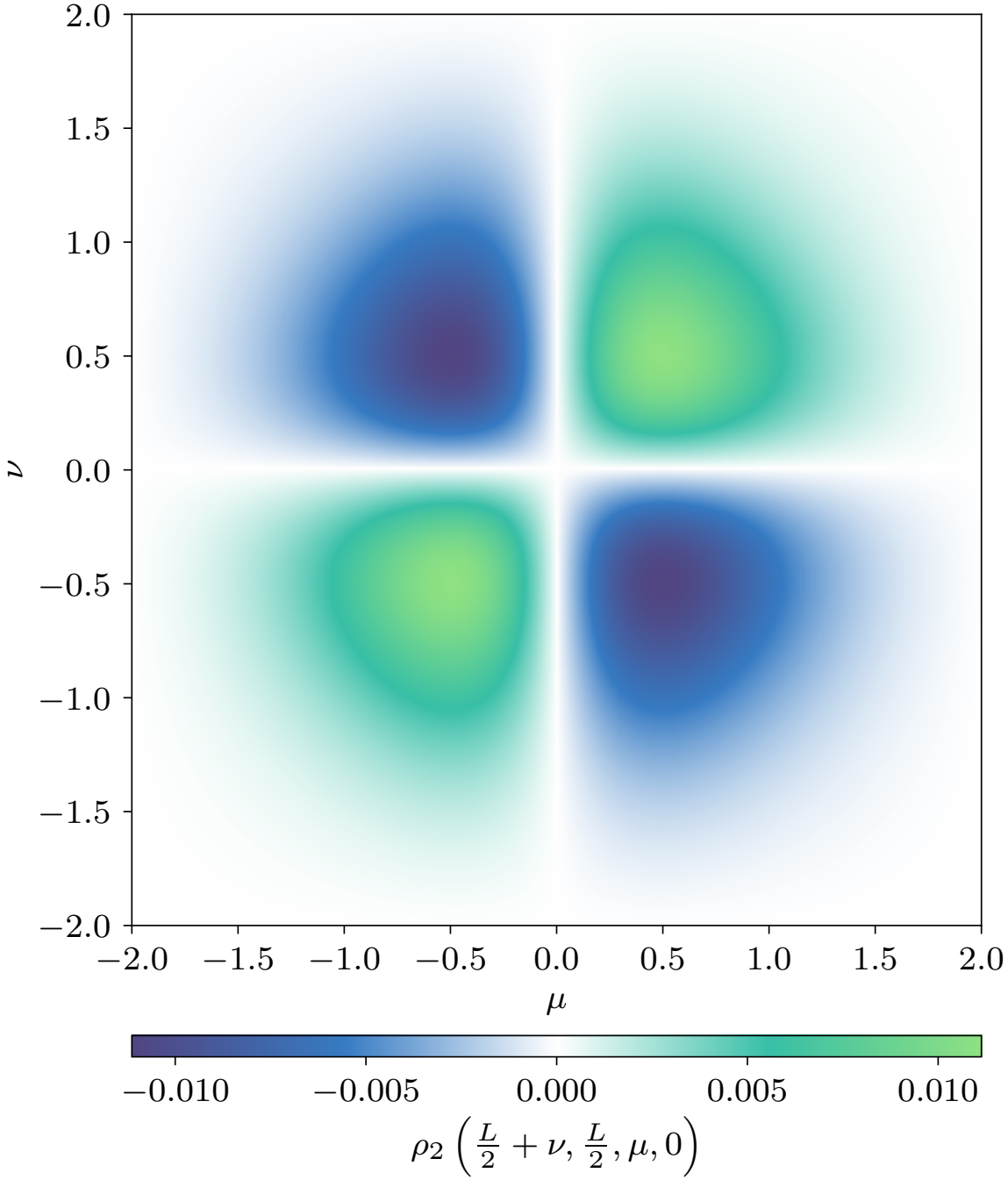

Figure 4.13: Heat map of $\rho_2(L/2+\nu, L/2, \mu, 0)$ in the attractive regime ($K > 1$). Positive (green) and negative (blue) lobes alternate across the nodal lines $\mu = \pm\nu$, consistent with the antisymmetric p-wave character of the pair wavefunction.

the cutoff, are necessary for comparison with the microscopics. Substituting the 2-RDM into expressions for the ground state energy and the static structure factor, reproduces numerical values with high accuracy in the TLL regime, confirming that the density matrix formalism is a practical tool for computing higher-order observables. Off-diagonal elements further indicate p-wave pairing in the attractive regime and signatures of $2k_F$ CDW order in the repulsive regime. The same matrix elements could be used to determine a wide class of observables, for example, interference fringe amplitudes in condensate experiments [128].

The present results invite several natural extensions. First, the method used here should generalize to any n, giving closed forms for higher n-body density matrices and thus opening a route to systematic calculations of the n-particle entanglement. In particular, the sub-leading $1/N$ term observed numerically in Rényi entropies for $n > 1$ [82, 88] can be traced to the structure of the exact 2-RDM, particularly the exponent λ. Second, a time-dependent version of this quantity would allow one to track the growth of correlations and entanglement after an interaction quantum quench. In particular, one could obtain an explicit expression for the exponent λ in the non-equilibrium case analogous to work that has previously been done for γ^2 [92]. Finally, because the underlying Hamiltonian involves at most two-body operators, higher RDMs are, in principle, unique functionals of the 1- and 2-RDMs [139]; explicit reconstruction in the Luttinger liquid context would provide a concrete test of that representability program.

If you knew Time as well as I do, said the Hatter,
You wouldn't talk about wasting it.
Lewis Carroll
Alice's Adventures in Wonderland

PARTICLE ENTANGLEMENT AFTER A QUANTUM QUENCH

5

This chapter contains text from published work by the author [92] with minor modifications where appropriate for this format. The author contributed significantly to the bosonization derivations of the one-body density matrix at and out of equilibrium as well as the Fourier transform to momentum space. Additionally, the author helped write these derivations in the manuscript. Matthias Thamm did the majority of the work including the numerical simulations, fitting of the data, production of figures, and writing of the manuscript with input from Hatem Barghathi. Adrian Del Maestro and Bernd Rosenow supervised this work and wrote the discussion and introduction.

5.1 Introduction

If a quantum system is in a pure state after a sudden change to the system – a quantum quench [24] – the growth of entanglement entropy under a spatial bipartition plays the role of thermal entropy [30, 31] in describing how expectation values of local observables can be computed from a statistical ensemble [140–143]. For systems of N indistinguishable particles, a bipartition can also be made in terms of subgroups of n and $N-n$ particles [33, 35, 99, 100]. This particle entanglement entropy provides complementary information as compared to the spatial mode entanglement and is sensitive to both interactions and particle statistics at leading order [32, 34, 90, 91, 93, 105, 109, 110, 112, 114, 115, 144],

phase transitions [102, 103], and possibly to many body localization [145, 146]. Unlike mode entanglement, particle entanglement is not sensitive to the choice of modes (e.g. spatial, momentum, or energy), and could play a role in characterizing phases of matter through the information content encoded in correlations between particles. There are also routes to potential experimental measurement, either through correlation function coherences [128, 129] or via its transfer to accessible modes [147]. In a dynamical setting, an equivalence was recently demonstrated between the increase of entropy densities under spatial and particle bipartitions in the asymptotic steady-state regime after a quantum quench in a system of interacting one dimensional fermions [87] in the limit $n, N \to \infty$; $n/N \sim$ const.

Numerical results also indicate that the particle entanglement entropy density is a decreasing function of the order n of the reduced density matrix, which can be understood in terms of higher-order correlations acting as a constraint on the available particle configurations. For an integrable model, it is even possible to obtain the entanglement entropy density after an interaction quench from knowledge of only the diagonal components of the $n = 2$ density matrix [148]. These results accentuate the potential of particle entanglement entropy as an alternative to the usual spatial entanglement in understanding non-classical correlations in non-equilibrium quantum dynamics.

Thus it is natural to explore the entanglement entropy associated with low order density matrices. The idea of expanding the entropy density as a series in irreducible correlations between groups of n particles is explicit in classical non-equilibrium mechanics [149, 150]. However, in general, density matrices are very challenging to compute, but in one dimension (1d), even after a quantum quench, bosonization gives access to low-order reduced density matrices as correlation functions of bosonic exponentials [47, 118, 151, 152]. Here, we study the properties of the $n = 1$ reduced density matrix (RDM), both in equilibrium and after a quantum quench, with a focus on the von Neumann and Rényi entropies. This represents the first step in the systematic expansion in terms of multi-particle

correlations discussed above. For $n = 1$, the 1-RDM is proportional to the familiar equal time Green function which captures the momentum distribution, and is experimentally accessible in a wide variety of scenarios (e.g. via interference [128, 129] or Raman scattering [153] in trapped low dimensional ultracold gasses, or through the spectral function in angle resolved photoemission spectroscopy [154]). Bounds have been proven on the spectrum of 1-RDMS, and there are conjectures for the spectrum of the 2-RDM [88, 155].

We perform exact computations of the 1-RDM for an interacting lattice model of spinless fermions in one dimension, the J-V model. This model, which can be exactly solved by mapping to the XXZ spin chain [156, 157] at fixed magnetization, has proven to be a fruitful playground for studying quasi-thermalization and the dynamics of correlation functions and spatial entanglement after a quantum quench [158–162]. Here, we are interested in particle entanglement entropy in this system, and apply large scale exact diagonalization (up to $N = 19$ particles on $L = 38$ sites at half filling), both in equilibrium and after an interaction quantum quench. Both the transient dynamics and asymptotic steady state after a quantum quench are analyzed by performing unitary time evolution starting from an initial state of free fermions to long times. These results are extended to even larger system sizes while preserving periodic boundary conditions using GPU accelerated time-dependent density matrix renormalization group (tDMRG) calculations allowing us to study systems up to $L = 102$ sites. Here, the presence of periodic boundary conditions is important, allowing for the computation of the momentum distribution directly from the eigenvalues of the 1-RDM, maintaining translational invariance and ensuring accuracy of measured quantities at small momenta.

We consider a wide range of attractive and repulsive interactions spanning a continuous and discrete quantum phase transition in the model. For a quantum quench to a state with strong interactions, outside the quantum liquid regime, we find that both the transient and long time momentum distribution can develop

non-monotonic behavior as a function of momentum q – a signature of strong spatial correlations and particle localization in the ground state. The large system sizes studied allow us to perform reliable finite size scaling to the thermodynamic limit where a comparison can be made with continuum field theory calculations.

Bosonization is routinely used to compute universal quantities, and here we use it to study the 1-RDM whose short-distance behavior reflects the dynamics of high energy excitations. This is accomplished by the introduction of an interaction cutoff (different from the often used UV lattice cutoff), which is needed due to the short-range nature of interactions in the J-V model under study. This cutoff is unambiguously determined from our equilibrium numerics and applied to make microscopic predictions after the quench via bosonization. Good agreement is found across the phase diagram for the 1-particle von Neumann and Rényi entanglement entropies highlighting the utility of continuum field theory to describe both short and long time dynamics.

In the following, we briefly describe the main results and contributions of this work. We study N one dimensional spinless fermions on a lattice of L sites with hopping J and nearest neighbor interaction V (see microscopic Hamiltonian in Equation 2.53 for details). For $|V/J| < 2$, the low energy sector is a Luttinger liquid, while the system undergoes a continuous quantum phase transition to an insulating solid phase at $V/J = 2$. For attractive interactions, there is a discontinuous transition to a phase separated clustered solid at $V/J = -2$. This phase diagram is reflected in Fig. 5.1 which shows the von Neumann entanglement entropy S_1 computed from the spectrum of the 1-RDM, $\rho_1(q)$:

$$S_1 = -\frac{N}{2k_F} \int dq \, \rho_1(q) \ln \rho_1(q) \, , \tag{5.1}$$

where k_F is the Fermi momentum at half-filling. Here we have subtracted off the 1-particle entanglement of free fermions: $S_{ff} = \ln N$ to highlight the role of interactions. At $V/J = 2$, there is a change of slope in the entanglement

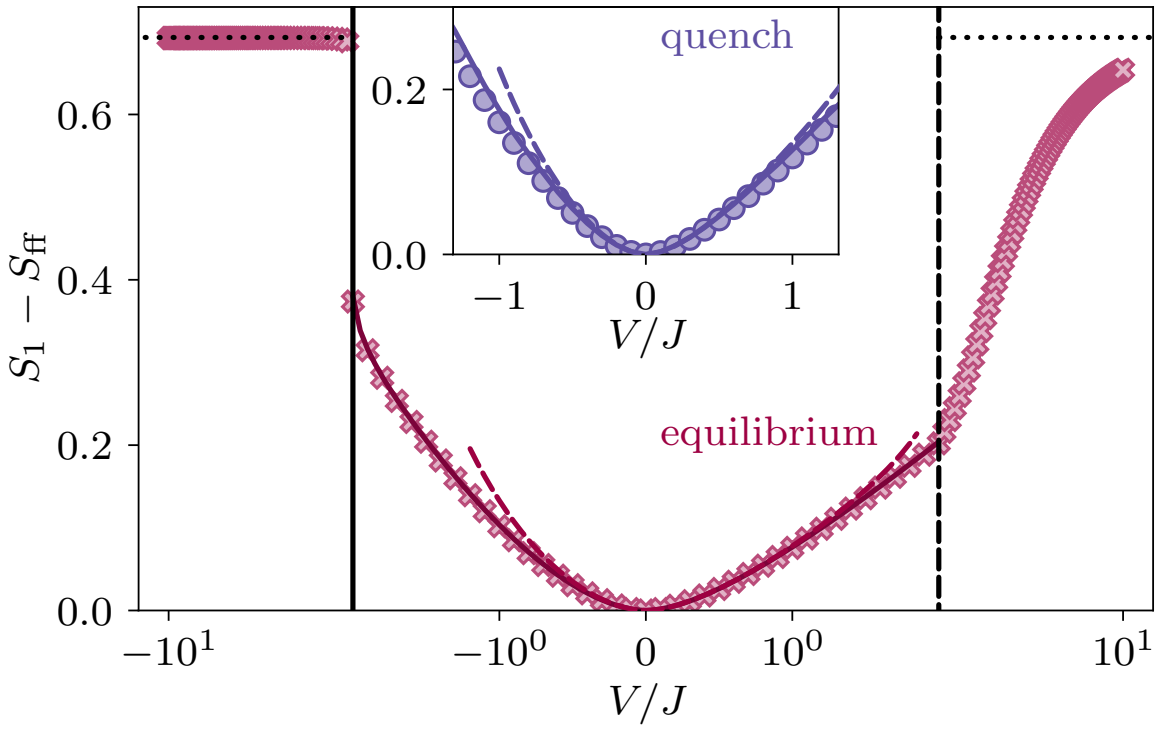

Figure 5.1: Interaction dependence of one particle von Neumann entanglement entropy S_1 obtained numerically from the J-V model and from an effective low energy Luttinger liquid calculation (dashed lines) with a fixed interaction cutoff. Here, S_{ff} is the entropy for free fermions. The main panel depicts the equilibrium ground state entropy with numerical data from DMRG for a system of $L = 102$ lattice sites at half filling (crosses). The solid line represents finite size scaling of numerical data to the thermodynamic limit. The excellent agreement with the finite size DMRG data shows that the system with $N = 51$ fermions is large enough to describe the thermodynamic limit accurately in the whole LL phase. The inset depicts finite size exact diagonalization results for $N = 12$ fermions on $L = 24$ sites after an interaction quantum quench (circles) in the asymptotic steady state. The solid line shows the thermodynamic limit of the numerical data obtained from finite size scaling the time averaged one particle entropy (circles) after the interaction quench. The dashed line is the result of non-equilibrium bosonization using the same value of the interaction cutoff as in the main panel.

as the system enters the solid phase via a second order transition, and $S_1 - S_{\mathrm{ff}}$ asymptotically approaches $\ln 2$ (dotted line) for $V/J \gg 2$ reflecting the two-fold degeneracy of the charge density wave ground state. Moving across $V/J = -2$, the entanglement entropy echoes the first-order transition by a sudden jump in $S_1 - S_{\mathrm{ff}}$ to $\approx \ln 2$ (dotted line). Here, the large entanglement entropy is due to the translational symmetry of the clustered N fermions state representing the solid phase. In the Luttinger liquid phase, we show the bosonization result for the entanglement as a dashed red line, for a fixed value of the interaction cutoff. The deviation for strong negative interactions reflects the divergence $K \to \infty$ of the Luttinger parameter when approaching the first order phase transition at $V/J = -2$. The solid red line represents the extrapolation to the thermodynamic limit of the numerical exact diagonalization and DMRG data, highlighting the reliable nature of our finite size scaling procedure. The inset shows the $t \to \infty$ asymptotic limit of the 1-particle entanglement entropy after the J-V model is quenched from non-interacting fermions to a final interaction strength V at $t = 0$ for a finite size system of $N = 12$ fermions on $L = 24$ sites. Here, the dashed line is computed via non-equilibrium bosonization using the same cutoff as in the equilibrium case. The solid purple line again shows the extrapolation to the thermodynamic limit. A comparison with the main panel shows the growth of entanglement after the quantum quench in this quantum liquid regime.

In translationally invariant systems, the 1-RDM depends only on the difference between the two spatial coordinates, and can hence be diagonalized by a Fourier transform. The resulting $\rho(q,t)$ obtained from exact diagonalization is displayed in Fig. 5.2 as a function of $2vt/L$, where t is the waiting time after the quench, v is the renormalized velocity of low energy excitations, and L is the system size.

Quasi-periodic oscillations, due to the presence of multiple velocity scales, whose amplitude increases with momentum q are observed.

For a strong interaction quench from non-interacting fermions to deep inside the phase separated cluster solid, the q-dependence of the distribution function at

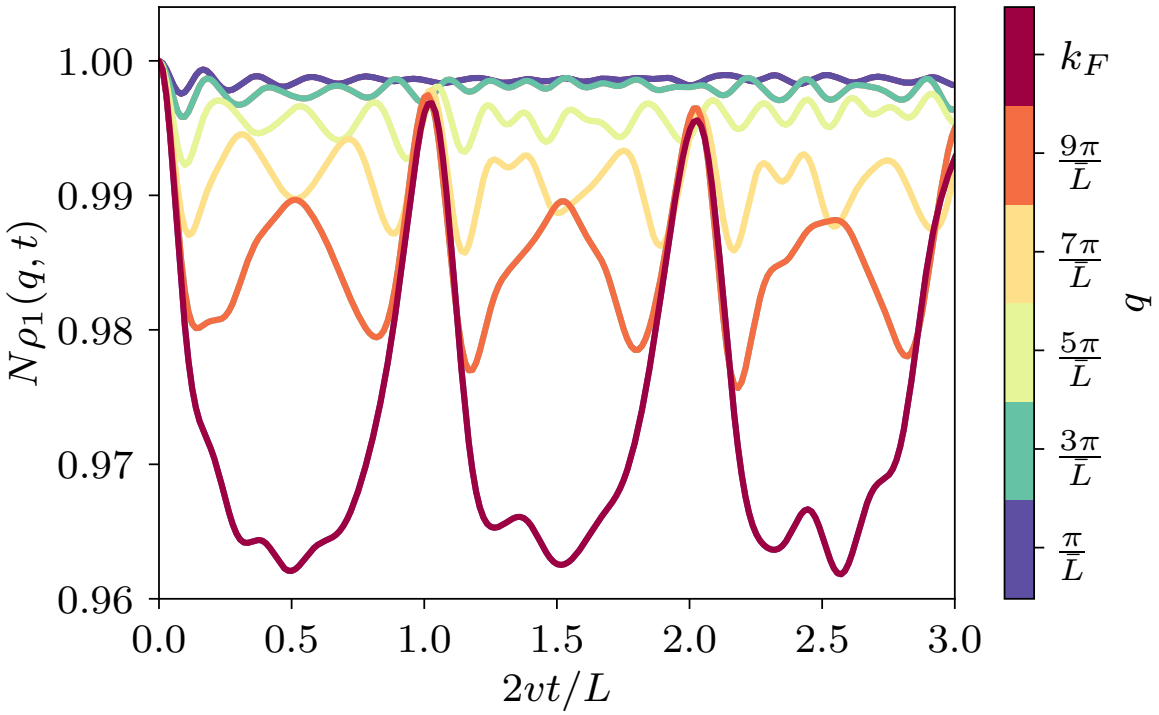

Figure 5.2: Dependence of eigenvalues of the one body density matrix ρ_1 on the rescaled waiting time $2vt/L$ after the quantum quench computed via exact diagonalization for a final interaction strength $V/J = -0.5$. We show a quarter of the spectrum with $0 < q < k_F$ for a system of $N = 12$ fermions on $L = 24$ lattice sites. The largest contributions to the one particle entanglement entropy come from the eigenvalues close to the Fermi levels which show the largest oscillation amplitude and the recurrence time $L/(2v)$ that appears in the entropy.

fixed waiting times can develop a non-monotonicity as seen in Figure 5.3. For times still in the transient range, this can occur near the Fermi momentum, whereas, at long waiting times, it appears even at small q. A detailed study of the interaction and time dependence of this quantity is discussed in Section 5.6.

The main contributions of this work are i) providing a definitive picture of the 1-RDM and entanglement in a one-dimensional integrable model both in equilibrium and after a quantum quench; and ii) utilizing a self-consistent procedure to regularize field theory computations to make predictions about the post-quench density matrix and entanglement entropy.

The remainder of the chapter is organized as follows. In Section II we introduce the microscopic lattice model under study and describe its phase diagram in detail. We then bosonize its low energy sector in Section III and derive an expression for the momentum distribution in equilibrium. This field theory calculation is then compared against exact diagonalization and DMRG results in Section IV. Section V explores the 1-particle entanglement entropy after an interaction quantum quench, again comparing field theory with numerical results. The explicit post-quench waiting time dependence of the 1-RDM is investigated in Section VI before we provide some final concluding remarks and possible future research directions in Section VII.

5.2 1-Particle Reduced Density Matrix in a Luttinger Liquid

In this chapter, we study the one-particle entanglement entropy from the J-V model in the LL phase (iii). In the following, we measure lengths in units of the lattice constant. We start with deriving an analytical result for the one body density matrix $\rho_1(x,0)$ for the corresponding LL model of length L. From the LL 1-RDM, we compute the one-particle entanglement entropy, and then compare with numerical results obtained for the J-V model. In this phase with intermediate

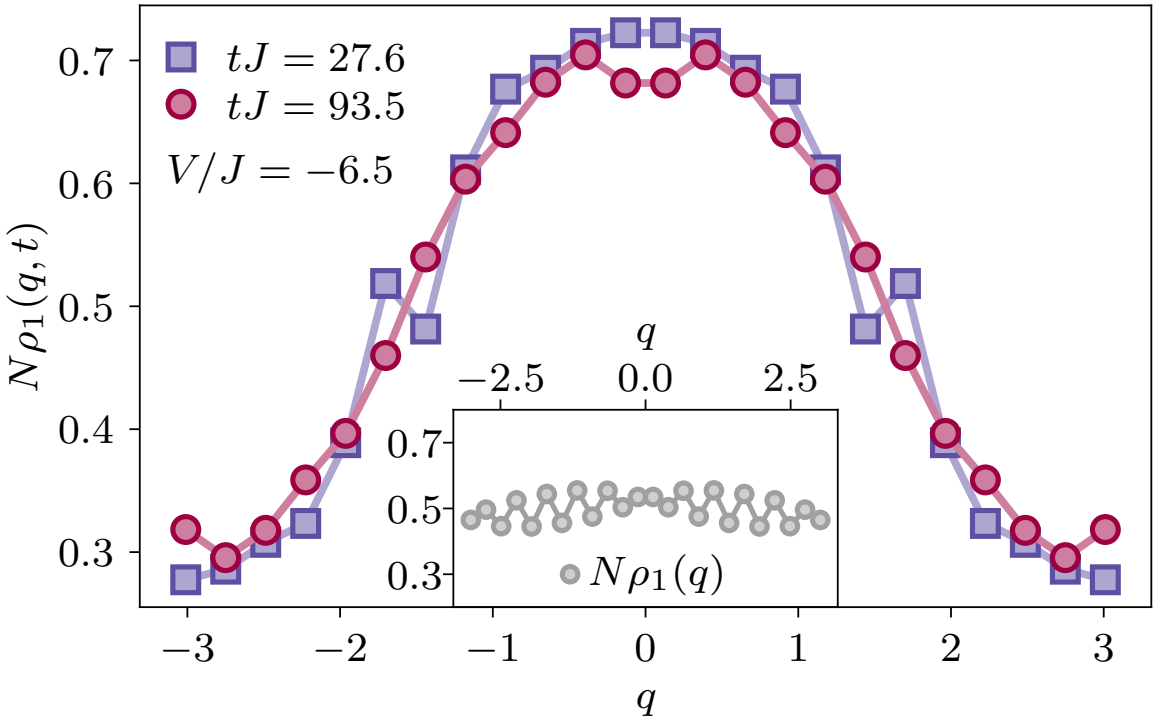

Figure 5.3: Momentum distribution function at two different times, after a quantum quench at $t = 0$ to a final interaction strength $V/J = -6.5$ deep in the phase separated clustered solid. The system consists of $N = 12$ fermions on a ring of $L = 24$ sites. The inset shows the equilibrium ground state distribution function which demonstrates pronounced oscillations due to the existence of a short momentum scale resulting from large clusters of N fermions. Lines are a guide to the eye.

interaction strength, observables are dominated by low energy excitations in the form of density fluctuations around a static average density background. Such fluctuations of the density are bosonic in nature, which allows us to describe the low energy physics with an effective Hamiltonian [47] in bosonization notation after linearizing the dispersion around the Fermi points

$$H = \sum_{q\neq 0} \left[\omega_0(q) + m(q)\right] b_q^\dagger b_q + \frac{1}{2}\sum_{q\neq 0} g_2(q)\left(b_q b_{-q} + b_q^\dagger b_{-q}^\dagger\right) , \tag{5.2}$$

where $b_q^\dagger$ (b_q) are bosonic creation (annihilation) operators with $[b_q, b_{q'}^\dagger] = \delta_{q,q'}$, $\omega_0(q) = v_F|q|$, and we work in units where $\hbar = 1$. The sum is taken over discrete momenta $q_n = n2\pi/L$ with $n \in \mathbb{Z}\setminus\{0\}$. The nearest-neighbor coupling in the lattice model has a finite interaction range, which we take into account by assuming that $g_2(q)$ and $m(q)$ vanish for momenta $q\varepsilon \gg 1$ larger than an interaction cutoff ε [*]. For small $|q|$, the parameters have a linear q dependence, $m(q) = g_4|q|$, $g_2(q) = g_2|q|$, where g_2 and g_4 can be related to the parameters of the J-V model as discussed below. As $\omega_0(q)$ is the dispersion for free fermions, the terms g_2 and g_4 are zero in this case. By comparing the final bosonization results with numerical simulations of the J-V chain the interaction cutoff can be unambiguously determined. The Hamiltonian Eq. (5.2) is quadratic in the boson operators and can therefore be solved analytically. In order to compute the one body density matrix, we use refermionization to express the fermionic field operators $\psi_\alpha(x)$ in terms of bosonic fields as

$$\psi_\alpha(x) = \frac{\chi_\alpha}{\sqrt{2\pi\eta}} e^{\imath(\varphi_{0,\alpha} + \alpha\frac{2\pi x}{L}N_\alpha)} e^{-\imath\phi_\alpha(x)} \tag{5.3}$$

$$\phi_\alpha(x) = -\sum_{q>0}\sqrt{\frac{2\pi}{qL}} e^{-q\eta/2}\left[e^{\imath\alpha qx} b_{\alpha q} + e^{-\imath\alpha qx} b_{\alpha q}^\dagger\right] , \tag{5.4}$$

[*]For the detailed implementation of the cutoff procedure see (Eq. (5.26))

where $\alpha = (-)1$ indicates right (left) moving fermions, $\chi_\alpha = e^{\alpha \imath \frac{\pi}{2} N_{-\alpha}}$ are Klein factors with $\chi_\alpha^\dagger \chi_\alpha = 1$, η is a short distance cutoff measured in units of the lattice spacing (not to be confused with the interaction cutoff ε), and $\phi_\alpha(x)$ are Hermitian operators [3, 46]. Here, N_α is the particle number operator, and $\varphi_{0,\alpha}$, N_α are zero mode operators satisfying the commutation relation $[N_\alpha, \varphi_{0,\alpha}] = i$. The one-body density matrix can be obtained from the one point correlation functions for left and right movers in terms of the fermion operators Eq. (5.3) via

$$\rho_1(x,0) = \frac{1}{N}\left[e^{-\imath k_F x} C_+(x,0) + e^{\imath k_F x} C_-(x,0)\right] \tag{5.5}$$

$$C_\alpha(x,0) = \langle \psi_\alpha^\dagger(x)\psi_\alpha(0)\rangle \tag{5.6}$$

with Fermi momentum $k_F = \pi N/L$.

To relate the results for the effective LL model to numerical results of the J-V model at half filling, we use Bethe ansatz results obtained via a mapping to the spin-1/2 XXZ chain [3]

$$K \equiv \sqrt{\frac{v_F + g_4 + g_2}{v_F + g_4 - g_2}} = \frac{\pi}{2\cos^{-1}\left(\frac{-V}{2J}\right)} \tag{5.7}$$

$$\frac{v}{J} = \frac{1}{1-(2K)^{-1}} \sin\left[\pi(1-(2K)^{-1})\right] \ , \tag{5.8}$$

where K is the LL interaction parameter, and $v|q|$ is the dispersion relation for low energy excitations. We use the above expressions for v and K in the diagonalized version of the LL Hamiltonian Eq. (5.2) to parametrize the interaction strength and velocity. We will see below that K and v are indeed the relevant parameters for describing the 1-RDM as K determines the exponent of the interaction contribution, and v is the velocity with which information spreads though the system after an interaction quantum quench.

The Hamiltonian Eq. (5.2) can be diagonalized using a Bogoliubov transformation

$$\begin{aligned} a_q &= \cosh(\theta_q) b_q + \sinh(\theta_q) b^\dagger_{-q} \\ a^\dagger_{-q} &= \sinh(\theta_q) b_q + \cosh(\theta_q) b^\dagger_{-q} \, , \end{aligned} \tag{5.9}$$

in contrast to simply diagonalizing the Hamiltonian in a basis $(b^\dagger_q, b_{-q})$ (as one would do for a fermionic BCS Hamiltonian), since this would not preserve the bosonic commutation relations [163, 164]. The choice of coefficients in Eq. (5.9) guarantees bosonic commutation relations $[a_q, a^\dagger_{q'}] = \delta_{q,q'}$, $[a_q, a_{q'}] = 0$, $[a^\dagger_q, a^\dagger_{q'}] = 0$, and one finds that

$$\begin{aligned} &\sum_q f(|q|) \frac{a^\dagger_q a_q}{\cosh^2(\theta_q) + \sinh^2(\theta_q)} \\ &= \sum_q f(|q|) b^\dagger_q b_q + f(|q|) \frac{\sinh(\theta_q)\cosh(\theta_q)}{\sinh^2(\theta_q) + \cosh^2(\theta_q)} \\ &\qquad \times \left(b_q b_{-q} + b^\dagger_q b^\dagger_{-q} \right) \, . \end{aligned} \tag{5.10}$$

Choosing $f(|q|) = \omega_0(q) + m(q)$ and $\tanh(2\theta_q) = g_2(q)/f(|q|)$, which in the limit $q \to 0$ is given by $g_2/(v_F + g_4)$, the Hamiltonian becomes diagonal

$$H = \sum_q \omega(q) a^\dagger_q a_q \tag{5.11}$$

$$\omega(q) = \sqrt{[\omega_0(q) + m(q)]^2 - g_2(q)^2} \equiv v|q| \, . \tag{5.12}$$

This allows us to evaluate the ground state expectation values

$$\langle a^\dagger_q a_{q'} \rangle = \delta_{qq'} f_b(q) \tag{5.13}$$

$$\langle a_q a_{q'} \rangle = 0 = \langle a^\dagger_q a^\dagger_{q'} \rangle \, , \tag{5.14}$$

where $f_b(q)$ is the Bose-Einstein distribution function with energies $\omega(q)$.

Using Eq. (5.3) in Eq. (5.5) together with the Baker-Hausdorff formula $e^A e^B = e^{A+B} e^{[A,B]/2}$, the one point correlation function becomes

$$C_\alpha(x,0) = \frac{1}{2\pi\eta} e^{\alpha \frac{\pi x}{L}[N_\alpha, \varphi_{0,\alpha}]} e^{\frac{1}{2}[\phi_\alpha(x), \phi_\alpha(0)]} \left\langle e^{\imath(\phi_\alpha(x) - \phi_\alpha(0))} \right\rangle . \tag{5.15}$$

Here, we use the boson cummulant formula $\left\langle e^{\imath(\phi_\alpha(x) - \psi_\alpha(0))} \right\rangle = e^{-\frac{1}{2}\langle(\phi_\alpha(x) - \psi_\alpha(0))^2\rangle}$, which is valid at equilibrium for a quadratic Hamiltonian, for any linear combination of bosons $\sum_n A_n b_n + B_n b_n^\dagger$. In addition,

$$\frac{1}{2}[\phi_\alpha(x), \phi_\alpha(0)] = \frac{1}{2} \sum_{q>0} \frac{2\pi}{qL} \left[e^{-q\imath(-\imath\eta - \alpha x)} - e^{-\imath q(-\imath\eta + \alpha x)} \right] . \tag{5.16}$$

Due to the regularization η, we can perform the q sum, where we use that for any complex number z with $\mathrm{Im}[z] > 0$ holds [46]

$$\sum_{q>0} \frac{2\pi}{qL} e^{-\imath q z} = -\ln\left[1 - e^{-\imath \frac{2\pi}{L} z}\right] \tag{5.17}$$

$$= -\ln\left[2\imath e^{-\imath \frac{\pi}{L} z} \sin\left(\frac{\pi}{L} z\right)\right] . \tag{5.18}$$

One needs to be careful when using logarithm laws with complex numbers, as we need to stay on the main branch of the logarithm: $\ln(z) = \ln(|z|) + \imath \arg(z)$. With this in mind, we find for Eq. (5.16)

$$\begin{aligned} \frac{1}{2}[\phi_\alpha(x), \phi_\alpha(0)] = \frac{1}{2}\Big\{ & -\ln\left[2\imath e^{-\imath \frac{\pi}{L}(-\alpha x - \imath\eta)} \sin\left(\frac{\pi}{L}(\alpha x + \imath\eta)\right)\right] \\ & + \ln\left[-2\imath e^{\imath \frac{\pi}{L}(-\alpha x + \imath\eta)} \sin\left(\frac{\pi}{L}(\alpha x - \imath\eta)\right)\right] \Big\} \end{aligned} \tag{5.19}$$

$$= -\frac{1}{2} \ln \left| \frac{\sin\left(\frac{\pi}{L}(\alpha x + \imath\eta)\right)}{\sin\left(\frac{\pi}{L}(\alpha x - \imath\eta)\right)} \right|$$

$$- \imath \arg\left[\sin\left(\frac{\pi}{L}(\alpha x + \imath\eta)\right)\right] - \imath\frac{\pi}{2} - \imath\frac{\pi}{L}\alpha x . \tag{5.20}$$

In the limit $\eta/x \to 0$, the arg term is o for $\alpha x > 0$ and $\pm\pi$ if $\alpha x < 0$ such that

$$\lim_{\eta/x\to 0} e^{\frac{1}{2}[\phi_\alpha(x),\phi_\alpha(0)]} = -\mathrm{sgn}(\alpha x)\imath e^{-\imath\frac{\pi}{L}\alpha x} \,. \tag{5.21}$$

In order to evaluate the expectation value in Eq. (5.15) by using the boson cummulant formula, we need the expectation values $\langle\phi_\alpha(x)\phi_\alpha(x')\rangle$. To compute them by utilizing the expectation values Eq. (5.13), we insert the inverse of the transformation Eq. (5.9) into the expression for $\phi_\alpha(x)$, Eq. (5.4), such that

$$\begin{aligned}\phi_\alpha(x) = -\sum_{q>0}\sqrt{\frac{2\pi}{qL}}e^{-q\eta/2}\Big[e^{\imath\alpha qx}\left(\cosh(\theta_q)a_q - \sinh(\theta_q)a^\dagger_{-q}\right)\\ + e^{-\imath\alpha qx}\left(\cosh(\theta_q)a^\dagger_q - \sinh(\theta_q)a_{-q}\right)\Big] \,.\end{aligned} \tag{5.22}$$

Using the expectation values of pairs for a_q operators with $\langle a^\dagger_q a_{q'}\rangle = \delta_{qq'}f_b(q)$, we find

$$\begin{aligned}\langle\phi_\alpha(x)\phi_\alpha(x')\rangle = \sum_{q>0}\frac{2\pi}{qL}e^{-q\eta}\times\Big\{e^{\imath\alpha(x-x')}\left[(1-f_b(q))\cosh^2(\theta_q) + f_b(q)\sinh^2(\theta_q)\right]\\ + e^{-\imath\alpha(x-x')}\left[f_b(q)\cosh^2(\theta_q) + (1-f_b(q))\sinh^2(\theta_q)\right]\Big\}.\end{aligned} \tag{5.23}$$

At zero temperature, the Bose-Einstein distribution becomes $f_b(q>0) = 0$, such that we find for the exponent appearing in the correlation function

$$\begin{aligned}-\frac{1}{2}\langle(\phi_\alpha(x)-\phi_\alpha(0))^2\rangle = \frac{1}{2}\sum_{q>0}\frac{2\pi}{qL}e^{-q\eta}\left(\cosh^2(\theta_q)+\sinh^2(\theta_q)-1+1\right)\\ \times\left[-2+e^{\imath\alpha qx}+e^{-\imath\alpha qx}\right] \,.\end{aligned} \tag{5.24}$$

Here, we added a zero $(-1+1)$ to separate the free term (5.18) from the interaction term of the correlation function. Including the -1 in the interaction term ensures that it vanishes in the non-interacting case where $\theta_q \to 0$. We now precisely define the interaction cutoff ε by using it to describe the q dependence of the interaction

term as [47]

$$\cosh^2(\theta_q) + \sinh^2(\theta_q) - 1 \approx \frac{K + K^{-1} - 2}{2} e^{-\varepsilon|q|} \tag{5.25}$$

$$\equiv \gamma_{\mathrm{eq}}^2 e^{-\varepsilon|q|} \,, \tag{5.26}$$

where now $K = \lim_{q\to 0} e^{2\theta_q}$ and γ_{eq} are independent of q. While ε appears to be a free parameter of the model, we will show later that for not too strong interactions, a fixed value can be chosen such that the analytic calculation reproduces numerical results from exact diagonalization and DMRG for a range of interaction strengths. In addition, ε regularizes the interaction part of the correlation function and therefore allows us to take the limit $\eta q \to 0$ when keeping εq finite.

At zero temperature, we use Eq. (5.18) to perform the q sums in Eq. (5.24), and find

$$\begin{aligned} F_\alpha^0(x;\eta) &\equiv -\frac{1}{2}\langle(\phi_\alpha(x) - \phi_\alpha(0))^2\rangle_0 \\ &= \frac{1}{2}\sum_{q>0} \frac{2\pi}{qL} e^{-\imath q(-\imath\eta)} \left[-2 + e^{\imath\alpha q x} + e^{-\imath\alpha q x}\right] \qquad (5.27) \\ &= \ln\left[-2\imath e^{-\frac{\pi}{L}\eta} \sin\left(\frac{\pi}{L}\imath\eta\right)\right] - \frac{1}{2}\ln\left[2\imath e^{-\imath\frac{\pi}{L}(\alpha x - \imath\eta)} \sin\left(\frac{\pi}{L}(\alpha x - \imath\eta)\right)\right] \\ &\quad - \frac{1}{2}\ln\left[2\imath e^{-\imath\frac{\pi}{L}(\alpha x + \imath\eta)} \sin\left(\frac{\pi}{L}(\alpha x + \imath\eta)\right)\right] \,, \qquad (5.28) \end{aligned}$$

such that the interaction term can be obtained from the free one by multiplying with a factor γ_{eq}^2 while changing the regularization to include the interaction cutoff, i.e. $\eta \to \eta + \varepsilon$,

$$-\frac{1}{2}\left[\langle(\phi_\alpha(x) - \phi_\alpha(0))^2\rangle - \langle(\phi_\alpha(x) - \phi_\alpha(0))^2\rangle_0\right] = \gamma_{\mathrm{eq}}^2 F_\alpha^0(x;\eta+\varepsilon) \,. \tag{5.29}$$

We use this and the translational invariance of the expectation value, i.e. $\langle\phi_\alpha(x)\phi(x')\rangle = \langle\phi_\alpha(x-x')\phi(0)\rangle$, to obtain the expectation value that appears

in the one point correlation function

$$e^{-\frac{1}{2}\langle(\phi_\alpha(x)-\phi_\alpha(0))^2\rangle} = \frac{-\imath \sin\left(\frac{\pi}{L}\imath\eta\right)}{\left|\sin\left(\frac{\pi}{L}\left(\alpha x+\imath\eta\right)\right)\right|}\left[\frac{\imath \sin\left(\frac{\pi}{L}\imath(\eta+\varepsilon)\right)}{\left|\sin\left(\frac{\pi}{L}\left(\alpha x+\imath(\eta+\varepsilon)\right)\right)\right|}\right]^{\gamma_{\rm eq}^2}. \tag{5.30}$$

Using Eq. (5.21) and Eq. (5.30) in the expression for the correlation function Eq. (5.15), taking the limit $\eta/x, \eta/L \to 0$, where $\sin(\pi\imath\eta/L)/\eta \to \pi\imath/L$, $\imath\sin(\imath b) = -|\sin(\imath b)|$, and $\sqrt{\sin(b+\imath c)\sin(-b+\imath c)} = \imath|\sin(b+\imath c)|$, we find

$$\begin{aligned} C_\alpha(x,0) &= \frac{\imath\pi}{2\pi L}\frac{\mathrm{sgn}(\alpha x)}{\left|\sin\left(\frac{\pi}{L}(\alpha x)\right)\right|}\left|\frac{\sin\left(\frac{\pi}{L}\imath\varepsilon\right)}{\sin\left(\frac{\pi}{L}\left(\alpha x+\imath\varepsilon\right)\right)}\right|^{\gamma_{\rm eq}^2} \\ &= \frac{\alpha\imath}{2\sin(\pi x/L)}\left|\frac{\sin(\pi\imath\varepsilon/L)}{\sin\left(\frac{\pi}{L}\left(x+\imath\varepsilon\right)\right)}\right|^{\gamma_{\rm eq}^2}. \end{aligned} \tag{5.31}$$

Using that $\alpha = -1$ for left movers and $\alpha = +1$ for right movers, we obtain the full one body density matrix Eq. (5.5)

$$\rho_1(x,0) = \rho_1^0(x,0)\left|\frac{\sin(\pi\imath\varepsilon/L)}{\sin\left(\frac{\pi}{L}\left(x+\imath\varepsilon\right)\right)}\right|^{\gamma_{\rm eq}^2} \tag{5.32}$$

$$\rho_1^0(x,0) = \frac{1}{N}\frac{\sin(k_F x)}{L\sin(\pi x/L)}. \tag{5.33}$$

We show in Appendix E that Eq. (5.33) is equivalent to the exact one body density matrix for non-interacting lattice fermions. Because x is a relative coordinate and we are interested in the short distance behavior that dominates the Fourier transform and the entropy, we consider the limit of large L with $x/L \ll 1$ and neglect terms of order $\mathcal{O}(x/L)$. For the leading term $L\sin(\pi x/L) \to \pi x$ we then arrive at the following expression for the one body density matrix:

$$\rho_1(x,0) = \frac{\sin(k_F x)}{N\pi x}\left(\frac{\varepsilon^2}{x^2+\varepsilon^2}\right)^{\gamma_{\rm eq}^2/2} + \mathcal{O}\left(\frac{x}{L}\right), \tag{5.34}$$

which is normalized such that $L\rho_1(0,0) = 1$ where $k_F = \pi N/L$. Because the particle number N appears explicitly in the normalization, we cannot directly take the thermodynamic limit. Therefore, we first compute the entropy density, and only then take the thermodynamic limit $1/N \to 0$. To diagonalize $\rho_1(x,0)$, we compute the Fourier transform which yields

$$\begin{aligned}\rho_1(q) &= \int_{-\infty}^{\infty} dx\, \rho_1(x,0) e^{-\imath q x} \\ &= \frac{\Gamma[\frac{1}{2}(-1+\gamma_{\mathrm{eq}}^2)]\sqrt{\pi}}{2\pi N \Gamma(\gamma_{\mathrm{eq}}^2/2)} \left[f_1(\tilde{q}) + f_1(-\tilde{q})\right] \\ &\quad - \frac{2\Gamma(-\gamma_{\mathrm{eq}}^2)\sin\left(\pi\gamma_{\mathrm{eq}}^2/2\right)}{2\pi N} \left[f_2(\tilde{q}) + f_2(-\tilde{q})\right] \end{aligned} \tag{5.35}$$

where $\tilde{q} = \varepsilon q$, $\tilde{k}_F = \varepsilon k_F$, $L/(2\pi)\int dq\, \rho_1(q) = 1$, and

$$\begin{aligned} f_1(\bar{q}) &= (\tilde{k}_F + \tilde{q})\, {}_1F_2\left[\left\{\frac{1}{2}\right\}, \left\{\frac{3}{2}, \frac{3-\gamma_{\mathrm{eq}}^2}{2}\right\}, \frac{1}{4}(\tilde{k}_F+\tilde{q})^2\right] \\ f_2(\tilde{q}) &= (\tilde{k}_F + \tilde{q})|\tilde{k}_F + \tilde{q}|^{\gamma_{\mathrm{eq}}^2 - 1} \\ &\quad \times {}_1F_2\left[\left\{\frac{\gamma_{\mathrm{eq}}^2}{2}\right\}, \left\{\frac{1+\gamma_{\mathrm{eq}}^2}{2}, \frac{2+\gamma_{\mathrm{eq}}^2}{2}\right\}, \frac{1}{4}(\tilde{k}_F+\tilde{q})^2\right]. \end{aligned}$$

Here, ${}_pF_q$ are the generalized hypergeometric functions. From the Fourier transformed one body density matrix $\rho_1(q)$ we obtain the fermionic distribution function as $N\rho_1(q)$, which in the absence of interactions $\gamma_{\mathrm{eq}} = 0$ reduces to a step function $\theta(|q| - k_F)$, and in presence of interactions decays like a power law (see Fig. 5.4).

Using that the 1-RDM is diagonal in Fourier space, we can directly compute the one-particle Rényi entanglement entropy

$$S_\alpha = \frac{1}{1-\alpha} \ln\left(\frac{N}{2k_F}\int dq\, \rho_1(q)^\alpha\right) \tag{5.36}$$

$$S_1 = -\frac{N}{2k_F}\int dq\, \rho_1(q) \ln \rho_1(q)\,, \tag{5.37}$$

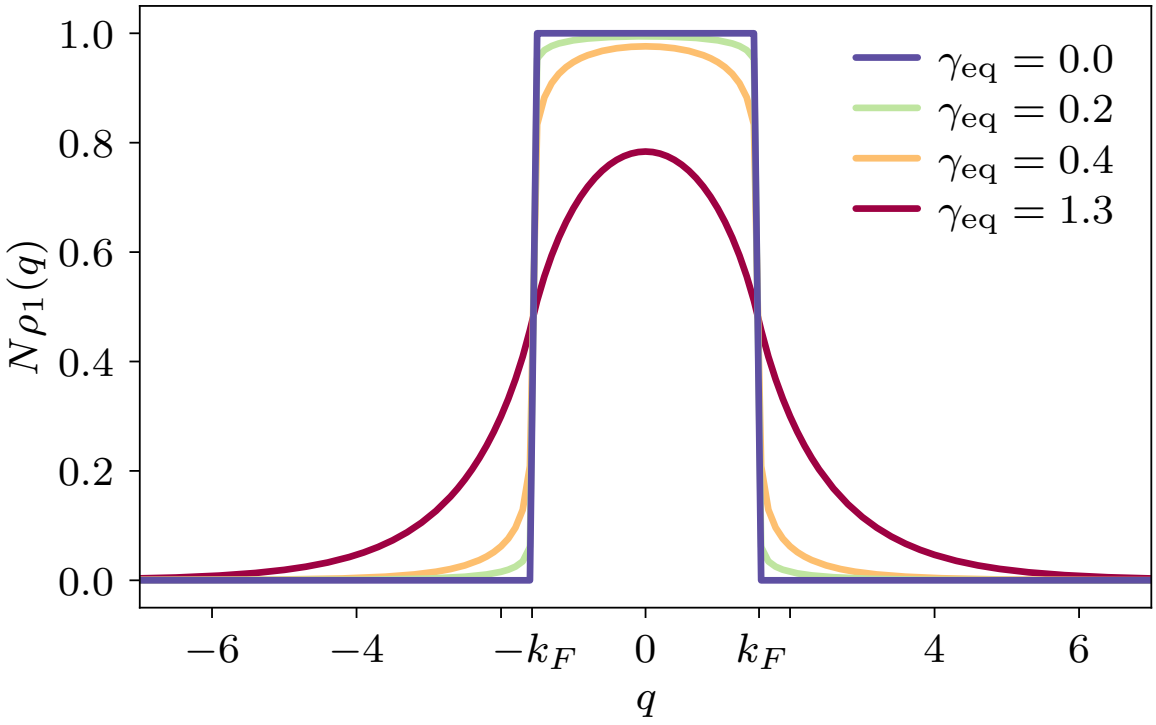

Figure 5.4: Distribution function $N\rho_1(q)$, Eq. (5.35), obtained from the $x/L \ll 1$ limit of the one body reduced density matrix in the Luttinger liquid model for a fixed interaction cutoff $\varepsilon = 0.84$ and various interaction strengths V/J. Without interactions, $\gamma_{\mathrm{eq}} = 0$, the distribution function is a step function up at the Fermi momenta $k_F = \pm\pi/2$.

where $\alpha = 1$ is the von Neumann entropy, and the factor $N/(2k_F) = (2\pi/L)^{-1}$ originates from turning the sums into integrals in the limit of large L. When comparing to numerical results, we additionally subtract the entropy for free fermions S_{ff}.

In the absence of interactions, $\gamma_{\text{eq}} = 0$, the one-body density is given by $\varrho_1^0(x,0)$ in Eq. (5.33). Performing the Fourier transform, we recover the expected zero temperature distribution function

$$N\varrho_1^0(q) = \theta(|q| - k_F) \, . \tag{5.38}$$

Using this expression in Eq. (5.37), one finds the free fermion von Neumann entropy [85, 86, 89, 117, 155, 165, 166]

$$S_{\text{ff}} = -\frac{N}{2k_F}\int_{-k_F}^{k_F} dq \, \frac{1}{N} \ln \frac{1}{N} = \ln(N) \, . \tag{5.39}$$

The same one-particle entanglement entropy is obtained for any other Rényi power $\alpha > 1$ [89], which can be seen from Eq. (5.36)

$$S_{\alpha,\text{ff}} = \frac{1}{1-\alpha} \ln \left(\frac{N}{2k_F} \int_{-k_F}^{k_F} dq \, \frac{1}{N^\alpha} \right) = \frac{1}{1-\alpha} \ln \frac{1}{N^{\alpha-1}} = \ln(N) = S_{\text{ff}} \, . \tag{5.40}$$

5.3 Numerical Results for Equilibrium 1-Particle Entanglement

To study how well the low energy field theory approach describes the J-V model in Eq. (2.53) in the LL phase and to fix the interaction cutoff, we perform a series of numerical calculations on finite sized systems. The software needed to reproduce all results is open source and has been made available online [167].

We first utilize exact diagonalization (ED), where we construct all $\binom{2N}{N}$ basis states for a lattice with $L = 2N$ sites and N fermions to determine the

corresponding matrix elements of Eq. (2.53) and construct the Hamiltonian as a sparse matrix. We then use the Lanczos algorithm [95] to determine the ground state $|\Psi_0\rangle$, from which the full density matrix can be determined as $\rho = |\Psi_0\rangle \langle\Psi_0|$. The reduced one-body density matrix is obtained by fixing one coordinate in the anti-symmetrized many particle wave function $\Psi_0(i_1, ..., i_N) = \langle i_1, ..., i_N|\Psi_0\rangle$ and tracing out the other $N-1$ particle positions [87]

$$\rho_1^{i_1,j_1} = \sum_{\substack{i_2,...,i_N \\ j_2,...,j_N}} \Psi_0^*(i_1, ..., i_N)\Psi_0(j_1, ..., j_N) \,. \tag{5.41}$$

As a second numerical approach, we consider approximate methods that allow us to consider much larger systems. For this, we obtain the ground state $|\Psi_0\rangle$ using DMRG, and the implementation of states as matrix product states (MPS) in `ITensors.jl` [119] allows us to directly compute the reduced one body density via

$$\rho_1^{i_1,j_2} = \frac{1}{N} \langle\Psi_0| \, c_{i_1}^\dagger c_{j_1} \, |\Psi_0\rangle \;, \tag{5.42}$$

where $c_i^\dagger$ is the creation operator on lattice site i.

From the reduced density matrix, we compute the one-particle Rényi entanglement entropy for Rényi index α using

$$S_\alpha = \frac{1}{1-\alpha} \ln(\mathrm{Tr}[\rho_1^\alpha]) \,, \tag{5.43}$$

where the von Neumann entropy is obtained as the limit $\alpha \to 1$:

$$S_1 = \mathrm{Tr}[\rho_1 \ln(\rho_1)] \,. \tag{5.44}$$

5.3.1 *Symmetry Decomposition of the Lattice Hamiltonian*

While ED provides approximation-free access to the ground state, scaling of the size of the Hamiltonian $\propto \binom{2N}{N}$ makes it prohibitive to consider systems with

$L \gtrsim 40$. Using a series of optimizations, we are able to compute one particle entanglement entropies with ED for systems with up to $N = 19$ fermions with 1TB of system memory. The crucial factor for reducing the complexity of the problem is the use the symmetries of the Hamiltonian Eq. (2.53), which we define below by their action on the occupation numbers of the states. We discuss the action of the symmetry operators on the fermion operators $c_i, c_i^\dagger$ in greater detail in the appendix. [†]

Translation symmetry

Translation symmetry T which moves each fermion one site to the right, *e.g.* $T|011001\rangle = |101100\rangle$, commutes with the Hamiltonian, $[H, T] = 0$, due to the boundary conditions, which allows us to group basis states in symmetry cycles such that each state of a cycle ν is mapped onto another state in the same cycle by T. Choosing one state $|\varphi_\nu\rangle$ from each cycle, the so-called cycle leader, we can define new basis states as linear combinations

$$|\phi_{\nu,q}\rangle = \frac{1}{\sqrt{M_\nu}} \sum_{m=1}^{M_\nu} e^{\imath \frac{2\pi q}{M_\nu}(m-1)} T^{m-1} |\varphi_\nu\rangle \ , \tag{5.45}$$

where M_ν is the length of cycle ν with $T^{M_\nu} = 1$ within the cycle. Because T commutes with H, the Hamiltonian becomes block diagonal when sorting the basis states according to the values of q. The main advantage of using this basis is that the ground state always lies in the $q = 0$ block [96], and it is therefore sufficient to compute and store only this single block, reducing the size of the required basis roughly by a factor of $1/L$.

Particle-hole symmetry

At half filling, the particle-hole operator P, which flips all occupation numbers $P|101001\rangle = |010110\rangle$ is another symmetry of the Hamiltonian which also

[†]For details, refer to the published work [92].

commutes with the translation operator, $[T, P] = 0$. Because $P^2 = 1$, the particle-hole operator has eigenvalues $n_P = \pm 1$. If $P\left|\phi_{\tilde{v},q}\right\rangle$ lies in a different cycle than $\left|\phi_{\tilde{v},q}\right\rangle$, we can use P to further subdivide the $q = 0$ block by using the projection $(1 \pm P)/\sqrt{2}$ onto its eigenstates

$$\left|\theta_{\tilde{v},q,n_P=\pm 1}\right\rangle = \frac{1}{\sqrt{2}}\left(\left|\phi_{\tilde{v},q}\right\rangle \pm P\left|\phi_{\tilde{v},q}\right\rangle\right) \ . \tag{5.46}$$

Reflection symmetry

The third symmetry we exploit is spatial inversion R, which reflects the occupation numbers $R\left|011011\right\rangle = \left|110110\right\rangle$ about a site and commutes with the Hamiltonian $[R, H] = 0$. However, in general, R does not commute with T, but fortunately in the $q = 0$ block translation and spatial inversion do commute. Since $R^2 = 1$, the eigenvalues are also given by $n_R = \pm 1$ and the projection operator is $(1 \pm R)/\sqrt{2}$. If R maps either $\left|\phi_{v,q}\right\rangle$ or $\left|\theta_{\tilde{v},q,n_P}\right\rangle$ into another cycle, projecting onto eigenstates of R further subdivides the $q = 0$ block of the Hamiltonian in analogy to Eq. (5.46).

We therefore only need to construct the $q = 0$, $n_R = +1$, $n_P = +1$ block of the Hamiltonian which is a major reduction in memory and time complexity for obtaining the ground state. We can further use translation symmetry in a similar way to reduce the computational effort when computing the reduced density matrix from the ground state. In addition, for our ED implementation, we encode states using a 64bit integer basis, where each bit of the binary representation of an integer represents the occupation number of the site at the corresponding position [168]. This has the advantage that symmetry operation can be implemented very efficiently using low-level bit operations and that we avoid all overhead of using vectors containing the occupation numbers for each state.

By forcing the ground state to be orthogonal to these states, we are able to consider systems with sizes $N = 51$ or larger at half filling with periodic boundary conditions. Fig. 5.5 shows the 1-particle entanglement entropy (crosses) calculated with DMRG for $N = 51$ for a large range of interaction strengths spanning all phases in the J-V model. For $V/J = -2$, the first order phase transition is clearly visible and $S_\alpha - S_{\text{ff}}$ remains stable, reaching the theoretical value $\ln(2)$ [33] for large negative V/J. For free fermions, where $V/J = 0$ in the LL phase, the one-particle entanglement entropy vanishes as expected [33]. Additionally, at the second-order phase transition into the charge density wave phase near $V/J = 2$, a change in the slope of the entropy is visible, which then slowly approaches the theoretical value $\ln(2)$ [33].

For comparison with field theory, we first estimate the thermodynamic limit $N \to \infty$ by finite size scaling of the numerical results for the one-particle entanglement entropy, with a general scaling form introduced by Haque *et al.* [33] and confirmed in subsequent works [91, 93]:

$$S_\alpha(N, V/J) = \ln(N) + A_\alpha(V/J) + \mathcal{O}(N^{-\lambda}) \,, \tag{5.47}$$

with $\lambda > 0$. In subsequent figures, we will focus on the behavior of the constant correction $A_\alpha(V/J)$ to the leading order logarithmic scaling.

For reliable finite size scaling, we calculate $S_\alpha - S_{\text{ff}}$ for systems with $N = 2, 3, \ldots, 19$ fermions using ED and fermion numbers between $N = 17$ and $N = 51$ using DMRG and then extrapolate linearly to $1/N \to 0$ (white filled circles in Fig. 5.5). We find very good $1/N$ scaling and excellent agreement between exact ED (colored circles in Fig. 5.5) and approximate DMRG (crosses in Fig. 5.5) everywhere in the LL phase.

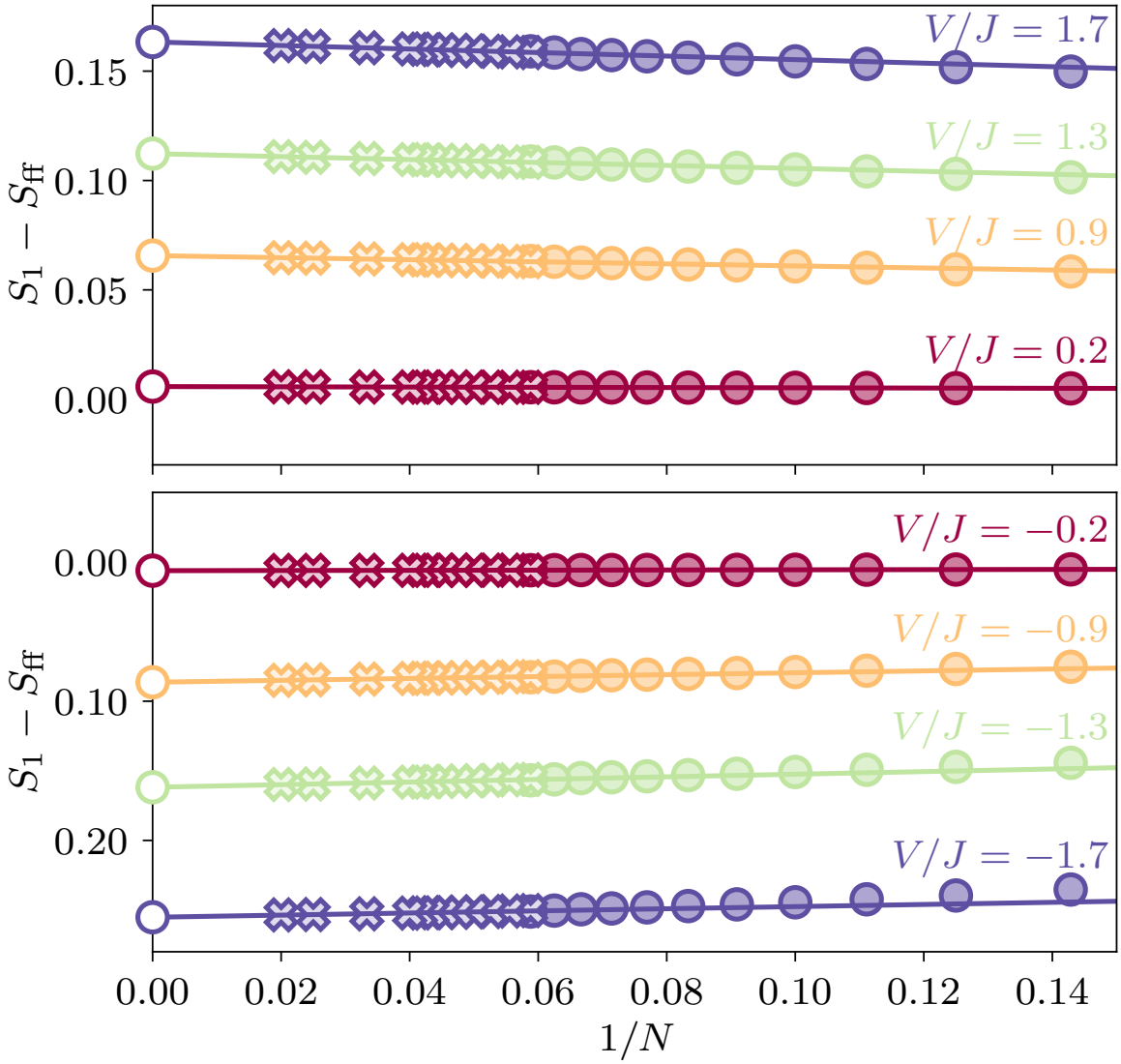

Figure 5.5: Finite size scaling of the equilibrium one-particle von Neumann entanglement entropy S_1 for various interaction strengths V/J where the free fermion contribution S_{ff} has been subtracted. Results obtained with DMRG (crosses) and ED (circles) are shown together along with a linear extrapolation to the thermodynamic limit $1/N \to 0$. ED provides access to lattices at half filling with up to $N = 19$ fermions and using DMRG lattices with more than $N = 51$ fermions can be studied.

5.4.1 *Comparison with Luttinger Liquid Theory*

We perform this finite size scaling for all calculated interaction strengths V/J and plot the constant contribution to the 1-particle entanglement entropies (A_α, circles) as a function of V/J in Fig. 5.6 along with the numerically integrated Luttinger liquid result from Eq. (5.35) and Eq. (5.43) (dashed lines) for a fixed interaction cutoff $\varepsilon = 0.84$ determined via fitting. We find excellent agreement between LL theory with this fixed cutoff and numerical results for the J-V model for small to moderate interaction strengths $-0.5 < V/J < 1.5$. Close to the phase transitions and especially for large negative interaction strengths $V/J \to -2$, where $\gamma_{\text{eq}} \to \infty$, significant deviations from the low energy LL theory are apparent.

To systematically study for which interactions the J-V model can be accurately described by the LL model, we fit the bosonization prediction for each interaction strength individually to the finite size scaled data for the von Neumann entropy $A_1(V/J)$ as defined in Eq. (5.47), to determine an effective interaction cutoff $\varepsilon_{\text{fit}}(V/J)$ (red circles in the main panel of Fig. 5.7). We find an extended region with $\varepsilon = 0.84$ (dashed, black line) for small negative and positive interactions V/J where the cutoff has minimal dependence on the interaction strength. With the obtained effective cutoff, we can fit the LL model at every point in the LL phase to the J-V model with excellent agreement as shown in the inset of Fig. 5.7 where we plot the 1-particle entanglement entropies from numerics and for the effective interaction cutoff ε_{fit}. An interaction dependent cutoff for large interactions is also a consequence of approximating the q dependence of the exponent γ_{eq} by the cutoff $e^{-\varepsilon|q|}$ in field theory calculations (see Eq. (5.26)) in order to make the q sums analytically tractable.

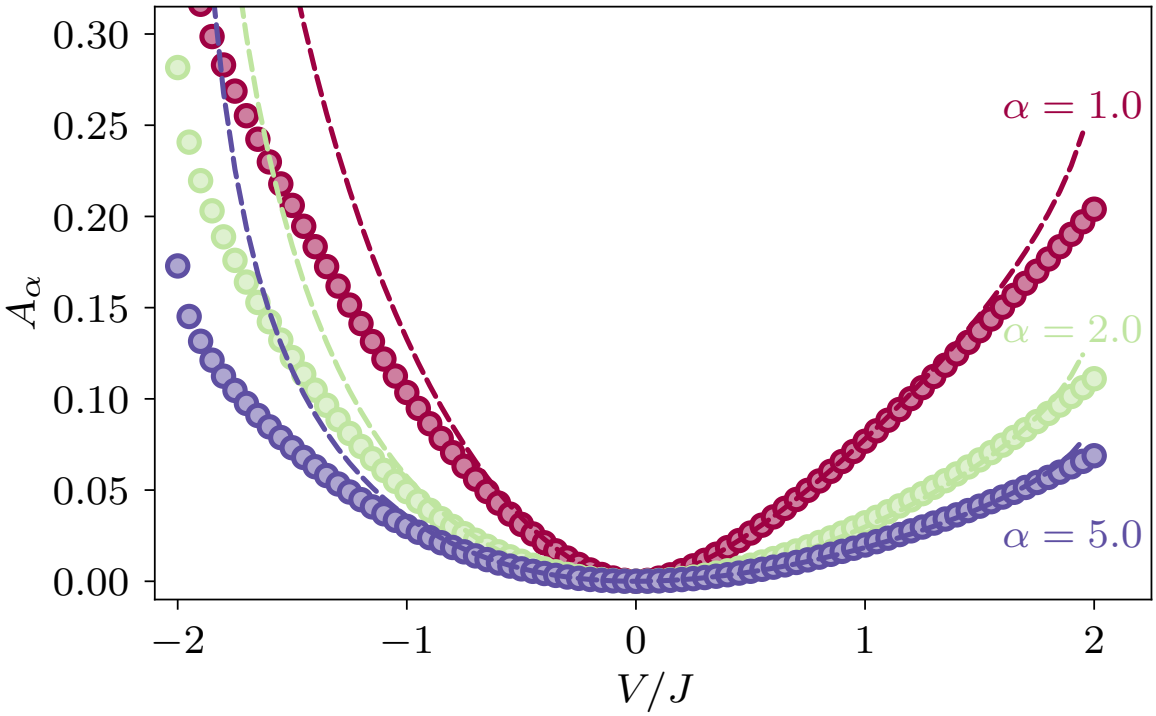

Figure 5.6: Interaction strength V/J dependence of the constant contribution to the 1-particle Rényi entanglement entropies extrapolated to the thermodynamic limit A_α for Rényi indices $\alpha = 1, 2$, and 5 together with the prediction from bosonization for a fixed interaction cutoff $\varepsilon = 0.84$. We find very good agreement between the Luttinger liquid prediction and the numerical results for the J-V model in region $V/J \in [-0.5, 1.5]$.

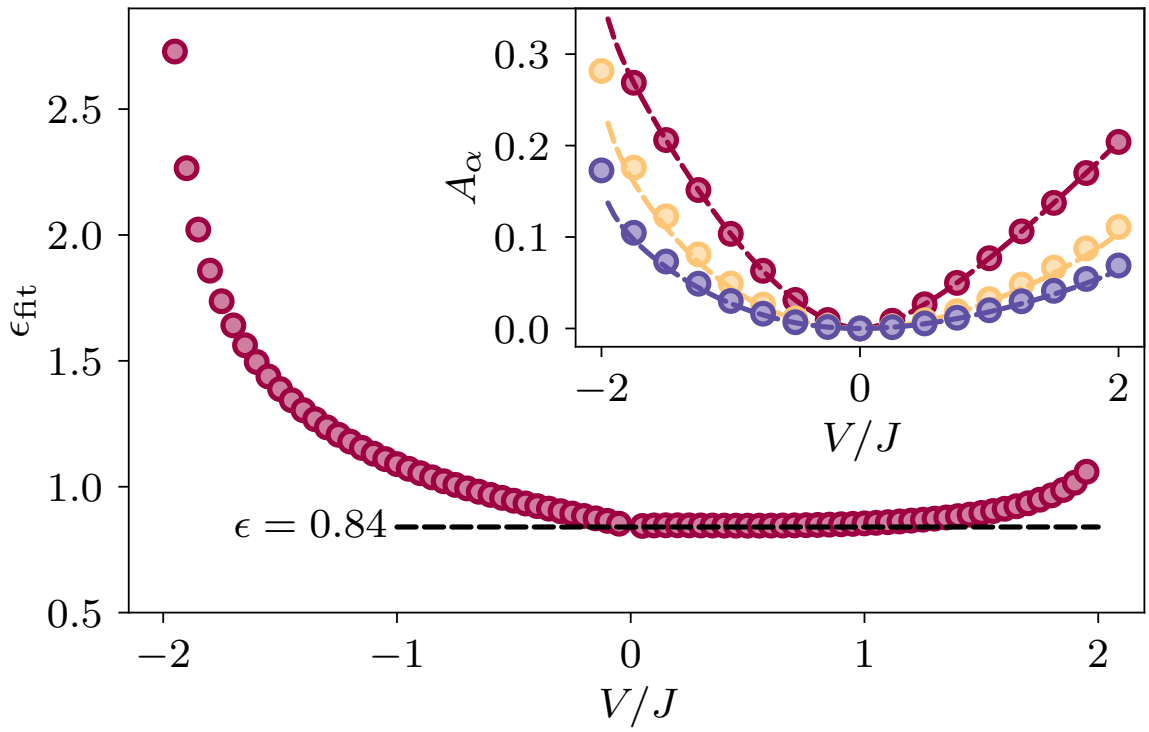

Figure 5.7: Effective interaction cutoff $\varepsilon_{\mathrm{fit}}$ as a function of the interaction strength V/J (red circles) obtained by fitting the Luttinger liquid prediction for the one-particle von Neumann entanglement entropy for each interaction strength individually to the numerical data of the J-V model. We find an extended flat region of the effective cutoff $\varepsilon = 0.84$ (dashed, black line) that is nearly independent of interaction strength. The inset depicts numerical results for the Rényi entropies with $\alpha = 1$ (red circles), $\alpha = 2$ (yellow circles), and $\alpha = 5$ (blue circles) together with the field theory prediction using the fitted interaction dependent cutoff $\varepsilon_{\mathrm{fit}}$.

5.5 1-Particle entanglement entropy after a quantum quench

We next consider free fermions for $t < 0$ and suddenly turn on the V/J interaction at $t = 0$, so that the J-V Hamiltonian for this quench is given by

$$H = -J \sum_{i=1}^{L} (c_{i+1}^{\dagger} c_i + c_i^{\dagger} c_{i+1}) + V(t) \sum_{i=1}^{L} n_i n_{i+1} \,, \tag{5.48}$$

with $V(t) = \theta(t)V$. This allows us to study the growth and spread entanglement entropy after the quench by considering the difference $S_\alpha - \ln(N)$, in which the entropy of free fermions is subtracted. We again start by computing the one body density

$$\rho_1(x, 0; t) = \frac{1}{N} \left[e^{-\imath k_F x} C_+(x, 0; t) + e^{\imath k_F x} C_-(x, 0; t) \right] \tag{5.49}$$

$$C_\alpha(x, 0; t) = \langle \psi_\alpha^{\dagger}(x, t) \psi_\alpha(0, t) \rangle \tag{5.50}$$

in the LL model

$$H = \sum_q \left[\omega_0(q) + m(q, t) \right] b_q^{\dagger}(t) b_q(t) + \frac{1}{2} \sum_q g_2(q, t) \left(b_q(t) b_{-q}(t) + b_q^{\dagger}(t) b_{-q}^{\dagger}(t) \right) \,, \tag{5.51}$$

where in this case $g_2(q, t) = \theta(t) g_2(q) = \theta(t) g_2 |q|$, $m(q, t) = \theta(t) g_4 |q|$, and again, $\omega_0(q) = v_F |q|$. Analogous to the equilibrium case, we can diagonalize the Hamiltonian for any fixed time $t > 0$ using the same Bogoliubov transformation Eq. (5.9) with $\tanh(2\theta_q) = g_2(q)/(\omega_0(q) + g_4(q))$, but now the operators $a_q(t)$ are

time dependent. For $t > 0$ this yields the diagonal Hamiltonian

$$H = \sum_q v|q| a_q^\dagger(t)\, a_q(t) \tag{5.52}$$

$$v = \sqrt{(v_F + g_4)^2 - g_2^2}\,. \tag{5.53}$$

Since the Hamiltonian for $t > 0$ is diagonal in the a_q operators, we can use the trivial time evolution

$$a_q(t) = e^{-\imath v|q|t} a_q\,. \tag{5.54}$$

Substituting this time evolution into the inverse of the transformation Eq. (5.9), we obtain the time evolution of the b_q operators as [47]

$$b_q(t) = w_q(t)\, b_q + u_q(t)\, b_{-q}^\dagger \tag{5.55}$$

$$\begin{aligned} w_q(t) &= \cos(v|q|t) - \imath \sin(v|q|t) \cosh\left(2\theta_q\right) \\ u_q(t) &= -\imath \sin(v|q|t) \sinh\left(2\theta_q\right)\,. \end{aligned} \tag{5.56}$$

A very important conceptual difference to the equilibrium case is that the Hamiltonian is not diagonal in the a_q operators for $t \to 0^-$, and therefore we cannot easily write down expectation values of the a_q operators. However, since H is diagonal in the b_q operators for $t \to 0^-$, we can use $b_q(t = 0) \equiv b_q$ and

$$\begin{aligned} \langle b_q^\dagger b_{q'} \rangle &= f_b(q) \delta_{q,q'} \\ \langle b_q b_{q'} \rangle &= 0 = \langle b_q^\dagger b_{q'}^\dagger \rangle\,. \end{aligned} \tag{5.57}$$

This together with the more complicated time evolution of the b_q operators Eq. (5.55) gives rise to a different exponent $\gamma \geq \gamma_{\text{eq}}$ as we show in the following. Up to Eq. (5.21) the calculation for the correlation function is analogous to the

equilibrium case such that

$$C_\alpha(x,t) = \frac{e^{\alpha\frac{\imath\pi x}{L}}}{2\pi\eta} e^{\frac{1}{2}[\phi_\alpha(x,t),\phi_\alpha(0,t)]} e^{-\frac{1}{2}\langle(\phi_\alpha(x,t)-\phi_\alpha(0,t))^2\rangle} \,. \tag{5.58}$$

The exponential $e^{\frac{1}{2}[\phi_\alpha(x,t),\phi_\alpha(0,t)]}$ is unchanged by the time dependence and is still given by Eq. (5.21). In order to evaluate $\langle\phi_\alpha(x,t)\phi_\alpha(0,t)\rangle$, we use the time evolution of the b_q operators from Eq. (5.55) in the definition of the bosonic fields

$$\begin{aligned}\phi(x,t) = -\sum_{q>0}\sqrt{\frac{2\pi}{qL}} e^{-\frac{q\eta}{2}} [e^{\imath\alpha qx}(w_q(t)b_{\alpha,q} + u_q(t)b^\dagger_{\alpha,-q}) \\ + e^{-\imath\alpha qx}(w^*_q(t)b^\dagger_{\alpha,q} + u^*_q(t)b_{\alpha,-q})] \,.\end{aligned} \tag{5.59}$$

Analogous to the equilibrium case, we use $\langle b^\dagger_q b_q\rangle = f_b(q)$, to obtain

$$\begin{aligned}\langle\phi(x,t)\phi(x',t)\rangle = &-\sum_{q>0}\frac{2\pi}{qL}e^{-q\eta} \\ &\times\Big\{e^{\imath\alpha q(x-x')}\left[(1-f_b(q))|w_q(t)|^2 + f_b(q)|u_q(t)|^2\right] \\ &+ e^{-\imath\alpha q(x-x')}\left[(1-f_b(q))|u_q(t)|^2 + f_b(q)|w_q(t)|^2\right]\Big\} \,.\end{aligned} \tag{5.60}$$

We again consider the zero temperature case with $f_b(q>0) = 0$. This allows us to rewrite the desired exponential term from Eq. (5.58) as follows

$$\begin{aligned}-\frac{1}{2}\langle(\phi_\alpha(x,t)-\phi_\alpha(0,t))^2\rangle = &\sum_{q>0}\frac{2\pi}{qL}e^{-q\eta}\left(|w_q(t)|^2 + |u_q(t)|^2\right) \\ &\times\left[-1 + \frac{1}{2}e^{\imath\alpha qx} + \frac{1}{2}e^{-\imath\alpha qx}\right] \,.\end{aligned} \tag{5.61}$$

Using $|w_q(t)|^2 + |u_q(t)|^2 = \cosh^2(2\theta_q) - \cos(2v|q|t)\sinh^2(2\theta_q)$, the above becomes

$$-\frac{1}{2}\langle(\phi_\alpha(x,t)-\phi_\alpha(0,t))^2\rangle = \sum_{q>0}\frac{2\pi}{qL}e^{-q\eta}\left(2\sin^2(v|q|t)\sinh^2(2\theta_q)+1\right) \times\left[-1+\frac{1}{2}e^{\imath\alpha qx}+\frac{1}{2}e^{-\imath\alpha qx}\right]. \tag{5.62}$$

We define the momentum dependence of interaction parameter in the quench case as

$$\sinh^2(2\theta_q) \approx \left(\frac{K-K^{-1}}{2}\right)^2 e^{-\varepsilon|q|} \equiv \gamma^2 e^{-\varepsilon|q|}. \tag{5.63}$$

The free term $\langle(\phi_\alpha(x,t)-\phi_\alpha(0,t))^2\rangle_0$ is equivalent to that in Eq. (5.28). To compute the interaction term, we need to compute the q-sum, where we can use Eq. (5.18) such that

$$\exp\left[\kappa\sum_{q>0}\frac{2\pi}{L}e^{-\imath qz(x)}\sin^2(v|q|t)\right] = \frac{[\sin\left(\frac{\pi}{L}(z(x)-2v|q|t)\right)\sin\left(\frac{\pi}{L}(z+2v|q|t)\right)]^{\kappa/4}}{\sin\left(\frac{\pi}{L}z(x)\right)^{\kappa/2}}. \tag{5.64}$$

The interaction term is then found to be

$$e^{-\frac{1}{2}\left[\langle(\phi_\alpha(x,t)-\phi_\alpha(0,t))^2\rangle-\langle(\phi_\alpha(x,t)-\phi_\alpha(0,t))^2\rangle_0\right]} \tag{5.65}$$

$$= \left|\frac{\sin\left(\frac{\pi}{L}(\imath(\eta+\epsilon))\right)}{\sin\left(\frac{\pi}{L}(\alpha x+\imath(\eta+\epsilon))\right)}\right|^{\gamma^2} \times\left|\frac{\sin\left(\frac{\pi}{L}(\alpha x+2vt+\imath(\eta+\epsilon))\right)}{\sin\left(\frac{\pi}{L}(2vt+\imath(\eta+\epsilon))\right)}\right|^{\gamma^2/2} \times\left|\frac{\sin\left(\frac{\pi}{L}(\alpha x-2vt+\imath(\eta+\epsilon))\right)}{\sin\left(\frac{\pi}{L}(-2vt+\imath(\eta+\epsilon))\right)}\right|^{\gamma^2/2}. \tag{5.66}$$

Inserting the above and Eq. (5.20) into Eq. (5.58), and taking the limit $\eta/L \to 0$, yields the correlation function for α-movers (correlations between fermions of the same species). Adding together the right and left movers as in Eq. (5.32) gives the final expression

$$\rho(x,t) = \rho_1^0(x,0) \left| \frac{\sin(\pi\imath\varepsilon/L)}{\sin(\pi(x+\imath\varepsilon)/L)} \right|^{\gamma^2} \times \left| \frac{\sin\left(\frac{\pi}{L}(x-2vt+\imath\epsilon)\right)\,\sin\left(\frac{\pi}{L}(x+2vt+\imath\epsilon)\right)}{\sin\left(\frac{\pi}{L}(-2vt+\imath\epsilon)\right)\,\sin\left(\frac{\pi}{L}(2vt+\imath\epsilon)\right)} \right|^{\gamma^2/2}. \tag{5.67}$$

The 1-RDM consists of the free part $\rho_1^0(x,0)$ Eq. (5.33), the interaction factor with exponent with $\gamma^2 \neq \gamma_{\text{eq}}^2$, and a time dependent oscillatory term with exponent $\gamma^2/2$. To obtain the one-particle entanglement entropy with Eq. (5.36), we need to numerically compute the Fourier transform of Eq. (5.67). However, we can already extract information about the time dependence from the real space correlation function. We find that the entropy obtained from the LL correlation function is strictly periodic with period $\Delta t = L/(2v)$ and plateaus centered around $t_{n,\text{plateau}} = L/(2v)(n+1/2), n \in \mathbb{N}_0$ (see inset of Fig. 5.8) corresponding to times where all sine functions turn into cosine functions in Eq. (5.67). Because the size of the plateaus is proportional to L and the time scale for increase and decrease from the plateaus is independent of L (inset Fig. 5.8), the average converges to the plateau value in the thermodynamic limit. We compute the plateau values for many system lengths by numerically Fourier transforming Eq. (5.67), evaluating the entanglement entropy at $t_{0,\text{plateau}}$, and performing finite size scaling to show the thermodynamic limit averaged entropies with blue circles in Fig. 5.8.

The steady state estimate of the entropy can also be analyzed by generalizing the scaling form introduced in Eq. (5.47) to include the post-quench waiting time:

$$A_\alpha(V/J,t) = \lim_{N\to\infty} S_\alpha(N,V/J,t) - \ln(N)\,. \tag{5.68}$$

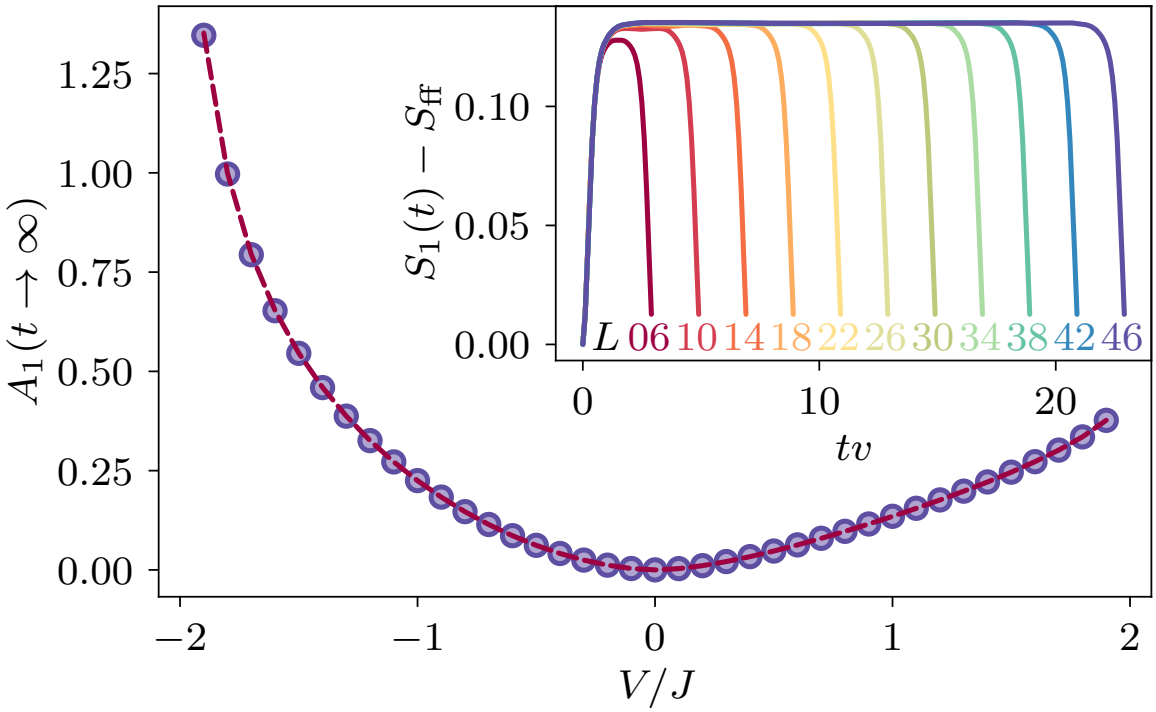

Figure 5.8: Thermodynamic limit growth of the 1-particle von Neumann entanglement entropy as a function of the interaction strength V/J after the quantum quench at $t = 0$ obtained from the Luttinger liquid steady state limit (red, dashed line) in Eq. (5.69). Blue circles show the result of finite size scaling of the plateau values shown in the inset. The inset depicts the first plateau of the entanglement entropy obtained by numerical integration from the time dependent one body density matrix in Eq. (5.67) for several system sizes $L = 2N$. We observe that the plateau size increases linearly with L while the region where the entropy increases to the plateau and the time scale where it drops from the plateau is independent of the system length. In the thermodynamic limit, the average of the entropy and the plateau values agree with each other. The main panel demonstrates that the plateau value of the entropy coincides with the entropy obtained from the steady state result for the 1-RDM in the thermodynamic limit.

Its steady state value can be obtained from the 1-RDM in the $x/L \ll 1$ limit (dashed, red line in Fig. 5.8) obtained from Eq. (5.67)

$$\rho_{t\to\infty}(x) = \frac{\sin(k_F x)}{N\pi x}\left(\frac{\varepsilon^2}{x^2+\varepsilon^2}\right)^{\gamma^2/2} + \mathcal{O}\left(\frac{x}{L}\right) , \tag{5.69}$$

similar to the equilibrium case Eq. (5.32) and Eq. (5.34) with γ_{eq} replaced by γ.

5.5.1 *Post-Quench Numerical Results*

Exact Diagonalization

We again use exact diagonalization to compute the waiting time dependence of the one-particle entanglement entropy after the quench. For this, we first obtain the ground state at $t < 0$ for free fermions $|\Psi(0)\rangle$ and compute the time evolution using the full set of eigenstates $|\Psi_\alpha\rangle$ and eigenvalues E_α for the final Hamiltonian with interaction strength V/J [87]

$$\begin{aligned} |\Psi(t)\rangle &= e^{-\imath tH}\,|\Psi(0)\rangle \\ &= \sum_\alpha e^{-\imath E_\alpha t}\,\langle\Psi_\alpha|\Psi(0)\rangle\,|\Psi_\alpha\rangle \ , \end{aligned} \tag{5.70}$$

where we can exploit that $\langle\Psi_\alpha|\Psi(0)\rangle$ is only non-zero for $|\Psi_\alpha\rangle$ from the $q = 0$ translational symmetry block. This still requires the full eigensystem of a dense block of the Hamiltonian whose size scales $\propto \binom{2N}{N}$ and a full diagonalization has a time complexity cubic in the Hamiltonian size, which limits us to a maximum of $N = 13$ fermions on the lattice. From $|\Psi(t)\rangle$, we obtain the density matrix $\rho(t) = |\Psi(t)\rangle\langle\Psi(t)|$ and trace out $N-1$ particle positions to obtain $\rho_1(|i-j|,t)$ enabling computation of the 1-particle entanglement entropy at each time t. We indeed observe the recurrence time $\Delta t = L/(2v)$ (Fig. 5.9a) predicted by the LL theory, which indicates that after the quench, density waves propagate with velocity v, (see Eq. (5.53)) through the lattice of length L, where the maximal

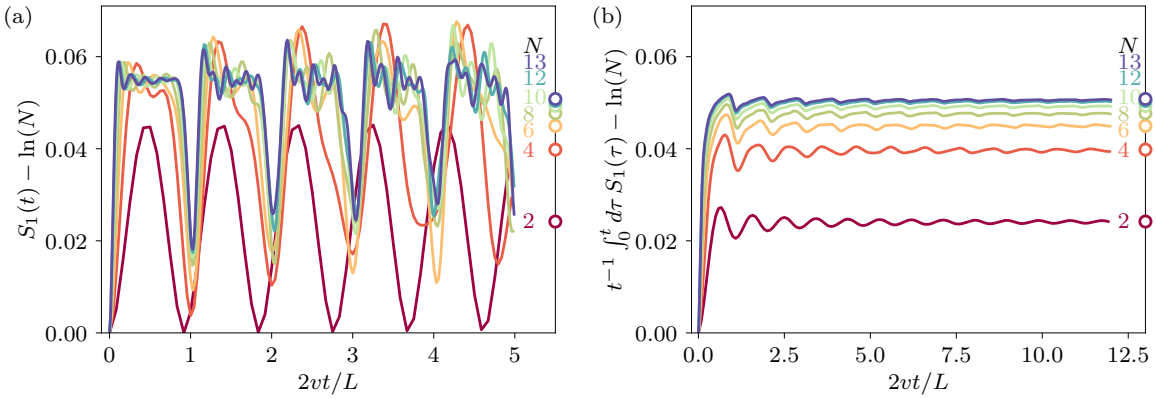

Figure 5.9: Evolution of the one-particle entanglement entropy after the quantum quench at $t = 0$ for systems with $L = 2N$ sites at an interaction strength of $V/J = -0.5$. (a) Rescaled waiting time $2vt/L$ dependence of the von Neumann entanglement entropy. (b) Running average of the von Neumann entanglement entropy depicting the convergence to the steady state entropy. We observe a steep increase of the entropy on a very short time scale after the quench and then recurrences with length N where the entropies oscillate around a constant steady state value (empty circles). The fast decrease in the distance between the steady state values with N suggests fast convergence to the thermodynamic limit.

distance between two points is $L/2$ due to the periodic boundary conditions. We show the waiting time dependence of the von Neumann entropy for several lattice sizes (solid lines) in Fig. 5.9a together with the steady state values (empty circles) obtained by averaging the entropy $S_1 - \ln(N)$ for times after the initial increase. Here, the entanglement entropy has plateaus with length proportional to L and regions, independent of the system size, where the entropy decreases and then increases to the next plateau. Convergence to the steady state can thus be understood from a running average (Fig. 5.9b), and in the thermodynamic limit, where the plateau size is infinite, the system reaches the steady state with entanglement entropy obtained by finite size scaling the entropy averages from the finite systems. Even for these relatively small systems, the fast decrease between consecutive steady state averages shows fast convergence to the thermodynamic limit. Such advantageous finite size scaling properties of the particle entanglement entropy were recently reported [87]. To estimate errors in the steady state averages, we use a blocking method [169] by consecutively averaging neighboring values in the time series and computing the error of the mean in each averaging step until it reaches a plateau. To further include errors due to the finite time step and the endpoint of the time series, we additionally divide the time series into the individual N_b recurrence blocks with entropy averages M_i and add the error of the means $\text{mean}(M_i)/\sqrt{N_b}$, as well as the difference between the mean of the entropy time series and the average of the M_i to the blocking error. To further enhance our ability to extrapolate to the thermodynamic limit post-quench, we perform time evolution using approximate methods in `ITensors.jl` [119].

Time Dependent Density Matrix Renormalization Group

To efficiently perform time evolution of the initial state obtained with DMRG as in the equilibrium case, we approximate the time evolution operator $e^{-\imath H \delta t}$ for a time

step δt by using a symmetrized second order Trotter decomposition [170, 171]

$$e^{-\imath\delta t\, H} \approx e^{-\imath\delta t\, h_{1,2}/2} e^{-\imath\delta t\, h_{2,3}/2} \dots e^{-\imath\delta t\, h_{L,1}/2} \times \\ \times\, e^{-\imath\delta t\, h_{L,1}/2} e^{-\imath\delta t\, h_{L-1,L}/2} \dots e^{-\imath\delta t\, h_{1,2}/2} + \mathcal{O}(\delta t^3)\,, \tag{5.71}$$

where $h_{i,i+1} = -J(c^\dagger_{i+1}c_i + c^\dagger_i c_{i+1}) + V n_i n_{i+1}$. To derive Eq. (5.71) the J-V Hamiltonian

$$H = \sum_{i=1}^{L} h_{i,i+1} = \sum_{i\,\text{even}} h_{i,i+1} + \sum_{i\,\text{odd}} h_{i,i+1} \equiv H_{\text{even}} + H_{\text{odd}} \tag{5.72}$$

is split into the two internally commuting parts H_{even} and H_{odd}. The commutator $[H_{\text{even}}, H_{\text{odd}}]$ is neglected, which introduces an error $\mathcal{O}(\delta t^3)$. To maintain accuracy, it is therefore necessary to chose a small time step δt such that performing time evolution for a finite time interval t can require a large number $t/\delta t$ of time consuming applications of the operator. Only by using GPUs for computing the time evolution were we able to perform the calculation for systems up to $N = 15$ fermions, which would be intractable with ED.

Finite size scaling

We compute the 1-particle entanglement entropy for different interaction strengths V/J to again linearly extrapolate to the thermodynamic limit, $1/N \to 0$, $1/L \to 0$ for fixed N/L (Fig. 5.10). In the case of small interactions, we can perform the time evolution on V100 GPUs for systems with up to $L = 30$ lattice sites, however, the ground states obtained with DMRG require more memory for larger interactions γ^2_{eq} to perform calculations to the same accuracy. While for intermediate interactions, $V/J \geq 1.3$ and $-0.9 \leq V/J < 0$, we achieve results up to $L = 28$ sites, the calculation exceeds GPU memory available to us for $L \geq 28$ in the case of very strong interactions $V/J \leq -1.3$. Nonetheless, these additional points of the 1-particle entanglement entropy obtained with the GPU accelerated

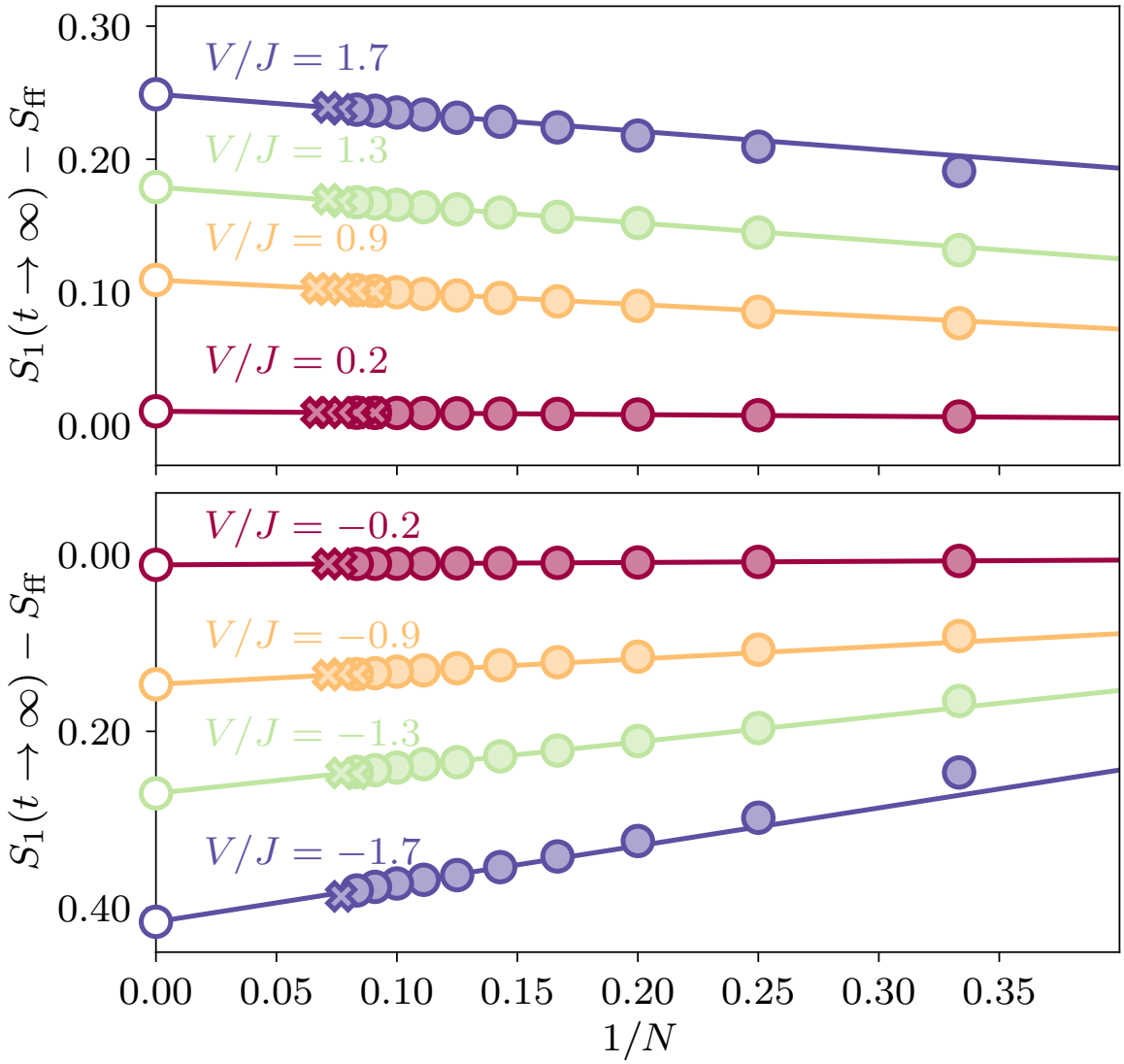

Figure 5.10: Finite size scaling of the steady state one-particle von Neumann entanglement entropy $S_1(t \to \infty)$ for various values of the post quench interaction strength V/J obtained with ED (filled circles) and with DMRG (filled crosses). We estimate the thermodynamic limit values of the entropy (empty circles) using linear extrapolation to $1/N \to 0$.

tDMRG allow for relative improvements of the thermodynamic limit extrapolation from finite size scaling by up to 1.2 % compared to using ED data alone. We find that even for these relatively small systems, linear extrapolation accurately describes the data in the whole Luttinger liquid phase. For all parameters where we compute 1-particle entanglement entropies for both ED (circles) and DMRG (crosses), we find excellent agreement.

5.5.2 *Comparison with Luttinger Liquid Theory*

Performing the finite size scaling for all computed interaction strengths V/J, we obtain the interaction dependence of the steady state 1-particle entanglement entropy in the thermodynamic limit (circles in Fig. 5.11) which we plot together with the entropy obtained from numerically computing the Fourier transform and numerically integrating the analytical steady state result from bosonization in Eq. (5.69) (dashed line, Fig. 5.11) for a fixed interaction cutoff $\varepsilon = 0.84$ determined in the ground state. We observe very similar agreement between results for the LL model and numerical results for the J-V model as in the equilibrium case Fig. 5.6 when using the same cutoff.

We again fit an effective interaction cutoff (blue pentagons in Fig. 5.12) at each interaction strength V/J separately to match the LL solution to the von Neumann entropy from the J-V model (red circles in the inset of Fig. 5.12). We find very good agreement with the interaction cutoff determined for the equilibrium ground state case (red circles in the main panel of Fig. 5.12) which suggests that the parameter ε of the LL calculation can be fixed by numerical analysis of the J-V model in the region $-0.5 < J/V < 1.5$, where the low energy LL approximation is most accurate resulting in $\varepsilon = 0.84$.

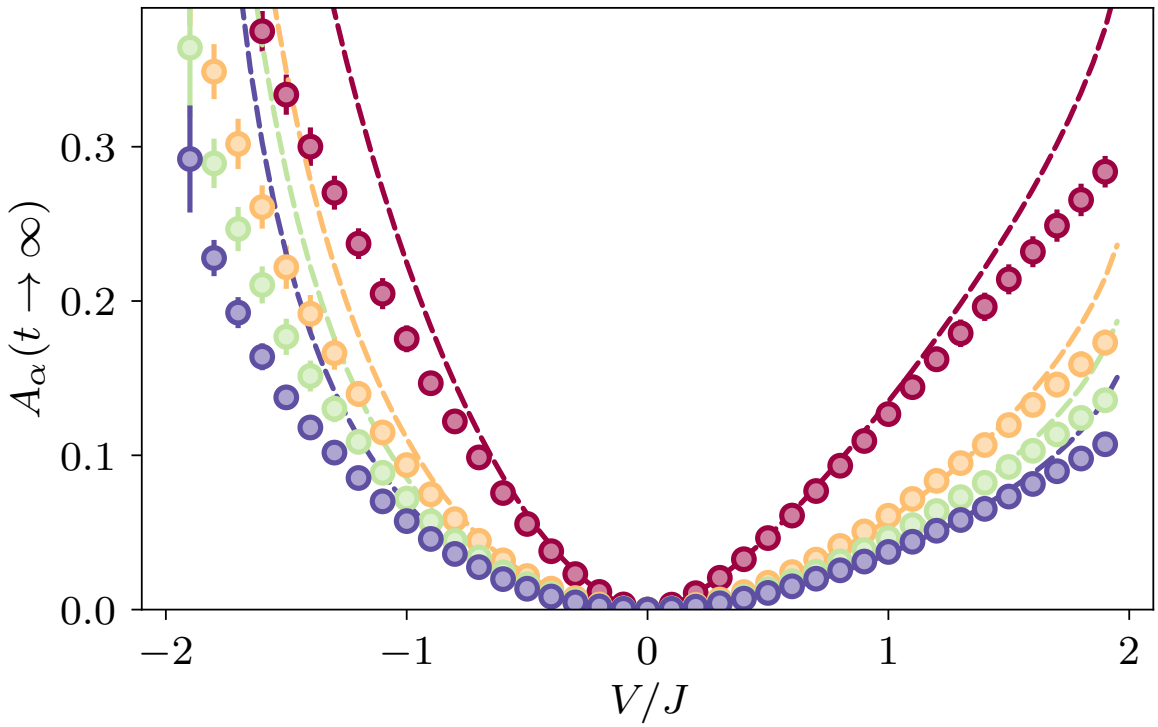

Figure 5.11: 1-particle entanglement entropies extrapolated from the numerical steady state estimates to the thermodynamic limit as a function of the post quench interaction strength V/J (circles) for Rényi indices $\alpha = 1$ (red), $\alpha = 2$ (yellow), $\alpha = 3$ (green), and $\alpha = 5$ (blue). Dashed lines depict the corresponding theory predictions from the steady states after the quench in the Luttinger liquid model using a fixed interaction cutoff $\varepsilon = 0.84$ obtained from ground state calculations. Similar to the equilibrium case, we find good agreement between LL prediction and numerical data for moderate interaction strengths.

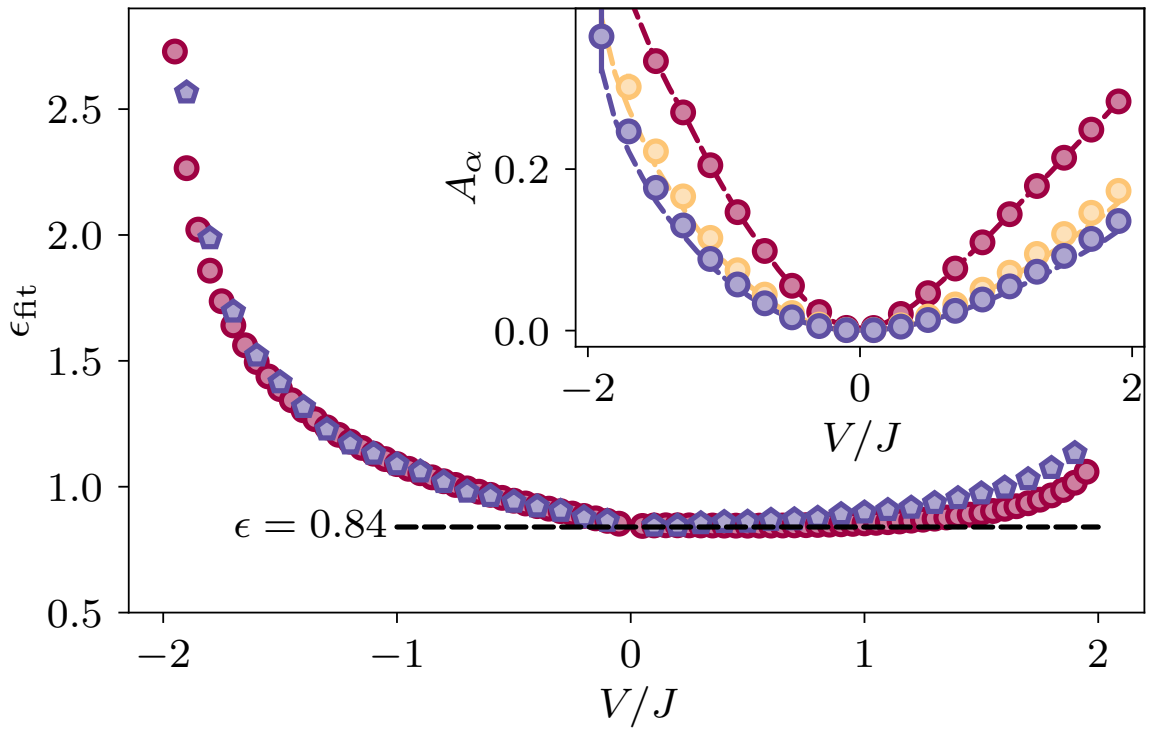

Figure 5.12: Interaction dependence of the effective cutoff $\varepsilon_{\mathrm{fit}}$ (blue pentagons) obtained by fitting the steady state of the Luttinger liquid model at each interaction strength V/J individually to the numerical data of the von Neumann entanglement entropy. For comparison, we show again the effective cutoff obtained from the ground state case (red circles) and find very good agreement with a quasi-plateau in the region $0 < V/J < 1$. The inset depicts numerical data for Rényi entropies with $\alpha = 1$ (red circles), $\alpha = 2$ (yellow circles), and $\alpha = 5$ (blue circles) together with the fitted field theory steady state predictions for the effective cutoff $\varepsilon_{\mathrm{fit}}$.

5.6 Time Dependence of the spectrum of the post-quench 1-body reduced density matrix

In this section, we utilize translational symmetry to monitor the time evolution of each eigenvalue of the 1-RDM. The initial state of free fermions $|\Psi(0)\rangle$ on the lattice is an eigenstate of the translation operator T, where $T|\Psi(0)\rangle = |\Psi(0)\rangle$. Also, the post-quench Hamiltonian commutes with the translation operator, $[H, T] = 0$, ensuring that the time evolved state $|\Psi(t)\rangle = e^{-\imath tH}|\Psi(0)\rangle$ is an eigenstate of T at all times, where $T|\Psi(t)\rangle = |\Psi(t)\rangle$.

If we now consider the elements of the two-point correlation matrix $\langle c_i^\dagger c_j \rangle_t$ at time t and use $c_i^\dagger c_j = T^\dagger c_{i+1}^\dagger c_{j+1} T$ for $i, j \in \{1, \ldots, L-1\}$, we can write $\langle c_i^\dagger c_j \rangle_t = \langle c_{i+1}^\dagger c_{j+1} \rangle_t$. For elements that cross the boundary, we need to include the phase factor $(-1)^{N-1}$ due to the corresponding boundary conditions, *e.g.*, $\langle c_i^\dagger c_L \rangle_t = (-1)^{N-1} \langle c_{i+1}^\dagger c_1 \rangle_t$. Therefore, the matrix is translationally invariant with a boundary phase $(-1)^{N-1}$ and can thus be diagonalized via Fourier transformation, where the diagonalized matrix represents the two-point correlation in terms of quasi-momenta modes, *i.e.*,

$$\langle \tilde{c}_q^\dagger \tilde{c}_{q'} \rangle_t = \delta_{q,q'} \langle n_q \rangle_t \,, \tag{5.73}$$

where $\tilde{c}_q = L^{-1/2} \sum_j e^{-\imath qj} c_j$ and $n_q = \tilde{c}_q^\dagger \tilde{c}_q$. Here, $q \in \{(2m - L + b_N)\,\pi/L : m = 0, 1, \ldots, L-1\}$, with $b_N = \frac{3-(-1)^N}{2}$. Accordingly, we obtain the momentum distribution function for the lattice fermions as

$$\rho_1(q, t) = \frac{1}{N} \langle n_q \rangle_t \,, \tag{5.74}$$

where the canonical ensemble condition $\sum_q \langle n_q \rangle_t = N$ fixes the normalization of $\rho_1(q, t)$ such that $\sum_q \rho_1(q, t) = 1$. Figure 5.13 demonstrates the time evolution of $N\rho_1(q, t)$ for different interaction strengths obtained from exact diagonalization for

a system with $N = 12$ fermions on $L = 24$ lattice sites. At time $t = 0$, we have the free fermionic occupation probabilities at zero temperature, where $\langle n_q \rangle_{t=0} = 1$ for $|q| \leq k_F$ and $\langle n_q \rangle_{t=0} = 0$ otherwise. After the quench, the occupation probabilities start to change, and the quench in the LL phase ($-2 < V/J < 2$) generates fluctuations that are more visible near the Fermi level and increase with increasing interaction strength. This is consistent with the effective low energy LL description. For $V/J = -1.8$, the effective thermalization following the abrupt quantum quench starts to invoke the extremes of the energy spectrum, where the linear approximation of the spectrum no longer holds and band curvature effects may be important. For comparison, we also consider a quench to an interaction strength of $V/J = -6.5$, which is outside of the Luttinger liquid phase. As illustrated in Fig. 5.13, the occupation probabilities show a flatter distribution and substantial fluctuations.

The time average of the distribution function $N\overline{\rho_1(q,t)}$ can provide information on quasi-thermalization after the quantum quench, as illustrated in Fig. 5.14. Here, $\overline{\rho_1(q,t)}$ shows a wider distribution, *i.e.*, larger entanglement entropy, if compared with the related equilibrium ground state distribution function $\rho_1(q)$. We can understand this by comparing the form of the steady-state 1-RDM $\rho_{t\to\infty}(x)$ (Eq. (5.69)) with the equilibrium one-body density function $\rho_1(x)$ (Eq. (5.34)). For the same interaction strength $V/J \neq 0$, we have $\gamma > \gamma_{\text{eq}}$, thus $\rho_{t\to\infty}(x)$ decays with x faster than $\rho_1(x)$. Consequently, their Fourier transformation should exhibit the opposite behavior.

In Fig. 5.15 we show the momentum distribution for fixed waiting times t after a strong interaction quench to $V/J = 20$, across the continuous phase transition to the density wave phase. We observe similar behavior as discussed in the

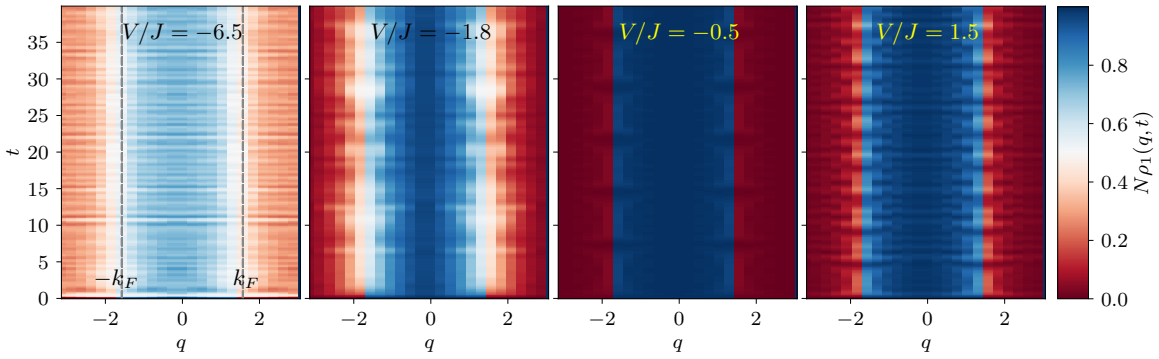

Figure 5.13: Exact diagonalization results for the time evolution of distribution function $N\rho_1(q,t)$ after a quantum quench for different values of the post quench interaction strength V/J. The initial state at $t = 0$ is the ground state of $N = 12$ non-interacting fermions hopping on a ring of $L = 24$ sites. The dashed vertical lines mark the Fermi momenta, around which the fluctuations are more pronounced. Increasing the interaction strength increases the amplitude of fluctuations.

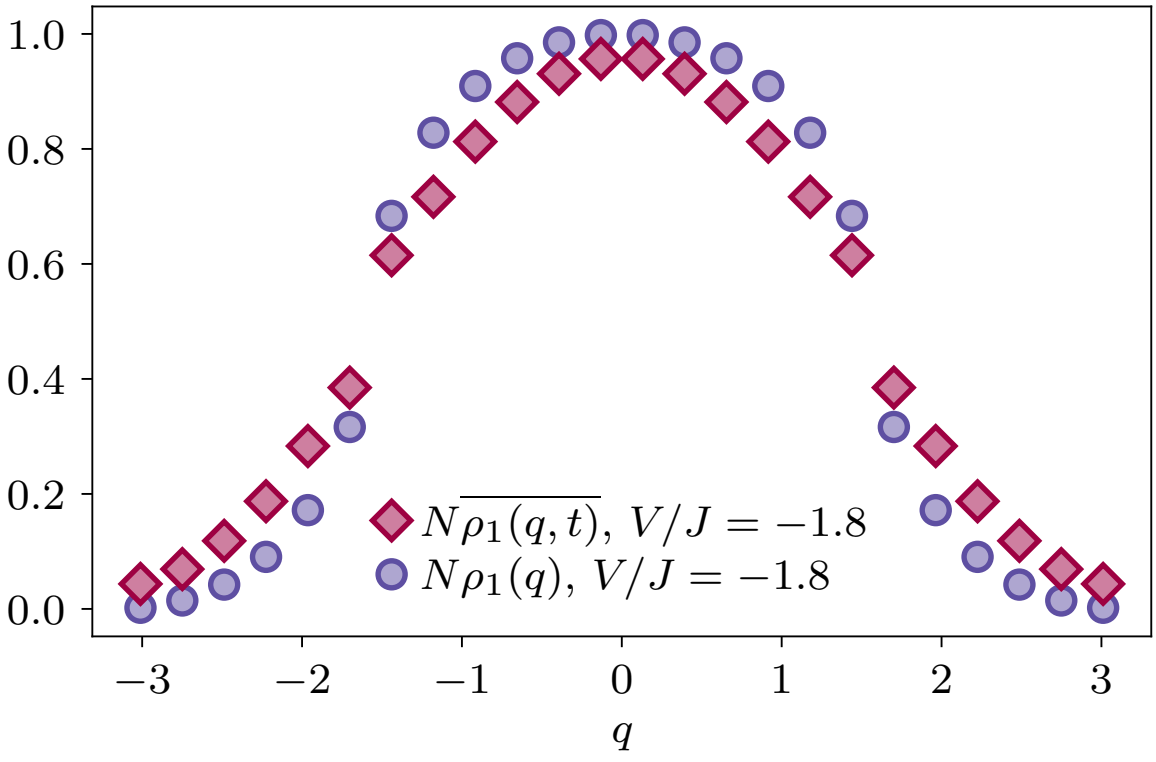

Figure 5.14: Comparison between the time average of the distribution function $N\overline{\rho_1(q,t)}$ (red diamonds) after a quench to interaction strength of $V/J = -1.8$ and the distribution function $N\rho_1(q)$ (blue circles) for the corresponding equilibrium case. The ED data is for a system of $N = 12$ fermions at half-filling.

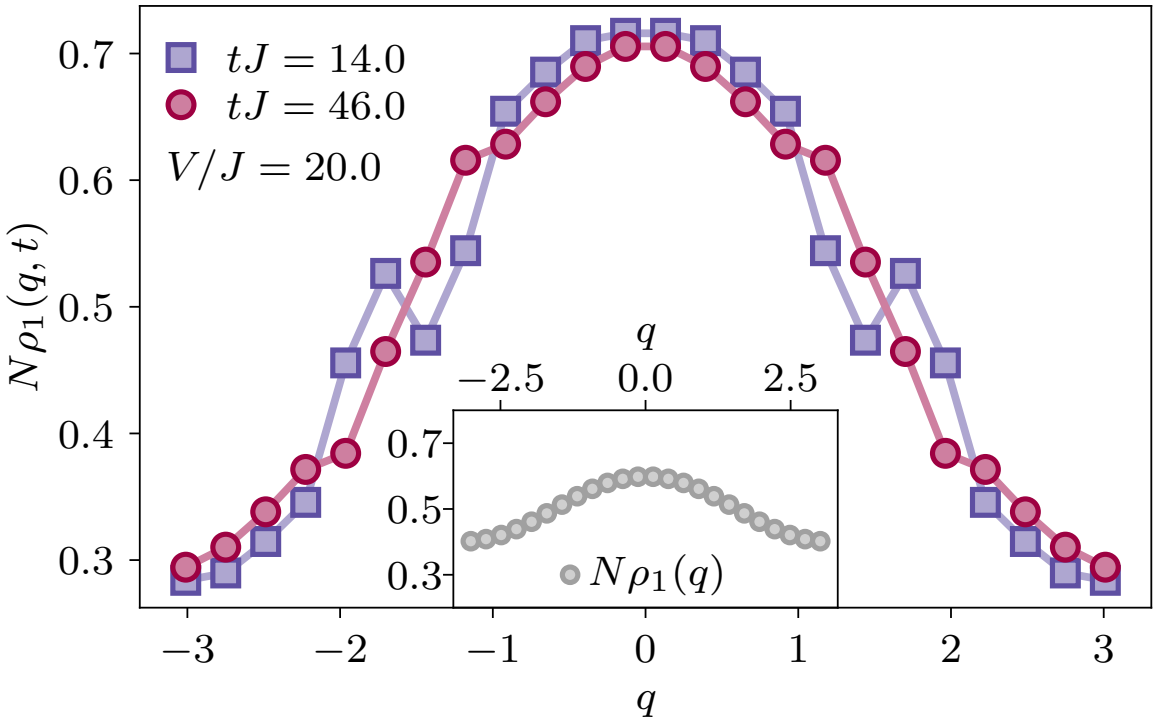

Figure 5.15: Momentum distribution function at two different times, after a quantum quench at $t = 0$ to a final interaction strength $V/J = 20$ deep in the density wave phase. The system consists of $N = 12$ fermions on a ring of $L = 24$ sites. The inset shows the equilibrium ground state distribution function for the same interaction strength. Lines are a guide to the eye.

introduction in Fig. 5.3 for a quench across the discrete phase transition, where the momentum distribution can develop non-monotonic behavior as a function of q.

5.7 Conclusions

In this chapter, we have reported on a comprehensive study of the one particle reduced density matrix and its associated von Neumann and Rényi entanglement entropies in the J-V lattice model of spinless fermions in one spatial dimension at half filling. We have considered entanglement both in the ground state of the interacting model, as well as after an interaction quantum quench starting from an initial state of non-interacting fermions. In both setups, we demonstrate that the 1-particle entanglement entropy is sensitive to the continuous and discrete phase transitions known to exist in this integrable model.

By carefully exploiting translation, reflection, and particle-hole symmetries of the lattice model in the presence of periodic boundary conditions, combined with advances in time-dependent density matrix renormalization group on massively parallel GPUs, we have pushed the boundaries of exact and approximate computations of the 1-particle entanglement entropy. Specifically, we study system sizes up to $L = 102$ sites in the ground state at half-filling, and up to $L = 30$ after the quantum quench. Here, periodic boundary conditions are essential to obtain the momentum distribution function via a simple Fourier transform of the one particle reduced density matrix. Access to these large system sizes are required for a reliable extrapolation to the thermodynamic limit.

For strong interaction quenches outside of the quantum liquid into the clustered solid ($V/J \ll -2$) or density wave ($V/J \gg 2$) phases, the momentum distribution function obtained from the spectrum of the one particle reduced density matrix can exhibit a non-monotonic dependence on momentum. This behavior can occur for both small and large values of q, and may highlight dynamic signatures of

the asymptotically flat momentum distributions in these two extreme limits of localized fermions.

For quenches within the quantum liquid regime, we can utilize continuum field theory calculations based on bosonization of the fermionic degrees of freedom within the Luttinger liquid phase ($|V/J| \leq 2$). With access to numerical predictions for $L \to \infty$, a comparison between field theory and numerical results is possible. We use a self-consistent approach for determining the interaction cutoff of the Luttinger model necessary due to the finite range nature of interactions in the lattice Hamiltonian. A fixed value of the cutoff is determined in the ground state, which can then be applied to the non-equilibrium post-quench dynamics. This provides a route to determining entanglement properties which depend on high energy degrees of freedom via bosonization.

Much work remains to be done to understand particle entanglement in interacting quantum many-body systems. For example, bosonization not only gives access to the one particle reduced density matrix, but higher order density matrices (e.g. $n = 2$) are also computable as correlation functions by similar methods. More generally, the 1-particle reduced density matrix is the starting point for an expansion of the entanglement entropy in terms of higher order density matrices. Such a research program will require generalizing the Kirkwood expansion of the thermal entropy in terms of irreducible distribution functions [149] to keep track of the required antisymmetrization of fermionic density matrices.

It was much pleasanter at home, when one wasn't always growing larger and smaller.
ALICE, *Alice's Adventures in Wonderland*

THE BEREZINSKII-KOSTERLITZ-THOULESS PHASE TRANSITION IN THE ONE DIMENSIONAL BOSE-HUBBARD MODEL

6

This chapter contains text from work by the author currently under review [172], with minor modifications where appropriate for this format. The author contributed significantly to the bosonization derivation of the particle fluctuations, the verification of the renormalization group equations used, and considering operators under different boundary conditions. They also made substantial contributions to the writing of the fluctuation derivation and discussion of boundary conditions, the introduction, and overall editing. Matthias Thamm performed the majority of the work including the numerical simulations, fitting of the data, scaling, production of figures, and writing with input from the coauthors. Adrian Del Maestro and Bernd Rosenow supervised this work.

6.1 INTRODUCTION

The Berezinskii-Kosterlitz-Thouless (BKT) transition [55, 173] is a remarkable infinite-order topological phase transition, originally discovered in the classical two-dimensional (2D) XY model. The low-temperature phase is characterized by algebraically decaying spin correlations, and the transition to a high-temperature disordered phase is driven by the unbinding of topological defects (vortex-antivortex pairs) due to thermal fluctuations. The location of the critical point is known from Monte Carlo [174–178] and tensor network simulations [179–181]. BKT physics has been found in a variety of systems, including the 2D Coulomb gas [182], superconducting films [183–188], Josephson junction arrays [189, 190],

superconductor-ferromagnetic-superconductor junctions [191], and lattice models at zero temperature [192, 193]. Near the transition, all these systems are expected to follow a renormalization group (RG) flow characteristic of the BKT universality class. Although this RG flow has been numerically demonstrated in the classical XY model [181, 194–198], its observation in quantum systems (with the transition driven by quantum instead of thermal fluctuations) remains a major challenge. This is due to a signature feature of BKT scaling – logarithmic system size dependence at criticality – necessitating costly large-scale numerical simulations of quantum systems.

The transition between superfluid and Mott insulator in the one-dimensional (1D) Bose-Hubbard (BH) model is a paradigmatic example of quantum BKT physics, corresponding to a 2D classical BKT transition via the quantum-to-classical mapping. The transition is governed by a competition between the kinetic energy of the bosons and the on-site repulsive interaction U. For small interactions, the system is in a superfluid phase, while it is in a Mott insulating phase when the on-site repulsion is dominant. This quantum phase transition has been experimentally observed in cold-atom systems [199, 200] and due to its intrinsic interest, a variety of theoretical studies have attempted to locate the critical point in the 1D BH model [201]. This includes approximate analytical approaches [73], exact diagonalization [202], density matrix renormalization group (DMRG) [64, 66, 203–207], infinite matrix product state simulations [208, 209], quantum Monte Carlo (QMC) [210–213], time evolving block decimation (TEBD) [214–217], and entanglement-based techniques [218]. While these studies have reported a range of critical interaction strengths with varying degrees of accuracy and precision, the expected BKT RG flow behavior remains unobserved.

A key difficulty in pinpointing the BKT RG flow in quantum simulations arises from boundary conditions. For open boundary conditions (OBC), a position-dependent vortex fugacity and superfluid stiffness must be introduced to account for "image vortices" induced by the system's edges [219–221], complicating direct

comparisons to RG predictions developed for infinite or periodic systems. This is a non-trivial boundary effect, with the emergent low-energy description taking on the form of a non-local Sine-Gordon model [219]. Capturing these subtleties is essential for extracting BKT scaling, and their neglect may explain the spread in critical parameters observed in DMRG studies with OBC [64, 66, 203–206].

In this chapter, we perform a theoretical analysis of the BKT transition in the 1D Bose-Hubbard model by combining periodic boundary conditions (PBC) DMRG with a systematic finite-size scaling analysis of bipartite particle number fluctuations [64]. Our main contributions are: (i) an observation of the BKT RG flow at a quantum phase transition, overcoming the boundary-related issues that affected previous studies; (ii) when using OBC, identifying the small fraction of the system near the center that can be used to extract observables compatible with infinite size RG predictions; and (iii) a high-precision determination of the critical interaction strength in the Bose-Hubbard model at unit filling with uncertainty quantification via a non-parametric Gaussian process model.

6.2 Model

We consider a one-dimensional system of interacting quantum particles at zero-temperature described by the Luttinger liquid Hamiltonian [3]

$$H_{\mathrm{LL}} = \int_0^L \mathrm{d}x \, \frac{u}{2\pi} \left[K(\partial_x \theta)^2 + \frac{1}{K}(\partial_x \phi)^2 \right] + \frac{V}{2\pi a} \cos(2\phi) \, , \tag{6.1}$$

with bosonic phase field $\theta(x)$, displacement field $\phi(x)$, and a pinning term due to a periodic lattice potential of strength V. Here, u is the velocity of excitations, a the lattice spacing, and $K > 1$ is the Luttinger parameter determined by the strength of repulsive interparticle interactions. In the low energy limit under the assumption of an average density ρ_0 and excitations causing small fluctuations around ρ_0, the

particle field operator $\psi(x)$ is related to the phase field via $\psi(x) \approx \sqrt{\rho(x)}e^{i\theta(x)}$, and the density profile is given by $\rho(x) \approx \partial_x\phi(x)/\pi \equiv \rho_0 + \partial_x\tilde{\phi}(x)/\pi$ [3, 49, 222, 223].

The Hamiltonian Eq. (6.1) has the form of a sine-Gordon model [3], which is known to host a Berezinskii-Kosterlitz-Thouless (BKT) phase transition [54, 55] at $K(L \to \infty) = 2$ close to which the RG flow is governed by the flow equations $\frac{\mathrm{d}K}{\mathrm{d}\ell} = -\left(\frac{\pi V}{E_r}\right)^2 \frac{K^2}{4}$ and $\frac{\mathrm{d}V}{\mathrm{d}\ell} = (2-K)V$ [3] with a characteristic energy scale $E_r = u\pi/a$ and $\ell = \ln L$ sets the RG scale.

The flow equations can be solved by the introduction of $\zeta(K, V)$ with $\mathrm{d}\zeta/\mathrm{d}\ell = 0$ [224]*, resulting in

$$2\ln\left(\frac{L_2}{L_1}\right) = \int_{K_2}^{K_1} \frac{\mathrm{d}K}{K^2(\ln(K/2) - \zeta) + 2K} \tag{6.2}$$

$$\zeta \equiv \frac{2}{K} + \ln\left(\frac{K}{2}\right) - \frac{\pi^2}{2}\left(\frac{V}{E_r}\right)^2 . \tag{6.3}$$

Given the values of (K_1, K_2) for two system sizes (L_1, L_2), solving Eq. (6.2) for ζ determines a line in the flow diagram $K(V; L)$ describing how K and V change when increasing the system size L (solid lines in Fig. 6.1). Knowledge of the flow line allows for the finite-size scaling of K to the thermodynamic limit $L \to \infty$. In the superfluid phase (SF), $\zeta > 1$, the Luttinger parameter K flows to a line of fixed points $K^*(\zeta) > 2$ and V to zero. The separatrix (dashed black), i.e. the critical flow line of the quantum phase transition, corresponds to $\zeta = 1$. For strong interactions, $\zeta < 1$, the system is in the Mott insulating (MI) phase where K flows to zero and V to infinity.

RG flow finite size scaling—Based on the RG flow, we can approximate the finite size scaling form of the Luttinger parameter K analytically in three regions of the

*The flow equations stated in the supplemental material of Ref. [224] contain a typo that is corrected in Eq. (6.2) and Eq. (6.3).

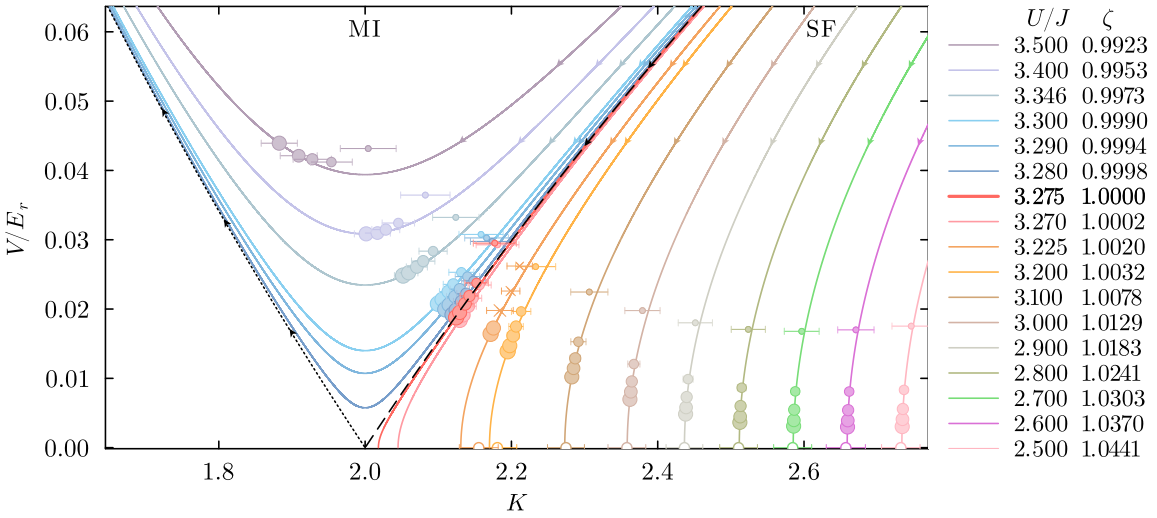

Figure 6.1: RG flow close to the BKT phase transition constructed from the numerical DMRG simulations for periodic boundary conditions via Eq. (6.2). Here, K is the Luttinger parameter, V the strength of the periodic lattice potential, $E_r = u\pi/a$ a characteristic energy scale, and U the interacting strength of the Bose-Hubbard model, Eq. (6.7), considered in the numerical simulations. The dashed black line is the separatrix marking the critical line of the phase transition with $\zeta(U_c/J) = 1$. To the right of the separatrix, the system is in the superfluid phase (SF), and to the left it is in the Mott insulating phase (MI). Each colored line corresponds to one value of $\zeta(U/J)$ obtained from the numerical results for the largest two system sizes for each U/J. Circles show the points for individual system sizes (larger circles correspond to larger L, $L \in \{16, 32, 48, 64, 96, 128\}$). Open circles are obtained by fits of the $L \to \infty$ limit of Eq. (6.9) to data obtained for infinite boundary conditions using the VUMPS algorithm [225]. Crosses are obtained from QMC. We estimate error bars on K by varying the fit intervals. We find excellent agreement of the DMRG data with the predicted RG flow and between the different methods.

BKT phase diagram:

$$K_{\mathrm{SF}} \sim K^* + \kappa_0 \left(\frac{L_0}{L}\right)^{2(K^*-2)} \tag{6.4}$$

$$K_{\mathrm{sep}} \sim 2 + \frac{1}{1/\kappa_0 + \ln L/L_0} \tag{6.5}$$

$$K_{\mathrm{MI}} \sim 1 + (1+\kappa_0)\left(\frac{L_0}{L}\right)^{8(1-\zeta)} . \tag{6.6}$$

For weak lattice potential strength V in the superfluid (SF) phase, we expand $K_{\mathrm{SF}} = K^* + \kappa$ for small κ resulting in the scaling Eq. (6.4). Here, $K(L_0) = K^* + \kappa_0$ for some system finite size L_0 with distance κ_0 from K^*. For the critical flow on the separatrix (sep), $\zeta = 1$ and $K^* = 2$, yielding the finite size scaling Eq. (6.5). In the insulating phase, as K flows to zero, one cannot expand for the asymptotic L dependence. However, $K(V)$ has a minimum at $K = 2$ close to which the scaling form is given by Eq. (6.6).

This shows that the finite size scaling is logarithmic on the separatrix and nearly-logarithmic, i.e. of power-law type with small exponent, close to it. Thus the functional form of the finite size scaling (even asymptotically) depends on the exact point in the phase diagram. This renders typical empirical $1/L$ extrapolations for $L \to \infty$ inaccurate, and requires utilization of the RG flow to produce accurate predictions of the thermodynamic limit behavior from finite size numerical simulations. Examples of the scaling forms in Eq. (6.4)–Eq. (6.6) are shown in Fig. 6.2 (dashed lines), together with numerical data obtained for the Bose-Hubbard model (circles, PBC; squares OBC) as described below.

6.2.1 *Bose-Hubbard model*

As an example system, we study the Bose-Hubbard model at zero temperature

$$H = -J \sum_{i=1}^{L} \left(b_i^\dagger b_{i+1} + b_{i+1}^\dagger b_i \right) + \frac{U}{2} \sum_{i=1}^{L} n_i(n_i - 1) \tag{6.7}$$

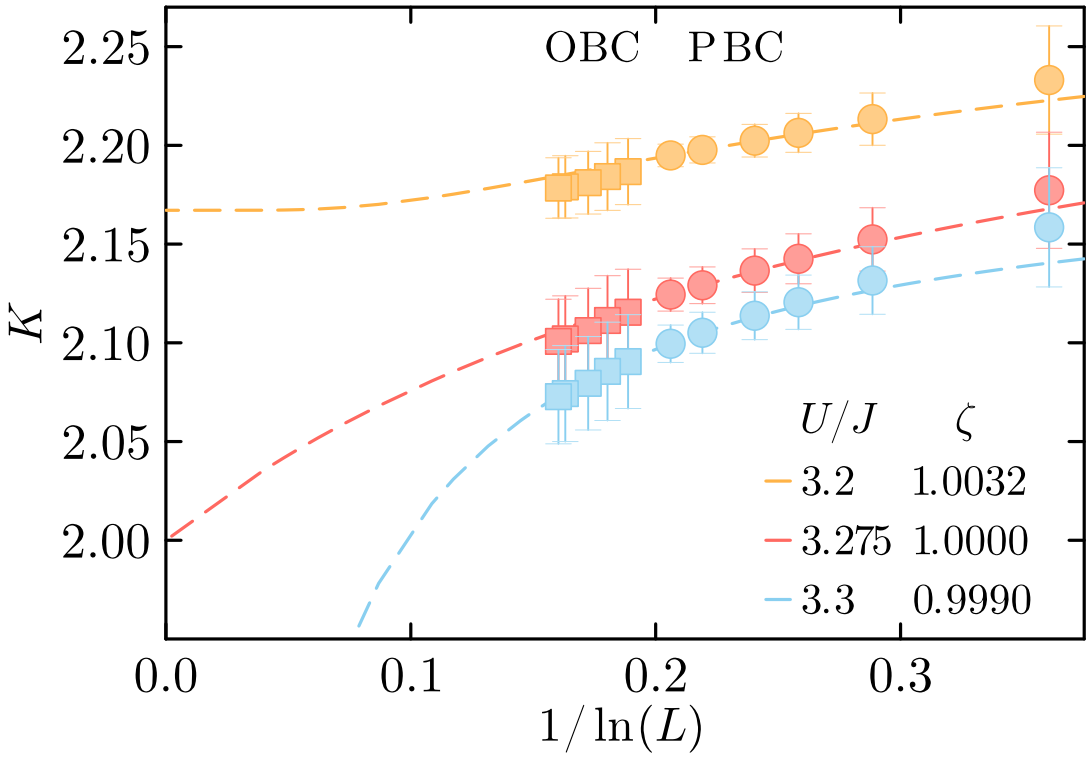

Figure 6.2: Finite size scaling of the Luttinger parameter as a function of the system size L according to the RG flow. The circles depict the results obtained from high precision DMRG calculations with open boundary conditions. Dashed lines show fits of the corresponding scaling form to the data. We show the three scaling regimes (i) in the superfluid phase according to Eq. (6.4) (upper orange curve), (ii) for the value of U closest to the separatrix using Eq. (6.5) (center red curve), and (iii) in the insulating phase according to Eq. (6.6) (bottom blue curve). Squares depict data obtained for open boundary conditions using a finetuned fitting interval for extraction of K [172].

on a one dimensional, periodic lattice of length L. Here, J is the nearest neighbor hopping strength, $U > 0$ the repulsive onsite interaction, b_i ($b_i^\dagger$) annihilates (creates) a boson on site i, and $n_i = b_i^\dagger b_i$ is the number operator for site i. For PBC, we identify $b_{L+1} = b_1$, while for OBC, $b_{L+1} = 0$. We consider unit filling where $\langle n_i \rangle = N/L = 1$.

The low energy sector of Eq. (6.7) can be described by the Luttinger liquid Hamiltonian Eq. (6.1) via bosonization, which allows for the relation of the interaction strength U to the Luttinger parameter K. Here, the density pinning term with pre-factor V/E_r is related to Umklapp processes on the lattice [226] and becomes interaction dependent. The Bose-Hubbard model thus exhibits a BKT phase transition between a Mott-insulating phase for $U > U_c$ ($K < 2$) and superfluid phase for $U < U_c$ ($K > 2$) and falls under the universality class of models following the RG flow described above [227] and depicted in Fig. 6.1. The critical point can then, in principle, be determined by inverting the unknown function $K(U/J)$.

We extract K from the fluctuations of the particle number in an interval $A = [0, \ell]$ defined as $\mathcal{F}(\ell) = \langle (\hat{N}_A - \langle \hat{N}_A \rangle)^2 \rangle$ [64], where the particle number operator is related to the density via $\hat{N}_A = \int_0^\ell dx\ \rho(x)$. Particle number fluctuations are proportional to the Luttinger parameter, and for PBC are given by

$$\mathcal{F}_{\text{pbc}}(\ell; K, \alpha) = \frac{1}{\pi^2} \langle [\tilde{\phi}(\ell) - \tilde{\phi}(0)]^2 \rangle \tag{6.8}$$

$$= \frac{K}{2\pi^2} \ln \left[1 + \frac{\sin^2(\pi \ell / L)}{\sinh^2(\pi \alpha / L)} \right] \tag{6.9}$$

with α a short-distance cutoff. The OBC case is discussed in Appendix F. For the region $\ell \sim L/2$ in the case of sufficiently large systems, such that $\ell/L \gg \alpha/L$, we can write $\mathcal{F}_{\text{pbc}}(\ell; K, \alpha) \approx \frac{K}{\pi^2} \ln \sin \frac{\pi \ell}{L} + A$ with constant $A \in \mathbb{R}$, allowing us to extract K as the slope of a linear fit to $\mathcal{F}_{\text{pbc}}$ plotted against $\frac{1}{\pi^2} \ln \sin \frac{\pi \ell}{L}$ as seen in Fig. 6.3.

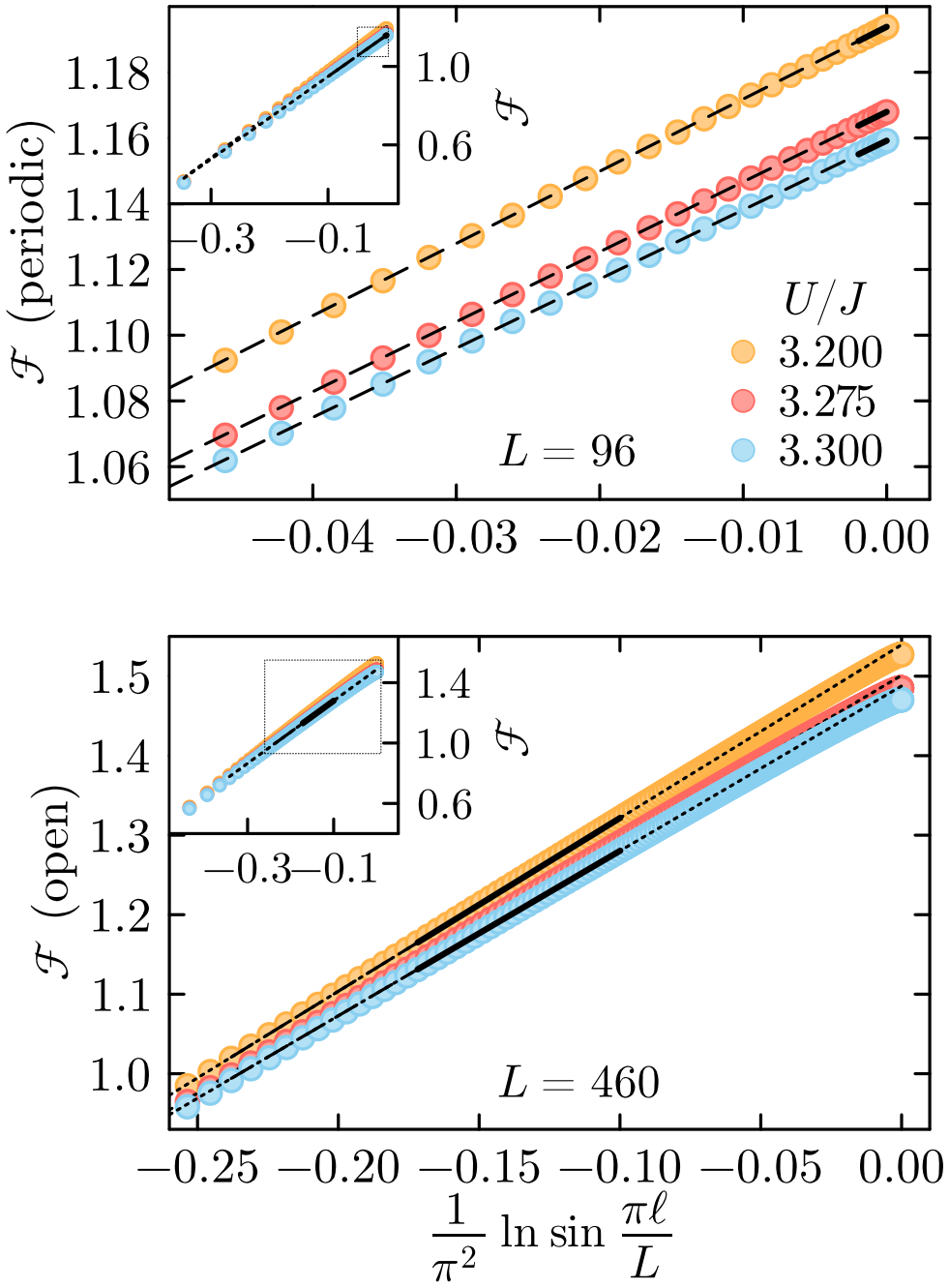

Figure 6.3: Extracting the Luttinger parameter K from the particle number fluctuations for different interaction strengths U/J. We fit Eq. (6.9) to the periodic boundary condition DMRG data (upper panel) for intervals close to $\ell = L/2$, i.e. $\ell \in [L/2 - L/16, L/2]$, with the extracted value of K being insensitive to the choice of fitting region. The bottom panel shows fits to the open boundary condition data, where we fit to a small center region $\ell \in [L/8.2 - L/16, L/8.2]$ such that ℓ covers the same absolute range as in the top panel. This restriction is necessary to mitigate the strong boundary effects for ℓ approaching $L/2$ which leads to a strong dependence of K on the fitting region, ultimately causing a large uncertainty in the extracted value.

6.3 Microscopic simulations

To numerically demonstrate the BKT RG flow for the Bose-Hubbard model, we perform high-precision numerical DMRG simulations for periodic chains of sizes up to $L = 128$ sites using the `ITensors.jl` software library [119]. For OBC, we perform simulations up to $L = 512$. We restrict the local site occupancy of bosons by $n_{\max} = 6$—larger than those typically used, which may not be sufficient when considering fluctuations [96]. Due to the non-periodic nature of the matrix product states used for the DMRG algorithm, the description of periodic systems requires large bond dimensions, which makes simulating large periodic systems challenging. Therefore, we carefully ensure the convergence of the DMRG algorithm by the following criteria: (i) no change in energy larger than 10^{-12} for consecutive sweeps, (ii) no change in the bond dimension for at least four sweeps using a truncation cutoff of 10^{-12}, and (iii) a final energy variance satisfying $\langle (H-E)^2 \rangle / E^2 < 10^{-11}$.

We perform DMRG calculations for many different values of the interaction U/J in both the superfluid and Mott insulating phase for different system sizes L. Next, we compute the particle number fluctuations $\mathcal{F}$ as a function of the subsystem size ℓ in the ground state. We then extract the Luttinger parameter as described below Eq. (6.9) (see Fig. 6.3) for each value of U/J and L. We linearly fit to the region $\ell \in [L/2 - \lfloor L/16 \rfloor, L/2]$ and obtain an error bar by varying the number of included points up to $\ell \in [L/4, L/2]$. As a consistency check, a similar procedure is performed using ground state lattice worm quantum Monte Carlo with details provided in the supplement [172]

For OBC, the bipartite fluctuations in Eq. (6.9) computed for the Luttinger model, depends on the location of the bipartition Appendix F. Near the center of the interval, the PBC and OBC expressions agree with each other. However, in the OBC case, the Luttinger parameter K acquires a strong spatial dependence due to the formation of image vortices at the boundaries [219]. This is in striking contrast to the assumption of a spatially constant K used in the derivation of

the LL prediction for bipartite fluctuations, which is valid only for a very small center interval in the presence of OBC. Extracting physically consistent values of K requires extensive fine-tuning of this region, which may be responsible for the scatter of previously reported critical points discussed in the introduction. For this reason, PBC offer advantages for studying the phase transition, despite their increased computational cost in DMRG.

Finally, approximate infinite matrix product state calculations can be performed directly in the thermodynamic limit using the `ITensorInfiniteMPS.jl` software implementing the VUMPS algorithm [228]. We find excellent agreement with the infinite system extrapolation of K (see open circles in Fig. 6.1) deep in the superfluid phase where $V = 0$. However, close to the phase transition there is a discrepancy between the infinite matrix product state approach and that extrapolated from finite L, which is plausible as the growth in entanglement [96] cannot be captured at finite bond dimension [229].

6.4 Demonstration of BKT flow

For each U/J, the extracted values of K for PBC at two consecutive system sizes are used in conjunction with Eq. (6.2) to determine a value of $\zeta(U/J)$. Then, Eq. (6.3) gives the associated value of V corresponding to the K of the smaller system size. Using the two largest values of L, this process gives the flow lines shown in Fig. 6.1 as well as their V-values. We obtain error bars by additionally computing ζ using values of the Luttinger parameters varied within their error bars and taking the maximum deviation. Thus, the observed agreement between flow lines and data points for smaller system sizes represents a stringent consistency check of BKT flow. Moreover, near the transition, we find excellent agreement with the predicted analytic scaling forms in Eq. (6.4)-Eq. (6.6) as seen in Fig. 6.2.

Reconstruction of the RG flow allows us to precisely locate the phase transition at U_c for which the flow with $\zeta(U_c/J) = 1$ follows the separatrix in Fig. 6.1. To

extract the critical point, we plot $\zeta(U/J)$ in Fig. 6.4 and employ a Gaussian process (GP) model and identify where the posterior mean predicts $\zeta(U_c/J) = 1$, yielding $U_c/J = 3.276(2)$ or $J/U_c = 0.3053(2)$. Uncertainty quantification is enabled via the posterior confidence interval of the GP [172]. Near the transition, we empirically observe $\zeta \propto U/J$, with large deviations outside it.

6.5 Conclusions

Finite-size scaling is derived from the renormalization group (RG), making it essential to obtain numerical data consistent with a given RG description. For the Berezinskii-Kosterlitz-Thouless transition, the RG framework for open boundary conditions is qualitatively different and significantly more complex than that for periodic boundary conditions. To ensure a robust data analysis, we have therefore obtained numerical data for periodic boundary conditions. We observed finite-size scaling behavior at the quantum phase transition in the one-dimensional Bose-Hubbard model consistent with the standard BKT RG flow, and obtained a high-precision estimate for the critical interaction strength at unit filling. Knowing its precise value may be important to quantify the effects of gapless modes and particle number fluctuations on entanglement [96, 230, 231]. We expect this approach to be useful in pinpointing critical points in other microscopic models where vortex proliferation is the dominant driver of the quantum phase transition.

Code Availability – All software and data used in this study are available online [232, 233].

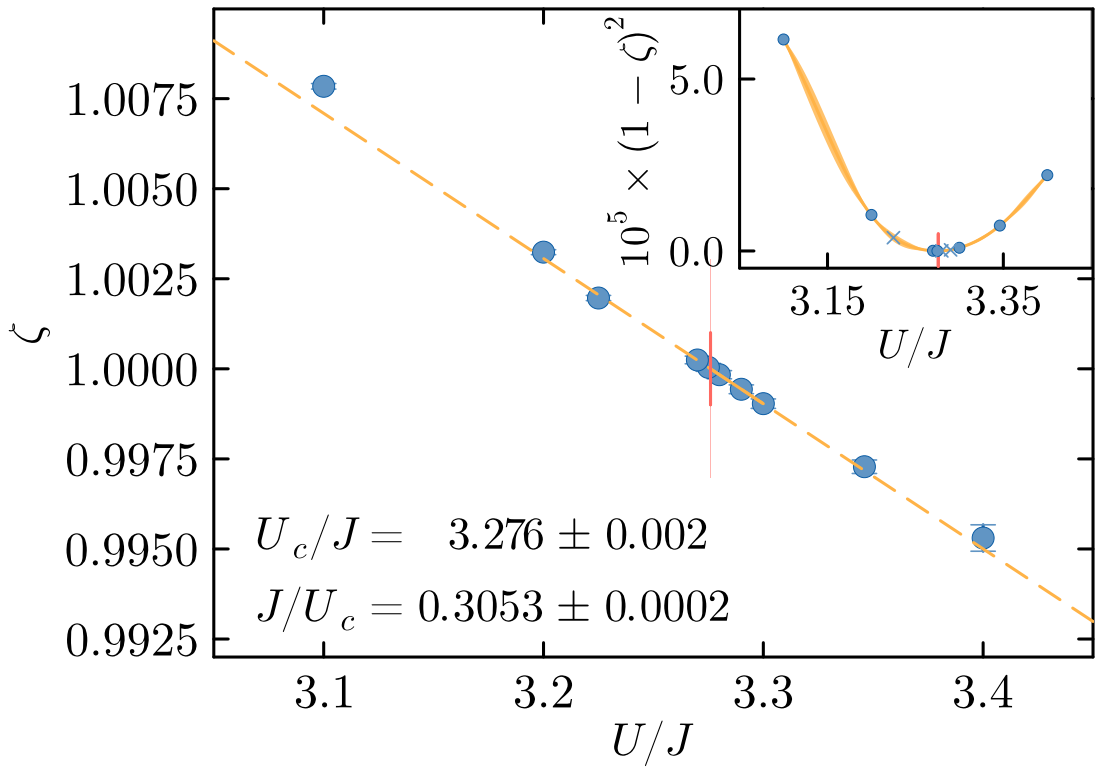

Figure 6.4: Dependence of the flow parameter ζ on the interaction strength U/J (ground truth, red circles). A Gaussian process (GP) is used to perform a non-parametric fit to the data, with the predicted posterior mean shown as a solid red line, accompanied by a red shaded region indicating the posterior confidence interval (CI). The critical point occurs when $\zeta = 1$ yielding $U_c/J = 3.276 \pm 0.002$ indicated by the vertical blue line, and a shaded region of uncertainty in the inset. Near the transition, a linear fit to $U/J \in \{3.275, 3.280, 3.290, 3.300\}$ (green dashed line) yields the same critical point and uncertainty, but away it deviates outside of error bars.

Everything's got a moral, if only you can find it.

The Duchess

Alice's Adventures in Wonderland

CONCLUSIONS 7

7.1 Overview

In this thesis, we investigated how entanglement and correlations emerge in one-dimensional quantum matter. Although the Tomonaga-Luttinger liquid provides a universal low-energy description, real systems introduce lattice spacing, UV cutoffs, and finite-size effects that modify this continuum picture. To bridge this gap, we combined three complementary approaches:

1. **Analytic field theory**, using tools such as bosonization, conformal field theory, and the renormalization group to extract universal structure and scaling.

2. **Large-scale numerical methods**, including the Density Matrix Renormalization Group (DMRG) and exact diagonalization, to compute observables beyond the reach of field theory and account for cutoff effects.

3. **Entanglement diagnostics**, especially Rényi entropies and reduced density matrices, to probe interaction effects, quantum statistics, and emergent phases.

In Section 2.6.2, we combined a bosonization result with exact diagonalization and GPU-accelerated DMRG to study the Rényi entanglement entropy $S_\alpha(n)$ between subsets of n and $N-n$ particles in the ground state of the one-dimensional

J-V model. By exploiting translation, reflection, and particle-hole symmetries, we obtained data for unprecedented system sizes, for a wide range of interactions. This allowed us to study the finite-size scaling of S_α as a function of the total number of particles N, the subsystem size n, the order of the Rényi entropy α, and the interaction V/J.

We confirmed the scaling form conjectured in Ref. [33] and extended it in two ways. First, in the limit $N \to \infty$, we found that interactions increased the entanglement beyond the free fermion value by an amount linearly proportional to n. Second, we identified an interaction-dependent correction that was *extensive* in N. Surprisingly, this correction had a leading-order term of $1/N$ when the subsystem size exceeded one. We encoded both effects in a proposed symmetric shape function $\Phi(n/N, V/J)$ that had a saddle-like profile, reflecting the entanglement induced by both attractive and repulsive interactions. We showed strong agreement between this shape function and the full data set.

Motivated by understanding the origin of the anomalous $1/N$ term, in Section 3.5, we derived an exact closed-form expression for the two-particle reduced density matrix of spinless fermions and introduced an interaction-dependent exponent λ. This exponent isolates the effects of scattering between right- and left-moving fermions, complementing the γ exponent present in the one-body density matrix, which describes interactions between fermions of the same chirality. Using a UV cutoff fitted from lattice data obtained through ED and DMRG, the 2-RDM expression can be used to obtain lattice-regularized expressions for the density-density correlator and the static structure factor. We showed that our analytic forms more accurately captured the periodic oscillations that arise from boundary conditions and finite size effects than previously derived expressions. Furthermore, the analytic results showed strong agreement with DMRG results for the J-V model at multiple filling fractions. The correlation function itself indicates signatures of the charge density wave phase and p-wave pairing at different interaction strengths. Finally, we demonstrated due to the presence of the

cutoff, the result contains information absent in a purely conformal field theory treatment.

We additionally considered correlation functions in non-equilibrium settings. In Section 4.6, we studied the one-particle Rényi entropy in the J–V chain at half-filling before and after a sudden interaction quench. This measure was sensitive to both the continuous transition to a clustered solid and the first-order transition to a charge-density wave. The entropy exhibited distinct plateaus at $\ln 2$ at both transitions, but varied continuously with interactions in the TLL phase. By analyzing the spectrum of the one-particle reduced density matrix, we found a non-monotonic structure in the post-quench momentum distribution, that was particularly pronounced when quenching deep into the clustered solid or CDW phases.

To interpret the dynamics, we performed a bosonization calculation in the TLL model by performing trivial time evolution on the bosonic operators and obtained a closed form expression for the one-body density matrix after the quench. Crucially, we developed a self-consistent fitting procedure to extract the ultraviolet cutoff ϵ from ground state data. In particular, we derived the correlation exponent γ^2 distinct from γ^2_{eq} and showed that the one-particle entanglement could be accurately captured by the continuum theory throughout the time evolution.

Finally, in Section 5.7, we turned to bosonic systems. We first bosonized the Bose–Hubbard chain and derived a closed-form expression for particle number fluctuations inside a subregion of length ℓ in terms of the Luttinger parameter K and ℓ. This formula proved crucial: when we attempted to fit open-boundary-condition (OBC) DMRG data, systematic deviations appeared, indicating that the fluctuations expression is strictly valid only for periodic boundary conditions (PBC). Switching to PBC data and applying a renormalization group guided finite-size scaling analysis, we extracted $K(L \to \infty)$ over a wide range of interaction ratios U/J. The resulting $K(U/J)$ values collapsed onto the analytical BKT flow lines expected for PBC, thereby resolving a three decade old discrepancy in

estimates of the critical coupling. Using the criterion $K = 2$ for the superfluid–Mott transition in the thermodynamic limit, we obtained the high-precision critical point $(U/J)_c = 3.276 \pm 0.002$.

7.2 Open Problems and Future Work

In this section, we discuss potential avenues for future work with particular focus on particle entanglement. We further discuss extensions of the correlation functions that can be computed through bosonization, which could be used to explore a wider class of models. Finally, we summarize experimental methods used to study correlation functions, which could lead to experimental verification of the expressions derived in this thesis and, by extension, the particle entanglement.

7.2.1 Particle Entanglement

Particle entanglement in the J-V model

A natural next step is to trace the origin of the subleading $1/N$ term that emerges in the scaling of $S_\alpha(n)$ for $n > 1$. Our exact expression for the two-particle reduced density matrix already revealed the exponent λ, associated with right-left scattering, which does not appear in the one-body case. To test whether λ generates the anomalous scaling, we need to first impose the quantum information normalization $\mathrm{Tr}\, æ_n = 1$, discretize the continuum expression on a periodic lattice, and construct the 2-RDM explicitly in the position basis. Potentially, we can perform a single analytic Fourier transform on one of the coordinates to move to momentum space, as particle entanglement is mode independent, and the diagonal matrix elements can be directly extracted as the eigenvalues. Exploiting lattice symmetries, we can numerically block diagonalize the matrix to fully obtain the spectrum. Focusing on attractive interaction strengths, we can isolate a regime in which γ remains positive while λ becomes strongly negative to study their respective contributions. In the

J-V model, this would be approaching the clustered solid phase, or $V/J \to -2$. Using the numerically obtained eigenvalues, we can reconstruct the Rényi entropies and perform a similar analysis as in Section 2.6.2 to see if we observe the $1/N$ term explicitly for the 2-particle entanglement. Furthermore, similar to Section 4.6, we expect the exponent λ to transform under time evolution, and it can be derived through a very similar procedure. This work is currently in progress.

Additional models

Having learned how to extract the ultraviolet cutoff self-consistently from DMRG data, we can repeat the analysis for the J-V-V' model, where the next-nearest neighbor interaction breaks integrability but can still be described by TLL theory at moderate couplings. As this chain still describes spinless fermions, we expect the same scaling form for the particle entanglement, as it comes directly from the expression for the correlation function, but with coefficients that depend smoothly on both V and V', which would further establish the universality of our framework.

Although we did not explicitly consider the bosonic case, Section 5.7 showed that bosonization can yield exact expressions for observables in bosonic systems, again with a short-distance cutoff that encapsulates microscopic details. The natural extension is to use the same field operators to derive the bosonic 1-RDM and perform a similar scaling analysis. We can benchmark the analytic predictions in the microscopic Bose-Hubbard and Lieb-Liniger models. Given that we already have high-precision QMC and DMRG data for the former, we can attempt to extract a similar scaling form to what has been done for the Lieb-Liniger model [93]. This study would help complete the picture of how particle statistics affect particle entanglement in one dimension.

7.2.2 *Correlation Functions*

We can also consider how correlation functions are modified in different types of systems. An immediate extension is to *spinful* Tomonaga-Luttinger liquids, where the diagonalized Hamiltonian separates into independent spin and charge sectors, or sums of the bosonized operators [46]. In this case, any two- or four-point correlation function should factorize into the product of a charge piece governed by K_ρ (which was already found in this thesis) and a spin piece governed by K_σ. This would enable the derivation of analytic forms that could apply directly to microscopic models such as the one-dimensional Hubbard chain [3]. Because both sectors remain gapless in the metallic phase, one can reuse the machinery developed here: fix the ultraviolet cutoff from lattice data and obtain expressions for density-density or pair-pair correlators. We can incorporate perturbations that are relevant in the RG sense, such as the $4k_F$ Umklapp scattering which is pronounced at half filling, by using additional cosine terms in the Hamiltonian. These can be treated perturbatively or via a Sine-Gordon resummation, to see how gaps modify the structure.

Another direction is to extend to *finite temperature*. Here, it is not as clear how to compute the exponentials of bosonic expectation values. However, mapping CFT vertex operators onto a cylinder of circumference $\beta = 1/T$ introduces a thermal length that modifies the power-law scaling [49]. With this substitution, one can derive Gibbs-ensemble generalizations of the two-point correlation, which could enable study of the mixed-state particle entanglement [234, 235].

Finally, we can analytically derive the *non-equal time* correlation functions. As the Hamiltonian is quadratic in bosonic fields $\phi(x,\tau)$ and $\theta(x,\tau)$, the correlation functions can be computed with standard Gaussian integral techniques [3]. First, using bosonization one would compute the correlation function in imaginary time (Euclidean space) τ. To recover the real time correlators, we would then need analytic continuation $\tau \to it + \epsilon$. Here, ϵ ensures convergence by damping

high-frequency components and selects the correct branch of the complex function. The choice of continuation enables us to obtain either time-ordered, retarded, or advanced correlators. This procedure is essential for connecting bosonization results with measurable quantities such as the dynamical structure factor or susceptibilities. Such dynamical correlators have more experimental relevance, underpinning pump-probe [236], angular resolved photoemission (ARPES) [154, 199, 237], and Bragg spectroscopy setups [36, 37, 238]. Extending the present framework to include time dependence would further tighten the link between low-energy field theory and real materials.

7.2.3 *Experimental Outlook*

Finally, we mention relevant experimental work that ties directly to the quantities considered in this thesis. First, the fermionic and bosonic single-particle density matrix is directly accessible through quantum-gas microscopes. A recent proposal for cold atoms [239] suggested engineering a controllable tunneling link between two distant sites and extracting the off-diagonal elements, ρ^1_{ij}, from occupation snapshots after two successive quenches. Because the protocol is applicable to both fermions and hard-core bosons, it provides a natural testbed for our fermionic density-matrix results and accessing the particle entanglement in ultracold gases.

In parallel, resonant inelastic x-ray scattering (RIXS) has evolved into a probe of many-body correlations in solids. A recent RIXS analysis [240] shows that the nonlinear part of the spectrum isolates four-fermion cumulants – precisely the building blocks of the two-particle RDM. By bounding the eigenvalues of the cumulant, the authors obtained an experimentally accessible witness of fermionic multipartite entanglement, akin to the particle entanglement discussed here.

Together, cold-atom microscopy and next-generation RIXS establish an experimental pathway for testing the correlation functions and particle entanglement scaling laws presented in this thesis.

7.3 Final Remarks

We hope the methods developed in this thesis provide a concrete start for embedding microscopic lattice effects into low-energy field theory descriptions. By focusing on particle entanglement, we have shown how n-particle Rényi entropies carry complementary information to the conventionally studied spatial entropies, distinguishing interaction- and statistics-driven correlations that are invisible to spatial cuts. Furthermore, we have outlined clear extensions of this work, such as integrability-breaking Hamiltonians, spinful liquids, finite-temperature ensembles, dynamical systems, and bosonic counterparts. Finally, we have demonstrated direct relevance to experimental methods, such as spectroscopy, resonant inelastic x-ray scattering, and cold atom microscopes. If there is a moral to this thesis, it is that the small details matter. Entanglement is not just a formal tool – it reflects how interactions, particle statistics, and system sizes shape the physics in meaningful ways. One-dimensional systems are especially good at revealing universal structure. To fully exploit their potential, many more details remain to be explored — leading us further down the rabbit hole.

BIBLIOGRAPHY

[1] F. D. M. Haldane. Effective Harmonic-Fluid Approach to Low-Energy Properties of One-Dimensional Quantum Fluids. *Phys. Rev. Lett.*, 47(25):1840, dec 1981. 1, 6, 21, 27, 52, 105, 106, 108, 110

[2] J. Voit. One-dimensional fermi liquids. *Reports on Progress in Physics*, 58:977–1116, 1995. 7, 23, 25, 121

[3] T. Giamarchi. *Quantum Physics in One Dimension*. Clarendon Press, Oxford, U.K., 2004. 1, 2, 7, 8, 16, 22, 28, 29, 30, 33, 36, 37, 51, 52, 93, 117, 121, 123, 136, 175, 176, 191, 254, 255

[4] J. Cardy. *Scaling and Renormalization in Statistical Physics*. Cambridge University Press, 1996. 1, 27, 28

[5] K. G. Wilson. The renormalization group: critical phenomena and the Kondo problem. *Reviews of Modern Physics*, 47:773–840, 1975. 1

[6] O. M. Auslaender, H. Steinberg, A. Yacoby, Y. Tserkovnyak, B. I. Halperin, K. W. Baldwin, L. N. Pfeiffer, and K. W. West. Spin-charge separation and localization in one dimension. *Science*, 308(5718):88–92, 2005. 1

[7] Y. Jompol, C. J. B. Ford, J. P. Griffiths, I. Farrer, G. A. C. Jones, D. Anderson, D. A. Ritchie, T. W. Silk, and A. J. Schofield. Probing spin-charge separation in a Tomonaga-Luttinger liquid. 325(5940):597, 2009. 1, 8

[8] R. Senaratne, D. Cavazos-Cavazos, C. L. Hung, and R. G. Hulet. Spin-charge separation in a one-dimensional fermi gas with tunable interactions. *Science*, 376(6595):1305–1308, 2022. 1

[9] K. Cedergren, R. Ackroyd, S. Kafanov, N. Vogt, A. Shnirman, and T. Duty. Insulating Josephson junction chains as pinned Luttinger liquids. *Physical Review Letters*, 119(16):167701, 2017. 2

[10] M. Bockrath, H. Cobden, D. J. Lu, G. Rinzler, A. E. Smalley, R. L. Balents, and L. McEuen, P.˙ Luttinger-liquid behaviour in carbon nanotubes. *Nature*, 397:598–601, 1999. 2

[11] H. Ishii et al. Direct observation of Tomonaga-Luttinger-liquid state in carbon nanotubes at low temperatures. *Nature*, 426:540–544, 2003.

[12] R. Egger and O. Gogolin, A.˙ Effective low-energy theory for correlated carbon nanotubes. *Physical Review Letters*, 79:5082–5085, 1997.

[13] L. Kane, C. L. Balents, and P.Ã. Fisher, M.˙ Coulomb interactions and mesoscopic effects in carbon nanotubes. *Physical Review Letters*, 79:5086–5089, 1997. 2

[14] J. Doe and A. Smith. Electronic transport and quantum phenomena in nanowires. *Chemical Reviews*, 123(4):1234–1256, 2023. 2

[15] B. Lee and C. Kim. Quantum transport in an ambipolar insb nanowire quantum dot device. *Physical Review B*, 111(11):115409, 2025. 2

[16] M. Foss-Feig, G. Pagano, A. C. Potter, and N. Y. Yao. Progress in trapped-ion quantum simulation. *arXiv preprint arXiv:2409.02990*, 2024. 2

[17] D. Jaksch, C. Bruder, J. I. Cirac, C. W. Gardiner, and P. Zoller. Cold bosonic atoms in optical lattices. *Physical Review Letters*, 81(15):3108–3111, 1998. 2

[18] R. Toda, M. Hieda, T. Matsushita, N. Wada, J. Taniguchi, H. Ikegami, S. Inagaki, and Y. Fukushima. Superfluidity of ^{4}He in one and three dimensions realized in nanopores. *Phys. Rev. Lett.*, 99:255301, 2007. 2

[19] T. Eggel, M. Oshikawa, and K. Shirahama. Four-dimensional xy quantum critical behavior of ^{4}He in nanoporous media. *Phys. Rev. B*, 84:020515, 2011.

[20] J. Taniguchi, K. Demura, and M. Suzuki. Dynamical superfluid response of ^{4}He confined in a nanometer-size channel. *Phys. Rev. B*, 88:014502, 2013.

[21] K. Demura, J. Taniguchi, and M. Suzuki. Dynamical superfluid response of ^{3}He-^{4}He solutions confined in a nanometer-size channel. *J. Phys. Soc. Jpn.*, 84:094604, 2015.

[22] B. Yager, J. Nyéki, A. Casey, B. P. Cowan, C. P. Lusher, and J. Saunders. Nmr signature of one-dimensional behavior of ^{3}He in nanopores. *Phys. Rev. Lett.*, 111:215303, 2013.

[23] A. Del Maestro, N. S. Nichols, T. R. Prisk, et al. Experimental realization of one dimensional helium. *Nature Communications*, 13:3168, 2022. 2

[24] Pasquale Calabrese and John Cardy. Time dependence of correlation functions following a quantum quench. *Phys. Rev. Lett.*, 96(13):136801, 2006. 2, 126

[25] J. Eisert, M. Friesdorf, and C. Gogolin. Quantum many-body systems out of equilibrium. *Nature Physics*, 11:124–130, 2015. 2

[26] A. Lukin, M. Rispoli, R. Schittko, M. E. Tai, A. M. Kaufman, S. Choi, V. Khemani, J. Léonard, and M. Greiner. Probing entanglement in a many-body-localized system. *Science*, 364:256, 2019. 3

[27] R. Islam, R. Ma, P. M. Preiss, M. E. Tai, A. Lukin, M. Rispoli, and M. Greiner. Measuring entanglement entropy in a quantum many-body system. *Nature*, 528:77, 2015.

[28] A. J. Daley, H. Pichler, J. Schachenmayer, and P. Zoller. Measuring entanglement growth in quench dynamics of bosons in an optical lattice. *Phys. Rev. Lett.*, 109:020505, 2012. 3

[29] P. Calabrese and J. Cardy. Entanglement entropy and quantum field theory. *Journal of Statistical Mechanics: Theory and Experiment*, 2004(06):P06002, 2004. 3

[30] P. Calabrese and J. Cardy. Evolution of entanglement entropy in one-dimensional systems. *J. Stat. Mech.: Theor. Exp.*, 2005(04):P04010, 2005. 40, 126

[31] V. Alba and P. Calabrese. Entanglement and thermodynamics after a quantum quench in integrable systems. *Proc. Nat. Acad. Sci.*, 114(30):7947, 2017. 3, 126

[32] M. Haque, Oleksandr Zozulya, and Kareljan Schoutens. Entanglement Entropy in Fermionic Laughlin States. *Phys. Rev. Lett.*, 98(6):060401, 2007. 3, 43, 50, 126

[33] M. Haque, O. S. Zozulya, and K. Schoutens. Entanglement between particle partitions in itinerant many-particle states. *J. Phys. A: Math. Theor.*, 42(50):504012, 2009. 41, 43, 49, 126, 148, 187

[34] O. S. Zozulya, M. Haque, K. Schoutens, and E. H. Rezayi. Bipartite entanglement entropy in fractional quantum Hall states. *Phys. Rev. B*, 76(12):125310, 2007. 43, 50, 126

[35] O. S. Zozulya, M. Haque, and K. Schoutens. Particle partitioning entanglement in itinerant many-particle systems. *Phys. Rev. A*, 78(4):042326, 2008. 3, 43, 49, 59, 126

[36] T. Kinoshita, T. Wenger, and D. S. Weiss. Local pair correlations in one-dimensional bose gases. *Phys. Rev. Lett.*, 95:190406, 2005. 3, 192

[37] E. D. Kuhnle, H. Hu, X.-J. Liu, P. Dyke, M. Mark, P. Hannaford, and C. J. Vale. Universal behavior of pair correlations in a strongly interacting fermi gas. *Phys. Rev. Lett.*, 105:070402, 2010. 3, 87, 92, 192

[38] H. Bethe. On the theory of metals. i. eigenvalues and eigenfunctions of the linear atomic chain. *Journal of Physics*, 71:205–226, 1931. 5

[39] S. Tomonaga. Remarks on Bloch's method of sound waves applied to many-fermion problems. *Progress of Theoretical Physics*, 5(4):544–569, 1950. 6, 8

[40] J. M. Luttinger. An exactly soluble model of a many-fermion system. *Journal of Mathematical Physics*, 4(9):1154–1162, 1963. 6

[41] D. C. Mattis and E. H. Lieb. Exact solution of a many-fermion system and its associated boson field. *Journal of Mathematical Physics*, 6(2):304–312, 1965. 6

[42] J. von Delft and H. Schoeller. Bosonization for beginners — refermionization for experts. *Annalen der Physik*, 510(4):225–305, 1998. 7

[43] S. Sachdev. *Quantum Phases of Matter*. Cambridge University Press, 2023. 7

[44] M. Auslaender, O. A. Yacoby, R. de Picciotto, W. Baldwin, K. N. Pfeiffer, L. and W. West, K.˙Tunneling spectroscopy of the elementary excitations in a one-dimensional wire. *Science*, 295(5556):825–828, 2002. 8

[45] F. D. M. Haldane. 'Luttinger liquid theory' of one-dimensional quantum fluids. i. properties of the Luttinger model and their extension to the general 1D interacting spinless Fermi gas. *Journal of Physics C: Solid State Physics*, 14(19):2585–2609, 1981. 8

[46] S. Eggert. One-dimensional quantum wires: A pedestrian approach to bosonization, 2009. 9, 93, 95, 136, 138, 191

[47] A. Iucci and M. A. Cazalilla. Quantum quench dynamics of the Luttinger model. *Phys. Rev. A*, 80(6):063619, 2009. 19, 20, 21, 52, 127, 135, 140, 154

[48] P. C. Hohenberg. Existence of long-range order in one and two dimensions. *Physical Review*, 158:383–386, 1967. 21

[49] M.A. Cazalilla. Bosonizing one-dimensional cold atomic gases. *Journal of Physics B: Atomic, Molecular and Optical Physics*, 37(7):S1, 2004. 21, 24, 176, 191, 254, 255

[50] P. Di Francesco, P. Mathieu, and D. Sénéchal. *Conformal Field Theory*. Springer, New York, 1997. 23

[51] A. M. Tsvelik. *Quantum Field Theory in Condensed Matter Physics*. Cambridge University Press, Cambridge, 2nd edition, 2003. 25

[52] A. Luther and I. Peschel. Single-particle states, kohn anomaly, and pairing fluctuations in one dimension. *Physical Review B*, 9(7):2911–2919, 1974. 27

[53] E. Fradkin. *Field Theories of Condensed Matter Physics*. Cambridge University Press, Cambridge, 2nd edition, 2013. 28

[54] J. M. Kosterlitz and D. J. Thouless. Ordering, metastability and phase transitions in two-dimensional systems. *J. of Phys. C: Sol. State Phys.*, 6(7):1181, April 1973. 28, 176

[55] V. L. Berezinskii. Destruction of long-range order in one-dimensional and two-dimensional systems having a continuous symmetry group i. classical systems. *Soviet Physics JETP*, 32:493, 1971. Originally published in Zh. Eksp. Teor. Fiz. 59, 907 (1970). 28, 173, 176

[56] J. V. José, L. P. Kadanoff, S. Kirkpatrick, and D. R. Nelson. Renormalization, vortices, and symmetry-breaking perturbations in the two-dimensional planar model. *Physical Review B*, 16:1217–1241, 1977. 29

[57] David R. Nelson and J. M. Kosterlitz. Universal jump in the superfluid density of two-dimensional superfluids. *Physical Review Letters*, 39:1201–1205, 1977. 29

[58] M. P. A. Fisher, P. B. Weichman, G. Grinstein, and D. S. Fisher. Boson localization and the superfluid–insulator transition. *Physical Review B*, 40:546–570, 1989. 32

[59] J. des Cloizeaux and M. Gaudin. Anisotropic linear magnetic chain. *Journal of Mathematical Physics*, 7:1384–1400, 1966. 33

[60] C. N. Yang and C. P. Yang. One-dimensional chain of anisotropic spin-spin interactions. i. proof of bethe's hypothesis for ground state in a finite system. *Physical Review*, 150:321–327, 1966. 33

[61] L. Gotta, L. Mazza, P. Simon, and G. Roux. Pairing in spinless fermions and spin chains with next-nearest-neighbor interactions. *Physical Review Research*, 3(1):013114, 2021. 35

[62] H. Barghathi, E. Casiano-Diaz, and A. Del Maestro. Operationally accessible entanglement of one-dimensional spinless fermions. *Phys. Rev. A*, 100:022324, Aug 2019. 36

[63] H. A. Gersch and G. C. Knollman. Quantum cell model for bosons. *Phys. Rev.*, 129:959–967, Jan 1963. 36

[64] S. Rachel, N. Laflorencie, H. F. Song, and K. Le Hur. Detecting quantum critical points using bipartite fluctuations. *Physical Review Letters*, 108(11):116401, March 2012. 37, 174, 175, 180

[65] J. Carrasquilla, S. R. Manmana, and M. Rigol. Scaling of the gap, fidelity susceptibility, and Bloch oscillations across the superfluid-to-Mott-insulator transition in the one-dimensional Bose-Hubbard model. *Phys. Rev. A*, 87:043606, Apr 2013.

[66] T. D. Kühner and H. Monien. Phases of the one-dimensional Bose-Hubbard model. *Phys. Rev. B*, 58:R14741–R14744, Dec 1998. 174, 175

[67] T. D. Kühner, Steven R. White, and H. Monien. One-dimensional bose-hubbard model with nearest-neighbor interaction. *Phys. Rev. B*, 61:12474–12489, May 2000.

[68] J. K. Freericks and H. Monien. Strong-coupling expansions for the pure and disordered Bose-Hubbard model. *Phys. Rev. B*, 53:2691–2700, Feb 1996.

[69] N. Elstner and H. Monien. Dynamics and thermodynamics of the bose-hubbard model. *Phys. Rev. B*, 59:12184–12187, May 1999.

[70] V. A. Kashurnikov and B. V. Svistunov. Exact diagonalization plus renormalization-group theory: Accurate method for a one-dimensional superfluid-insulator-transition study. *Phys. Rev. B*, 53:11776–11778, May 1996.

[71] S. Ejima, H. Fehske, and F. Gebhard. Dynamic properties of the one-dimensional bose-hubbard model. *Europhys. Letters*, 93(03), 2011.

[72] S. M. A. Rombouts, K. Van Houcke, and L. Pollet. Loop updates for quantum Monte Carlo simulations in the canonical ensemble. *Phys. Rev. Lett.*, 96:180603, May 2006.

[73] W. Krauth. Bethe ansatz for the one-dimensional boson Hubbard model. *Phys. Rev. B*, 44(17):9772–9775, November 1991. 174

[74] R. V. Pai, R. Pandit, H. R. Krishnamurthy, and S. Ramasesha. One-dimensional disordered Bosonic Hubbard model: A density-matrix renormalization group study. *Phys. Rev. Lett.*, 76:2937–2940, Apr 1996.

[75] G.G. Batrouni, R. T. Scalettar, and G. T. Zimanyi. Quantum critical phenomena in one-dimensional bose systems. *Phys. Rev. Lett.*, 65:1765–1768, Oct 1990.

[76] M. Pino, J. Prior, A. M. Somoza, D. Jaksch, and S. R. Clark. Reentrance and entanglement in the one-dimensional bose-hubbard model. *Phys. Rev. A*, 86:023631, Aug 2012.

[77] M. Läuchli and C. Kollath. Spreading of correlations and entanglement after a quench in the one-dimensional bose-hubbard model. *J. Stat. Mech.: Theor. Exp.*, 2008, 2008. 37

[78] L. Boltzmann. On the relation between the second law of the mechanical theory of heat and probability calculus, respectively the propositions about thermal equilibrium. *Proceedings of the Imperial Academy of Sciences*, 76:373–435, 1877. 37

[79] J. W. Gibbs. *Elementary Principles in Statistical Mechanics*. Yale University Press, 1902. 37

[80] C. E. Shannon. A mathematical theory of communication. *Bell System Technical Journal*, 27:379–423, 1948. 37

[81] J. von Neumann. *Mathematical Foundations of Quantum Mechanics*. Springer, 1932. 39

[82] H. Radhakrishnan, M. Thamm, H. Barghathi, B. Rosenow, and A. Del Maestro. A scaling function for the particle entanglement of fermions. *J. Stat. Mech.: Theor. Exp.*, 2023(05):08310, 2023. 40, 45, 49, 114, 125

[83] P. Löwdin. Quantum theory of many-particle systems. I. physical interpretations by means of density matrices, natural spin-orbitals, and convergence problems in the method of configurational interaction. *Phys. Rev.*, 97(6):1474, 1955. 41

[84] T. Ando. Properties of fermion density matrices, url = https://journals.aps.org/rmp/abstract/10.1103/RevModPhys.35.690, volume = 35, year = 1963. *Rev. Mod. Phys.*, (3):690.

[85] A. J. Coleman. Structure of Fermion Density Matrices. *Rev. Mod. Phys.*, 35(3):668, 1963. 50, 144

[86] F. Sasaki. Eigenvalues of fermion density matrices. *Phys. Rev.*, 138(5B):1338, 1965. 41, 43, 144

[87] A. Del Maestro, H. Barghathi, and B. Rosenow. Equivalence of spatial and particle entanglement growth after a quantum quench. *Phys. Rev. B*, 104(19):195101, 2021. 41, 47, 85, 127, 145, 159, 161

[88] E. A. Carlen, E. H. Lieb, and R. Reuvers. Entropy and entanglement bounds for reduced density matrices of fermionic states. *Communications in Mathematical Physics*, 344(3):655, 2016. 43, 50, 125, 128

[89] M. Lemm. On the entropy of fermionic reduced density matrices, 2017. 43, 50, 144

[90] H. Katsura and Y. Hatsuda. Entanglement entropy in the Calogero–Sutherland model. *J. Phys. A: Math. Theor.*, 40(46):13931, 2007. 43, 50, 126

[91] H. Barghathi, E. Casiano-Diaz, and A. Del Maestro. Particle partition entanglement of one dimensional spinless fermions. *J. Stat. Mech.: Theor. Exp.*, 2017(8):083108, 2017. 43, 50, 59, 126, 148

[92] M. Thamm, H. Radhakrishnan, H. Barghathi, B. Rosenow, and A. Del Maestro. One-particle entanglement for one-dimensional spinless fermions after an interaction quantum quench. *Phys. Rev. B*, 106(16):165116, 2022. 43, 46, 47, 53, 56, 63, 68, 92, 96, 98, 114, 125, 126, 146

[93] C. M. Herdman and A. Del Maestro. Particle partition entanglement of bosonic Luttinger liquids. *Phys. Rev. B*, 91(18):184507, 2015. 43, 45, 50, 126, 148, 190

[94] N. Killoran, M. Cramer, and M. B. Plenio. Extracting Entanglement from Identical Particles. *Phys. Rev. Lett.*, 112(15):150501, 2014. 45

[95] C. Lanczos. An iteration method for the solution of the eigenvalue problem of linear differential and integral operators. *J. Res. Natl. Bur. Stand.*, 45(4):255, 1950. 46, 145

[96] H. Barghathi, C. Usadi, M. Beck, and A. Del Maestro. Compact unary coding for bosonic states as efficient as conventional binary encoding for fermionic states. *Phys. Rev. B*, 105:L121116, Mar 2022. 46, 146, 182, 183, 184

[97] S. R. White. Density matrix formulation for quantum renormalization groups. *Phys. Rev. Lett.*, 69:2863–2866, Nov 1992. 47

[98] S. R. White and R. M. Noack. Real-space quantum renormalization groups. *Phys. Rev. Lett.*, 68:3487–3490, Jun 1992. 47

[99] P. Zanardi. Quantum entanglement in fermionic lattices. *Phys. Rev. A*, 65(4):042101, 2002. 49, 126

[100] Y. Shi. Quantum entanglement of identical particles. *Phys. Rev. A*, 67(2):024301, 2003. 126

[101] A. Bulgac. Entanglement entropy, single-particle occupation probabilities, and short-range correlations, 2022. 49

[102] L.-A. Wu, M. S. Sarandy, and D. A. Lidar. Quantum phase transitions and bipartite entanglement. *Physical review letters*, 93(25):250404, 2004. 50, 127

[103] B. Wei. Linking phase transitions and quantum entanglement at arbitrary temperature. *Physical Review A*, 97(4):042115, 2018. 50, 127

[104] S. Iblisdir, J. I. Latorre, and R. Orús. Entropy and exact matrix-product representation of the laughlin wave function. *Phys. Rev. Lett.*, 98:060402, Feb 2007. 50

[105] S. Pu, A. C. Balram, and Z. Papić. Local density of states and particle entanglement in topological quantum fluids, 2022. 126

[106] A. Hudomal, N. Regnault, and I. Vasić. Bosonic fractional quantum hall states in driven optical lattices. *Phys. Rev. A*, 100:053624, Nov 2019.

[107] Z. Liu and H. Fan. Particle entanglement in rotating gases. *Phys. Rev. A*, 81:062302, Jun 2010. 50

[108] C. Simon. Natural entanglement in Bose-Einstein condensates. *Phys. Rev. A.*, 66, 2002. 50

[109] C. M. Herdman, P. N. Roy, R. G. Melko, and A. Del Maestro. Particle entanglement in continuum many-body systems via quantum Monte Carlo. *Phys. Rev. B*, 89(14):140501(R), 2014. 50, 126

[110] C. M. Herdman, S. Inglis, P. N. Roy, R. G. Melko, and A. Del Maestro. Path-integral Monte Carlo method for Rényi entanglement entropies. *Phys. Rev. E*, 90(1):013308, 2014. 126

[111] Mohd. Imran, M. A. H. Ahsan, and M. Rafat. Novel phases in rotating Bose condensed gas: vortices and quantum correlation, 2022. 50

[112] L. Rammelmüller, W. J. Porter, J. Braun, and J. E. Drut. Evolution from few- to many-body physics in one-dimensional fermi systems: One- and two-body density matrices and particle-partition entanglement. *Phys. Rev. A*, 96(3):033635, September 2017. 50, 126

[113] F. Iemini, T. O. Maciel, and R. O. Vianna. Entanglement of indistinguishable particles as a probe for quantum phase transitions in the extended Hubbard model. *Phys. Rev. B*, 92(7):075423, 2015. 87

[114] D. L. B. Ferreira, T. O. Maciel, R. O. Vianna, and F. Iemini. Quantum correlations, entanglement spectrum, and coherence of the two-particle reduced density matrix in the extended Hubbard model. *Phys. Rev. B*, 105(11):115145, 2022. 50, 126

[115] R. Santachiara, F. Stauffer, and D. C. Cabra. Entanglement properties and momentum distributions of hard-core anyons on a ring. *J. Stat. Mech.: Theor. Exp.*, 2007(05):05003, 2007. 50, 126

[116] P. Calabrese and J. Cardy. Entanglement entropy and quantum field theory. *J. Stat. Mech.: Theor. Exp.*, 2004(06):06002, 2004. 50

[117] B. C. Carlson and Joseph M. Keller. Eigenvalues of Density Matrices. *Phys. Rev.*, 121(3):659, 1961. 51, 144

[118] M. A. Cazalilla. Effect of Suddenly Turning on Interactions in the Luttinger Model. *Phys. Rev. Lett.*, 97(15):156403, 2006. 56, 93, 96, 127

[119] M. Fishman, S. R. White, and E. M. Stoudenmire. The ITensor Software Library for Tensor Network Calculations. *SciPost Phys. Codebases*, page 4, 2022. 61, 113, 145, 161, 182

[120] H. Radhakrishnan, M. Thamm, H. Barghathi, B. Rosenow, and A. Del Maestro, 2023. All code, scripts and data used in this work are included in a GitHub repository: https://github.com/DelMaestroGroup/papers-code-scalingParticleEE. 62, 68

[121] E. Casiano-Diaz, C. M. Herdman, and A. Del Maestro. A path integral ground state Monte Carlo algorithm for entanglement of lattice bosons, 2022. 85

[122] E. Altman, E. Demler, and M. D. Lukin. Probing many-body states of ultracold atoms via noise correlations. *Phys. Rev. A*, 70:013603, Jul 2004. 87

[123] M. Boll, T. A. Hilker, G. Salomon, A. Omran, J. Nespolo, L. Pollet, I. Bloch, and C. Gross. Spin- and density-resolved microscopy of antiferromagnetic correlations in Fermi-Hubbard chains. *Science*, 353(6305):1257–1260, 2016. 87

[124] T. L. Yang, P. Grišins, Y. T. Chang, Z. H. Zhao, C. Y. Shih, T. Giamarchi, and R. G. Hulet. Measurement of the dynamical structure factor of a 1d interacting fermi gas. *Phys. Rev. Lett.*, 121:103001, Sep 2018. 87, 92

[125] A. Bulgac, M. Kafker, and I. Abdurrahman. Measures of complexity and entanglement in fermionic many-body systems, 2022. 87

[126] D. A. Mazziotti. Structure of fermionic density matrices: Complete n-representability conditions. *Phys. Rev. Lett.*, 108:263002, Jun 2012. 87

[127] P. Naldesi, A. Elben, A. Minguzzi, D. Clément, P. Zoller, and B. Vermersch. Fermionic correlation functions from randomized measurements in programmable atomic quantum devices. *Phys. Rev. Lett.*, 131:060601, Aug 2023. 87

[128] A. Polkovnikov, E. Altman, and E. Demler. Interference between independent fluctuating condensates. *Proc. Nat. Acad. Sci.*, 103(16):6125, 2006. 125, 127, 128

[129] V. Gritsev, E. Altman, E. Demler, and A. Polkovnikov. Full quantum distribution of contrast in interference experiments between interacting one-dimensional Bose liquids. *Nature Phys.*, 2(10):705, 2006. 87, 127, 128

[130] S. Moitra and R. Sensarma. Building entanglement entropy out of correlation functions for interacting fermions. *Phys. Rev. B*, 108:174309, Nov 2023. 87

[131] D. L. B. Ferreira, T. O. Maciel, R. O. Vianna, and F. Iemini. Quantum correlations, entanglement spectrum, and coherence of the two-particle reduced density matrix in the extended Hubbard model. *Phys. Rev. B*, 105(11):115145, 2022. 87

[132] N. Baldelli, B. Kloss, M. Fishman, and A. Wietek. Fragmented superconductivity in the hubbard model as solitons in ginzburg-landau theory. *arXiv preprint arXiv:2307.11820*, 2023. 87, 92, 123

[133] N. H. Aase and A. Sudbø. Dominant superconducting correlations in a luttinger liquid induced by spin fluctuations. *Phys. Rev. B*, 106:L241102, Dec 2022. 87

[134] R. Mukhopadhyay, C. L. Kane, and T. C. Lubensky. Sliding luttinger liquid phases. *Phys. Rev. B*, 64:045120, Jul 2001.

[135] C. L. Kane, A. Stern, and B. I. Halperin. Pairing in luttinger liquids and quantum hall states. *Phys. Rev. X*, 7:031009, Jul 2017. 87

[136] C. Nayak. Density-wave states of nonzero angular momentum. *Physical Review B*, 62(8):4880, 2000. 87, 121

[137] M. A. Cazalilla. Bosonizing one-dimensional cold atomic gases. *Journal of Physics B: Atomic, Molecular and Optical Physics*, 37(7):S1, mar 2004. 105, 240

[138] G. Giuliani and G. Vignale. *Quantum Theory of the Electron Liquid*. Cambridge University Press, Cambridge, 2005. 117

[139] D. A. Mazziotti. Contracted schrödinger equation: Determining quantum energies and two-particle density matrices without wave functions. *Phys. Rev. A*, 57:4219–4234, Jun 1998. 125

[140] M. Srednicki. Chaos and quantum thermalization. *Phys. Rev. E*, 50(2):888, 1994. 126

[141] M. Rigol, V. Dunjko, and M. Olshanii. Thermalization and its mechanism for generic isolated quantum systems. *Nature*, 452(7189):854, 2008.

[142] A. Polkovnikov, K. Sengupta, A. Silva, and M. Vengalattore. Colloquium: Nonequilibrium dynamics of closed interacting quantum systems. *Rev. Mod. Phys.*, 83(3):863, 2011.

[143] L. D'Alessio, Y. Kafri, A. Polkovnikov, and M. Rigol. From quantum chaos and eigenstate thermalization to statistical mechanics and thermodynamics. *Adv. in Phys.*, 65(3):239, 2016. 126

[144] F. Iemini, T. O. Maciel, and R. O. Vianna. Entanglement of indistinguishable particles as a probe for quantum phase transitions in the extended Hubbard model. *Phys. Rev. B*, 92(7):075423, 2015. 126

[145] S. Lin, B. Sbierski, F. Dorfner, C. Karrasch, and F. Heidrich-Meisner. Many-body localization of spinless fermions with attractive interactions in one dimension. *SciPost Physics*, 4(1), January 2018. 127

[146] M. Hopjan, F. Heidrich-Meisner, and V. Alba. Scaling properties of a spatial one-particle density-matrix entropy in many-body localized systems. *Phys. Rev. B*, 104(3):035129, 2021. 127

[147] N. Killoran, M. Cramer, and M. B. Plenio. Extracting Entanglement from Identical Particles. *Phys. Rev. Lett.*, 112(15):150501, 2014. 127

[148] A. Del Maestro, H. Barghathi, and B. Rosenow. Measuring postquench entanglement entropy through density correlations. *Phys. Rev. Research*, 4:L022023, Apr 2022. 127

[149] J. G. Kirkwood and E. M. Boggs. The Radial Distribution Function in Liquids. *J. Chem. Phys.*, 10(6):394, 1942. 127, 172

[150] H. S. Green. *The Molecular Theory of Fluids*. Norh-Holland, Amsterdam, 1952. 127

[151] G. S. Uhrig. Interaction quenches of Fermi gases. *Phys. Rev. A*, 80(6):061602(R), 2009. 127

[152] B. Dóra, M. Haque, and G. Zaránd. Crossover from Adiabatic to Sudden Interaction Quench in a Luttinger Liquid. *Phys. Rev. Lett.*, 106(15):156406, 2011. 127

[153] T. Dao, A. Georges, J. Dalibard, C. Salomon, and I. Carusotto. Measuring the One-Particle Excitations of Ultracold Fermionic Atoms by Stimulated Raman Spectroscopy. *Phys. Rev. Lett.*, 98(24):240402, 2007. 128

[154] A. Damascelli. Probing the Electronic Structure of Complex Systems by ARPES. *Phys. Scr.*, T109:61, 2004. 128, 192

[155] M. Lemm and M. M. Wilde. Information-theoretic limitations on approximate quantum cloning and broadcasting. *Phys. Rev. A*, 96(1):012304, 2017. 128, 144

[156] J. Des Cloizeaux. A Soluble Fermi–Gas Model. Validity of Transformations of the Bogoliubov Type. *Journal of Mathematical Physics*, 7(12):2136–2144, 1966. 128

[157] C. N. Yang and C. P. Yang. One-Dimensional Chain of Anisotropic Spin-Spin Interactions. I. Proof of Bethe's Hypothesis for Ground State in a Finite System. *Physical Review*, 150(1):321–327, 1966. 128

[158] S. R. Manmana, S. Wessel, R. M. Noack, and A. Muramatsu. Strongly Correlated Fermions after a Quantum Quench. *Phys. Rev. Lett.*, 98(21):210405, 2007. 128

[159] S. R. Manmana, S. Wessel, R. M. Noack, and A. Muramatsu. Time evolution of correlations in strongly interacting fermions after a quantum quench. *Physical Review B*, 79(15):155104, April 2009.

[160] M. Rigol. Breakdown of thermalization in finite one-dimensional systems. *Physical Review Letters*, 103(10):100403, sep 2009.

[161] M. S. Foster, T. C. Berkelbach, D. R. Reichman, and E. A. Yuzbashyan. Quantum quench spectroscopy of a Luttinger liquid: Ultrarelativistic density wave dynamics due to fractionalization in an xxz chain. *Physical Review B*, 84(8):085146, August 2011.

[162] E. Coira, F. Becca, and A. Parola. Quantum quenches in one-dimensional gapless systems. *The European Physical Journal B*, 86(2), February 2013. 128

[163] N. N. Bogoljubov. On a new method in the theory of superconductivity. *Il Nuovo Cimento (1955-1965)*, 7(6):794–805, 1958. 137

[164] A. G. Del Maestro and M. J. P. Gingras. Quantum spin fluctuations in the dipolar Heisenberg-like rare earth pyrochlores. *Journal of Physics: Condensed Matter*, 16(20):3339–3353, 2004. 137

[165] C. N. Yang. Concept of off-diagonal long-range order and the quantum phases of liquid He and of superconductors. *Rev. Mod. Phys.*, 34(4):694, 1962. 144

[166] S. Cheong and C. L. Henley. Many-body density matrices for free fermions. *Phys. Rev. B*, 69(7):075111, 2004. 144

[167] M. Thamm, H. Radhakrishnan, H. Barghathi, B. Rosenow, and A. Del Maestro. All code, scripts and data used in this work are included in a GitHub repository: https://github.com/DelMaestroGroup/papers-code-OneParticleEntanglementEntropy. *https://github.com/DelMaestroGroup*, 2022. 144

[168] H. Q. Lin. Exact diagonalization of quantum-spin models. *Phys. Rev. B*, 42(10):6561, 1990. 147

[169] H. Flyvbjerg and H. G. Petersen. Error estimates on averages of correlated data. *The Journal of Chemical Physics*, 91(1):461–466, 1989. 161

[170] M. Suzuki. Generalized Trotter's formula and systematic approximants of exponential operators and inner derivations with applications to many-body problems. *Communications in Mathematical Physics*, 51(2):183–190, 1976. 162

[171] S. Paeckel, T. Köhler, A. Swoboda, S. R. Manmana, U. Schollwöck, and C. Hubig. Time-evolution methods for matrix-product states. *Ann. Phys.*, 411:167998, 2019. 162

[172] M. Thamm, H. Radhakrishnan, H. Barghathi, C. M. Herdman, A. Biswas, B. Rosenow, and A. Del Maestro. Berezinskii-Kosterlitz-Thouless renormalization group flow at a quantum phase transition. *arXiv preprint arXiv:2502.18622*, 2025. 13 pages, 8 figures. 173, 179, 182, 184

[173] J. M. Kosterlitz and D. J. Thouless. Ordering, metastability and phase transitions in two-dimensional systems. *Journal of Physics C*, 6:1181–1203, 1973. 173

[174] H. Weber and P. Minnhagen. Monte carlo determination of the critical temperature for the two-dimensional XY model. *Phys. Rev. B*, 37(10):5986–5989, April 1988. 173

[175] Yun-Da Hsieh, Ying-Jer Kao, and Anders W. Sandvik. Finite-size scaling method for the Berezinskii–Kosterlitz–Thouless transition. *J. Stat. Mech: Theor. Exp.*, 2013(09):P09001, September 2013.

[176] A. W. Sandvik and R. G. Melko. Ground-state phases and quantum phase transitions in a two-dimensional spin-1/2 XY model with four-spin interactions. *Ann. Phys.*, 321(7):1651–1668, July 2006.

[177] W. Zhang, J. Liu, and T. Wei. Machine learning of phase transitions in the percolation and XY models. *Phys. Rev. E*, 99(3):032142, March 2019.

[178] P. H. Nguyen and M. Boninsegni. Superfluid transition and specific heat of the 2D X-Y model: Monte Carlo simulation. *App. Sci.*, 11(11):4931, January 2021. 173

[179] L. Vanderstraeten, B. Vanhecke, A. M. Läuchli, and F. Verstraete. Approaching the Kosterlitz-Thouless transition for the classical XY model with tensor networks. *Phys. Rev. E*, 100(6):062136, December 2019. 173

[180] R. G. Jha. Critical analysis of two-dimensional classical XY model. *J. Stat. Mech: Theor. Exp.*, 2020(8):083203, August 2020.

[181] A. Ueda and M. Oshikawa. Resolving the Berezinskii-Kosterlitz-Thouless transition in the two-dimensional XY model with tensor-network-based level spectroscopy. *Phys. Rev. B*, 104(16):165132, October 2021. 173, 174

[182] P. Minnhagen. The two-dimensional coulomb gas, vortex unbinding, and superfluid-superconducting films. *Rev. Mod. Phys.*, 59(4):1001, 1987. 173

[183] A.T. Fiory, A.F. Hebard, and W.I. Glaberson. Superconducting phase transitions in indium/indium-oxide thin-film composites. *Phys. Rev. B*, 28(9):5075, 1983. 173

[184] D. Matthey, N. Reyren, J.M. Triscone, and T. Schneider. Electric-field-effect modulation of the transition temperature, mobile carrier density, and in-plane penetration depth of $NdBa_2Cu_3O_7-\delta$ thin films. *Phys. Rev. Lett.*, 98(5):057002, 2007.

[185] A. Kamlapure, M. Mondal, M. Chand, A. Mishra, J. Jesudasan, V. Bagwe, L. Benfatto, V. Tripathi, and P. Raychaudhuri. Measurement of magnetic penetration depth and superconducting energy gap in very thin epitaxial nbn films. *App. Phys. Lett.*, 96(7), 2010.

[186] P.K. Rout and R.C. Budhani. Interface superconductivity in $La_{1.48}Nd_{0.4}Sr_{0.12}CuO_4/La_{1.84}Sr_{0.16}CuO_4$ bilayers. *Phys. Rev. B*, 82(2):024518, 2010.

[187] A.M. Goldman. The Berezinskii–Kosterlitz–Thouless transition in superconductors. In *40 Years of Berezinskii–Kosterlitz–Thouless Theory*, pages 135–160. World Scientific, 2013.

[188] A. Y. Mironov, D. M. Silevitch, T. Proslier, S. V. Postolova, M. V. Burdastyh, A. K. Gutakovskii, T. F. Rosenbaum, V. V. Vinokur, and T. I. Baturina. Charge Berezinskii-Kosterlitz-Thouless transition in superconducting NbTiN films. *Sci. Rep.*, 8(1):4082, 2018. 173

[189] L. Capriotti, A. Cuccoli, A. Fubini, V. Tognetti, and R. Vaia. *Berezinskii-Kosterlitz-Thouless Transition in Josephson Junction Arrays*, pages 203–216. Springer Netherlands, Dordrecht, 2004. 173

[190] C. G. L. Bøttcher, F. Nichele, J. Shabani, C. J. Palmstrøm, and C. M. Marcus. Berezinskii-Kosterlitz-Thouless transition and anomalous metallic phase in a hybrid Josephson junction array. *Phys. Rev. B*, 110:L180502, Nov 2024. 173

[191] A. Reich, D. S. Shapiro, and A. Shnirman. Berezinskii-Kosterlitz-Thouless transitions in a topological superconductor-ferromagnet-superconductor junction. *arXiv:2410.22514*, 2024. 174

[192] Z. Hadzibabic, P. Krüger, M. Cheneau, B. Battelier, and J. Dalibard. Berezinskii–Kosterlitz–Thouless crossover in a trapped atomic gas. *Nature*, 441(7097):1118–1121, 2006. 174

[193] C. Castelnovo, C. Chamon, C. Mudry, and P. Pujol. Zero-temperature Kosterlitz–Thouless transition in a two-dimensional quantum system. *Ann. Phys.*, 322(4):903–934, 2007. 174

[194] R. G. Melko, A. W. Sandvik, and D. J. Scalapino. Aspect-ratio dependence of the spin stiffness of a two-dimensional XY model. *Phys. Rev. B*, 69(1):014509, January 2004. 174

[195] A. Masaki-Kato, S. Yunoki, and D. S. Hirashima. Quantum Monte Carlo study of the superfluid density in quasi-one-dimensional systems of hard-core bosons: Effect of the suppression of phase slippage. *Phys. Rev. B*, 100(22):224515, December 2019.

[196] Robert Schaffer, Anton A. Burkov, and Roger G. Melko. Superfluid phases of lattice bosons with ring-exchange interaction. *Phys. Rev. B*, 80(1):014503, July 2009.

[197] S. A. Owerre. Spin wave theory of spin-1/2 xy model with ring exchange on a triangular lattice. *Can. J. Phys.*, 91(7):542–547, July 2013.

[198] H. Shao, W. Guo, and A. W Sandvik. Monte carlo renormalization flows in the space of relevant and irrelevant operators: Application to three-dimensional clock models. *Phys. Rev. Lett.*, 124(8):080602, 2020. 174

[199] T. Stöferle, H. Moritz, C. Schori, T. Köhl, and T. Esslinger. Transition from a strongly interacting 1D superfluid to a Mott insulator. *Physical Review Letters*, 92(13):130403, 2004. 174, 192

[200] E. Haller, R. Hart, M. J. Mark, J. G. Danzl, L. Reichsöllner, M. Gustavsson, M. Dalmonte, G. Pupillo, and H. Nägerl. Pinning quantum phase transition for a Luttinger liquid of strongly interacting bosons. *Nature*, 466:597–600, 2010. 174

[201] K. V. Krutitsky. Ultracold bosons with short-range interaction in regular optical lattices. *Phy. Rep.*, 607:1–101, 2016. 174

[202] V. F. Elesin, V. A. Kashurnikov, and L. A. Openov. Mott-insulator-superfluid-liquid transition in a 1D boson. *JETP Lett.*, 60(3), 1994. 174

[203] G. Roux, T. Barthel, I. P. McCulloch, C. Kollath, U. Schollwöck, and T. Giamarchi. Quasiperiodic Bose-Hubbard model and localization in one-dimensional cold atomic gases. *Phys. Rev. A*, 78(2):023628, August 2008. 174, 175

[204] D. Rossini and R. Fazio. Phase diagram of the extended bose–hubbard model. *New J. Phys.*, 14(6):065012, jun 2012.

[205] A. M. Läuchli and C. Kollath. Spreading of correlations and entanglement after a quench in the one-dimensional Bose–Hubbard model. *J. Stat. Mech: Theor. Exp.*, 2008(05):P05018, May 2008.

[206] S. Ejima, H. Fehske, and F. Gebhard. Dynamic properties of the one-dimensional Bose-Hubbard model. *Europhys. Lett.*, 93(3):30002, February 2011. 175

[207] J. Carrasquilla, S. R Manmana, and M. Rigol. Scaling of the gap, fidelity susceptibility, and bloch oscillations across the superfluid-to-Mott-insulator transition in the one-dimensional Bose-Hubbard model. *Phys. Rev. A*, 87(4):043606, 2013. 174

[208] L. Cincio, M. M. Rams, J. Dziarmaga, and W. H. Zurek. Universal shift of the fidelity susceptibility peak away from the critical point of the Berezinskii-Kosterlitz-Thouless quantum phase transition. *Phys. Rev. B*, 100(8):081108, 2019. 174

[209] M. M Rams, P. Czarnik, and L. Cincio. Precise extrapolation of the correlation function asymptotics in uniform tensor network states with application to the Bose-Hubbard and XXZ models. *Phys. Rev. X*, 8(4):041033, 2018. 174

[210] G. G. Batrouni and R. T. Scalettar. World-line quantum Monte Carlo algorithm for a one-dimensional Bose model. *Phys. Rev. B*, 46(14):9051–9062, October 1992. 174

[211] M. Gerster, M. Rizzi, F. Tschirsich, P. Silvi, R. Fazio, and S. Montangero. Superfluid density and quasi-long-range order in the one-dimensional disordered Bose–Hubbard model. *New J. Phys.*, 18(1):015015, January 2016.

[212] V. A. Kashurnikov, A. V. Krasavin, and B. V. Svistunov. Mott-insulator-superfluid-liquid transition in a one-dimensional bosonic Hubbard model: Quantum Monte Carlo method. *JETP Lett.*, 64(2):99–104, July 1996.

[213] S. Bergkvist, A. Rosengren, R. Saers, E. Lundh, M. Rehn, and A. Kastberg. Transition from a two-dimensional superfluid to a one-dimensional Mott insulator. *Phys. Rev. Lett.*, 99(11):110401, September 2007. 174

[214] J. Zakrzewski and D. Delande. Accurate determination of the superfluid-insulator transition in the one-dimensional Bose-Hubbard model. *AIP Conf. Proc.*, 1076(1):292–300, November 2008. 174

[215] I. Danshita and A. Polkovnikov. Superfluid-to-mott-insulator transition in the one-dimensional Bose-Hubbard model for arbitrary integer filling factors. *Phys. Rev. A*, 84(6):063637, December 2011.

[216] M. Pino, J. Prior, A. M. Somoza, D. Jaksch, and S. R. Clark. Reentrance and entanglement in the one-dimensional Bose-Hubbard model. *Phys. Rev. A*, 86:023631, Aug 2012.

[217] Z. Zuo, S. Yin, X. Cao, and F. Zhong. Scaling theory of the Kosterlitz-Thouless phase transition. *Phys. Rev. B*, 104(21):214108, December 2021. 174

[218] D. Contessi, A. Recati, and M. Rizzi. Phase diagram detection via gaussian fitting of number probability distribution. *Phys. Rev. B*, 107(12):l121403, March 2023. 174

[219] A. N. Artemov. 2D vortex gas in a superconducting finite width strip. *J. Low Temp. Phys.*, 139(1–2):3, April 2005. 174, 175, 182

[220] A. Holz and C. Gong. Boundary correlation functions and interface formation in two-dimensional solids. *Physica A: Stat. Mech. App.*, 146(1–2):255, 1987.

[221] F Falo, L M Floria, and R Navarro. Monte Carlo simulations of finite-size effects in Kosterlitz Thouless systems. *J. Phys.: Cond. Matt.*, 1(31):5139–5150, August 1989. 174

[222] A. E Mattsson, S. Eggert, and H. Johannesson. Properties of a Luttinger liquid with boundaries at finite temperature and size. *Physical Review B*, 56(24):15615, 1997. 176, 254

[223] Sebastian Eggert and Ian Affleck. Magnetic impurities in half-integer-spin heisenberg antiferromagnetic chains. *Physical Review B*, 46(17):10866, 1992. 176, 254

[224] G. Boéris, L. Gori, M. D. Hoogerland, A. Kumar, E. Lucioni, L. Tanzi, M. Inguscio, T. Giamarchi, C. D'Errico, G. Carleo, G. Modugno, and L. Sanchez-Palencia. Mott transition for strongly interacting one-dimensional bosons in a shallow periodic potential. *Phys. Rev. A*, 93(1):011601, January 2016. 176

[225] V. Zauner-Stauber, L. Vanderstraeten, M. T. Fishman, F. Verstraete, and J. Haegeman. Variational optimization algorithms for uniform matrix product states. *Phys. Rev. B*, 97(4):045145, 2018. 177

[226] T. Giamarchi. Mott transition in one dimension. *Physica B: Cond. Matt.*, 230–232:975–980, February 1997. 180

[227] F. D. M. Haldane. Effective Harmonic-Fluid Approach to Low-Energy Properties of One-Dimensional Quantum Fluids. *Phys. Rev. Lett.*, 47(25):1840, 1981. 180

[228] V. Zauner-Stauber, L. Vanderstraeten, M.T. Fishman, F. Verstraete, and J. Haegeman. Variational optimization algorithms for uniform matrix product states. *Phys. Rev. B*, 97(4):045145, 2018. 183

[229] M. Yang and S. R. White. Time-dependent variational principle with ancillary Krylov subspace. *Phys. Rev. B*, 102:094315, Sep 2020. 183

[230] M. A. Metlitski and T. Grover. Entanglement entropy of systems with spontaneously broken continuous symmetry. *arXiv:1112.5166*, 2011. 184

[231] B. Kulchytskyy, C. M. Herdman, S. Inglis, and R. G. Melko. Detecting Goldstone modes with entanglement entropy. *Phys. Rev. B*, 92:115146, Sep 2015. 184

[232] M. Thamm, A. Biswas, and A. Del Maestro. Github repository. `https://github.com/DelMaestroGroup/papers-code-BKTFlowBoseHubbard`, 2025. 184

[233] M. Thamm and A. Del Maestro. Raw quantum Monte Carlo data for the 1D Bose Hubbard model. `https://zenodo.org/records/14879282`, 2025. 184

[234] P. Calabrese, J. Cardy, and E. Tonni. Finite temperature entanglement negativity in conformal field theory. *J. Physics A: Mathematical and Theoretical*, 2015(48):015006, 2015. 191

[235] T. Lu and T. Grover. Structure of quantum entanglement at a finite temperature critical point. *Physical Review Research*, 2(4):043345, 2020. 191

[236] H. M. Yoo, M. Korkusinski, D. Miravet, K. W. Baldwin, K. West, L. Pfeiffer, P. Hawrylak, and R. C. Ashoori. Time, momentum, and energy resolved pump-probe tunneling spectroscopy of two-dimensional electron systems. *Nature Communications*, 14(1):7440, 2023. 192

[237] A. Damascelli, Z. Hussain, and Z. Shen. Angle-resolved photoemission studies of the cuprate superconductors. *Reviews of Modern Physics*, 75(2):473–541, 2003. 192

[238] L. Perfetti, P. A. Loukakos, M. Lisowski, U. Bovensiepen, H. Berger, S. Biermann, P. S. Cornaglia, A. Georges, and M. Wolf. Time evolution of the electronic structure of 1T-TaS_2 through the insulator–metal transition. *Physical Review Letters*, 97(6):067402, 2006. 192

[239] P. Ardila, Luis A., M. Heyl, and A. Eckardt. Measuring the single-particle density matrix for fermions and hard-core bosons in an optical lattice. *Phys. Rev. Lett.*, 121:260401, Dec 2018. 192

[240] T. Liu, Luogen Xu, J. Liu, and Y. Wang. Entanglement witness for indistinguishable electrons using solid-state spectroscopy. *Phys. Rev. X*, 15:011056, Mar 2025. 192

[241] A. M. Tsvelik. *Quantum Field Theory in Condensed Matter Physics*. Cambridge University Press, 2 edition, 2003. 236

[242] M. A. Cazalilla, R. Citro, T. Giamarchi, E. Orignac, and M. Rigol. One dimensional bosons: From condensed matter systems to ultracold gases. *Rev. Mod. Phys.*, 83(4):1405–1466, 2011. 254

APPENDICES

RÉNYI ENTANGLEMENT ENTROPY UNDER TWO BIPARTITIONS

A

In this appendix, we derive the von Neumann entanglement entropy for two spinless bosons occupying two lattice sites under the one-dimensional Bose–Hubbard model at unit filling for both a spatial and particle bipartition.

A.1 The two-site Bose–Hubbard Hamiltonian

The general Bose–Hubbard Hamiltonian in one dimension reads

$$H \;=\; -J\sum_i \big(b_i^\dagger\, b_{i+1} + \text{h.c.}\big) \;+\; \frac{U}{2}\sum_i n_i(n_i-1) \;-\; \sum_i \mu_i\, n_i\,,$$

where J is the nearest-neighbor hopping amplitude, U the on-site interaction strength, and μ_i the local chemical potential. In what follows, we set $\mu_i = 0$ on both sites. The bosonic creation and annihilation operators satisfy

$$b^\dagger\,|n\rangle = \sqrt{n+1}\,|n+1\rangle\,, \qquad b\,|n\rangle \;=\; \sqrt{n}\,|n-1\rangle\,, \tag{A.1}$$

and $n_i = b_i^\dagger\, b_i$ counts the number of bosons on site i. We focus on the subspace with exactly two bosons distributed over two sites (labelled 1 and 2).

Splitting the Hamiltonian into kinetic (hopping) and interaction parts, $H = H_{\text{K.E.}} + V_{\text{int}}$, we have, for two sites,

$$H_{\text{K.E.}} \;=\; -J\,\big(b_1^\dagger\, b_2 + b_2^\dagger\, b_1\big)\,V_{\text{int}} \;=\; \frac{U}{2}\Big[n_1(n_1-1) + n_2(n_2-1)\Big]. \tag{A.2}$$

A.2 Spatial entanglement

A.2.1 Matrix representation

Since there are two bosons on two sites, the Hilbert space (with no more than two bosons per site) is spanned by the occupation–number basis:

$$\{\ |2,0\rangle\ ,\ |1,1\rangle\ ,\ |0,2\rangle\ \}, \quad \text{where } |n_1,\, n_2\rangle \equiv |n_1\rangle_A \otimes |n_2\rangle_B\ .$$

We now compute the matrix elements of $H_{\text{K.E.}}$ and V_{int} in this basis.

(i) Hopping term $H_{\text{K.E.}}$: Using

$$b_1^\dagger\, b_2\ |n_1, n_2\rangle = \sqrt{n_2}\,\sqrt{n_1+1}\ |n_1+1, n_2-1\rangle\ ,$$

one finds that $|2,0\rangle$ and $|0,2\rangle$ do not couple directly, while both couple to $|1,1\rangle$ with amplitude $-\sqrt{2}\,J$. All diagonal matrix elements of $H_{\text{K.E.}}$ vanish, since hopping changes the occupation. Explicitly:

$$\begin{aligned}
&\langle 2,0|\ H_{\text{K.E.}}\ |2,0\rangle = 0, \quad \langle 1,1|\ H_{\text{K.E.}}\ |1,1\rangle = 0, \quad \langle 0,2|\ H_{\text{K.E.}}\ |0,2\rangle = 0,\\
&\langle 2,0|\ H_{\text{K.E.}}\ |1,1\rangle = -J\langle 2,0|b_1^\dagger\, b_2 + b_2^\dagger\, b_1|1,1\rangle = -\sqrt{2}\,J,\\
&\langle 1,1|\ H_{\text{K.E.}}\ |2,0\rangle = -\sqrt{2}\,J,\\
&\langle 1,1|\ H_{\text{K.E.}}\ |0,2\rangle = -\sqrt{2}\,J,\\
&\langle 0,2|\ H_{\text{K.E.}}\ |1,1\rangle = -\sqrt{2}\,J,\\
&\langle 2,0|\ H_{\text{K.E.}}\ |0,2\rangle = 0, \quad \langle 0,2|\ H_{\text{K.E.}}\ |2,0\rangle = 0.
\end{aligned}$$

Therefore, in the ordered basis $\{|2,0\rangle, |1,1\rangle, |0,2\rangle\}$,

$$H_{\text{K.E.}} = \begin{pmatrix} 0 & -\sqrt{2}\,J & 0 \\ -\sqrt{2}\,J & 0 & -\sqrt{2}\,J \\ 0 & -\sqrt{2}\,J & 0 \end{pmatrix}. \tag{A.3}$$

(ii) Interaction term V_{int}: Recall

$$V_{\text{int}} = \frac{U}{2}\big[n_1(n_1-1) + n_2(n_2-1)\big].$$

Nonzero contributions arise only when any site has at least two bosons. In our basis:

$$\begin{aligned} \langle 2,0|\ V_{\text{int}}\ |2,0\rangle &= \frac{U}{2}\big[2\cdot(2-1) + 0\cdot(0-1)\big] = U, \\ \langle 1,1|\ V_{\text{int}}\ |1,1\rangle &= \frac{U}{2}\big[1\cdot(1-1) + 1\cdot(1-1)\big] = 0, \\ \langle 0,2|\ V_{\text{int}}\ |0,2\rangle &= \frac{U}{2}\big[0\cdot(0-1) + 2\cdot(2-1)\big] = U, \\ \langle i,j|\ V_{\text{int}}\ |k,\ell\rangle &= 0, \quad \text{for any off-diagonal basis states,} \end{aligned}$$

by orthogonality of distinct Fock states. Thus,

$$V_{\text{int}} = \begin{pmatrix} U & 0 & 0 \\ 0 & 0 & 0 \\ 0 & 0 & U \end{pmatrix}. \tag{A.4}$$

(iii) Full Hamiltonian: Summing the two contributions,

$$H \;=\; H_{\text{K.E.}} + V_{\text{int}} \;=\; \begin{pmatrix} U & -\sqrt{2}\,J & 0 \\ -\sqrt{2}\,J & 0 & -\sqrt{2}\,J \\ 0 & -\sqrt{2}\,J & U \end{pmatrix}. \tag{A.5}$$

A.2.2 *Reduced density matrix*

Let the normalized ground-state wavefunction of Eq. (A.5) be

$$|\Psi\rangle \;=\; \alpha\;|2,0\rangle \;+\; \beta\;|1,1\rangle \;+\; \gamma\;|0,2\rangle\;, \tag{A.6}$$

where the coefficients $\alpha, \beta, \gamma \in \mathbb{C}$ are determined by diagonalizing the 3×3 matrix in Eq. (A.6) and normalizing $|\alpha|^2 + |\beta|^2 + |\gamma|^2 = 1$.

The full density operator is

$$\rho \;=\; |\Psi\rangle\,\langle\Psi| \;=\; \begin{pmatrix} \alpha\,\alpha^* & \alpha\,\beta^* & \alpha\,\gamma^* \\ \beta\,\alpha^* & \beta\,\beta^* & \beta\,\gamma^* \\ \gamma\,\alpha^* & \gamma\,\beta^* & \gamma\,\gamma^* \end{pmatrix}, \tag{A.7}$$

in the basis $|2,0\rangle\,, |1,1\rangle\,, |0,2\rangle$. To compute the entanglement entropy for the spatial bipartition (A = site 1, B = site 2), we compute the reduced density matrix $\rho_A = \mathrm{Tr}_B\,\rho$. We label the local Fock states on site 2 by $\{|0\rangle\,, |1\rangle\,, |2\rangle\}_B$. Then

$$\begin{aligned} \rho_A \;&=\; \sum_{n_B=0}^{2} {}_B\langle n_B|\;\rho\;|n_B\rangle_B \\ &=\; {}_B\langle 0|\;\rho\;|0\rangle_B \;+\; {}_B\langle 1|\;\rho\;|1\rangle_B \;+\; {}_B\langle 2|\;\rho\;|2\rangle_B\,. \end{aligned} \tag{A.8}$$

Since

$$|\Psi\rangle = \alpha\;|2\rangle_A \otimes |0\rangle_B \;+\; \beta\;|1\rangle_A \otimes |1\rangle_B \;+\; \gamma\;|0\rangle_A \otimes |2\rangle_B\,,$$

the partial traces yield

$${}_B\langle 0|\;\rho\;|0\rangle_B \;=\; |\alpha|^2\;|2\rangle_A\,\langle 2|_A\,, \quad {}_B\langle 1|\;\rho\;|1\rangle_B \;=\; |\beta|^2\;|1\rangle_A\,\langle 1|_A\;{}_B\langle 2|\;\rho\;|2\rangle_B \;=\; |\gamma|^2\;|0\rangle_A\,\langle 0|_A\,.$$

Hence, in the local basis $\{|2\rangle_A, |1\rangle_A, |0\rangle_A\}$,

$$\rho_A = \begin{pmatrix} |\alpha|^2 & 0 & 0 \\ 0 & |\beta|^2 & 0 \\ 0 & 0 & |\gamma|^2 \end{pmatrix}. \tag{A.9}$$

A.2.3 Von Neumann entropy

The von Neumann entanglement entropy is

$$S_A \;=\; -\,\mathrm{Tr}\big(\rho_A \,\ln \rho_A\big).$$

Since ρ_A is already diagonal with eigenvalues $|\alpha|^2$, $|\beta|^2$, and $|\gamma|^2$, we have

$$S_A \;=\; -\Big(\,|\alpha|^2 \,\ln|\alpha|^2 \;+\; |\beta|^2 \,\ln|\beta|^2 \;+\; |\gamma|^2 \,\ln|\gamma|^2\Big). \tag{A.10}$$

A.3 Particle entanglement

A.3.1 Matrix representation

We label the two indistinguishable bosons as "particle 1" and "particle 2" (fictitious labels), and let site indices be 1 or 2. The two-particle basis (symmetric under exchange) can be taken as

$$\{|1_1, 2_1\rangle,\; |1_1, 2_2\rangle,\; |1_2, 2_1\rangle,\; |1_2, 2_2\rangle\},$$

where $|1_i, 2_j\rangle$ means particle 1 is on site i, and particle 2 on site j. In this basis, the ground state (which is symmetric under exchange) is

$$|\Psi\rangle = \alpha\;|1_1, 2_1\rangle \;+\; \frac{\beta}{\sqrt{2}}\big(|1_1, 2_2\rangle + |1_2, 2_1\rangle\big) \;+\; \gamma\;|1_2, 2_2\rangle\,,$$

with $\alpha = \gamma$ by reflection symmetry and normalization $2|\alpha|^2 + |\beta|^2 = 1$.

A.3.2 Full density matrix

In the ordered basis $\{|1_1, 2_1\rangle, |1_1, 2_2\rangle, |1_2, 2_1\rangle, |1_2, 2_2\rangle\}$,

$$\rho = |\Psi\rangle\langle\Psi| = \begin{pmatrix} |\alpha|^2 & \frac{\alpha\beta^*}{\sqrt{2}} & \frac{\alpha\beta^*}{\sqrt{2}} & \alpha\gamma^* \\ \frac{\beta\alpha^*}{\sqrt{2}} & \frac{|\beta|^2}{2} & \frac{|\beta|^2}{2} & \frac{\beta\gamma^*}{\sqrt{2}} \\ \frac{\beta\alpha^*}{\sqrt{2}} & \frac{|\beta|^2}{2} & \frac{|\beta|^2}{2} & \frac{\beta\gamma^*}{\sqrt{2}} \\ \gamma\alpha^* & \frac{\gamma\beta^*}{\sqrt{2}} & \frac{\gamma\beta^*}{\sqrt{2}} & |\gamma|^2 \end{pmatrix},$$

where $\gamma = \alpha$.

A.3.3 Reduced density matrix

To obtain the reduced density for "particle 1" (subsystem A), we trace out "particle 2" (subsystem B):

$$\rho_A = \mathrm{Tr}_B(\rho) = \sum_{j=1}^{2} {}_B\langle 2_j| \ \rho \ |2_j\rangle_B .$$

We label single-particle basis states for A as $\{|1_1\rangle, |1_2\rangle\}$. Then

$$\rho_A = \begin{pmatrix} |\alpha|^2 + \frac{|\beta|^2}{2} & \frac{\alpha\beta^* + \beta\gamma^*}{\sqrt{2}} \\ \frac{\alpha^*\beta + \beta^*\gamma}{\sqrt{2}} & |\gamma|^2 + \frac{|\beta|^2}{2} \end{pmatrix}.$$

Using $\gamma = \alpha$ and $2|\alpha|^2 + |\beta|^2 = 1$, the diagonal entries each become $\frac{1}{2}$. Moreover,

$$\alpha\beta^* + \beta\gamma^* = 2\alpha\beta^*, \quad \alpha^*\beta + \beta^*\gamma = 2\alpha^*\beta,$$

so

$$\rho_A = \begin{pmatrix} \frac{1}{2} & \sqrt{2}\,\alpha\,\beta^* \\ \sqrt{2}\,\alpha^*\,\beta & \frac{1}{2} \end{pmatrix}.$$

A.3.4 Von Neumann entropy

The eigenvalues $\lambda_\pm$ of ρ_A satisfy

$$\det\Big(\rho_A - \lambda I\Big) = \Big(\tfrac{1}{2} - \lambda\Big)^2 - 2\,|\alpha\,\beta|^2 \;=\; 0,$$

i.e.

$$\lambda^2 - \lambda + \Big(\tfrac{1}{4} - 2\,|\alpha\,\beta|^2\Big) = 0.$$

Since $|\beta|^2 = 1 - 2|\alpha|^2$,

$$2\,|\alpha\,\beta|^2 = 2\,|\alpha|^2\,(1 - 2|\alpha|^2) = 2\,\alpha^2 - 4\,\alpha^4, \quad \text{(assuming real } \alpha, \beta\text{)}.$$

Thus,

$$\lambda_\pm = \frac{1 \pm \sqrt{1 - 4\big(\frac{1}{4} - 2\alpha^2 + 4\alpha^4\big)}}{2} = \frac{1 \pm 2\sqrt{-4\alpha^4 + 2\alpha^2}}{2}.$$

The particle partition entanglement entropy is

$$S_A^{(\text{particle})} = -\sum_{s=\pm} \lambda_s\,\ln\lambda_s = -\,\big(\,\lambda_+\ln\lambda_+ + \lambda_-\ln\lambda_-\big).$$

Here α is determined by diagonalizing the full Hamiltonian in Section A.1, and $\beta = \sqrt{1 - 2\alpha^2}$.

A.4 Explicit ground-state coefficients as functions of U and J

In the two-boson, two-site Bose–Hubbard model, the Hamiltonian in the $\{|2,0\rangle, |1,1\rangle, |0,2\rangle\}$ basis is

$$H = \begin{pmatrix} U & -\sqrt{2}\,J & 0 \\ -\sqrt{2}\,J & 0 & -\sqrt{2}\,J \\ 0 & -\sqrt{2}\,J & U \end{pmatrix}.$$

Because H commutes with the translation operator T, one can block-diagonalize H into irreducible subspaces with a definite translation eigenvalue. In particular,

$$T|1,1\rangle = |1,1\rangle, \quad T|2,0\rangle = |0,2\rangle, \quad T^2|2,0\rangle = |2,0\rangle.$$

Hence

$$\phi_+ = \tfrac{1}{\sqrt{2}}\big(|2,0\rangle + |0,2\rangle\big), \quad \phi_- = \tfrac{1}{\sqrt{2}}\big(|2,0\rangle - |0,2\rangle\big),$$

are eigenvectors of T with eigenvalues $+1$ and -1, respectively. The sector spanned by $\{\phi_+, |1,1\rangle\}$ carries translation eigenvalue $+1$, while ϕ_- is a one-dimensional sector with eigenvalue -1. Since the ground state lies in the symmetric $(+1)$ sector, we focus on the 2×2 block acting on $\{\phi_+, |1,1\rangle\}$.

A.4.1 Block-diagonalization

First, reorder rows and columns of H by swapping the second and third basis vectors:

$$H = \begin{pmatrix} U & -\sqrt{2}J & 0 \\ -\sqrt{2}J & 0 & -\sqrt{2}J \\ 0 & -\sqrt{2}J & U \end{pmatrix} \longrightarrow \begin{pmatrix} U & 0 & -\sqrt{2}J \\ 0 & U & -\sqrt{2}J \\ -\sqrt{2}J & -\sqrt{2}J & 0 \end{pmatrix}.$$

Next, we apply a 45° rotation R on the first two rows and columns to switch from $\{|2,0\rangle, |0,2\rangle\}$ to $\{\phi_+, \phi_-\}$, where

$$R = \begin{pmatrix} \cos 45^\circ & \sin 45^\circ & 0 \\ -\sin 45^\circ & \cos 45^\circ & 0 \\ 0 & 0 & 1 \end{pmatrix} = \begin{pmatrix} \frac{1}{\sqrt{2}} & \frac{1}{\sqrt{2}} & 0 \\ -\frac{1}{\sqrt{2}} & \frac{1}{\sqrt{2}} & 0 \\ 0 & 0 & 1 \end{pmatrix}.$$

Under this rotation,

$$R^T \begin{pmatrix} U & 0 & -\sqrt{2}J \\ 0 & U & -\sqrt{2}J \\ -\sqrt{2}J & -\sqrt{2}J & 0 \end{pmatrix} R = \begin{pmatrix} U & 0 & -2J \\ 0 & U & 0 \\ -2J & 0 & 0 \end{pmatrix}.$$

Finally, we cam reverse the earlier row-/column swaps to return to the original ordering $\{|2,0\rangle, |1,1\rangle, |0,2\rangle\}$. The net result is a block-diagonal Hamiltonian of the form

$$H \longrightarrow \begin{pmatrix} U & -2J & 0 \\ -2J & 0 & 0 \\ 0 & 0 & U \end{pmatrix}.$$

Thus (i) one eigenvalue is simply

$$\lambda_0 = U \quad \text{(from the one-dimensional } \phi_- \text{ sector)},$$

and (ii) the remaining two eigenvalues arise from the 2×2 block $\begin{pmatrix} U & -2J \\ -2J & 0 \end{pmatrix}$. Its characteristic equation is

$$\det\Big(\begin{pmatrix} U & -2J \\ -2J & 0 \end{pmatrix} - \lambda\, I\Big) = (U-\lambda)\,(0-\lambda) - 4J^2 = 0,$$

$$\implies \lambda^2 - U\lambda - 4J^2 = 0 \implies \lambda_\pm = \frac{U \pm \sqrt{U^2 + 16J^2}}{2}.$$

The lowest eigenvalue is therefore

$$\lambda_- \;=\; \frac{U - \sqrt{U^2 + 16J^2}}{2}.$$

A.4.2 Ground state coefficients

Let $|\Psi\rangle = \alpha\ |2,0\rangle \ +\ \beta\ |1,1\rangle \ +\ \gamma\ |0,2\rangle$ be the normalized ground-state eigenvector of H with energy λ_-. By symmetry under translation (and reflection), one expects $\alpha = \gamma$. Enforcing

$$H\ |\Psi\rangle \;=\; \lambda_-\ |\Psi\rangle$$

in components gives

$$\begin{pmatrix} U-\lambda_- & -\sqrt{2}\,J & 0 \\ -\sqrt{2}\,J & -\lambda_- & -\sqrt{2}\,J \\ 0 & -\sqrt{2}\,J & U-\lambda_- \end{pmatrix} \begin{pmatrix} \alpha \\ \beta \\ \gamma \end{pmatrix} = 0.$$

Setting $\gamma = \alpha$ and noting that $-\lambda_- = -\frac{U-\sqrt{U^2+16J^2}}{2}$, the first row yields

$$(U - \lambda_-)\,\alpha \;-\; \sqrt{2}\,J\,\beta \;=\; 0 \;\;\Longrightarrow\;\; \Big(U - \tfrac{U-\sqrt{U^2+16J^2}}{2}\Big)\alpha = \sqrt{2}\,J\,\beta.$$

We have

$$U - \lambda_- = U - \frac{U - \sqrt{U^2+16J^2}}{2} = \frac{U + \sqrt{U^2+16J^2}}{2}.$$

Therefore,

$$\frac{U+\sqrt{U^2+16\,J^2}}{2}\,\alpha = \sqrt{2}\,J\,\beta \;\;\Longrightarrow\;\; \beta \;=\; \frac{U+\sqrt{U^2+16J^2}}{2\sqrt{2}\,J}\,\alpha.$$

We define the dimensionless ratio

$$U' \;=\; \frac{U}{J} \quad\Longrightarrow\quad \beta = \left[\frac{U' + \sqrt{(U')^2+16}}{2\sqrt{2}}\right]\alpha.$$

Using the normalizationTr $æ_A = 1$ $|\alpha|^2 + |\beta|^2 + |\gamma|^2 = 1$ with $\gamma = \alpha$ gives

$$1 \;=\; 2\,|\alpha|^2 + |\beta|^2 = 2\,\alpha^2 \;+\; \left[\frac{U' + \sqrt{(U')^2+16}}{2\sqrt{2}}\right]^2 \alpha^2.$$

With some algebra we obtain,

$$\alpha = \sqrt{\frac{4}{(U')^2 + U'\sqrt{(U')^2+16}+16}}.$$

Recalling $\gamma = \alpha$ and $\beta = \big[\frac{U'+\sqrt{(U')^2+16}}{2\sqrt{2}}\big]\alpha$, we obtain the closed-form coefficients

$$\alpha \;=\; \gamma = \sqrt{\frac{4}{U'^2 + U'\,\sqrt{U'^2+16}\,+16}}, \tag{A.11}$$

$$\beta = \left[\frac{U' + \sqrt{U'^2+16}}{2\,\sqrt{2}}\right]\alpha, \tag{A.12}$$

where $U' = U/J$. These satisfy $|\alpha|^2 + |\beta|^2 + |\gamma|^2 = 2\alpha^2 + \beta^2 = 1$.

Eq. (A.12) and Eq. (A.12) thus provide explicit analytic expressions for the ground-state coefficients in terms of the microscopic parameters U and J. Substituting these into S_{spatial} and S_{particle} yields the curves plotted in Fig. 2.8.

ONE PARTICLE ENTANGLEMENT FOR FREE FERMIONS

B

We want to directly prove that the second Rényi 1-particle entanglement entropy for free fermions is given by $\ln N$. Taking the trace of the square of the one-body density matrix squared, we have

$$\begin{aligned} \mathrm{Tr}\left[(\rho_1^0)^2\right] &= \int_{-L/2}^{L/2} dx_2 \int_{-L/2}^{L/2} dx_1 \frac{1}{N^2} \frac{\sin^2(\pi N|x_1 - x_2|/L)}{L^2 \sin^2(\pi|x_1 - x_2|/L)} \\ &= \frac{2}{N^2 L} \int_0^{L/2} dx \frac{\sin^2(N\pi x/L)}{\sin^2(\pi x/L)}, \end{aligned} \tag{B.1}$$

where we have used the translational invariance of the system and made the substitution $x = |x_2 - x_1|$. Next, we make the substitute $x = \theta L/\pi$, which yields

$$\mathrm{Tr}\left[(\rho_1^0)^2\right] = \frac{2}{N^2\pi} \int_0^{\pi/2} d\theta \frac{\sin^2(N\theta)}{\sin^2(\theta)}. \tag{B.2}$$

After we simplify the integral, we define the function $I(N) = \int_0^{\pi/2} d\theta \frac{\sin^2(N\theta)}{\sin^2(\theta)}$. We also define another function to be the difference

$$\begin{aligned} J(N) &= I(N+1) - I(N) \\ &= \int_0^{\pi/2} d\theta \frac{\sin^2([N+1]\,\theta) - \sin^2(N\theta)}{\sin^2(\theta)} \\ &= \int_0^{\pi/2} d\theta \frac{\sin([2N+1]\theta)}{\sin(\theta)}. \end{aligned} \tag{B.3}$$

Again taking the discrete difference of $J(N)$ this time

$$\begin{aligned} J(N+1) - J(N) &= \int_0^{\pi/2} d\theta \frac{\sin([2N+3]\theta) - \sin([2N+1]\theta)}{\sin(\theta)} \\ &= 2\int_0^{\pi/2} d\theta \cos([2N+2]\theta) \\ &= 0, \end{aligned} \tag{B.4}$$

and thus

$$J(N+1) = J(N) = \ldots = J(0). \tag{B.5}$$

We can use this to compute the value of the function $J(N)$ for any N, where

$$\begin{aligned} J(0) &= \int_0^{\pi/2} d\theta \frac{\sin(\theta)}{\sin(\theta)} \\ &= \frac{\pi}{2} = J(N). \end{aligned} \tag{B.6}$$

Plugging this back into Eq. (B.6), we get

$$I(N+1) - I(N) = \frac{\pi}{2}, \tag{B.7}$$

which immediately dictates that

$$\begin{aligned} I(N) &= I(N-1) + \frac{\pi}{2} = \ldots = I(0) + \frac{N\pi}{2} \\ I(0) &= \int_0^{\pi/2} d\theta \frac{\sin^2(N\theta)}{\sin^2(\theta)} = 0 \\ I(N) &= \frac{N\pi}{2}. \end{aligned} \tag{B.8}$$

We can use this in Eq. (B.8),

$$\begin{aligned} \mathrm{Tr}\left[(\rho_1^0)^2\right] &= \frac{2}{N^2\pi} I(N) = \frac{1}{N} \\ \rightarrow S_2(n=1) &= -\ln \mathrm{Tr}\left[(\rho_1^0)^2\right] = \ln N \end{aligned} \tag{B.9}$$

as expected for free fermions.

DERIVATION OF THE TWO BODY DENSITY MATRIX FROM CONFORMAL FIELD THEORY

C

In this appendix, we apply conformal field theory (CFT) techniques to the Luttinger liquid and obtain the two-body density matrix entirely from the operator–product expansion (OPE) of vertex operators $V_\beta(z) = e^{i\beta\phi(z)}$, which are primary fields of the free compact boson CFT discussed in the main text. Following Ref. [241], the holomorphic four-point function factorizes as

$$\left\langle e^{i\beta_1\phi(z_1)} e^{i\beta_2\phi(z_2)} e^{i\beta_3\phi(z_3)} e^{i\beta_4\phi(z_4)} \right\rangle = \prod_{i>j} (z_i - z_j)^{-\beta_i\beta_j}, \tag{C.1}$$

with an identical antiholomorphic copy. Eq. (C.1) arises by repeatedly combining vertex operators via the OPE and using $\langle\phi(z)\phi(0)\rangle = -\ln|z|^2$. We will later contrast this *universal* result with our microscopic calculation, where ultraviolet (UV) cut-off effects and q-dependent interactions modify the exponents and introduce non-universal amplitudes absent from a pure CFT treatment.

C.1 Rewriting the Hamiltonian

We begin with the Luttinger Hamiltonian

$$H = \frac{v}{2\pi} \int_0^L \left[K^{-1}(\partial_x\phi)^2 + K(\partial_x\theta)^2\right] dx,$$

and rewrite it in terms of right- and left-moving fields $\phi_{R/L} = \frac{1}{2}(\phi \mp \theta)$. To exploit the CFT correlator, Eq. (C.1), we diagonalize the quadratic form,

$$H = \frac{v}{2\pi} \int_0^L \left[(\partial_x\tilde{\phi}_R)^2 + (\partial_x\tilde{\phi}_L)^2\right] dx, \tag{C.2}$$

so that $\tilde{\phi}_{R/L}$ obey the free boson action of Eq. (C.2) with compactification radius $R^2 = K$. In this basis, the vertex operators $V_{\alpha,\beta}(z,\bar{z}) = e^{i[\alpha\tilde{\phi}_R(z)+\beta\tilde{\phi}_L(\bar{z})]}$ retain the conformal weights $(\Delta,\bar{\Delta}) = (\alpha^2 K/4\pi, \beta^2 K/4\pi)$ introduced earlier.

C.1.1 *Bogoliubov transformation*

The canonical diagonalization is just a Bogoliubov rotation of the oscillator modes. Writing the original bosons a_q in terms of new modes b_q we have

$$\begin{aligned} a_q &= \cosh\theta_q\, b_q + \sinh\theta_q\, b^\dagger_{-q}, \\ a^\dagger_{-q} &= \sinh\theta_q\, b_q + \cosh\theta_q\, b^\dagger_{-q}, \end{aligned}$$

or, in matrix form,

$$\begin{pmatrix} a_q \\ a^\dagger_{-q} \end{pmatrix} = \begin{pmatrix} \cosh\theta_q & \sinh\theta_q \\ \sinh\theta_q & \cosh\theta_q \end{pmatrix} \begin{pmatrix} b_q \\ b^\dagger_{-q} \end{pmatrix}.$$

The inverse transformation reads

$$\begin{aligned} b_q &= \cosh\theta_q\, a_q - \sinh\theta_q\, a^\dagger_{-q}, \\ b^\dagger_{-q} &= -\sinh\theta_q\, a_q + \cosh\theta_q\, a^\dagger_{-q}, \end{aligned}$$

which eliminates the K-dependent off-diagonal terms and casts the Hamiltonian in the conformal basis.

C.1.2 *Rewriting operators*

We bosonize the chiral fermion fields as

$$\Psi_\alpha(x) = \frac{e^{i\alpha\pi/2}}{\sqrt{2\pi\eta}}\, e^{i\left(\varphi_{0,\alpha}+\alpha\frac{2\pi x}{L}N_\alpha\right)} e^{-i\phi_\alpha(x)}, \tag{C.3}$$

where the Klein factors $\varphi_{0,\alpha}$ and N_α ensure the correct anticommutation rules. The bosonic fields read

$$\phi_\alpha(x) = -\sum_{q>0} C(q)\left[e^{i\alpha qx}\, b_{\alpha q} + e^{-i\alpha qx}\, b_{\alpha q}^\dagger\right], \qquad C(q) = \sqrt{\tfrac{2\pi}{qL}}\, e^{-q\eta/2}. \tag{C.4}$$

The exponentials $e^{\pm i\phi_\alpha}$ coincide with the *vertex operators* $V_{\pm 1}(z) = e^{\pm i\tilde{\phi}_R(z)}$ and $e^{\pm i\tilde{\phi}_L(\bar{z})}$ introduced in Section 2.2; they are primary fields whose OPE fully determines the two-body density matrix via Eq. (C.4).

To diagonalize the Hamiltonian in a conformal basis we define new bosonic operators $a_{\alpha q}$ and corresponding fields

$$\tilde{\phi}_\alpha(x) = -\sum_{q>0} C(q)\left[e^{i\alpha qx}\, a_{\alpha q} - e^{-i\alpha qx}\, a_{\alpha q}^\dagger\right]. \tag{C.5}$$

The fields relate through a *momentum-independent* Bogoliubov rotation,

$$\phi_R = \cosh\theta\, \tilde{\phi}_R + \sinh\theta\, \tilde{\phi}_L, \qquad \phi_L = \cosh\theta\, \tilde{\phi}_L + \sinh\theta\, \tilde{\phi}_R, \tag{C.6}$$

which corresponds to rescaling the compactification radius ($K = e^{2\theta}$). This constant θ keeps the theory fully conformal: no q-dependent interaction remains, so the OPE of primary vertex operators applies.

C.1.3 *Transforming the Hamiltonian*

Substituting $\phi = \phi_R + \phi_L$ and $\theta = \phi_R - \phi_L$ into the Luttinger Hamiltonian yields

$$H = \frac{v}{2\pi}\int_0^L dx\left[(K + K^{-1})\left((\partial_x\phi_R)^2 + (\partial_x\phi_L)^2\right) + 2(K^{-1} - K)\,\partial_x\phi_R\,\partial_x\phi_L\right]. \tag{C.7}$$

Inserting the rotated fields $\tilde{\phi}_{R/L}$ diagonalizes the quadratic form:

$$H = \frac{v}{2\pi}\int_0^L dx\left[(\partial_x\tilde{\phi}_R)^2 + (\partial_x\tilde{\phi}_L)^2\right], \tag{C.8}$$

because $\sinh^2\theta + \cosh^2\theta = \frac{1}{2}(K + K^{-1})$ and $\sinh\theta\cosh\theta = \frac{1}{4}(K - K^{-1})$. The Hamiltonian now matches the free boson CFT fixed point, and all correlators follow directly from the OPE of primary vertex operators described earlier.

C.2 Computing reduced density matrices

With the Hamiltonian fully diagonalized, the vertex operator prefactors in Eq. (C.8) equal one. For the one-body reduced density matrix (1-RDM) we write

$$\begin{aligned}\langle \Psi_R^\dagger(x_2)\Psi_R(x_1)\rangle &= \left\langle e^{-i\cosh\theta\,\tilde{\phi}_R(x_2)} e^{i\cosh\theta\,\tilde{\phi}_R(x_1)}\right\rangle \left\langle e^{-i\sinh\theta\,\tilde{\phi}_L(x_1)} e^{i\sinh\theta\,\tilde{\phi}_L(x_2)}\right\rangle \\ &= \frac{1}{(x_2-x_1)^{\cosh^2\theta}}\,\frac{1}{(x_2-x_1)^{\sinh^2\theta}} \\ &= \frac{1}{(x_2-x_1)^{\cosh^2\theta+\sinh^2\theta}} = \frac{1}{(x_2-x_1)^{\gamma^2+1}},\end{aligned} \tag{C.9}$$

where $\gamma^2 \equiv \cosh^2\theta + \sinh^2\theta - 1 = (K + K^{-1} - 2)/2$. The interacting and non-interacting contributions thus combine into a single scaling exponent $\gamma^2 + 1$, which we can see as analogous to our non-interacting sine functions and interacting terms in the bosonization case.

For completeness, we list the chiral four-point functions obtained by the same OPE procedure (valid for an infinite system):

$$\left\langle \Psi_R^\dagger(x_1)\Psi_R^\dagger(x_2)\Psi_R(x_3)\Psi_R(x_4)\right\rangle = \frac{(x_4-x_3)^{\gamma^2+1}\,(x_2-x_1)^{\gamma^2+1}}{(x_3-x_1)^{\gamma^2+1}\,(x_3-x_2)^{\gamma^2+1}\,(x_4-x_1)^{\gamma^2+1}\,(x_4-x_2)^{\gamma^2+1}}, \tag{C.10}$$

$$\left\langle \Psi_R^\dagger(x_1)\Psi_L^\dagger(x_2)\Psi_R(x_3)\Psi_L(x_4)\right\rangle = \frac{(x_2-x_1)^{\lambda}\,(x_4-x_3)^{\lambda}}{(x_4-x_1)^{\lambda}\,(x_3-x_2)^{\lambda}\,(x_3-x_1)^{\gamma^2+1}\,(x_4-x_2)^{\gamma^2+1}}, \tag{C.11}$$

$$\left\langle \Psi_R^\dagger(x_1)\Psi_L^\dagger(x_2)\Psi_L(x_3)\Psi_R(x_4)\right\rangle = \frac{(x_2-x_1)^{\lambda}\,(x_4-x_3)^{\lambda}}{(x_3-x_1)^{\lambda}\,(x_4-x_2)^{\lambda}\,(x_4-x_1)^{\gamma^2+1}\,(x_3-x_2)^{\gamma^2+1}}. \tag{C.12}$$

The correlators derived above assume an infinite system, i.e. the complex plane. To obtain expressions for a finite ring of length L, or periodic boundary conditions [137], we map the plane to a cylinder of circumference L by the conformal transformation

$$z \;=\; e^{\frac{2\pi}{L}w}, \qquad w \;=\; v\tau + ix, \tag{C.13}$$

where $x \in [0, L)$ is the spatial coordinate and τ is Euclidean time. Under Eq. (C.13), a primary field of weight Δ transforms as

$$\mathcal{O}(w) \;=\; \left(\tfrac{dz}{dw}\right)^{-\Delta}\mathcal{O}(z) \;=\; \left(\tfrac{2\pi}{L}\,e^{\frac{2\pi}{L}w}\right)^{-\Delta}\mathcal{O}(z).$$

Setting all operators at equal imaginary time ($\tau = 0$) and using $z_i - z_j \mapsto \frac{L}{\pi}\sin\!\left[\pi(x_i-x_j)/L\right]$, we obtain the finite-size replacements

$$(x_i - x_j) \;\longrightarrow\; \frac{L}{\pi}\,\sin\!\left[\frac{\pi}{L}(x_i-x_j)\right]. \tag{C.14}$$

Applying Eq. (C.14) to the 1-RDM gives

$$\left\langle \Psi_R^\dagger(x_2)\Psi_R(x_1)\right\rangle_{\text{Cylinder}} \;=\; \left[\frac{\pi/L}{\sin\!\left(\pi(x_2-x_1)/L\right)}\right]^{\gamma^2+1},$$

which reduces to the plane result when $L \to \infty$.

Every factor $(x_i - x_j)^{-\alpha}$ in the plane expressions acquires the same sine substitution:

$$(x_i - x_j)^{-\alpha} \longrightarrow \left[\frac{\pi/L}{\sin\big(\pi(x_i - x_j)/L\big)}\right]^{\alpha}.$$

We can immediately see from this that while conformal field theory can account for finite-size effects and lead us to the interaction dependent scaling exponents, it misses details present in our bosonization expression captured by the UV cutoff and the non-universal prefactors.

DERIVATION OF THE DENSITY-DENSITY CORRELATION FUNCTION

D

The correlation function is given by

$$\begin{aligned}
&\langle \Psi^\dagger(x_2')\Psi^\dagger(x_1')\Psi(x_1)\Psi(x_2)\rangle = \\
&\frac{|\sin(\frac{i\pi\epsilon}{L})|^{2\gamma^2}\cos k_F(x_1'+x_2'-x_1-x_2)}{2L^2}\frac{s_0 h_0^{\gamma^2}}{s_+ s_- h_+^{\gamma^2} h_-^{\gamma^2}} \\
&+\frac{|\sin(\frac{i\pi\epsilon}{L})|^{2\gamma^2}\cos k_F(x_1'+x_2-x_1-x_2')}{2L^2}\frac{h_0^{\lambda}}{s_+ h_-^{\gamma^2} h_+^{\lambda}} \\
&-\frac{|\sin(\frac{i\pi\epsilon}{L})|^{2\gamma^2}\cos k_F(x_1'+x_1-x_2'-x_2)}{2L^2}\frac{h_0^{\lambda}}{s_+ h_+^{\gamma^2} h_-^{\lambda}}.
\end{aligned} \tag{D.1}$$

We want to rewrite this in a way that separates the interaction dependent components of the correlation function. We define a new exponent $\delta = \gamma^2 - \lambda$ and utilize the trignometric identity $\cos(A-B) = \cos(A+B) + 2\sin(A)\sin(B)$. Simplifying and rearranging the terms, the correlation function is now

$$\begin{aligned}
\langle \Psi^\dagger(x_2')\Psi^\dagger(x_1')\Psi(x_1)\Psi(x_2)\rangle = &\frac{|\sin\left(\frac{i\pi}{L}\epsilon\right)|^{2\gamma^2} h_0^{\lambda}}{2L^2 s_+ s_- h_+^{\gamma^2} h_-^{\gamma^2}} \\
&\times \cos(k_F(x_1'+x_2'-x_1-x_2))[s_0 h_0^{\delta} + s_+ h_+^{\delta} - s_- h_-^{\delta}] \\
&+\frac{h_0^{\lambda}}{h_+^{\lambda}}\langle \Psi^\dagger(x_2')\Psi(x_2)\rangle_{int}\langle \Psi^\dagger(x_1')\Psi(x_1)\rangle_{int} \\
&-\frac{h_0^{\lambda}}{h_-^{\lambda}}\langle \Psi^\dagger(x_2')\Psi(x_1)\rangle_{int}\langle \Psi^\dagger(x_1')\Psi(x_2)\rangle_{int}
\end{aligned} \tag{D.2}$$

where $\langle \Psi^\dagger(x_2), \Psi(x_1)\rangle_{int}$ is the one body reduced density matrix,

$$\langle \Psi^\dagger(x_2)\Psi(x_1)\rangle_{int} = \rho_1^0(x_1,x_2)\frac{|\sin(\frac{i\pi}{L}\epsilon)|^{\gamma^2}}{|\sin(\frac{\pi}{L}((x_2-x_1)+i\epsilon)|}$$
$$\rho_1^0(x_1,x_2) = \frac{\sin(k_F(x_2-x_1))}{L\sin(\frac{\pi}{L}(x_2-x_1))} \tag{D.3}$$

We simplify the expression by introducing the relative coordinates $r = x_2 - x_1$, $r' = x_2' - x_1'$, and center-of-mass coordinates $R = \frac{x_1+x_2}{2}$, $R' = \frac{x_1'+x_2'}{2}$, with $\Delta R = R' - R$. The two-body density matrix becomes:

$$\begin{aligned}\langle \Psi^\dagger(x_2')\Psi^\dagger(x_1')\Psi(x_1)\Psi(x_2)\rangle = {} & \frac{|\sin\left(\frac{i\pi}{L}\epsilon\right)|^{2\gamma^2}h_0^\lambda}{L^2 h_+^{\gamma^2}h_-^{\gamma^2}}\cos\left(\frac{2\pi}{L}k_F\Delta R\right) \\ & \times\left\{\frac{(h_0^\Delta - h_0^\Delta)\cos\left(\frac{\pi}{L}(r-r')\right)+(h_+^\Delta-h_0^\Delta)\cos\left(\frac{\pi}{L}(r+r')\right)}{\cos\left(\frac{\pi}{L}(r-r')\right)\cos\left(\frac{2\pi}{L}\Delta R\right)\left[\cos\left(\frac{\pi}{L}(r+r')\right)-\cos\left(\frac{2\pi}{L}\Delta R\right)\right]}\right. \\ & \left. + \frac{(h_-^\Delta - h_+^\Delta)\cos\left(\frac{2\pi}{L}\Delta R\right)}{\cos\left(\frac{\pi}{L}(r-r')\right)\cos\left(\frac{2\pi}{L}\Delta R\right)\left[\cos\left(\frac{\pi}{L}(r+r')\right)-\cos\left(\frac{2\pi}{L}\Delta R\right)\right]}\right\} \\ & + \frac{h_0^\lambda}{h_+^\lambda}\langle\Psi^\dagger(x_2')\Psi(x_2)\rangle_{\text{int}}\langle\Psi^\dagger(x_1')\Psi(x_1)\rangle_{\text{int}} \\ & - \frac{h_0^\lambda}{h_-^\lambda}\langle\Psi^\dagger(x_2')\Psi(x_1)\rangle_{\text{int}}\langle\Psi^\dagger(x_1')\Psi(x_2)\rangle_{\text{int}}.\end{aligned}$$

where we used the identity $\sin(A)\sin(B) = \frac{\cos(A-B)}{2} - \frac{\cos(A+B)}{2}$. As $K = 1$, the exponent $\delta = \gamma^2 - \lambda$ goes to zero along with $\gamma^2 = \lambda = 0$. In the non-interacting limit, the ratios h_0/h_+ and h_0/h_- will go to one, and the first term vanishes. Eq. (D.3) becomes $\langle \Psi^\dagger(x_2')\Psi^\dagger(x_1')\Psi(x_1)\Psi(x_2)\rangle_{free} =$

$\langle \Psi^\dagger(x_2')\Psi(x_2)\rangle_{free}\langle \Psi^\dagger(x_1')\Psi(x_1)\rangle_{free} - \langle \Psi^\dagger(x_2')\Psi(x_1)\rangle_{free}\langle \Psi^\dagger(x_1')\Psi(x_2)\rangle_{free}$ as expected.

$$\begin{aligned}
\rho(x_2', x_1', x_1, x_2) &= \langle \Psi^\dagger(x_2')\Psi^\dagger(x_1')\Psi(x_1)\Psi(x_2)\rangle \\
&= \frac{|h_\epsilon|^{2\gamma^2}|h_{\epsilon,0}|^\lambda}{2L^2 h_{0,+}h_{0,-}|h_{\epsilon,+}h_{\epsilon,-}|^{\gamma^2}} \\
&\times \cos\left(k_F(x_1' + x_2' - x_1 - x_2)\right) \\
&\times \left[h_{0,0}|h_{\epsilon,0}|^\Delta + h_{0,+}|h_{\epsilon,+}|^\Delta - h_{0,-}|h_{\epsilon,-}|^\Delta\right] \\
&+ \frac{|h_{\epsilon,0}|^\lambda}{|h_{\epsilon,+}|^\lambda}\langle \Psi^\dagger(x_2')\Psi(x_2)\rangle\langle \Psi^\dagger(x_1')\Psi(x_1)\rangle \\
&- \frac{|h_{\epsilon,0}|^\lambda}{|h_{\epsilon,-}|^\lambda}\langle \Psi^\dagger(x_2')\Psi(x_1)\rangle\langle \Psi^\dagger(x_1')\Psi(x_2)\rangle
\end{aligned} \tag{D.4}$$

This expression can be written more compactly as $\rho(x_2', x_1', x_1, x_2) = F(X - Y) + W$ where

$$\begin{aligned}
F &= \frac{|h_\epsilon|^{2\gamma^2}|h_{\epsilon,0}|^\lambda}{2L^2|h_{\epsilon,-}h_{\epsilon,+}|^{\gamma^2}} \\
&\times \cos\left(k_F(x_1' + x_2' - x_1 - x_2)\right) \\
X &= \frac{|h_{\epsilon,0}|^\Delta - |h_{\epsilon,-}|^\Delta}{h_{0,+}} \\
Y &= \frac{|h_{\epsilon,0}|^\Delta - |h_{\epsilon,+}|^\Delta}{h_{0,-}} \\
W &= \frac{|h_{\epsilon,0}|^\lambda}{|h_{\epsilon,+}|^\lambda}\langle \Psi^\dagger(x_2')\Psi(x_2)\rangle\langle \Psi^\dagger(x_1')\Psi(x_1)\rangle \\
&- \frac{|h_{\epsilon,0}|^\lambda}{|h_{\epsilon,-}|^\lambda}\langle \Psi^\dagger(x_2')\Psi(x_1)\rangle\langle \Psi^\dagger(x_1')\Psi(x_2)\rangle
\end{aligned}$$

We use the following notation to indicate the various limits, $F_1 = \lim_{x_1' \to x_1} F, F_2 = \lim_{x_2' \to x_2} F_1$, and $F_3 = \lim_{x_2 \to x_1} F_2$. Similarly, we can define the limits for X, Y, Z. Then, we can compute the $x_1' \to x_1$ limit of $\rho(x_2', x_1', x_1, x_2)$ as $F_1(X_1 - Y_1) + W_1$. $F_2(X_2 - Y_2) + W_2$ gives the diagonal elements needed for the density-density correlation function. Finally, we can check that in the limit $r \to 0$ ($x_2 \to x_1$),

$F_3(X_3 - Y_3) + W_3$ gives zero as expected. We start with the F limits which can be done through direct substitution,

$$\begin{aligned} F_1 &= \lim_{x_1' \to x_1} \frac{|h_\epsilon|^{2\gamma^2} |h_{\epsilon,0}|^\lambda}{2L^2 |h_{\epsilon,-} h_{\epsilon,+}|^{\gamma^2}} \\ &\quad \times \cos\left(k_F(x_1' + x_2' - x_1 - x_2)\right) \\ &= \frac{|h_\epsilon|^{2\gamma^2} |h_\epsilon(x_2' - x_1, x_2 - x_1)|^\lambda \cos\left(k_F(x_2' - x_2)\right)}{2L^2 |h_\epsilon(x_1 - x_2, x_2' - x_1)|^{\gamma^2} |h_\epsilon(x_2' - x_2, x_1' - x_1)|^{\gamma^2} |h_\epsilon|^{\gamma^2}} \end{aligned} \tag{D.5}$$

$$F_2 = \frac{|\sin\left(\frac{\pi}{L}((x_2 - x_1) + i\epsilon)\right)|^{2\lambda - 2\gamma^2}}{2L^2} \tag{D.6}$$

$$F_3 = \frac{|h_\epsilon|^{2\lambda - 2\gamma^2}}{2L^2} \tag{D.7}$$

We perform the first two limits of X through direct substitution as well,

$$X_1 = \frac{|h_\epsilon(x_2' - x_1, x_2 - x_1)|^\Delta - |h_\epsilon(x_2' - x_2, 0)|^\Delta}{h_0(x_1 - x_2, x_2' - x_1)} \tag{D.8}$$

$$X_2 = -\frac{|\sin\left(\left(\frac{\pi}{L}((x_2 - x_1) + i\epsilon)\right)\right)|^{2\Delta} - |\sin\left(\frac{i\pi}{L}\epsilon\right)|^{2\Delta}}{\sin^2\left(\frac{\pi}{L}(x_2 - x_1)\right)} \tag{D.9}$$

The third limit, $r \to 0$, is slightly more complicated, so we rewrite the renormalized chord length as $|\sin(x + i\epsilon)|^2 = \sinh^2\left(\frac{\pi}{L}\epsilon\right) + \sin^2\left(\frac{\pi}{L}x\right)$ with the corresponding derivative $\frac{d}{dx}|\sin(x + i\epsilon)|^2 = \frac{\pi}{L}\sin\left(\frac{2\pi}{L}x\right)$. Using the relative coordinate, $r = x_2 - x_1$,

$$\begin{aligned} X_3 &= -\lim_{r \to 0} \frac{|\sin\left(\frac{\pi}{L}(r + i\epsilon)\right)|^{2\Delta} - |\sin\left(\frac{i\pi}{L}\epsilon\right)|^{2\Delta}}{\sin^2\left(\frac{\pi}{L}r\right)} \\ &= -\lim_{r \to 0} \frac{(\sinh^2\left(\frac{\pi}{L}\epsilon\right) + \sin^2\left(\frac{\pi}{L}r\right))^\Delta - |\sin\left(\frac{i\pi}{L}\epsilon\right)|^{2\Delta}}{\sin^2\left(\frac{\pi}{L}r\right)} \\ &= -\lim_{r \to 0} \frac{\Delta(\sinh^2\left(\frac{\pi}{L}\epsilon\right) + \sin^2\left(\frac{\pi}{L}r\right))^{\Delta - 1} \frac{d}{dx}[+\sin^2\left(\frac{\pi}{L}r\right)] - 0}{\frac{d}{dx}[\sin^2\left(\frac{\pi}{L}r\right)]} \\ &= -\Delta|\sin\left(\frac{i\pi}{L}\epsilon\right)|^{2\Delta - 2}. \end{aligned} \tag{D.10}$$

We expect the same result for the Y_3 limit as in the limit $r \to 0$, we want $X_3 - Y_3 = 0$. We deploy L'Hôpital's rule twice to obtain the first two limits. Taking the limit of the numerator of Y, we have

$$\begin{aligned}\frac{\partial}{\partial x_1'} Y_{\text{num}} = \frac{\partial}{\partial x_1'} \Big[&\left|\sin\left(\tfrac{\pi}{L}((x_2' - x_1') + i\epsilon)\right)\right|^{\Delta} \left|\sin\left(\tfrac{\pi}{L}((x_2 - x_1) + i\epsilon)\right)\right|^{\Delta} \\ &- \left|\sin\left(\tfrac{\pi}{L}((x_1' - x_2) + i\epsilon)\right)\right|^{\Delta} \left|\sin\left(\tfrac{\pi}{L}((x_2' - x_1) + i\epsilon)\right)\right|^{\Delta} \Big] \\ - \frac{\Delta}{2}\frac{\pi}{L} &\left|\sin\left(\tfrac{\pi}{L}((x_2 - x_1) + i\epsilon)\right)\right|^{\Delta} \left|\sin\left(\tfrac{\pi}{L}((x_2' - x_1') + i\epsilon)\right)\right|^{\Delta-2} \\ &\times \sin\left(\tfrac{2\pi}{L}(x_2' - x_1')\right) \\ - \frac{\Delta}{2}\frac{\pi}{L} &\left|\sin\left(\tfrac{\pi}{L}((x_2' - x_1) + i\epsilon)\right)\right|^{\Delta} \left|\sin\left(\tfrac{\pi}{L}((x_1' - x_2) + i\epsilon)\right)\right|^{\Delta-2} \\ &\times \sin\left(\tfrac{2\pi}{L}(x_1' - x_2)\right). \end{aligned} \tag{D.11}$$

The limit of the denominator is

$$\begin{aligned}\frac{\partial}{\partial x_1'} \sin\left(\frac{\pi}{L}(x_1' - x_1)\right) \sin\left(\frac{\pi}{L}(x_2' - x_2)\right) = \\ \frac{\pi}{L} \cos\left(\frac{\pi}{L}(x_1' - x_1)\right) \sin\left(\frac{\pi}{L}(x_2' - x_2)\right).\end{aligned}$$

The full expression for Y_1 is therefore given by

$$\begin{aligned} Y_1 &= -\frac{\Delta}{2} \lim_{x_1' \to x_1} \frac{\frac{\pi}{L}|\sin\left(\frac{\pi}{L}((x_2 - x_1) + i\epsilon)\right)|^{\Delta} (|\sin\left(\frac{\pi}{L}((x_2' - x_1') + i\epsilon)\right)|^2)^{\Delta/2-1} \sin\left(\frac{2\pi}{L}(x_2' - x_1')\right)}{\frac{\pi}{L}\cos\left(\frac{\pi}{L}(x_1' - x_1)\right)\sin\left(\frac{\pi}{L}(x_2' - x_2)\right)} \\ &+ \frac{\Delta}{2} \lim_{x_1' \to x_1} \frac{\frac{\pi}{L}|\sin\left(\frac{\pi}{L}((x_2' - x_1) + i\epsilon)\right)|^{\Delta} (|\sin\left(\frac{\pi}{L}((x_1' - x_2) + i\epsilon)\right)|^2)^{\Delta/2-1} \sin\left(\frac{2\pi}{L}(x_1' - x_2)\right)}{\frac{\pi}{L}\cos\left(\frac{\pi}{L}(x_1' - x_1)\right)\sin\left(\frac{\pi}{L}(x_2' - x_2)\right)} \\ &= -\frac{\Delta}{2}(|\sin\left(\frac{\pi}{L}((x_2' - x_1) + i\epsilon)\right)||\sin\left(\frac{\pi}{L}((x_2 - x_1) + i\epsilon)\right)|)^{\Delta-2} \\ &\times \frac{|\sin\left(\frac{\pi}{L}((x_2 - x_1) + i\epsilon)\right)|^2 \sin\left(\frac{2\pi}{L}(x_2' - x_1)\right) + |\sin\left(\frac{\pi}{L}((x_2' - x_1) + i\epsilon)\right)|^2 \sin\left(\frac{2\pi}{L}(x_1 - x_2)\right)}{\sin\left(\frac{\pi}{L}(x_2' - x_2)\right)} \end{aligned} \tag{D.12}$$

Taking the derivative of the numerator gives us

$$\frac{\partial}{\partial x_1'}\mathcal{Y}_{\text{num}} = -\frac{\Delta\pi}{L}\left|\sin\frac{\pi}{L}\left[(x_2-x_1)+i\epsilon\right]\right|^{\Delta}\left|\sin\frac{\pi}{L}\left[(x_2'-x_1')+i\epsilon\right]\right|^{\Delta-2}\sin\frac{2\pi}{L}(x_2'-x_1') - \frac{\Delta\pi}{L}\left|\sin\frac{\pi}{L}\left[(x_2'-x_1)+i\epsilon\right]\right|^{\Delta}\left|\sin\frac{\pi}{L}\left[(x_1'-x_2)+i\epsilon\right]\right|^{\Delta-2}\sin\frac{2\pi}{L}(x_1'-x_2).$$

Now, the limit of the denominator is given by,

$$\frac{\partial}{\partial x_1'}\Big[\sin\tfrac{\pi}{L}(x_1'-x_1)\,\sin\tfrac{\pi}{L}(x_2'-x_2)\Big] = \frac{\pi}{L}\,\cos\tfrac{\pi}{L}(x_1'-x_1)\,\sin\tfrac{\pi}{L}(x_2'-x_2).$$

Therefore, we arrive at

$$\begin{aligned}\mathcal{Y}_1 = -\frac{\Delta}{2}\,&\frac{1}{\sin\frac{\pi}{L}(x_2'-x_2)}\\ &\times\Bigg[\left|\sin\frac{\pi}{L}\left[(x_2-x_1)+i\epsilon\right]\right|^{\Delta}\left|\sin\frac{\pi}{L}\left[(x_2'-x_1)+i\epsilon\right]\right|^{\Delta-2}\sin\tfrac{2\pi}{L}(x_2'-x_1)\\ &\quad+\left|\sin\frac{\pi}{L}\left[(x_2'-x_1)+i\epsilon\right]\right|^{\Delta}\left|\sin\frac{\pi}{L}\left[(x_1-x_2)+i\epsilon\right]\right|^{\Delta-2}\sin\tfrac{2\pi}{L}(x_1-x_2)\Bigg].\end{aligned} \tag{D.13}$$

Now for the limit $x_2' \to x_2$, define

$$\mathcal{Y}_1' = |\sin\tfrac{\pi}{L}[(x_2-x_1)+i\epsilon]|^2\sin\tfrac{2\pi}{L}(x_2'-x_1) + |\sin\tfrac{\pi}{L}[(x_2'-x_1)+i\epsilon]|^2\sin\tfrac{2\pi}{L}(x_1-x_2).$$

Differentiating with respect to x_2',

$$\frac{\partial\mathcal{Y}_1'}{\partial x_2'} = \frac{2\pi}{L}|\sin\tfrac{\pi}{L}[(x_2-x_1)+i\epsilon]|^2\cos\tfrac{2\pi}{L}(x_2'-x_1) + \frac{\pi}{L}\sin\tfrac{2\pi}{L}(x_1-x_2)\sin\tfrac{2\pi}{L}(x_2'-x_1),$$

while

$$\frac{\partial}{\partial x_2'}\sin\tfrac{\pi}{L}(x_2'-x_2) = \frac{\pi}{L}\cos\tfrac{\pi}{L}(x_2'-x_2).$$

A second application of L'Hôpital yields

$$Y_2 = -\frac{\Delta}{2}\,|\sin\tfrac{\pi}{L}[(x_2-x_1)+i\epsilon]|^{2\Delta-4}\Big[2|\sin\tfrac{\pi}{L}[(x_2-x_1)+i\epsilon]|^2\cos\tfrac{2\pi}{L}(x_2-x_1) - \sin^2\tfrac{2\pi}{L}(x_2-x_1)\Big]. \tag{D.14}$$

Finally, for the limit $x_2 \to x_1$, we get

$$Y_3 = \lim_{x_2\to x_1} Y_2 = -\Delta\big|\sin\tfrac{i\pi}{L}\epsilon\big|^{2\Delta-2},$$

in agreement with the independent result for X_3 as expected.

Finally we evaluate the W limits. First we write,

$$W = \frac{h_0^\lambda}{h_+^\lambda}\,\langle\Psi^\dagger(x_2')\Psi(x_2)\rangle_{\rm int}\langle\Psi^\dagger(x_1')\Psi(x_1)\rangle_{\rm int} - \frac{h_0^\lambda}{h_-^\lambda}\,\langle\Psi^\dagger(x_2')\Psi(x_1)\rangle_{\rm int}\langle\Psi^\dagger(x_1')\Psi(x_2)\rangle_{\rm int}, \tag{D.15}$$

where the one-body reduced density matrix is

$$\langle\Psi^\dagger(x_2)\Psi(x_1)\rangle_{\rm int} = \rho_1^0(x_1,x_2)\,\frac{\big|\sin\big(\frac{i\pi}{L}\epsilon\big)\big|^{\gamma^2}}{\big|\sin\big(\frac{\pi}{L}[(x_2-x_1)+i\epsilon]\big)\big|^{\gamma^2}}, \tag{D.16}$$

$$\rho_1^0(x_1,x_2) = \frac{\sin\big[k_F(x_2-x_1)\big]}{L\,\sin\big(\frac{\pi}{L}(x_2-x_1)\big)}. \tag{D.17}$$

We can insert these to obtain

$$
\begin{aligned}
W = &\left|\sin\!\left(\tfrac{\pi}{L}[(x_2'-x_1')+i\epsilon]\right)\right|^{\lambda}\left|\sin\!\left(\tfrac{\pi}{L}[(x_2-x_1)+i\epsilon]\right)\right|^{\lambda}\left|\sin\!\left(\tfrac{i\pi}{L}\epsilon\right)\right|^{2\gamma^2}\\
&\times\Bigg\{\frac{\sin[k_F(x_2'-x_2)]\,\sin[k_F(x_1'-x_1)]\left|\sin\!\left(\tfrac{\pi}{L}[(x_2'-x_2)+i\epsilon]\right)\right|^{-\gamma^2}}{L^2\,\sin\!\left(\tfrac{\pi}{L}(x_2'-x_2)\right)\,\sin\!\left(\tfrac{\pi}{L}(x_1'-x_1)\right)\left|\sin\!\left(\tfrac{\pi}{L}[(x_1'-x_2)+i\epsilon]\right)\right|^{\lambda}\left|\sin\!\left(\tfrac{\pi}{L}[(x_2'-x_1)+i\epsilon]\right)\right|^{\lambda}}\\
&\quad\times\frac{1}{\left|\sin\!\left(\tfrac{\pi}{L}[(x_1'-x_1)+i\epsilon]\right)\right|^{\gamma^2}}\\
&\quad-\frac{\sin[k_F(x_2'-x_1)]\,\sin[k_F(x_1'-x_2)]\left|\sin\!\left(\tfrac{\pi}{L}[(x_2'-x_1)+i\epsilon]\right)\right|^{-\gamma^2}}{L^2\,\sin\!\left(\tfrac{\pi}{L}(x_2'-x_1)\right)\,\sin\!\left(\tfrac{\pi}{L}(x_1'-x_2)\right)\left|\sin\!\left(\tfrac{\pi}{L}[(x_2'-x_2)+i\epsilon]\right)\right|^{\lambda}\left|\sin\!\left(\tfrac{\pi}{L}[(x_1'-x_1)+i\epsilon]\right)\right|^{\lambda}}\\
&\quad\times\frac{1}{\left|\sin\!\left(\tfrac{\pi}{L}[(x_1'-x_2)+i\epsilon]\right)\right|^{\gamma^2}}\Bigg\}.
\end{aligned}
\tag{D.18}
$$

Taking the first limit,

$$
\begin{aligned}
W_1 = &\left|\sin\tfrac{\pi}{L}[(x_2'-x_1)+i\epsilon]\right|^{\lambda}\left|\sin\tfrac{\pi}{L}[(x_2-x_1)+i\epsilon]\right|^{\lambda}\left|\sin\tfrac{i\pi}{L}\epsilon\right|^{2\gamma^2}\\
&\times\Bigg[\frac{\frac{k_F}{L}\,\sin[k_F(x_2'-x_2)]\,\left|\sin\tfrac{\pi}{L}[(x_2'-x_2)+i\epsilon]\right|^{-\gamma^2}}{L\,\sin\!\left(\tfrac{\pi}{L}(x_2'-x_2)\right)\,\left|\sin\tfrac{\pi}{L}[(x_1-x_2)+i\epsilon]\right|^{\lambda}\,\left|\sin\tfrac{\pi}{L}[(x_2'-x_1)+i\epsilon]\right|^{\lambda}\,\left|\sin\tfrac{i\pi}{L}\epsilon\right|^{\gamma^2}}\\
&\quad-\frac{\sin[k_F(x_2'-x_1)]\,\sin[k_F(x_1-x_2)]\,\left|\sin\tfrac{\pi}{L}[(x_2'-x_1)+i\epsilon]\right|^{-\gamma^2}}{L^2\,\sin\!\left(\tfrac{\pi}{L}(x_2'-x_1)\right)\,\sin\!\left(\tfrac{\pi}{L}(x_1-x_2)\right)\,\left|\sin\tfrac{\pi}{L}[(x_2'-x_2)+i\epsilon]\right|^{\lambda}\,\left|\sin\tfrac{i\pi}{L}\epsilon\right|^{\lambda}}\\
&\quad\times\frac{1}{\left|\sin\tfrac{\pi}{L}[(x_1-x_2)+i\epsilon]\right|^{\gamma^2}}\Bigg].
\end{aligned}
\tag{D.19}
$$

Next, $x_2'\to x_2$ yields

$$
W_2=\rho_0^2-\left|\sin\tfrac{i\pi}{L}\epsilon\right|^{2\gamma^2-2\lambda}\frac{\sin^2[k_F(x_2-x_1)]}{L^2\sin^2(\frac{\pi}{L}(x_2-x_1))}\frac{1}{\left|\sin\!\left(\tfrac{\pi}{L}[(x_2-x_1)+i\epsilon]\right)\right|^{2\gamma^2-2\lambda}}.
\tag{D.20}
$$

Finally, letting $x_2 \to x_1$ gives

$$W_3 = \rho_0^2 - \left|\sin\tfrac{i\pi}{L}\epsilon\right|^{2\gamma^2-2\lambda}\left|\sin\tfrac{i\pi}{L}\epsilon\right|^{-2\gamma^2+2\lambda}\frac{N^2}{L^2} = 0.$$

We can now assemble the final limits. Starting with $x_1' \to x_1$:

$$\begin{aligned}
\lim_{x_1'\to x_1}\langle\Psi^\dagger(x_2')\Psi^\dagger(x_1')\Psi(x_1)\Psi(x_2)\rangle &= F_1(X_1-Y_1)+W_1 \\
&= \frac{\left|\sin\frac{i\pi}{L}\epsilon\right|^{2\gamma^2}\left|\sin\frac{\pi}{L}[(x_2'-x_1)+i\epsilon]\right|^{\lambda}\left|\sin\frac{\pi}{L}[(x_2-x_1)+i\epsilon]\right|^{\lambda}}{2L^2\left|\sin\frac{\pi}{L}[(x_1-x_2)+i\epsilon]\right|^{\gamma^2}\left|\sin\frac{\pi}{L}[(x_2'-x_1)+i\epsilon]\right|^{\gamma^2}\left|\sin\frac{\pi}{L}[(x_2'-x_2)+i\epsilon]\right|^{\gamma^2}\left|\sin\frac{i\pi}{L}\epsilon\right|^{\gamma^2}} \\
&\quad\times\cos\big[k_F(x_2'-x_2)\big] \\
&\quad\times\Bigg\{\frac{\left|\sin\frac{\pi}{L}[(x_2'-x_1)+i\epsilon]\right|^{\Delta}\left|\sin\frac{\pi}{L}[(x_2-x_1)+i\epsilon]\right|^{\Delta}-\left|\sin\frac{\pi}{L}[(x_2'-x_2)+i\epsilon]\right|^{\Delta}\left|\sin\frac{i\pi}{L}\epsilon\right|^{\Delta}}{\sin\big(\frac{\pi}{L}(x_1-x_2)\big)\sin\big(\frac{\pi}{L}(x_2'-x_1)\big)} \\
&\qquad+\frac{\Delta}{2}\Big[\left|\sin\tfrac{\pi}{L}[(x_2'-x_1)+i\epsilon]\right|\left|\sin\tfrac{\pi}{L}[(x_2-x_1)+i\epsilon]\right|\Big]^{\Delta-2} \\
&\qquad\quad\times\frac{\left|\sin\frac{\pi}{L}[(x_2-x_1)+i\epsilon]\right|^2\sin\big(\frac{2\pi}{L}(x_2'-x_1)\big)+\left|\sin\frac{\pi}{L}[(x_2'-x_1)+i\epsilon]\right|^2\sin\big(\frac{2\pi}{L}(x_1-x_2)\big)}{\sin\big(\frac{\pi}{L}(x_2'-x_2)\big)}\Bigg\} \\
&\quad+\left|\sin\tfrac{\pi}{L}[(x_2'-x_1)+i\epsilon]\right|^{\lambda}\left|\sin\tfrac{\pi}{L}[(x_2-x_1)+i\epsilon]\right|^{\lambda}\left|\sin\tfrac{i\pi}{L}\epsilon\right|^{2\gamma^2} \\
&\qquad\times\Bigg[\frac{\frac{N}{L}}{\left|\sin\frac{\pi}{L}[(x_1-x_2)+i\epsilon]\right|^{\lambda}\left|\sin\frac{\pi}{L}[(x_2'-x_1)+i\epsilon]\right|^{\lambda}}\cdot\frac{\sin\big[k_F(x_2'-x_2)\big]}{L\sin\big(\frac{\pi}{L}(x_2'-x_2)\big)} \\
&\qquad\quad\cdot\frac{\left|\sin\frac{i\pi}{L}\epsilon\right|^{\gamma^2}}{\left|\sin\frac{\pi}{L}[(x_2'-x_2)+i\epsilon]\right|^{\gamma^2}} \\
&\qquad-\frac{\left|\sin\frac{\pi}{L}[(x_2'-x_2)+i\epsilon]\right|^{-\lambda}\left|\sin\frac{i\pi}{L}\epsilon\right|^{-\lambda}\sin\big[k_F(x_2'-x_1)\big]\sin\big[k_F(x_1-x_2)\big]}{L^2\sin\big(\frac{\pi}{L}(x_2'-x_1)\big)\sin\big(\frac{\pi}{L}(x_1-x_2)\big)\left|\sin\frac{\pi}{L}[(x_2'-x_1)+i\epsilon]\right|^{\gamma^2}} \\
&\qquad\quad\times\frac{1}{\left|\sin\frac{\pi}{L}[(x_1-x_2)+i\epsilon]\right|^{\gamma^2}}\Bigg].
\end{aligned} \tag{D.21}$$

Finally, we can obtain an expression for the density-density correlation function.

$$\lim_{x_2' \to x_2} \lim_{x_1' \to x_1} \left\langle \Psi^\dagger(x_2')\, \Psi^\dagger(x_1')\, \Psi(x_1)\, \Psi(x_2) \right\rangle = F_2(X_2 - Y_2) + W_2$$

$$= \frac{\left|\sin\!\left(\frac{\pi}{L}[(x_2 - x_1) + i\epsilon]\right)\right|^{2\lambda - 2\gamma^2}}{2\,L^2} \Bigg\{ - \frac{\left|\sin\!\left(\frac{\pi}{L}[(x_2 - x_1) + i\epsilon]\right)\right|^{2\Delta} \; - \; \left|\sin\!\left(\frac{i\pi}{L}\,\epsilon\right)\right|^{2\Delta}}{\sin^2\!\left(\frac{\pi}{L}\,(x_2 - x_1)\right)}$$

$$+ \; \frac{\Delta}{2} \left|\sin\!\left(\frac{\pi}{L}[(x_2 - x_1) + i\epsilon]\right)\right|^{2\Delta - 4}$$

$$\times \left[2 \left|\sin\!\left(\frac{\pi}{L}[(x_2 - x_1) + i\epsilon]\right)\right|^2 \cos\!\left(\frac{2\pi}{L}\,(x_2 - x_1)\right) \; - \; \sin^2\!\left(\frac{2\pi}{L}\,(x_2 - x_1)\right) \right] \Bigg\}$$

$$+ \; \rho_0^2 \; - \; \frac{\left|\sin\!\left(\frac{i\pi}{L}\,\epsilon\right)\right|^{2\Delta} \sin^2\!\left(k_F\,(x_2 - x_1)\right)}{L^2 \, \sin^2\!\left(\frac{\pi}{L}\,(x_2 - x_1)\right) \left|\sin\!\left(\frac{\pi}{L}[(x_2 - x_1) + i\epsilon]\right)\right|^{2\Delta}}. \tag{D.22}$$

COMPARISON WITH LATTICE GREEN FUNCTION E

Consider a 1D lattice with L sites and periodic boundary conditions, where lengths are measured in units of the lattice constant. The Hamiltonian for N free fermions is given by

$$H = -2\sum_k \cos(k) c_k^\dagger c_k \ , \tag{E.1}$$

where we measure energies in units of the hopping (i.e. $J = 1$). Here, our quantization condition for periodic boundary conditions is

$$k_m = \frac{2\pi}{L} m \quad \text{with} \quad m \in [-N, N) \ . \tag{E.2}$$

For N odd, the ground state is $|\Psi\rangle = \prod_{|k|<k_F} c_k^\dagger |0\rangle$ with $k_F = \pi(N-1)/L$ and the momentum distribution is

$$n_k = \langle c_k^\dagger c_k \rangle = \begin{cases} 1 & |k| < k_F \\ 0 & \text{otherwise} \end{cases} \ . \tag{E.3}$$

To compute the Green function, we define the Fourier transform:

$$c_j = \frac{1}{\sqrt{L}} \sum_k \mathrm{e}^{\imath k j} c_k \ . \tag{E.4}$$

Thus we can write:

$$\langle c_i^\dagger c_j \rangle = \frac{1}{L} \sum_{k,k'} \mathrm{e}^{-\imath k i} \mathrm{e}^{\imath k' j} \langle c_k^\dagger c_{k'} \rangle \tag{E.5}$$

$$= \frac{1}{L} \sum_{|m|<(N-1)/2} \mathrm{e}^{-\imath 2\pi m\, |i-j|/L}$$

$$= \frac{1}{L} \frac{\sin \frac{\pi N}{L}|i-j|}{\sin \frac{\pi}{L}|i-j|} \ . \tag{E.6}$$

The normalization condition that $\mathrm{Tr}\rho_1 = 1$ gives us:

$$\rho_1(|i-j|) = \frac{1}{NL}\frac{\sin\left(\frac{\pi N}{L}|i-j|\right)}{\sin\left(\frac{\pi}{L}|i-j|\right)} \,. \tag{E.7}$$

This gives the same result as Eq. (E.7) by using $x \to (i-j)$.

FLUCTUATIONS FOR PERIODIC BOUNDARY CONDITIONS

F

For a system of length L with periodic boundary conditions (PBC), the boson field operators are given by [49, 222, 223, 242]

$$\phi_{\mathrm{pbc}}(x) = \phi_0 + \pi x \frac{N}{L} - \frac{\mathrm{i}\pi}{L} \sum_{q\neq 0} \sqrt{\frac{L|q|}{2\pi}} \frac{1}{q} e^{-\alpha|q|/2 - \mathrm{i}qx} \left(b_q^\dagger + b_{-q}\right) \tag{F.1}$$

$$\equiv \phi_0 + \pi x \frac{N}{L} + \tilde{\phi}_{\mathrm{pbc}} \tag{F.2}$$

$$\theta_{\mathrm{pbc}}(x) = \theta_0 + \pi x \frac{J}{L} + \frac{\mathrm{i}\pi}{L} \sum_{q\neq 0} \sqrt{\frac{L|q|}{2\pi}} \frac{1}{|q|} e^{-\alpha|q|/2 - \mathrm{i}qx} \left(b_q^\dagger - b_{-q}\right) \ , \tag{F.3}$$

where b_q ($b_q^\dagger$) are bosonic annihilation (creation) operators, ϕ_0, θ_0 are zero modes and α is a short-range interaction cutoff. We consider the density to leading order in the fields [3] $\rho_{\mathrm{pbc}}(x) \approx \partial_x \phi_{\mathrm{pbc}}(x)/\pi \approx \rho_0 + \partial_x \tilde{\phi}_{\mathrm{pbc}}/\pi$ and for the purpose of computing the fluctuations, we neglect the $\cos(2\phi_{\mathrm{pbc}})$ term in the Luttinger Hamiltonian, main text Eq. (1).

Defining $\tilde{\phi}_{\mathrm{pbc}}$ allows us to explicitly separate the density background ρ_0 from the fluctuations.

We can express the particle number operator by explicitly computing the integral of the density operator over the subregion $A \in [0, \ell]$ as

$$\hat{N}_A = \ell\rho_0 + \frac{1}{\pi}[\tilde{\phi}_{\mathrm{pbc}}(l) - \tilde{\phi}_{\mathrm{pbc}}(0)] \ . \tag{F.4}$$

In terms of the particle number operator, the fluctuations are given by

$$\mathcal{F}_{\mathrm{pbc}}(\ell; K, \alpha) = \frac{1}{\pi^2} \langle [\tilde{\phi}_{\mathrm{pbc}}(\ell) - \tilde{\phi}_{\mathrm{pbc}}(0)]^2 \rangle \ . \tag{F.5}$$

Under our assumptions, diagonalizing the Hamiltonian is equivalent to a rescaling of the boson field operators $\tilde{\phi}_{\mathrm{pbc}}(x) \to \sqrt{K}\tilde{\phi}_{\mathrm{pbc}}(x)$, $\tilde{\theta}_{\mathrm{pbc}}(x) \to \sqrt{K}^{-1}\tilde{\theta}_{\mathrm{pbc}}(x)$ [3].

This allows us to explicitly compute the expectation value, yielding the expression for the fluctuations stated in the main text $\mathcal{F}_{\text{pbc}} = \frac{K}{2\pi^2} \ln\left[1 + \frac{\sin^2(\pi\ell/L)}{\sinh^2(\pi\alpha/L)}\right]$.

F.1 Fluctuations for open boundary conditions

In the case of open boundary conditions (OBC), the displacement field can be written as

$$\phi_{\text{obc}}(x) = \phi_B + \frac{\pi x}{L} N + i \sum_{q>0} \sqrt{\frac{\pi}{qL}} e^{-\alpha q/2} \sin(qx) \left[b_q - b_q^\dagger\right] \tag{F.6}$$

$$\equiv \phi_B + \frac{\pi x}{L} N + \tilde{\phi}_{\text{obc}}(x) \,, \tag{F.7}$$

where $\phi_B \neq n\pi$ is a constant, such that the density vanishes at the ends of the chain [49].

Here, the density operator including oscillating terms, is given by [3]

$$\rho_{\text{obc}}(x) = \partial_x \phi_{\text{obc}}(x) \sum_{n=-\infty}^{\infty} \delta(\phi_{\text{obc}}(x) - n\pi) = \frac{1}{\pi} \partial_x \phi_{\text{obc}}(x) \sum_{p=-\infty}^{\infty} e^{-i2p\phi_{\text{obc}}(x)} \,. \tag{F.8}$$

F.1.1 Leading order fluctuations

To leading order, $m = n = 0$, we can compute the particle number fluctuations in an interval $A = [x, x+\ell]$ of length ℓ in analogy to the periodic case. We find

$$\begin{aligned}\mathcal{F}_{\text{obc}}(\ell; x) &= \frac{1}{\pi^2} \sum_{q>0} \frac{\pi K}{L} \frac{1}{q} e^{-\alpha q} \left[\sin(q(x+\ell)) - \sin(qx)\right]^2 \\ &= \frac{K}{\pi^2} \ln \left| \frac{\sin\left[\frac{\pi}{L}\left(\frac{\ell}{2} - \frac{i\alpha}{2}\right)\right] \sqrt{\sin\left[\frac{\pi}{L}\left(x + \ell - \frac{i\alpha}{2}\right)\right] \sin\left[\frac{\pi}{L}\left(x - \frac{i\alpha}{2}\right)\right]}}{\sin\left[\frac{\pi}{L}\left(x + \frac{\ell}{2} - \frac{i\alpha}{2}\right)\right] \sinh\left[\frac{\pi\alpha}{2L}\right]} \right| \,.\end{aligned} \tag{F.9}$$

If we put the interval at the left boundary $x = 0$, the thermodynamic limit, $L \to \infty$, expression of $\mathcal{F}_{\text{obc}}$ does not agree with that for the periodic case, and we would not expect the RG flow to be the same. However, if we center the interval A in the wire, choosing $x = (L - \ell)/2$, we fully recover the asymptotic form of the fluctuation formula from the periodic case

$$\mathcal{F}_{\text{obc}}\left(\ell; x = \frac{L-\ell}{2}\right) = \frac{K}{2\pi^2} \ln\left(1 + \frac{\sin^2(\pi\ell/L)}{\sinh^2(\pi\alpha/L)}\right) \approx \frac{K}{\pi^2} \ln \sin \frac{\pi\ell}{L} + A \,. \quad \text{(F.10)}$$

In contrast, if one considers the interval $[0, \ell]$ starting at the left edge, the fluctuations become

$$\mathcal{F}_{\text{obc}}(\ell; x = 0) = \frac{K}{4\pi^2} \ln\left(1 + \frac{\sin^2(\pi\ell/L)}{\sinh^2(\pi\alpha/2L)}\right) \,. \quad \text{(F.11)}$$

In the thermodynamic limit, this result differs from the periodic case, as $x = 0$ for $L \to \infty$ corresponds to a semi-infinite chain.

F.1.2 Including higher order terms

To leading order $m = n = 0$, the result does not capture boundary effects such as Friedel oscillations that are present in an open chain. All terms n, m can be computed analytically using

$$\rho(x) = \frac{-i}{2\pi} \sum_{n=-\infty}^{\infty} \partial_x \left[\frac{1}{n} e^{2ni(\pi\rho_0 x + \phi(x))}\right] \,, \quad \text{(F.12)}$$

and interchanging the derivative with the sum before integrating the density. By introducing Green functions $G_0(x) = \langle \tilde{\phi}^2_{\text{obc}}(x) \rangle \equiv \ln F_0(x)$ and $G_1(x, y) \equiv$

$\ln F_1(x,y) = \langle \tilde{\phi}_{\text{obc}}(x)\tilde{\phi}_{\text{obc}}(y)\rangle$, we can express the fluctuations as

$$\begin{aligned}\mathcal{F}(\ell;x) = \frac{-1}{4\pi^2}\sum_{nm}\frac{1}{nm}\mathrm{e}^{2i(n+m)(\pi\rho_0 x+\phi_B)}\Bigg[\\ \mathrm{e}^{2(m+n)i\pi\rho_0\ell}\left(F_0^{-2(n+m)^2}(x+\ell) - F_0^{-2(m^2+n^2)}(x+\ell)\right) \\ + F_0^{-2(m+n)^2}(x) - F_0^{-2(m^2+n^2)}(x) \\ - 2\mathrm{e}^{2mi\pi\rho_0\ell}F_0^{-2m^2}(x+\ell)F_0^{-2n^2}(x)\left(F_1^{-4nm}(x+\ell,x)-1\right)\Bigg]. \end{aligned} \tag{F.13}$$

One can explicitly compute the Green functions, yielding

$$F_0(x) = \left(1 + \frac{\sin^2\left(\frac{\pi x}{L}\right)}{\sinh^2\left(\frac{\pi\alpha}{2L}\right)}\right)^{\frac{K}{4}} \tag{F.14}$$

$$F_1(x,y) = \left(\frac{\cos\left(\frac{\pi}{L}(x+y)\right) - \cosh\left(\frac{\pi\alpha}{L}\right)}{\cos\left(\frac{\pi}{L}(x-y)\right) - \cosh\left(\frac{\pi\alpha}{L}\right)}\right)^{\frac{K}{4}}. \tag{F.15}$$

However, we find that including the higher order terms has effectively no effect on the fluctuations, as the $n = m = 0$ term dominates the expression. We therefore do not include them in the comparison below.

VITA

Harini Radhakrishnan was born and raised in Columbia, Maryland. After watching *Interstellar* and bugging her high school physics teacher about special relativity, she discovered a lasting passion for the subject. She earned a B.S. in Mathematics, with a minor in Physics, from the University of Chicago in 2019.

In August 2020, she began her Ph.D. in physics at the University of Tennessee–Knoxville. After two years as a Graduate Teaching Assistant, she joined the research group of Professor Adrian Del Maestro as a Graduate Research Assistant. Her research investigated particle entanglement and other observables in one-dimensional microscopic systems through the lens of field theory. This work resulted in several peer-reviewed publications and conference presentations. In 2024, she received the Marion-Fowler outstanding graduate student award from the physics department at the University of Tennessee. She defended her doctoral dissertation in June 2025.

In September 2025, she will begin a Postdoctoral Research Associate position in Professor Jörn Venderbos' group at Drexel University, where she will focus on topological and magnetic systems – particularly novel phases and formal diagnostics for real materials. She is incredibly grateful for the support and encouragement from her mentors, friends, and family.